THESIS

THE EFFECTS OF A REALISTIC HOLLOW CATHODE PLASMA CONTACTOR MODEL ON THE SIMULATION OF BARE ELECTRODYNAMIC TETHER SYSTEMS

Submitted by

Derek M. Blash

Department of Mechanical Engineering

In partial fulfillment of the requirements

For the Degree of Master of Science

Colorado State University

Fort Collins, Colorado

Fall 2013

Master's Committee:

Advisor: John D. Williams

Thomas H. Bradley
Raymond S. Robinson

Abstract

THE EFFECTS OF A REALISTIC HOLLOW CATHODE PLASMA CONTACTOR MODEL ON THE SIMULATION OF BARE ELECTRODYNAMIC TETHER SYSTEMS

The region known as Low-Earth Orbit (LEO) has become populated with artificial satellites and space debris since humanities initial venture into the region. This has turned LEO into a hazardous region. Since LEO is very valuable to many different countries, there has been a push to prevent further buildup and talk of even deorbiting spent satellites and debris already in LEO. One of the more attractive concepts available for deorbiting debris and spent satellites is a Bare Electrodynamic Tether (BET). A BET is a propellantless propulsion technique in which two objects are joined together by a thin conducting material. When these tethered objects are placed in LEO, the tether sweeps across the magnetic field lines of the Earth and induces an electromotive force (*emf*) along the tether. Current from the space plasma is collected on the bare tether under the action of the induced *emf*, and this current interacts with the Earth's magnetic field to create a drag force that can be used to deorbit spent satellites and space debris. A Plasma Contactor (PC) is used to close the electrical circuit between the BET and the ionospheric plasma. The PC requires a voltage and, depending on the device, a gas flow to emit electrons through a plasma bridge to the ionospheric plasma. The PC also can require a plasma discharge electrode and a heater to condition the PC for operation. These parameters as well as the PC performance are required to build an accurate simulation of a PC and, therefore, a BET deorbiting system. This thesis focuses on the development, validation, and implementation of a simulation tool to model the effects of a realistic hollow cathode PC system model on a BET deorbit system.

ACKNOWLEDGEMENTS

My time spent at CSU was one of the best experiences I have ever had and without the amazing opportunity and contributions my advisor, Dr. John D. Williams, provided me with, it would not have been possible. His expertise, instruction, and encouragement lead to the successful completion of this thesis. Special thanks are also given to the professors on my committee, Dr. Thomas H. Bradley and Dr. Raymond S. Robinson, for their support, instruction, and understanding during the completion of this thesis.

I would like to also acknowledge the contributions of my fellow plasma contactor researchers: Mr. Rafael A. Martinez, Dr. Casey C. Farnell, and Dr. Kan Xie, whose reports and experimental work lead to the development of the hollow cathode plasma contactor model presented in this thesis. In addition, the supportive and free exchange of simulation results, ideas, and countless emails and phone conversions with Dr. Sven G. Bilén's group at Pennsylvania State University, specifically Mr. Jesse K. McTernan, and with Dr. Gonzalo Sánchez-Arriaga and his colleagues in Dr. Juan Sanmartin's group at the Universidad Politécnica de Madrid that lead to the completion and validation of SimBETS for use in this thesis.

Great thanks also go to my colleagues for their great support and company during the year and a half I spent at the CSU Engineering Research Center. I hope you all the best.

I would like to thank my parents, Michael and Laura Blash, for their support and funding that gave me the opportunity to have a great life even when times were difficult. My thanks also go out to my girlfriend, Cara Hope, for her support and help these past few years. I am lucky to have her in my life.

Great thanks are also due to Leif Anderson for building this LaTeX document class, allowing me to meet the graduate school formatting requirements with no effort on my part.

TABLE OF CONTENTS

CHAPTER 1

INTRODUCTION

The region known as Low-Earth Orbit (LEO), located between $\sim\ 200\,km$ and $2,000\,km$ above Earth, has been relatively unpopulated for most of the Earth's life, being filled mostly with small rocks and ice. However, since 1958, humanity has begun to investigate and populate this area with artificial satellites. This population increase would not be an issue if the satellites were traveling at low relative velocities, however, relative orbital speeds can be in the hypervelocity range of 7 to $8\,km/s$, or $15,000$ to $18,000\,mi/h$. Figure 1.1 shows the damage a hypervelocity impact can have on a thick piece of metal.

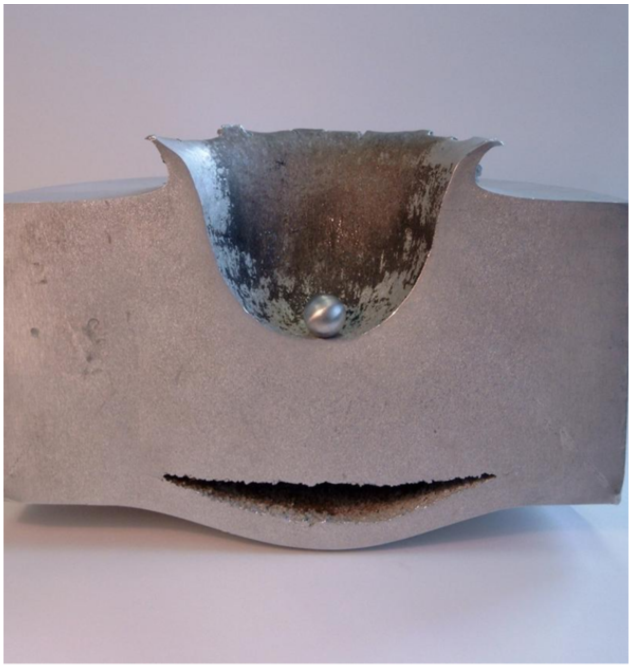

FIGURE 1.1. A hypervelocity impact [1].

As an increasing number of satellites populate a particular region, like the 98 ± 2^o inclination [2], the chances of these objects impacting other objects in a higher or lower inclination increases exponentially. If the collision occurs in a high population region, the resulting fragmentation could impact other objects and create more debris. This chain reaction could be so catastrophic that it would create a debris cloud that would prevent any safe use of satellites in LEO. This is known as the Kessler syndrome [3]. The Kessler syndrome is a run-away chain reaction of the collisions between objects in orbit that leads to a densely populated debris field. Since LEO is very valuable to so many countries, there has recently been a push to prevent further buildup of spent satellites and talk of even deorbiting spent satellites and debris already in LEO.

Much like recycling of waste on Earth, recycling and properly deposing of spent satellites and space debris is being considered for LEO [4]. However, this is much more difficult than current recycling methods on Earth's surface due to the excessive cost associated with launching mass into LEO. As of June 2013, Space Exploration Technologies Corporation, also known as Space X, offered the lowest price ($5000/kg [5]) to place a satellite into LEO using their Falcon 9 expendable launch vehicle. Since atmospheric drag and other effects are so minimal in LEO, satellites remain in orbit for many decades. Consequently, the space industry is now required to remove rocket stages and spent satellites after their mission is complete. A standard method of removal is the use of chemical rockets; however, they require a large amount of propellant mass due to their relatively low specific impulse. Another method focuses on electrically powered propulsion devices like ion and Hall thrusters. These devices are highly efficient in their use of propellant mass, but require long mission times due to their low thrust. They also require a complex gas feed, storage, and large on-board power system. Noting these issues, space agencies, private space enterprises, and universities around the world have begun working on improved methods for deorbiting spent satellites. Many different ideas have been proposed including: orbital refueling and recycling stations

[6, 7], space tethers [8, 9], space based laser-induced thrusters [9] and even adhesive collection objects [9]. The most ideal method would be a reliable, efficient thruster system that does not require any propellant, on-board power, is easy to manufacture and implement, and is highly reliable. Of the proposed concepts, a space tether, more specifically an Electro-Dynamic Tether (EDT), is a likely candidate to meet these ideal specifications and is the focus of this thesis.

An EDT is a propellantless propulsion technique in which two objects are joined together by a thin conducting material [10]. When these tethered objects are placed in LEO, the tether sweeps across the magnetic field lines of the Earth. This interaction induces an electromotive force (*emf*) along the conducting cable. Current can then be collected using a collection device, a bare tether collection scheme is described below. This current flows down the conductive tether and interacts with the Earth's magnetic field and creates a force. Depending on whether the system is passive (letting electrons naturally flow in the tether) or active (forcing electrons to flow against the imposed *emf*), this propulsion technique can be used to either lower or raise the orbit of an object, respectively.

1.1. Objective

Colorado State University (CSU) has been working with other universities and space agencies to develop the EDT concept into a flight-ready system for regular use in future missions. The main focus for these EDT systems is their implementation on new objects being sent up into LEO. This focus will help prevent the space debris issue from getting any worse. However, there are still many issues associated with EDTs that are preventing their deployment on LEO satellites. Some of these issues include component reliability [8], catastrophic failure due to the chances of the tether being cut by debris [10, 11], tether strength degradation due to high temperatures caused by ohmic and solar heating [8], librational instabilities [10, 12, 13], and incomplete modeling and prediction simulations [14, 15, 16]. CSU is currently focusing on the modeling, simulation, and testing of a Hollow Cathode Plasma Contactor (HCPC) system for EDTs. The plasma contactor (PC) is important to the operation of an EDT because it is used to close the electrical circuit between the EDT and the ionospheric plasma. The details of a PC are discussed in Section 1.5.5. As a result of the PC's importance to an EDT, the main objectives of this thesis include:

- Development of a bare EDT design decision support tool that includes a realistic HCPC system.
- Discovery of operational requirements of the system and the sensitivities of EDT system mass due to these requirements.
- Identifications of strengths and weaknesses of bare EDTs..

1.2. Overview of Thesis Sections

The information provided above was a brief introduction to the topics and studies that will be discussed. There are 4 chapters associated with this thesis. Chapter 1 discusses the objective of the thesis and provides background information for readers unfamiliar with EDTs. This background, presented in the sections below, includes a brief overview of the debris and spent satellites currently in orbit and the dangers they pose, the fundamentals of an EDT, the components of an EDT, EDT flight history, EDT systems analyses, and EDT systems performed to date. Chapter 2 discusses the specifics of the models used in the simulation tool developed in this thesis. This tool was design to simulate bare electrodynamic tether systems during orbital propagation and is thus called SimBETS. The models include: orbital mechanics and orbital propagation models focusing on mulitple coordinate system transformations and the Runga-Kutta-Fehlberg (4,5) method; EDT models; and atmospheric, ionospheric, and magnetic field models. Chapter 3 describes the validation of SimBETS and the various Software-In-the-Loop (SIL) and Hardware-In-the-Loop (HIL) tests performed using the simulation. Chapter 3 also presents and discusses the results of the systems analysis. Chapter 4 provides conclusions and recommendations for future work.

1.3. Debris and Spent Satellites

Space debris can be considered any object orbiting Earth that has broken apart from a larger object. Spent satellites are usually lumped into this description even though the vehicle is still intact. Debris can range from car sized dead satellites to paint chips separated from spent upper-rocket stages. Due to the high orbital velocity these objects travel at, when one impacts another object, the results can be devastating. As a reference for how dangerous this debris can be, the shuttle mission STS-92 in 2000 had a paint chip of 0.33 x 0.76 mm impact one of the windows of the craft and dig a pit 1.90 mm in depth and 10 mm in diameter [17]. As of 2009, more than 19,000 items greater than 5 cm in size were under constant surveillance by ground and space based systems. More than 300,000 objects smaller than 1 cm are estimated to exist at altitudes below 2000 km [18]. Comparing the number of pieces of known debris present in LEO today to the number of pieces in the 1960's when humanity began to venture into this area is astounding. Figure 1.2 is a representation of the increasingly populated space around our planet.

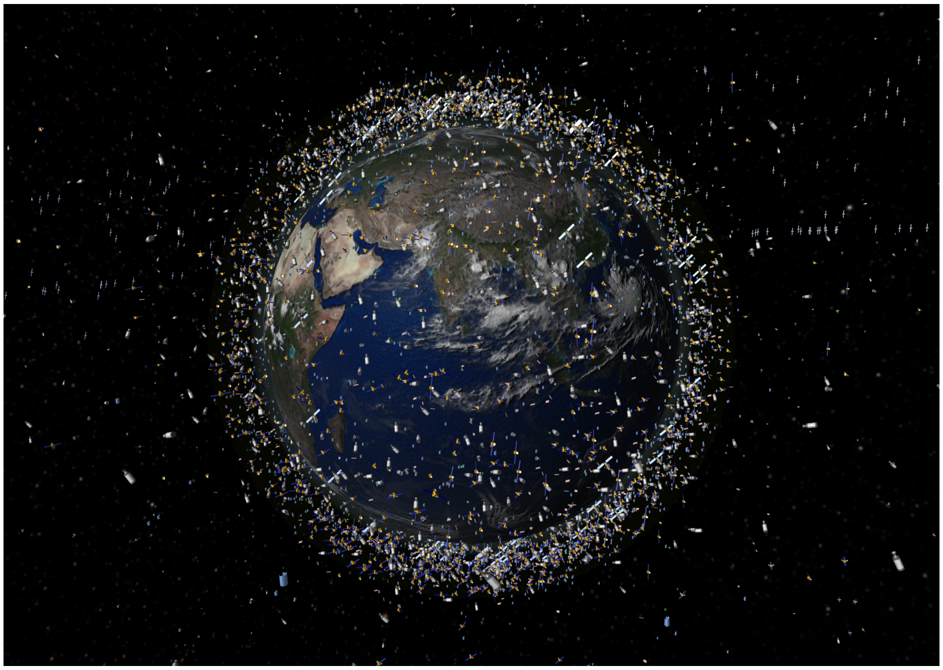

FIGURE 1.2. Artist rendering of the orbital debris and spent satellites currently in LEO [1].

Soon, if current space activity continues, a possible situation known as the Kessler syndrome could be inflicted on the LEO region. The Kessler syndrome, also known as the collisional or ablation cascade, was posed by Donald J. Kessler in 1978 at NASA [3]. It can be described as a scenario in which the density of objects in LEO is high enough such that the collisional rate increases exponentially until the entire population, still in use or dead, is reduced to sub-critical sizes [1, 3]. The implications of this is the possible rendering of the space environment nearly unusable for current and future generations [3]. However, various methods, especially EDTs, have the ability to help prevent the Kessler Syndrome diagnosis from occurring.

1.4. Electro-Dynamic Tether Fundamentals

As an EDT sweeps across the Earth's ionosphere, several physical interactions occur between the tether and the ionosphere including gravity gradient stabilization, electron and ion collection, current and magnetic field interaction, atmospheric drag, electron emission, and electron transport through the ionosphere.

1.4.1. Gravity Gradient Stabilization

An orbiting object will always orbit a gravitational body based on the objects center of gravity. This is even true for a tethered satellite (TS). Depending on an objects position and velocity, it could have an orbit different than an object only meters away. This variation is due to the required balance between centrifugal and gravitational forces for an orbiting object. In a non-rotating TS, the upper mass experiences higher centrifugal force while the lower mass experiences higher gravitational force. Because the two satellites are tethered, they cannot continue on their own orbital paths. The result is the TS following the orbital path of its center of gravity, which is located somewhere along the tether. This means the tension in the tether makes up for the unbalanced gravitational and centrifugal forces on the upper and lower masses. Because of these forces, the tether also naturally aligns itself with the pull of gravity along the local vertical. This results in gravity gradient stabilization as shown in Figure 1.3.

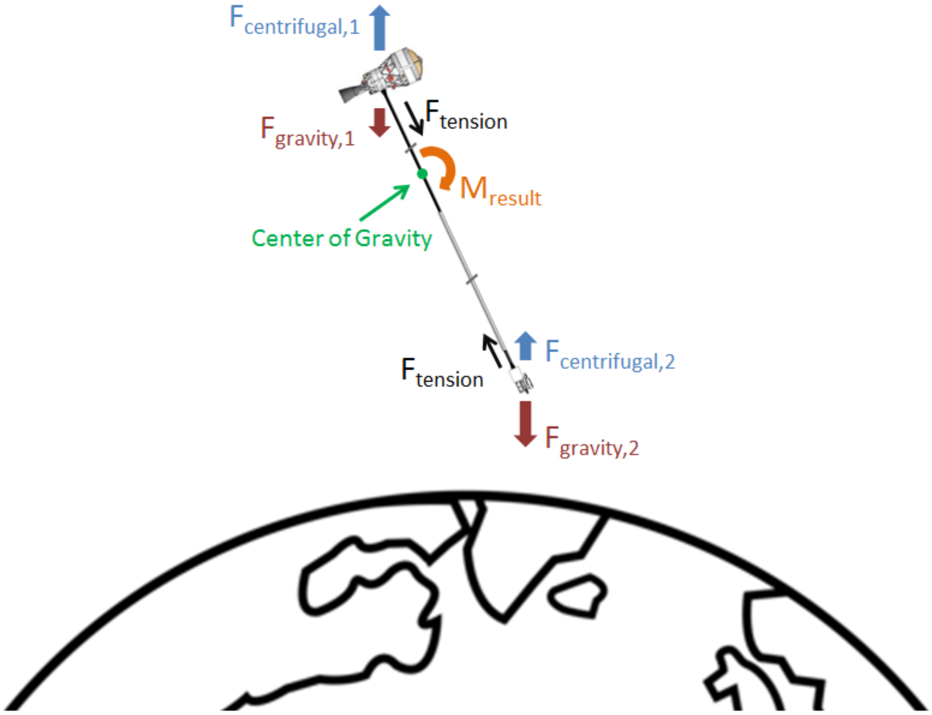

FIGURE 1.3. Gravity gradient stabilization between two tethered satellites. In a near vertical orientation the balance of the centrifugal and gravitation forces on each end body of the tether are not equal, forcing the tether to account for the difference. With no perturbing forces, the resulting force at each end body produces a moment that rotates the tether to a stable point in which the forces at each end body are aligned along the local vertical of the Earth.

Gravity gradient stabilization is an important factor in TS operation because it allows the tether to sweep across the Earth's magnetic field and generate an electric potential between the tether ends. Another note on gravity gradient stabilization is the magnitude of tension generated from this phenomenon. As the tether length increases, the TS is increasingly more prone to stay in this configuration therefore increasing the stability of the system. More information on gravity gradient analysis can be found in the Tethers in Space Handbook [8], the Dynamics of Tethered Space Systems [19], and the Guide Book for Analysis of Tether Applications [12].

1.4.2. Electron and Ion Collection

The ionosphere of the Earth is a region of the atmosphere that is ionized by incoming solar radiation, therefore, the ionospher, is a plasma. A plasma is a mixture of ions, neutral atoms, and electrons and is therefore subject to electrodynamic effects. As such, when an electric potential develops between a conductive tether and the plasma environment due to electromagnetic induction, charged particles will either be repelled or attracted. Attracted particles will be collected by the biased surface while repelled particles will be returned to the space plasma. The collection of these charged particles to the biased surface is defined by the Orbital Motion Limited (OML) theory assuming certain criteria are met. The OML theory and its applicability to surfaces in a plasma will be explained in Chapter 2 based on references [20, 21, 22].

1.4.3. Current and Magnetic Field Interaction

The Earth's interior consists of a dense hot liquid made of ferritic material such as nickel and iron. The resulting convection in the core creates the Earth's magnetic field [23] and also allows an EDT to create thrust and drag. As an EDT intersects the magnetic field lines of the Earth, an electric potential is built along the tether. Equation 1 describes the electric potential induced in the EDT,

$$\mathbf{E_m} = \mathbf{v_{relative}} \times \mathbf{B} \tag{1}$$

In Equation 1, E_m is the electric field strength, $\mathbf{v_{relative}}$ is the relative velocity of the EDT with respect to the Earth (since the Earth rotates), and $\mathbf{B}$ is the Earth's magnetic field strength. For a certain orbit, there is a given velocity and magnetic field strength, around

$7.5\,km/s$ and $20\,\mu T$, which produces an electric potential of around $0.15\,V/m$ (which equals$\sim$ $150\,V$ electromotive force for a $1\,km$ bare tether section) in equatorial orbits. The length of the tether multiplied by the induced electric field yields the *emf* across the tether. Depending on the tether, electron density, and the *emf*, this could allow the tether to collect upwards of $10-20\,A$. This is important because the interaction of this current and the Earth's magnetic field creates a Lorentz force. The larger the Lorentz force, the higher the orbital decay rate. Equation 2 is the Lorentz force equation in terms of current conducted in a solid interacting with a magnetic field,

$$\mathbf{F} = \int_0^{\mathbf{L}} \mathbf{I}\mathrm{d}\hat{l} \times \mathbf{B} \tag{2}$$

In Equation 2, **F** is the force created and **I** is the current. Forces for a $5\,km$ tether can reach values as high as $0.5-1\,N$, which is adequate to deorbit most satellites in a relatively short period.

At its heart, an EDT works much like an electric generator or motor. An electric generator generates electrical power by converting motional energy into electrical energy. Operation in this mode is known as the passive mode of an EDT system and can theoretically operate without any extra energy provided to the system. The electrical motor mode generates motion by converting electrical energy to kinetic energy. This mode, in an EDT system, is known as the active mode. It is so named because the system must carry an on-board power source to overcome the electric potential created by the orbital motion. This thesis is focused on the passive or short circuit mode, which is useful for deorbiting debris and spent satellites.

1.4.4. Atmospheric Drag

An object in LEO is subject to atmospheric drag, which becomes significant at altitudes below $s \sim 300\,km$. The International Space Station (ISS) and other satellites are under this force continuously, and, they are required to periodically reboost themselves to their proper orbits to avoid premature re-entry. As such, an EDT sees atmospheric drag forces as well as the Lorentz forces. The atmospheric drag on an EDT, however, is more significant than on a regular satellite because the EDT has a significantly larger projected area, on the order of $40\,m^2$ for a $2\,km$ tether. Yet, unlike the ISS and operating LEO satellites, increased drag force is ideal for deorbiting debris because it decreases the amount of time the object spends in orbit. Therefore, an EDT only needs to bring an object down to $\sim 300\,km$ such that atmospheric drag can take over. More information on the atmosphere and atmospheric drag can be found in Ch. 2 and in references [24, 25, 26].

1.4.5. Electron Emission

Multiple methods allow for electrons to be emitted into the space plasma. The system most used today is the HCPC and is the focus of this thesis. A hollow cathode plasma contactor (HCPC) itself, is a relatively simple device that consists of a cathode tube, low work function insert, heater, and keeper as shown in Figure 1.4.

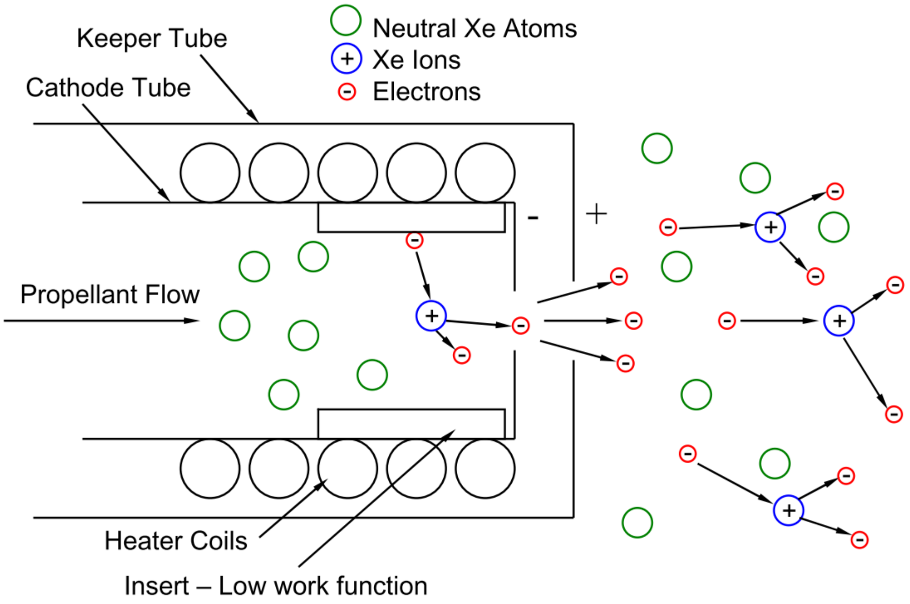

FIGURE 1.4. Diagram of a hollow cathode plasma contactor (HCPC). Electrons are extracted from the low work function insert to sustain the plasma and supply the electron to the ionospheric plasma [27].

A HCPC connects with the ionosphere by emitting a dense plume of ionized gas. This plasma is produced by first flowing expellant through the hollow cathode tube and heating the low work function insert embedded inside the hollow cathode. Once the insert is hot, it will begin to emit electrons off the surface. The positively biased keeper pulls electrons from inside the cathode tube out into the open space around the cathode orifice. The plasma plume produced here expands from the cathode and keeper and forms a conductive plasma bridge to the ionosphere, which allows electrons to flow from the cathode into the ionosphere and thus creates an electrical connection [27].

1.4.6. ELECTRON TRANSPORT THROUGH THE IONOSPHERE

The movement of emitted electrons back to the electron collection area of the tether is somewhat of an unknown phenomenon. Some theories suggest the electrons move from the

HCPC into the space plasma and then follow magnetic field lines toward the poles where the density of the field lines and plasma is high enough for the electrons to cross magnetic field lines and then follow the field lines back down to the bare tether. More information on this topic can be found in reference [14].

1.5. The Electro-Dynamic Tether System

There are many different components in an EDT as shown in Figure 1.5. The EDT consists of an inert, bare-conductive, and insulation-wrapped conductive tether; an electron emitting system; electronics; tether deployer; structural supports; and protective outer layers. The materials used in each component are chosen such that performance criteria and failure limits meet flight standards. The following sections briefly discuss the EDT system and its components, materials, and configurations, along with the current issues plaguing these components.

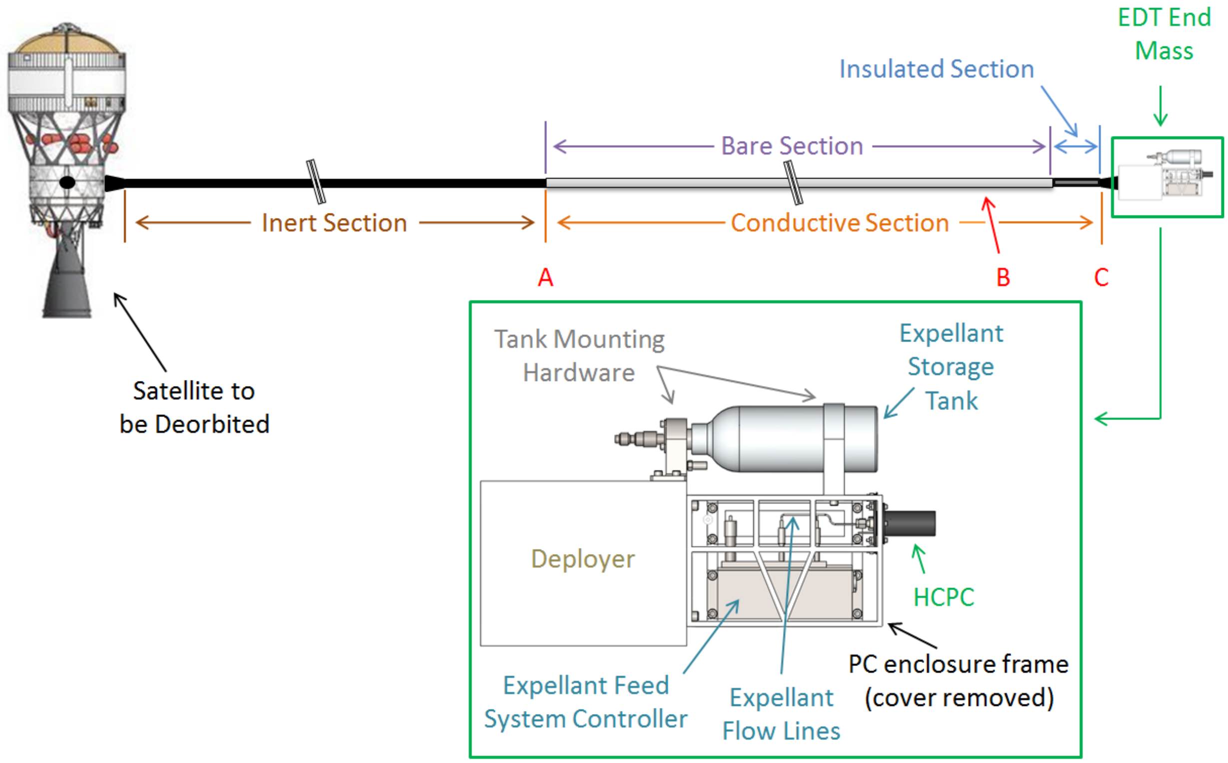

Figure 1.5. Diagram of the components of a passive bare EDT system.

1.5.1. Satellite to be Deorbited

Another important component of an EDT deorbiting system is the satellite being deorbited. In fact, a deorbiting mission will depend almost entirely on the satellite's dimensions, mass, mass distribution, configuration, payload, and left over fuel. Each of these parameters affect how the EDT system will be designed and optimized. The dimensions of the satellite will affect the atmospheric drag force produced on the satellite. The mass of the satellite will determine tether length, width, thickness, and amount of xenon required for the HCPC system. The placement of an EDT system on the satellite of interest can determine maximum dimensions and overall design due to limited space inside an expendable launch vehicle. Overall, the EDT is designed around the satellite for deorbit and, therefore, requires the EDT design to be highly flexible.

1.5.2. The Tether

The electrodynamic tether consists of two parts:

1.5.2.1. The Inert Section

A tether is made up of three parts: an inert section, a conductive section, and an insulated-conductive section. The inert section is made up of an electrically insulative, low density material meant to separate the satellite being deorbited from the conductive section of the tether. The inert section also adds stability while minimizing added mass. It is typical to have the inert section be equal to the length of the conductive section.

1.5.2.2. The Conductive and Insulated Conductive Sections

For a bare EDT, the conductive section of the tether is left bare with only the portion nearest the HCPC insulated. Typically the insulated length is about a few hundred meters. The insulation length is used to decrease the likelihood of current exiting the PC and immediately returning to the tether.

The following text refers to Figure 1.6. When a portion of a tether is left bare to collect electrons, portion AB, the electric potential will decrease due to electron collection and *emf*, however, the current will build until the tether and the space plasma potential are equal, point B. Once this occurs, the tether begins to attract ions and decrease the current. Electron collection is much greater than ion collection due to the mass and size of ions being much greater than electrons, and, therefore, causing the ions to move much slower. The decrease in current due to ion collection is so small, it cannot be seen in Figure 1.6. It is often so small that it is even left out of most simulations. The last bit of information that can be gathered from Figure 1.6 is the voltage profiles dipping below $0\,V$ into the negative biased region, reaching $-50\,V$ at point C. Ideally, this is undesirable, but realistic models of the HCPC require this negative bias to emit electrons back to the ionosphere. SimBETS consideration of point C is the main focus of this thesis. For more information on this topic, see Chapter 2 and reference [20].

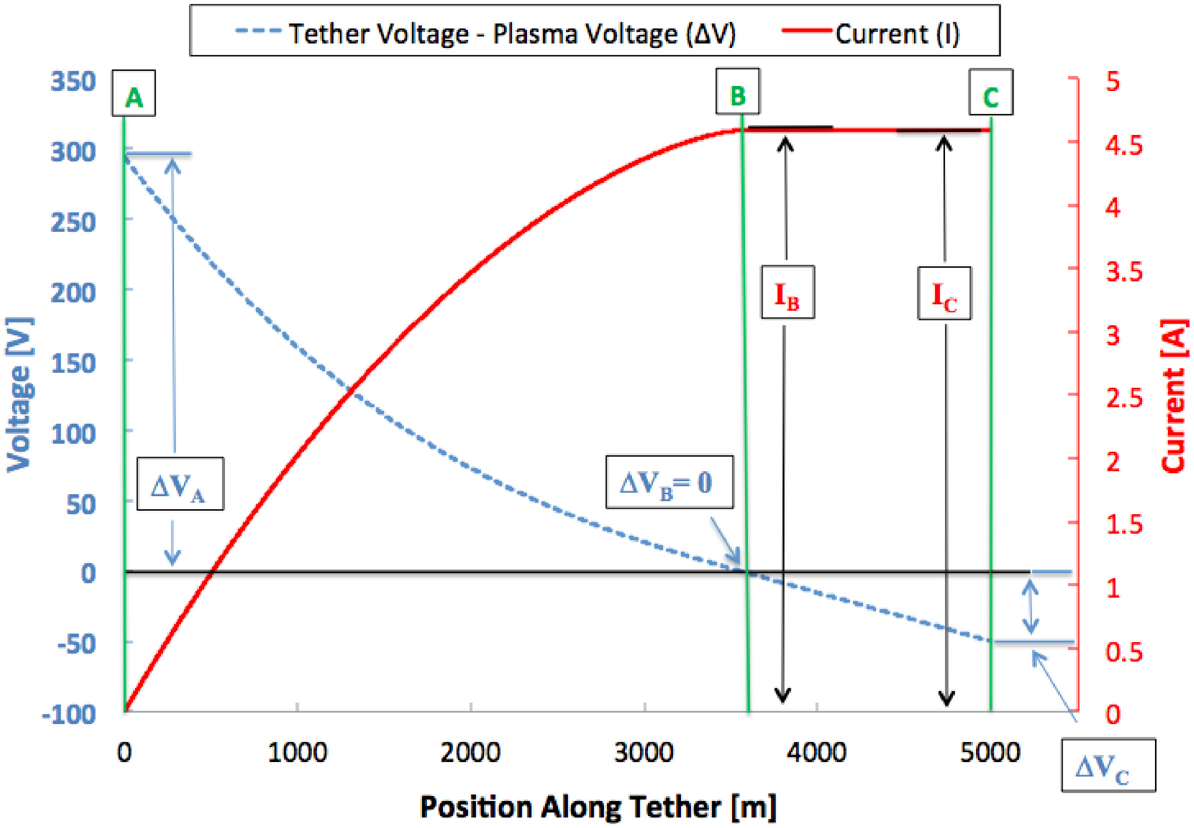

FIGURE 1.6. Current and voltage profiles along a $5\,km$ bare tether.

1.5.2.3. TETHER ISSUES

Ever since the idea was originally suggested, space tethers and more specifically EDTs have come across multiple road blocks, despite the relative simplicity of the idea. Of most concern is the EDT's likelihood of harming other equipment operating in orbit if the tether was struck and severed by debris. To combat this issue, researchers use models to predict tether cut probability. Also, new tether designs including braided, weaved, expanded, and ribbon tethers have been suggested to increase cut survivability [28]. As for collision issues, more advanced tether simulation codes have become available for predicting the path of an EDT. Knowing the path allows for collision issues to be addressed during mission planning.

Other issues associated with tether flights include: tether instability such as libration, material failure due to space environment degradation or excessive loading, deploying and braking issues, electron collection and emission modeling, electrical arcing, and insufficient power production in certain orbits. All of these issues are currently being worked on around the globe. So much work is being done that it is believed regular EDT and space tether operations could be a reality in the next 5 to 10 years. More information on tether research issues can be found in references [8, 29].

1.5.3. Deployer

Due to the excessive length of an EDT, a system must be used that holds the packaged tether until it is needed. Once this necessity is reached, this system then has to deploy the tether in a proper manner. This system is known as a deployer and can be quite complicated due to the length of some tethers. This system must handle storage, initial deployment (since gravity and centrifugal forces are not large enough to pull the two ends apart), controlled deployment for most of the length, and controlled braking for the final length to prevent the tether from fully extending and sending the end mass rebounding back toward the deployer. Of the systems studied in the EDT field, the deployer has been covered the most as described in references [8, 29, 30]. In this thesis, the deployer is a black box that is assumed to have successfully deployed the tether and only affects the simulations by adding mass.

1.5.4. Electronics

As current exits the conductive section of the tether, it enters into the end mass where power can be harvested to drive electrical loads [14, 16]. Of most importance, other than the plasma contactor, is the electronics associated with the plasma contacting system. The harvested power provided by the tether must be, at a minimum, enough to operate the PC so it can emit the required current to the space plasma. Without the PC, current will not flow through the system and, therefore, render the system and the tether useless. Specifically considering a hollow cathode plasma contacting system, the electrical energy must be used to: run the electronics that control the flow system, electrically heat the hollow cathode during low current emission operation, and provide the electrical bias on the keeper to maintain the plasma discharge present. For more information on EDT electronic systems see references [14, 15, 31].

1.5.5. Plasma Contactor Overview

To complete the circuit between the EDT and the space plasma, charge must be flowed from the EDT system back into the ionosphere. This is accomplished by the use of a PC device. There are many different ways to return electrons back to the space environment however, the scientific community is focusing on the use of three active electron emitting technologies. These plasma contacting devices are: HCPCs, Thermionic Emission Cathodes (TECs), and Field Emitter Arrays (FEAs). This thesis focuses on the use of a HCPC.

See Section 2.2.4 for more information on HCPCs. More information is also available in references [14, 32, 33].

1.6. Past Work

The idea of a tether extending upward into the reaches of space has been considered since the end of the 19th century. The idea was initially inspired by the Eiffel Tower in Paris, France. From there, it progressed towards space elevators and then tethered satellites. This idea has inspired multiple analyses to be performed on the subject, which have led to many space flights. These milestones provided scientists with new information on the subject and lead to new challenges, many relating to EDTs. Below is a brief discussion of the EDT related flights, analyses, and achievements that have been completed to date. Information on other tethered flights can be found in references [8, 19].

1.6.1. Past and Future Flights

Below is a brief overview of the EDT orbital and suborbital flights that have flown. For more information on other tethered satellite flights including sounding rockets see references [8, 34, 35].

1.6.1.1. CHARGE 2

The first EDT related flight was a sub-orbital flight on board a sounding rocket in December of 1985. A sounding rocket flight consists of a rocket traveling to an altitude near the desired orbital altitude and completing an experiment near the peak of its projectile-like flight path. The experiment only lasts a few minutes since the craft is not traveling at the necessary orbital velocity to keep it aloft, however, these flights have provided valuable results for space tethers for a fraction of the price of launching into orbit. The Cooperative High Altitude Rocket Gun Experiment-2 (CHARGE-2) was a joint venture between Japan and NASA. The flight was meant to focus on measuring payload charging and returned currents during periods of electron emission. Secondary objectives focused on the plasma processes associated with direct and pulsed current firings using a low-powered electron beam source [36].

The flight resulted in proving that it was possible to enhance electron current collection capabilities of positively charged satellites by means of deliberate neutral gas release into an undisturbed space plasma. The enhanced electron collection performance was attributed to the partial ionization of the neutral gas [37]. For more information see reference [36].

1.6.1.2. TSS-1

The second EDT related flight was aboard the Space Shuttle in July 1992 in which a Tethered Satellite System (TSS) mission was launched. The mission itself was meant to verify the tether concept of gravity gradient stabilization and provide a research facility for plasma and plasma electrodynamics. The mission was cut short however when last minute design changes resulted in a failure of the deployer and prevented the TSS from deploying. The TSS only deployed $250\,m$ but provided an unexpected benefit in the discovery that a short tether deployed from an object is far more stable than expected. The flight also settled several short deployment dynamics issues and helped reduce safety concerns. For more information see references [8, 29].

1.6.1.3. TSS-1R

Due to the partial success of TSS-1, TSS-1R (standing for TSS-1 Reflight) was flown in February of 1996. The TSS-1R was launched on the STS-75 shuttle mission with the intent to deploy a 20.7 km conductive tether. The motion of the conductive tether through the Earth's magnetic field combined with the excessive length of the tether produced a significant *emf* that drove current through the tether. During the flight, the tether was only deployed to 19.7 km, but this was close enough to the full deployment length to allow for useful data collection. The results included measuring the *emf* [38], satellite end mass potential [37], the shuttle potential [39], the current in the tether [40], the changing resistance in the tether [41], the charged particle distributions around a highly charged spherical satellite [42], and the ambient electric field [38]. An additional discovery was enhanced collection of current to the spherical end mass when held at potentials above a given threshold. This particular result showed some numerical models to be a few orders of magnitude lower than the observed currents [43]. The mission was considered a great success and allowed for improvements in the modeling of electron collection [40], the understanding of the interaction of bodies with surrounding plasma, and the understanding of the production of electrical power [44]. The TSS-1R experiment, however, was cut short when an electrical arc developed between a pin hole in the tether insulation and the space plasma near the shuttle. The arc severed the tether and ended the mission. For more information see references [8, 14, 29].

1.6.1.4. PMG

On June 26, 1993, the Plasma Motor Generator (PMG) experiment was launched on a Delta II rocket as a secondary payload. This tether was only 500 m long and made from 18-gauge copper wire. A simple passive braking system was used in this mission in which the innermost layers of wire were wound onto a weak adhesive coating on the deployer core [29]. The mission also demonstrated the ability of a HCPC to connect with the ambient space plasma and generate external current closure of currents up to $0.33\,A$, with external voltage drops on the order of $25\,V$ [29]. Even though a flight hardware failure occurred, the system's ability to collect and emit electrons was established. The system also demonstrated both the boost, altitude raising mode, and the deboost, altitude lowering mode, and power generating mode. The successful PMG experiment led to the use of HCPCs for grounding of the ISS [29].

1.6.1.5. T-REX

T-REX, or Tether Technologies Rocket Experiment, was a Japanese Aerospace Exploration Agency sponsored sounding rocket experiment launched in late August 2010. The T-REX was developed to test a bare EDT, the fast ignition of a hollow cathode, and a "Foldaway Flat Tether Deployment System". When launched, the tether of $309\,m$ was deployed to about $130\,m$ of its full length in the allotted time frame. The flight also showed successful fast ignition of a hollow cathode, but problems were encountered in the tether biasing phases of the experiment [45].

1.6.1.6. Grounded Flights: ProSEDS

NASA Propulsive Small Expendable Deployer System (ProSEDS) mission was developed to fully test the bare EDT concept and determine the accuracy of the Orbital Motion Limited (OML) theory. The ProSEDS mission was suppose to deploy a $5\,km$ tether and collect up to $2\,A$ of current from the ionosphere. The current would then interact with the Earth's magnetic field, produce a Lorentz drag thrust, and deorbit the system at more than $5\,km/day$.

The ProSEDS mission was originally planned to fly in the early 2000's, however, it was canceled due to the Space Shuttle Columbia accident. The mission itself is still available for completion in the future, but there are currently no organizations taking on this initiative at the present time. For further discussion and analysis on the ProSEDS mission see references [11, 30, 34, 46, 47, 48, 49].

1.6.2. Past System Studies

Since before the first mechanical-only tethered system test in the Gemini program, multiple studies have been performed to predict the results of space tethers. Of these systems, the most notable EDT systems analyses have been performed in the last 20 years. For more information on these studies, see references [15, 16, 31, 34, 50, 51, 52]. However, very few systems studies have been performed that include a detailed description of a PC subsystem.

Fuhrhop et al. completed a study that compared various electron emission technologies and compared their efficiency and power consumption [51]. However, the model used for the HCPC is relatively outdated and not believed to represent the device that would be used for operation. McTernan et al. completed multiple studies using a software package called TeMPEST in which he added several energy storage and harvesting concepts [15, 16, 31]. These studies are well done; but they use the overly simplified HCPC model discussed in reference [14].

Ahedo et al. has performed multiple systems studies relating to EDTs using non-dimensionalized solutions of the electron collection equations [50]. These studies focus on voltage and current profiles, efficiencies, and trade-offs between chemical, electric, and EDT propulsion devices. All of these studies, however, assume the cathodic voltage is ideal, i.e. zero volts. Therefore, these analyses only allow one to perform basic system studies. To date, studies using a realistic HCPC model implemented into a detailed EDT simulation have yet to be published.

1.6.3. EDT Simulations

There are several computational codes for analyzing features of space tethers. These codes range from dynamics and control simulations to energy harvesting and systems optimization. The most notable codes relating to the research in this thesis are those developed by Brian Gilchrist's group at University of Michigan, Ann Arbor known as TeMPEST (Tethered Mission Planning Evaluation Software Tool) [34, 53] and Dr. Juan Sanmartin's group at University of Madrid known as BETsMA (Bare Electrodynamic Tethers Modeling and Analysis) software. Other EDT codes exist for specific analyses, for example, Dr. Sven Bil*é*n's group at Pennsylvania State University developed a simulation for modeling energy harvesting modules. Other codes exist including GTOSS (Generalized Tether Object Simulation System) [54] and TetherSim [55], which has been developed by Tethers Unlimited, LLC of Seattle, WA.

CHAPTER 2

Models of EDT Process and Components

To simulate an EDT in orbit under the effects of electrodynamic and atmospheric drag, multiple models have to be combined. The following is an explanation of these. A summary of smaller, second-order effects is also presented.

2.1. Orbital Mechanics and Orbital Propagation with Respect to Time Model

Orbital mechanics models can be either extremely complex or relatively simple depending on the accuracy desired. For this particular simulation, it was desired to have a more accurate simulation in terms of the object's trajectory and less accurate in terms of smaller effects like gravitational anomalies, which can play large roles in long-term, non-deorbiting missions. Below is an explanation of the coordinate systems and orbital propagation models used in the simulation.

2.1.1. Coordinate Systems (CS)

When propagating the orbit of an object a reference frame must be chosen such that the results can be compared and used to predict further behavior. Below is a brief explanation of the CSs used in the EDT simulation.

2.1.1.1. Geodetic Coordinate System

The most well-known CS is the geographic CS. This CS, also known as the rotating Earth CS, is based on a spherical CS in which the azimuthal angle is the longitude measured from the Greenwich Meridian (positive degree heading East and ranging from $-180^o \, to \, 180^o$), the elevation angle is the latitude measured from the Equator (positive degrees heading North and ranging from $-90^o \, to \, 90^o$), and the radial distance from the center of the Earth minus the average radius of the Earth, or latitude-averaged altitude. A more accurate representation is the geodetic CS. The geodetic CS tries to account for the geoid-like shape of the Earth. Instead of comparing the desired position to a sphere with the mean radius of the Earth, the geodetic system adjusts height and latitude based on a standard ellipsoid or geoid defined by the scientific community. This is important to consider because at relatively large inclined orbits, the local height and latitude is different from the spherical-based version. The variation is due to the local vertical not running through the center of the Earth. Figure 2.1 shows the differences between spherical and geodetic altitude.

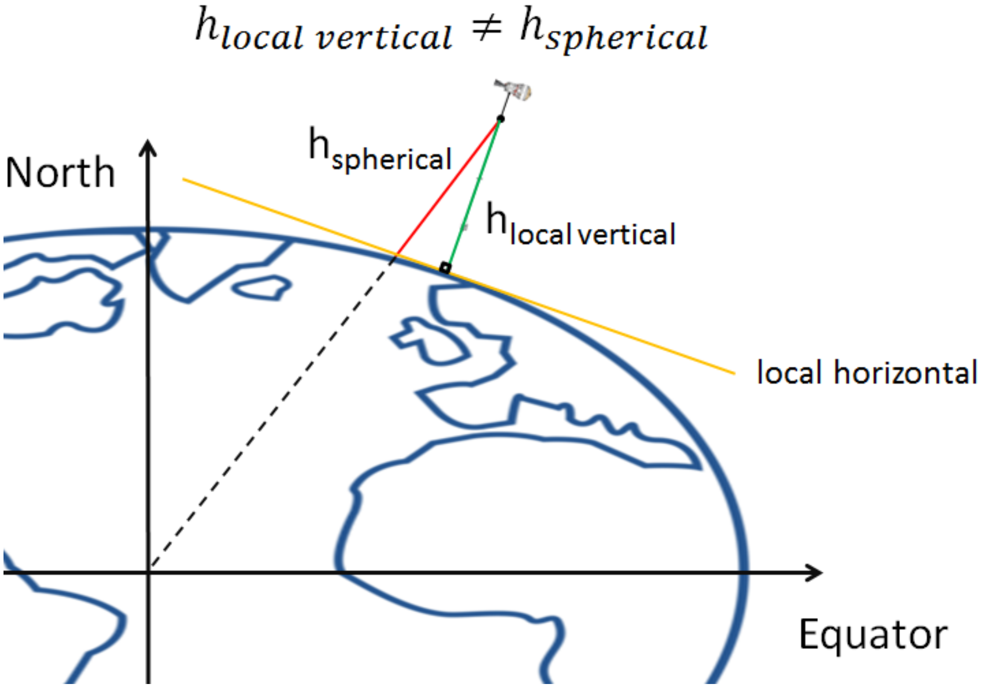

Figure 2.1. Geographic latitude and longitude variation due to the oblateness of the Earth from a satellite's perspective. Note the spherical-based altitude is not equal to the local altitude. This deviation is because of the ellipsoid/geoid like shape of the Earth.

Another consideration when using the geodetic CS is what ellipsoid/geoid should be referenced. Multiple references have been developed for use in different areas of science. The reference used in this thesis is called WGS84 and stands for World Geodetic System 1984. The system was originally established in 1984 and is the standard for use in cartography, geodesy, and navigation with the most well-known example being U.S. Global Positioning Systems [57]. It is based on an ellipsoid shape and, therefore, is not well-defined in certain parts of the world. Figure 2.2 shows an exaggerated view of the differences between an ellipsoid, geoid, and the actual shape of the surface of the Earth.

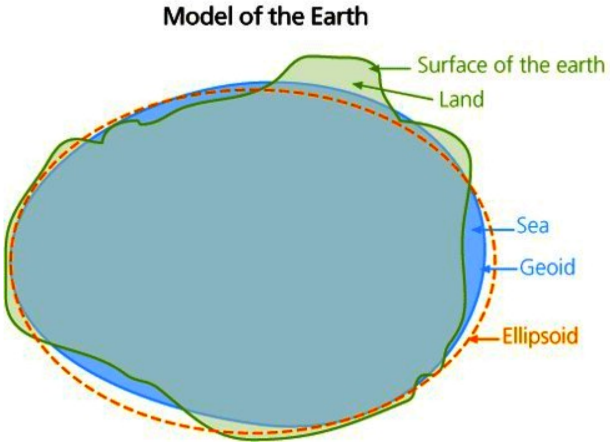

Figure 2.2. Shape of the Earth's surface overlaid with an ellipsoid [58]. The ellipsoid shape shown here is similar to the WGS84 ellipsoid used in this thesis.

The longitudinal range for the geodetic CS is $-180^o \, to \, 180^o$ with positive longitudes heading East from the Greenwich Meridian and the latitude range is from $-90^o \, to \, 90^o$ with positive latitudes heading North from the Equator. The geodetic CS is used in space science and the altitude minimum is $\sim\, 100\, km$ due to the large atmospheric drag seen at that altitude. The maximum altitude of the geodetic CS is undefined, however, the International Reference Ionosphere model range extends only to $2000\, km$. For more information on the geodetic CS, see reference [59, 60].

2.1.1.2. EARTH CENTERED INERTIAL COORDINATE SYSTEM (ECI)

The Earth Centered Inertial (ECI) CS is a Cartesian-based CS meant to provide astronomers and other scientists with a fixed, or non-rotating, reference frame with respect to the stars. The origin of the ECI CS is located at the center of the Earth with the x-axis pointing towards the vernal equinox, the y-axis pointing 90^o East about the celestial equator, and the z-axis aligned with the spin axis of the Earth (celestial North Pole). Figure 2.3 is a depiction of the Earth Centered Inertial CS.

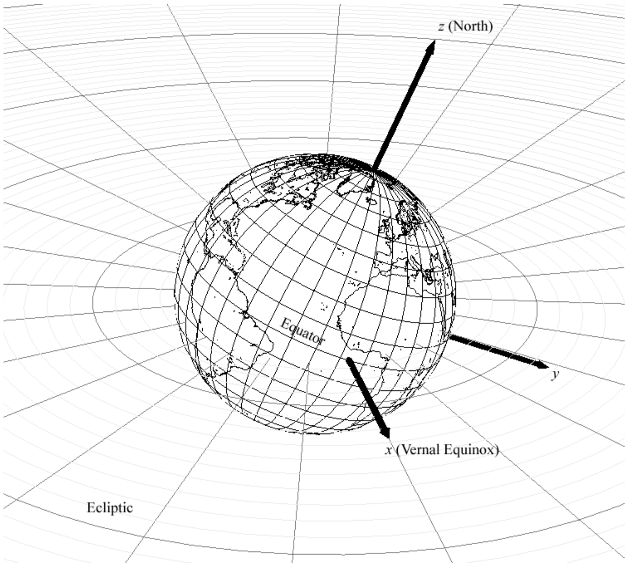

FIGURE 2.3. Earth Centered Inertial (ECI) Coordinate System (CS) [61].

All orbital propagation in the SimBETS simulation code is done in the ECI CS to avoid any rotating reference frame complications. For more information on the ECI CS, see references [60, 62].

2.1.1.3. EARTH CENTERED EARTH FIXED COORDINATE SYSTEM (ECEF)

The ECEF CS is a Cartesian-based CS much like the ECI CS, however, its x-axis is fixed to the zero degrees longitude, zero degrees latitude point on the Earth, with the y-axis pointing 90 degrees East and the z-axis aligned with the Earth's North Pole. Because the x, y, and z-axis are fixed to points on the Earth, they rotate with the Earth as time progresses. Therefore, this CS is not used in SimBETS other than to link the ECI CS to the geodetic CS. Figure 2.4 is a depiction of the ECEF CS.

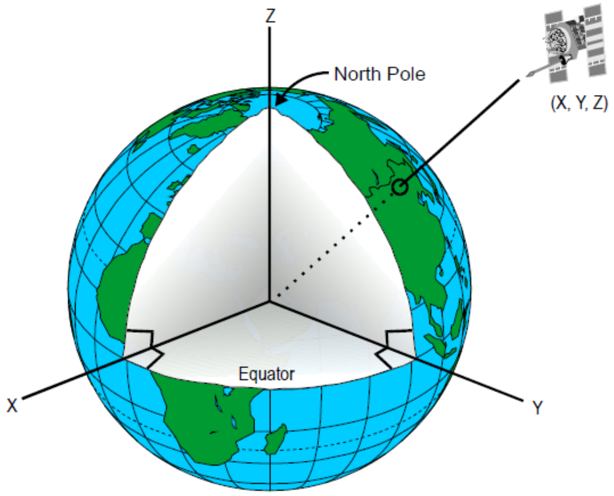

Figure 2.4. Earth-Centered, Earth-Fixed (ECEF) CS [63].

2.1.1.4. North-East-Down Coordinate System (NED)

The NED CS is only used in SimBETS to interpret the IGRF-11 magnetic field model (discussed in Section 2.3) and is useful because it is a local CS allowing for magnetic field vectors to be easily defined. The NED CS's origin is located at a geodetic-based longitude, latitude, and altitude. The x-axis of the NED CS points North, the y-axis points East, and the z-axis points down. This system allows for a vector to indicate the direction and strength of the magnetic field at the desired geodetic position. Figure 2.5 is a representation of the NEU CS on an ECEF CS at a point on the Earth. The NEU CS is similar to the NED CS but with the "Down" axis is pointing in the "Up" direction.

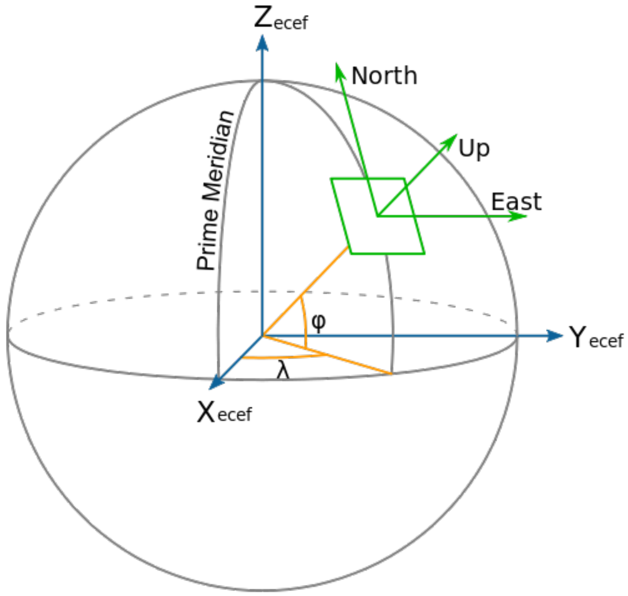

FIGURE 2.5. The North-East-Up (NEU) CS on an ECEF CS [59].

2.1.1.5. COORDINATE SYSTEM CONVERSIONS

Each CS must be related to another CS for proper mathematical computations to be performed. Therefore, conversion algorithms must be used. To convert between the geodetic CS and the ECEF CS and back, MATLAB conversion functions were used. These algorithms relate to the ECEF CS by spherical to Cartesian based equations but instead of relating the altitude and latitude to a sphere, those values are related to the WGS84 ellipsoid. This allows for proper conversion between the two CSs.

To convert from the NED CS to ECEF, rotation matrices were used to rotate the North axis 90 degrees minus the current latitude about the East axis such that it is in the same plane as the x and z-axis. Then another rotation was performed about the Down axis to account for the current location of the EDT and the rotation of the Earth. This rotation matrix can be found in reference [64].

To convert between the ECEF coordinate system and the ECI coordinate system, similar rotation matrices are used as in the NED to ECEF conversion. In this rotation scheme, rotation about the z-axis is performed to account for the rotation of the Earth and the variation between the vernal equinox and the Greenwich meridian. The variation between the vernal equinox and the Greenwich meridian is usually solved by using a Julian date and, therefore, is a standard used by the community. This Julian date variation was not used in the results below. Instead, an offset was calculated and used for the day in which each study was performed, which was chosen to be April 15th, 2012, a date near the solar median. SimBETS does not account for the variation in this offset as time propagates, and, therefore, this is a source of error. Because a significant variation only occurs over a large amount of simulation time, much longer than the average time to deorbit, this assumption is considered acceptable.

2.1.2. Classical Orbital Elements (COE)

The orbit of an object around a large body is defined by six parameters known as the classical orbital elements. These six parameters are: angular momentum ($\mathbf{h}$), eccentricity ($\mathbf{e}$), inclination (i), right ascension of the ascending node ($RAAN$), argument of perigee (ω), and the true anomaly (θ). Figure 2.6 shows how the COEs relate to the state vectors, also known as position and velocity vectors, in the ECI CS.

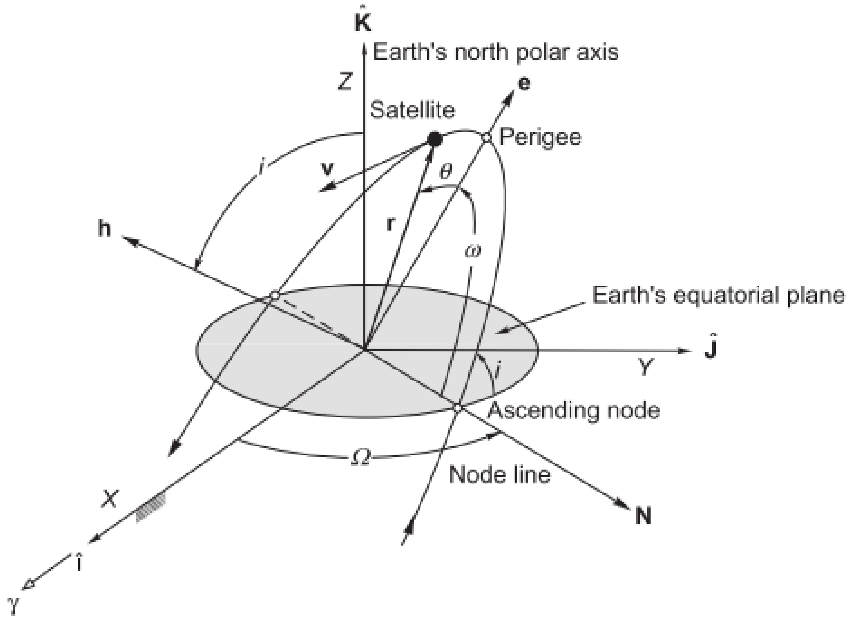

FIGURE 2.6. Geocentric equatorial frame and the orbital elements [60].

Multiple attributes of the satellite's trajectory can be easily deduced as well as its position in the ECI CS discussed above. However, propagating an orbit with the COEs is much more challenging than using the three-dimensional, Cartesian-based orbital motion equations. Consequently, the COEs are only used in SimBETS to output parameters for analysis. To calculate these parameters, the algorithms provided by Howard Curtis in his book Orbital Mechanics for Engineering Students, Section 4.4 [60] were used.

2.1.3. RUNGA-KUTTA-FEHLBERG (4,5) (RKF45)

The orbital propagation of a satellite relative to a large body is considered an initial value problem. This is because the propagation evolves through time and is dependent on the previous point in the iteration. Multiple numerical methods are available for solving such problems; however, the numerical family of Runga-Kutta methods are ideally suited for this problem because of their robustness, fast computational time, and the relative stability of the equation. Reference [65] contains more information on Runga-Kutta methods and their associated properties.

The specific method chosen for orbital propagation was the Runga-Kutta-Fehlberg (4,5) method. The Fehlberg Runga-Kutta method is embedded into the Runga-Kutta numerical solving family, and, therefore, contains all of the characteristics of the standard methods. The variation occurs in the addition of one more computation per iteration. By performing this extra computation, the error in the solution can be calculated and then controlled using the higher-order embedded method that allows for an adaptive time step size. The solving technique for the RKF45 method begins by providing the RKF45 algorithm with initial conditions. Then, using the RKF45 Butcher Table, the slope at $t = 0$ can be found and the next point in the propagation can be determined with a desired tolerance.

2.1.4. RATE EQUATIONS

The differential equation that allows for orbital propagation is known as the fundamental equation of relative two-body motion, which is written as...

$$\ddot{\mathbf{r}} = -\frac{\mu}{r^3}\mathbf{r} + \frac{\mathbf{F}}{m_2}, \tag{3}$$

In Equation 3, $\ddot{\mathbf{r}}$ is the acceleration vector in the ECI CS, μ is the gravitational standard parameter that is defined as the gravitational constant times the mass of the orbited body such as Earth is given by $G * m_1$, r is the magnitude of the position vector, $\mathbf{r}$, $\mathbf{F}$ is the force applied to the body of interest, and m_2 is the mass of the body of interest. Equation 3 is a non-linear, second-order differential equation that governs the motion of mass m_2 relative to mass m_1. By solving for the acceleration of m_2 at certain points in time given an initial position and velocity, the next point in the propagation can be found using the numerical technique discussed in Section 2.1.3.

2.1.5. Orbital Effects Not Considered

There currently are multiple effects not accounted for in the SimBETS program when it comes to orbital propagation. The most notable are gravitational effects due to the Sun and Moon and the effects caused by the Earth's uneven distribution of mass about its center. Equation 3 is meant to describe the relative motion of one point mass to another and therefore does not account for the third and fourth bodies, the Sun and Moon, and the "lumpiness" of the Earth. These effects can play significant roles in determining the long-term behavior of orbits, but they are not important for the relatively short-term deorbit maneuvers considered here.

2.2. Electro-Dynamic Tether Model

The EDT model chosen for SimBETS is a dumbbell-style, partially bare, electrically conductive tether with a hollow cathode plasma contactor system with the satellite mass being the upper mass and the ballast mass being the lower mass consisting of the deployer and HCPC system. Furthermore, only prograde orbits are considered with inclination less than or equal to 71^o.

2.2.1. Dumbbell-style Tether under Gravity Gradient Stabilization Forces

As discussed in Chapter 1, as a tether orbits the Earth, the unbalanced gravitational and centrifugal forces at each end mass combined with the tension provided by the tether causes the tether to remain taut. These forces also cause the tether to remain oriented to the local vertical. The introduction of an inert section in the tether increases the stability due to this effect and, therefore, makes the tether act more like a rigid body. This makes the tether orbit and EDT analysis easier by allowing for the dumbbell-style tether assumption to be made. This assumption states that the tether and its end mass act like a rigid body and do not deform. This assumption is somewhat poor because the tether can see non-negligible deformation due to electrodynamic and gravitational resonances, which can lead to, bending, whipping, somersaulting, and large transient tether tension forces.

The other assumption made in this analysis relates to the local vertical alignment of the tether. Because the gravity gradient stabilization forces relate to the pull of gravity, the tether will rotate about its center of gravity as it orbits the Earth to remain aligned with the local vertical. This assumption is valid as long as the tether does not see large resonant effects that would cause the tether to librate, and the addition of the inert section of the tether minimizes this possibility [8].

2.2.2. Electron and Ion Collection

There exist multiple theories as to how electrons and ions are collected on a bare tether moving through the ionospheric plasma and the Earth's magnetic field at hyper velocities. The regime that best describes electron and ion collection to a biased bare tether in a collisionless, Maxwellian plasma is known as OML theory. The theory states that if the radius of a two-dimensionally defined electrode is small relative to the Debye length and there is neither space-charge nor magnetic-guiding effects, the collected current will be orbital-motion limited (OML) and take the largest value for the given geometry and potential bias [20]. This theory predicts the current collected by an EDT in the ionosphere very well, however, other effects not accounted for due to the collisionless, non-moving, Maxwellian plasma assumption can cause deviations from the predicted current. Figure 2.7 is a depiction of the physical effects in play near the TSS-1R end body, a spherical anode, as it is traveling through the ionosphere.

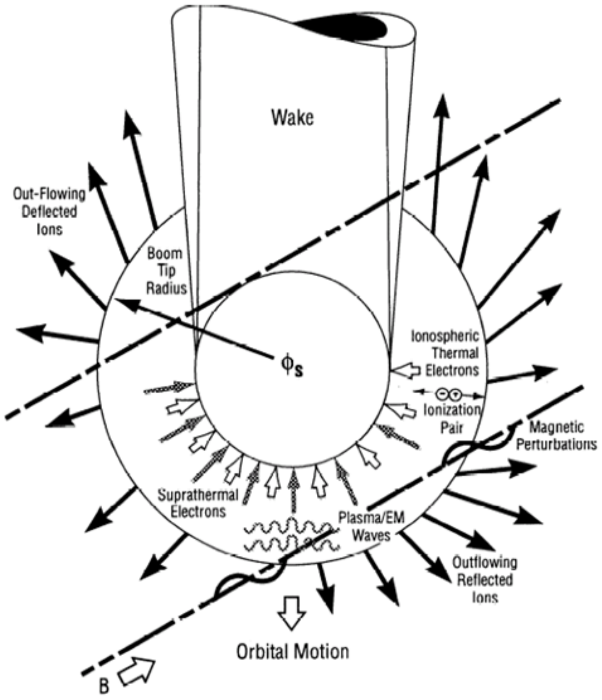

FIGURE 2.7. A composite schematic of the physical effects and characteristics observed in the near environment of the TSS satellite [66].

The bare conducting tether electron/ion collection idea was first formalized by Sanmartin and Martinez-Sanchez [20]. They note that the most area efficient current collecting cylindrical surface is one that has an effective radius or width on the order of a Debye length where the current collection is orbital motion limited (OML).

The collection of electrons/ions to a bare conducting tether is described with a coupled set of first order differential equations. The collection of electrons to a biased bare conducting tether grows along the length of the tether as one moves from the positive end, point A, to point B where the tether voltage is equal to the space plasma potential. The rate of current change per unit length is defined by Equation 4.

$$\frac{\mathrm{d}I}{\mathrm{d}y} = \begin{cases} \frac{eN_ep}{\pi}\sqrt{\frac{2e\Delta V}{m_e}} & \text{if } V_t - V_p < 0 \\ -\frac{eN_ip}{\pi}\sqrt{-\frac{2e\Delta V}{m_i}} & \text{if } V_t - V_p < 0 \\ 0 & \text{if tether is insulated} \end{cases} \tag{4}$$

In Equation 4, e is the charge of an electron, N_e is the electron density, p is the perimeter of tether, V_t is the tether potential, V_p is the plasma potential, and m_e is the mass of an electron.

The tether potential varies along its length as well, and the rate of change of potential versus position is given by Equation 5 - 7.

$$\frac{\mathrm{d}V_t}{\mathrm{d}y} = \frac{I}{\sigma A_{cs}} \tag{5}$$

$$\frac{\mathrm{d}V_p}{\mathrm{d}y} = -E_m \tag{6}$$

$$\frac{\mathrm{d}\Delta V}{\mathrm{d}y} = \frac{\mathrm{d}V_t}{\mathrm{d}y} - \frac{\mathrm{d}V_p}{\mathrm{d}y} \tag{7}$$

In Equation 5 - 7, σ is the conductivity of the material of the tether, A_{cs} is the cross-sectional area of the tether, and E_m is the motionally induced electric field in the tether. Figure 2.8 (a) and (b) show the resulting current and voltage along a tether for a typical tether length, width, thickness, and for typical ionospheric conditions.

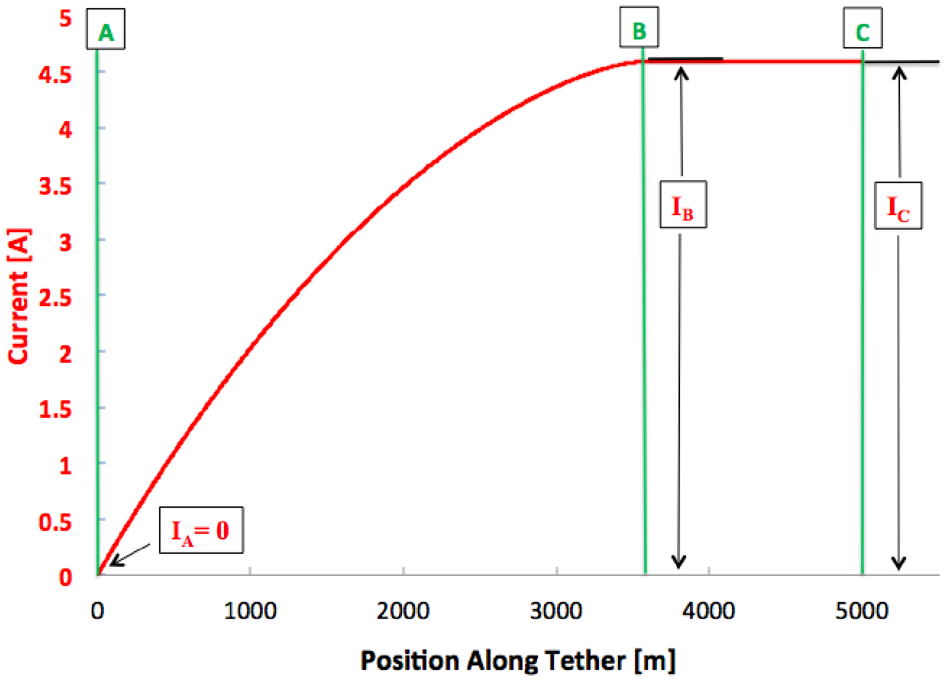

(a) Current versus position.

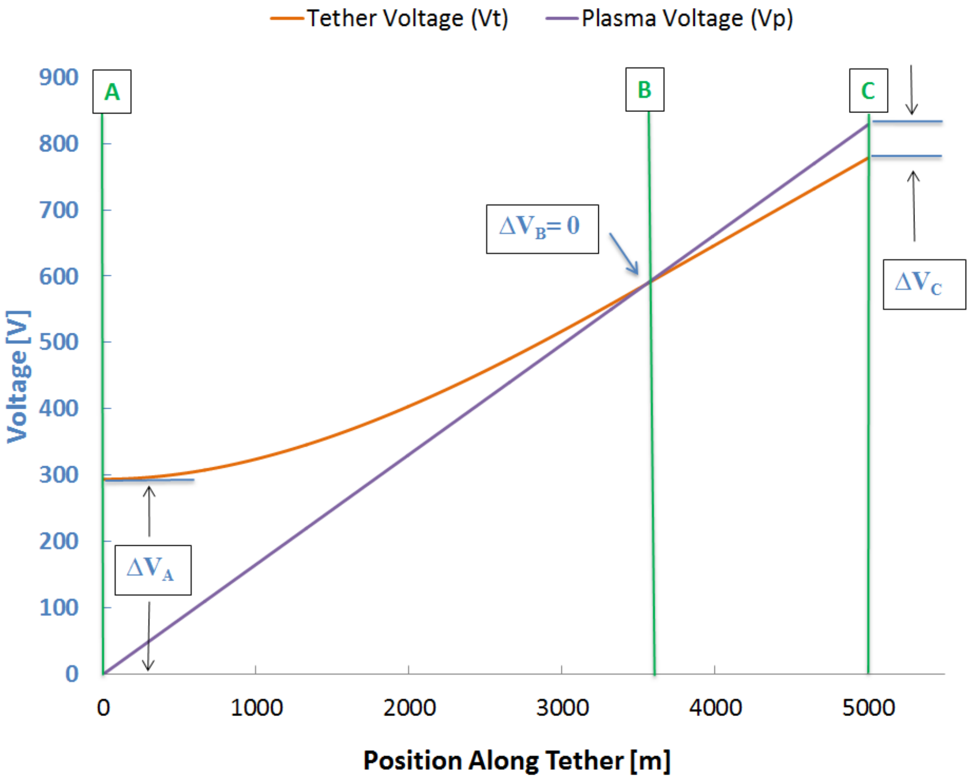

(b) Voltage versus position.

FIGURE 2.8. Current and voltage profiles along the conductive section of tether.

This particular set of equations is a boundary value problem (BVP) because the solution is constrained by boundary conditions. These boundary conditions are:

$$\begin{cases} I\,|_{y=0} = 0 \\ V_p\,|_{y=0} = 0 \\ V_t\,|_{y=0} = V_A \end{cases} \tag{8}$$

and

$$\begin{cases} I\,|_{y=L} = I_C \\ V_p\,|_{y=L} = E_m L \\ V_t\,|_{y=L} = V_p\,|_{y=L} - V_{Contactor} \end{cases} \tag{9}$$

To solve this problem, SimBETS uses MATLAB's "bvp5c" solver. By providing the solver with an initial guess, the boundary conditions, and a curve that represents the supposed shape of the set of equations above, a solution can be found. The solver itself is "...a finite difference code that implements the four-stage Lobatto IIIa formula. This is a collocation formula and the collocation polynomial provides a C_1-continuous solution that is fifth-order accurate uniformly in [a,b][1]. The formula is implemented as an implicit Runge-Kutta formula." [67]. The relative tolerance used in the solver is the default tolerance of 1×10^{-3}. This corresponds to a 0.1 % accuracy. MATLAB's BVP solver routine was chosen over

---

[1] a is the left boundary and b is the right boundary

the implementation of custom code because it is trust-worthy, reliable, peer-reviewed, and computational fast.

The change in the current and voltage profiles of this BVP can vary greatly with the ionosphere and magnetic field of the Earth. As a result, Figures 2.9 and Figures 2.10 show these profiles at local extrema orbital environment conditions. The main points for these profiles focus on: the current collected at point C, I_C; the anode voltage, ΔV_A; and the cathode voltage, ΔV_C.

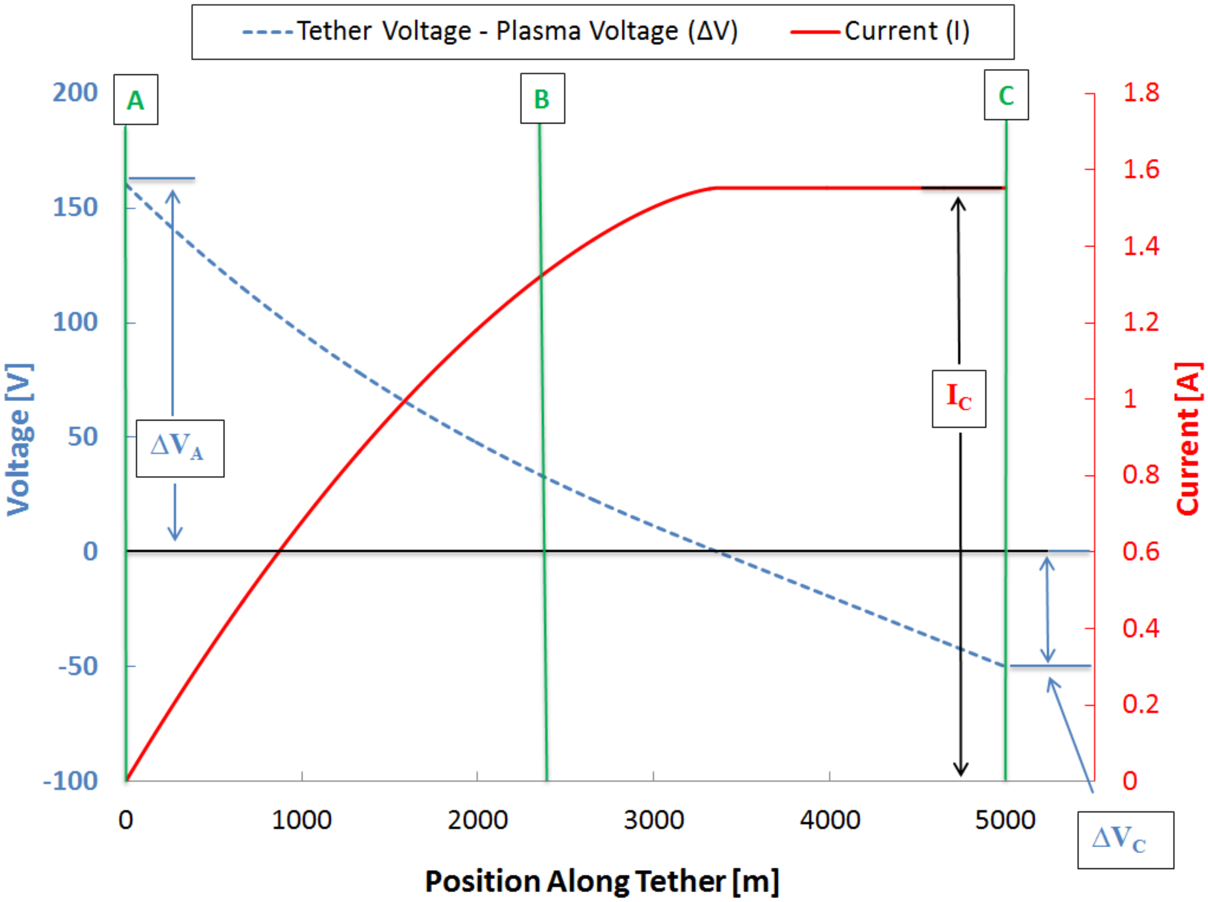

FIGURE 2.9. Current and voltage versus position along the tether at orbital parameters and ionospheric plasma conditions that result in a low tether current and electrodynamic drag force.

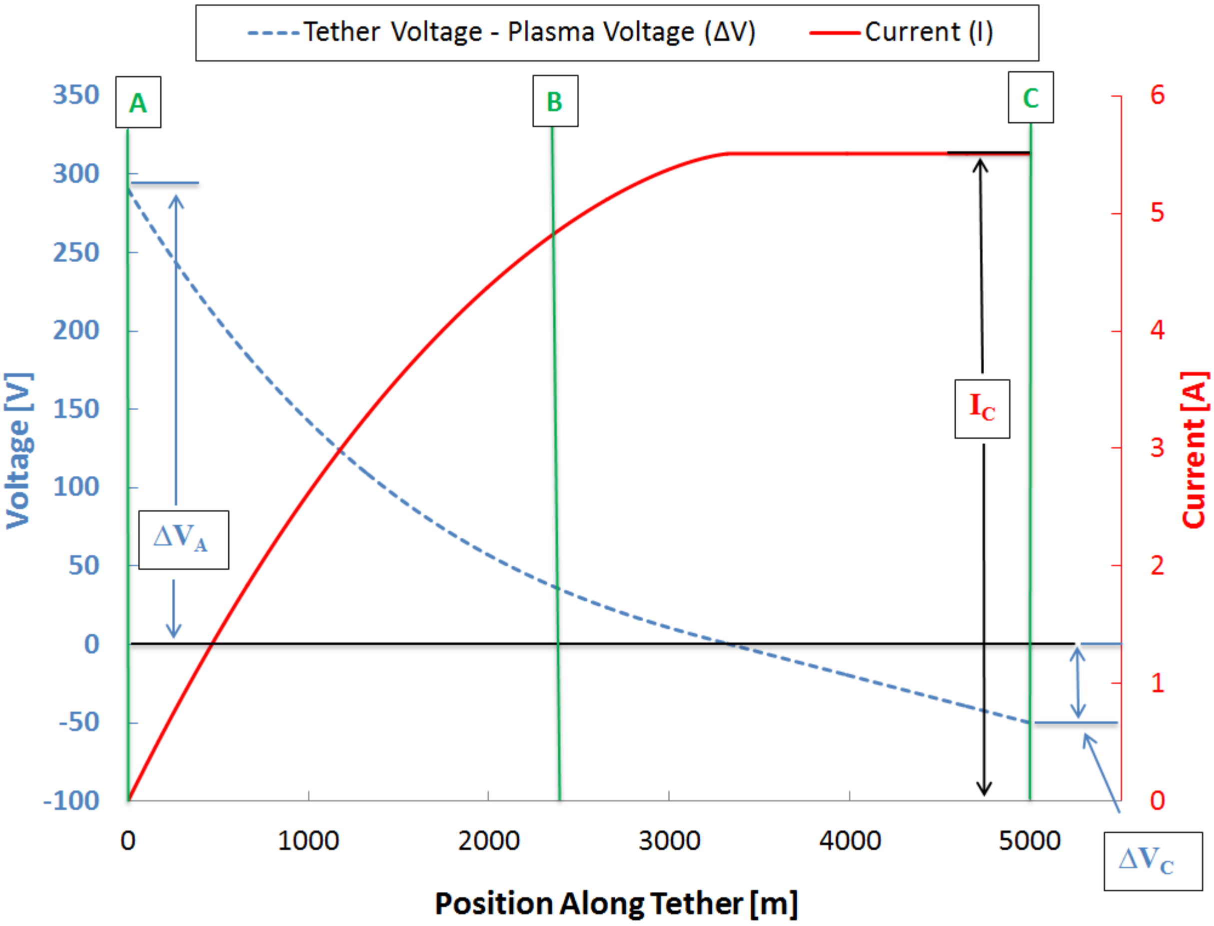

FIGURE 2.10. Current and voltage versus position along the tether at orbital parameters and ionospheric plasma conditions that result in a high tether current and electrodynamic drag force.

2.2.3. ELECTRODYNAMIC AND ATMOSPHERIC DRAG

As described in Chapter 1, as current flows in a conductive material that is moving across the magnetic field lines of the Earth, a force is generated. The force generated by this interaction can be substantial enough to deorbit a satellite in a relatively short period of time. Atmospheric drag also plays a small but important role in the deorbiting process. As the EDT system gets closer to the Earth, however, more and more atmospheric drag is induced and the system begins to deorbit faster under the combined drag forces. The sum of these forces that act on the system over time determines the deorbit time. The caveat to this statement is that the EDT created drag is not exactly in the same direction as the atmospheric drag. This deviation from the atmospheric vector direction of the EDT is caused by the EDT not crossing the magnetic field lines at right angles. The result of this deviation is a precessing, teetering, expanding and contracting orbit that varies the RAAN, argument of perigee, eccentricity, and inclination. Examples of this can be seen Figure 2.11, a plot of the rotation of the RAAN as a function of time, and Figure 2.12, a plot of the variation in the inclination of the orbit as a function of time.

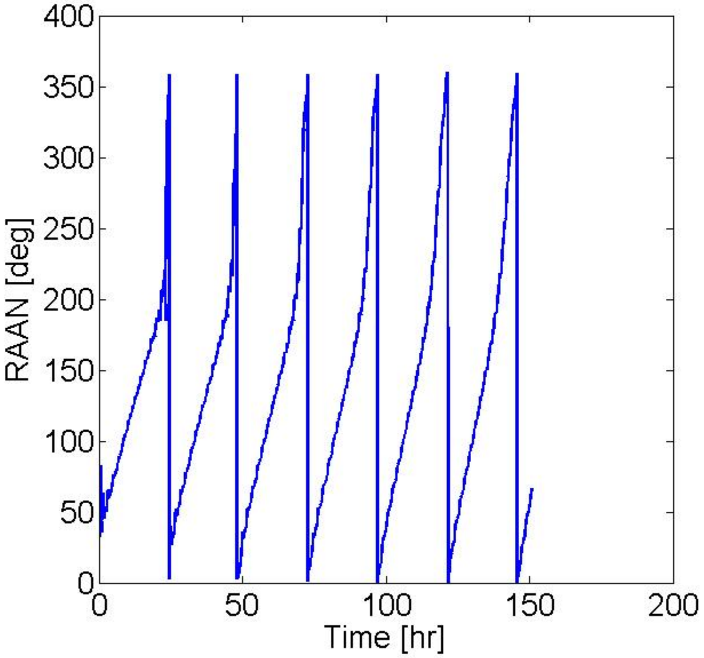

FIGURE 2.11. Procession of the Right Ascension of the Ascending Node (RAAN) for an equatorial EDT deorbit mission. The relatively rapid variation in the RAAN is due to the poorly defined nature of the RAAN for a nearly equatorial and circular orbit.

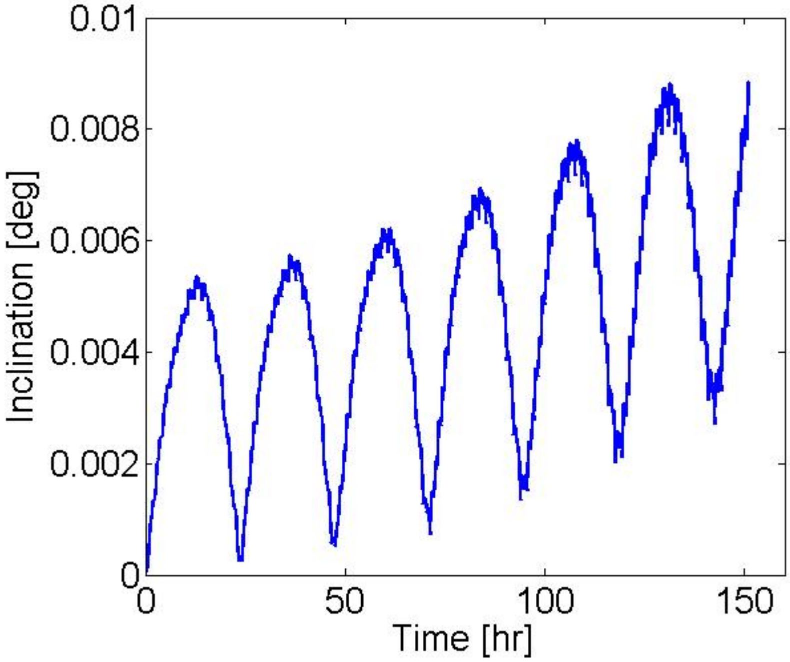

Figure 2.12. Teetering of the inclination of the orbit as a function of time.

This is noteworthy because it matches previous analyses done on EDTs. It also has the potential for satellite orbits to be changed using these systems.

2.2.4. Electron Emission

The electron emission model in SimBETS is currently defined by the user. The program asks initially if the contactor model is a constant or varying voltage model. If the constant voltage model is chosen, the user inputs a set contactor voltage. If the user specifies a varying voltage, the program calls a contactor function and then SimBETS provides it an initial guess for the current and voltage at point C. The algorithm then calculates the voltage it can run at when emitting the requested current. The function then outputs this value and SimBETS checks to see if the emitted current matches the requested current, if it does not;

it provides the function with a new guess for the current and voltage. This is, therefore, an iterative solved problem and can result in failure depending on the model.

The main advantage this model has to other models is its ability to allow a user to provide experimental input data for a contactor running under variable conditions. The model can also be changed for new and different models as long as the inputs and the outputs of the function remain the same. The model must be based off an HCPC system because the simulation assumes expellant is used as the satellite's orbit propagates.

The model itself was based off data taken from $0.64\,cm$ graphite keeper, HCPC with magnet rings around the base and a neutral confinement cylinder. This HCPC is known as the BET (bare electrodynamic tether) HCPC. However,due to the available experimental setups the HCPC could not be run using a continuous flow rate like what is designed into the baseline EDT end mass system. This required the use of multiple curves at different flow rates and then linearly interpolating between them at the proper flow rate. Figure 2.14 is a plot of the bias current versus bias voltage at different flow rates for the BET HCPC, Figure 2.13.

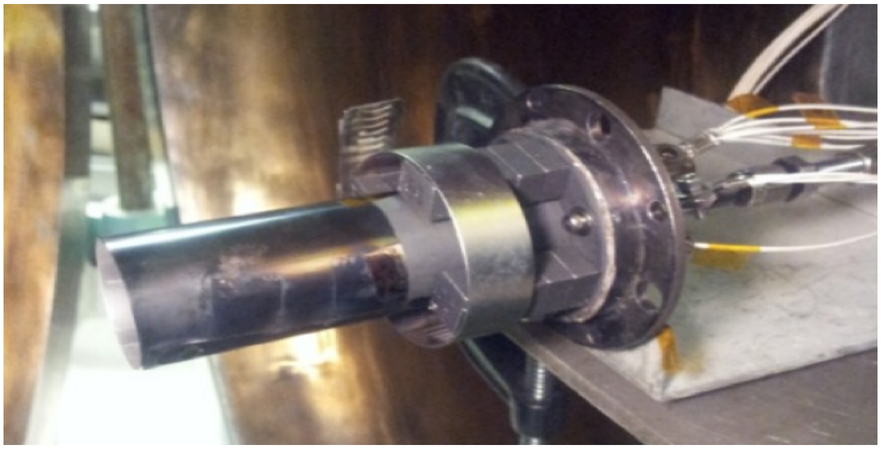

Figure 2.13. BET HCPC configuration with 4 × 4 magnet stacks equally spaced around the base and a $2.54\,cm$ long neutral confinement cylinder. The magnetic field and neutral confinement features enhance the plasma bridge and the reduce the coupling voltage at low flowrates.

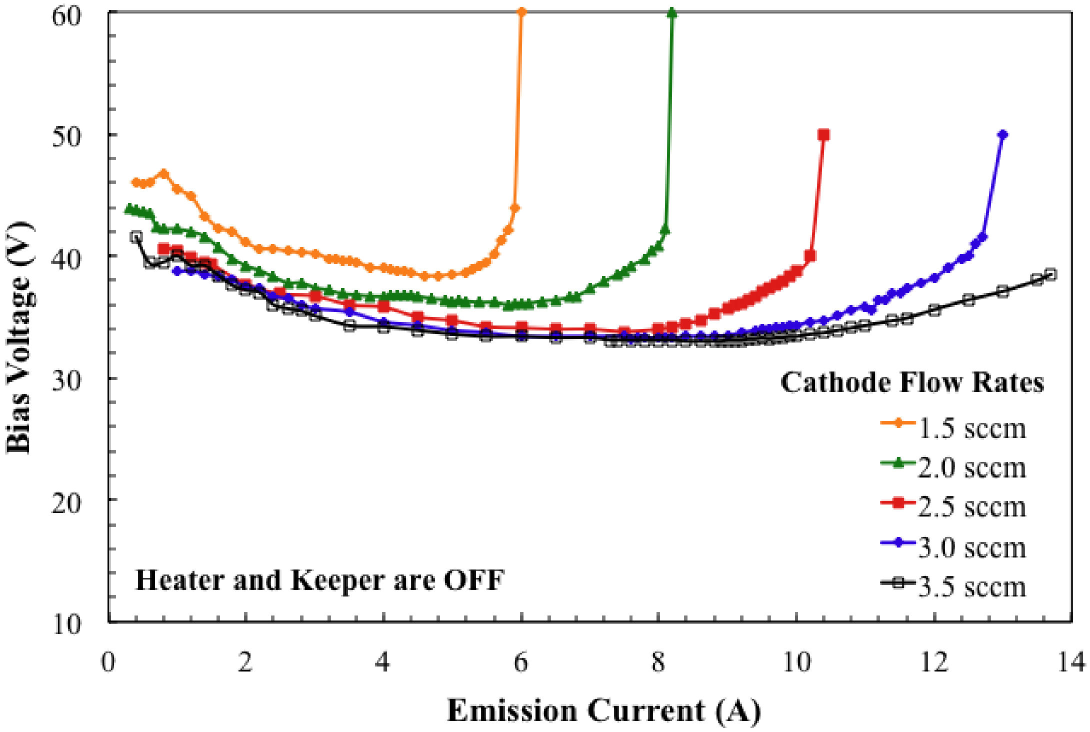

FIGURE 2.14. Bias voltage versus bias current at multiple flowrates for the BET HCPC configuration shown in Figure 2.13.

Of most importance in Figure 2.14 is the shape of the curves. They all have very similar shapes and each curve is ideal for its specific flow rate. It should also be noted the curves do not go to zero. This is because the heater and keeper were turned off for this experiment. Currents below 1 A do not produce high enough plasma densities that allow for adequate bombardment of the cathode insert surface. The heater is, therefore, used to increase the plasma density and provide stability to the flow. The keeper must be turned on below 1 A because as the plasma density drops, the plasma bridge connecting the plasma inside the cathode to the ambient plasma of the ionosphere becomes more and more resistive and the natural bias created between the plasmas is no longer enough to pull the plasma inside the cathode tube to the ambient plasma. Thus, the keeper is used to assist in this process.

To account for this non-zero beginning point, multiple points were guessed that aligned the zero current-zero voltage point with the beginning points of each curve. This was done to make the curves smooth, much like how the real curves would look. By then fitting curves, (varying orders of polynomials worked best) to the two different sections of these plots, where section one is the region below $1\,A$ and section two is the region above $1\,A$, a reasonable estimate of a real continuous curve was created.

If a system using a discrete flow rate curve was used, each curve corresponding to the desired flow rate in the plot above would be used and switched between. If a desired flow rate sat in between these curves, a rounding procedure at each current would have to be done. Considering continuously adjustable flow rates, these curves will not suffice. Figure 2.15 shows this continuously varying flow rate.

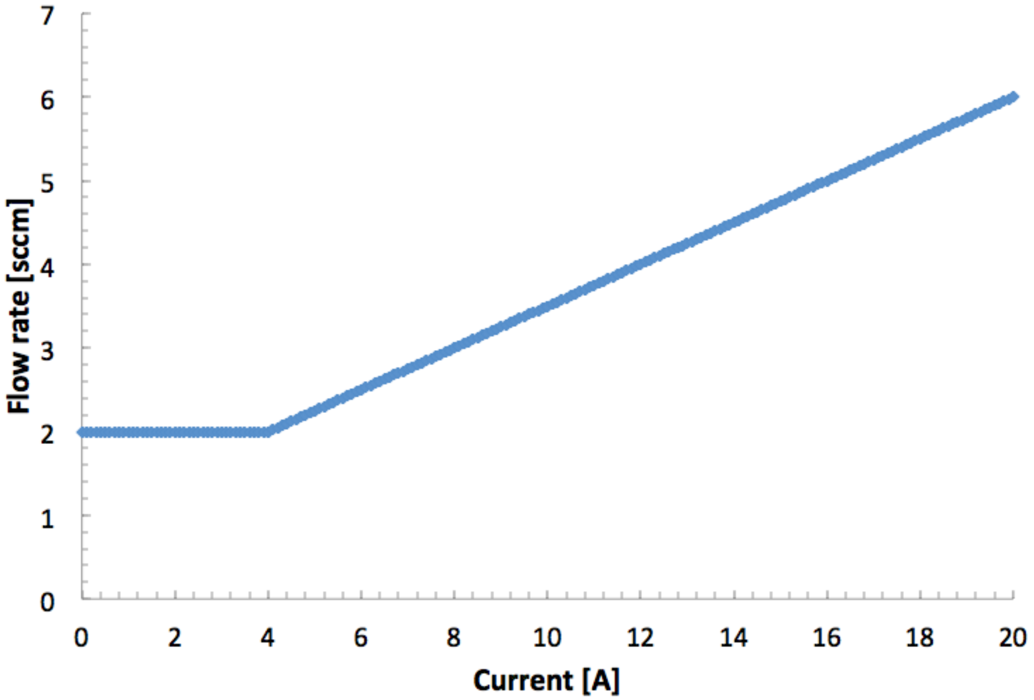

FIGURE 2.15. Proposed model of flowrate as a function of tether current. Higher HCPC emission currents require higher flowrates to avoid unfavorable operating conditions.

Because the flow rate increases linearly after $4\,A$, using any one curve fit of the plots in Figure 2.14 will not work. Instead, the curve fit corresponding to $2\,sccm$ was used until $4\,A$ was reached. At this point, the flow rate begins to increase/decrease linearly passing through each of the curves seen in Figure 2.14. As a result, an interpolation must be completed between the two curves.

In order to gain information about the bias voltage at currents above $12\,A$, the $3.5\,sccm$ curve was extended and then another curve was estimated based on the $3.5\,sccm$ experimental data. Final interpolation between these two curves was completed up to $4\,sccm$. All values above this flow rate were assumed to lie along the estimated $4\,sccm$ extended curve. Considering the shape of the other curves with respect to the estimated curve as well as the amount of time an EDT spends at these high of currents, it can be said this estimated curve is valid for use. Compiling these interpolated points and then fitting polynomial curves to the two sections result in the curve seen in Figure 2.16.

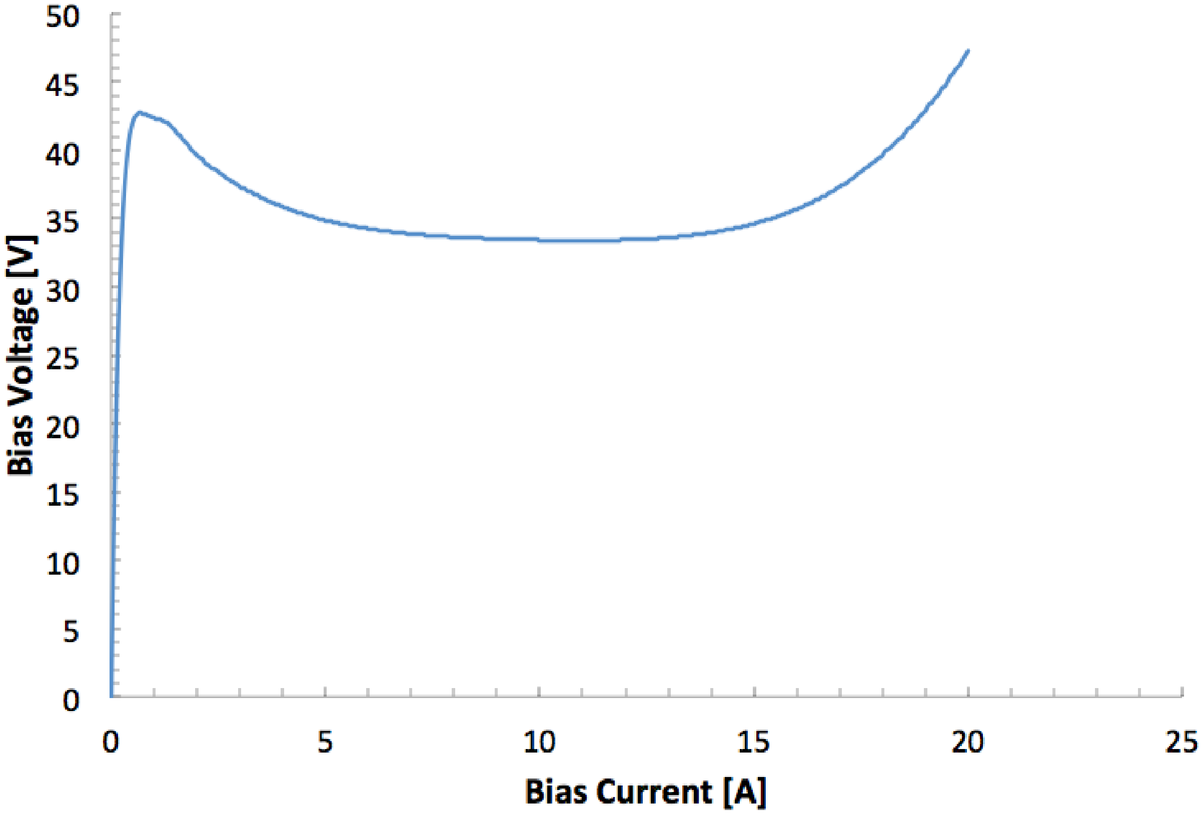

FIGURE 2.16. Modeled bias current versus voltage for the proposed HCPC system. This plot was generated using Figure 2.15 and the data presented in Figure 2.16.

Using this curve, the BVP solver is given an initial guess for the voltage at the end of the tether. The current is then solved for and checked against this curve. If the guessed voltage aligns with the bias voltage output by the curve then the correct voltage for the boundary condition has been found, otherwise, a new value is guessed.

2.2.5. PAST PLASMA CONTACTOR MODELS

Two plasma contactor models have been explored since the plasma contactor became important in maintaining spacecraft potential. Unfortunately, these models do not represent current plasma contactors. The model most notably used comes from Fuhrhop who uses experimental data from Williams and Wilbur [38]. The model is developed by fitting a curve to the data and then extracting hollow cathode voltage versus current emission from it such that it can be placed in a simulation. Other models, detailed in references [68, 69], provide notable but less substantial results.

This thesis uses more recent data collected on plasma contactors operating at low flowrates. These measurements are described above in Section 2.2.4.

2.3. Orbital Environment and Associated Models

An EDT is completely reliant on the conditions of the environment it is in, therefore, it is important to understand and correctly model this environment. Since the orbital environment is extremely important in the telecommunication field, there have been large developments in fields relating to the modeling of the ionosphere, magnetic field, and air density. SimBETS uses three different orbital environment models, specifically the International Reference Ionosphere version 2007, International Geomagnetic Reference Field: eleventh generation, and a fitted air density model valid below $300\,km$. Note the fitted air density model provides negligible drag on the EDT above $300\,km$. For more information on these models, see references [70, 71].

2.4. System Mass Estimation

The end mass system consists of multiple components including a deployer, electrical conversion hardware, controlling electronics, structural components, and a plasma contacting system. Each of these components can affect the EDT's success and thus must be thoroughly developed if a flight EDT is desired, however, SimBETS considers each of these components/systems to be ideal, and, excluding the HCPC system, they only contribute to the simulation by adding mass. Figure 2.17 is a depiction of a base EDT end mass design.

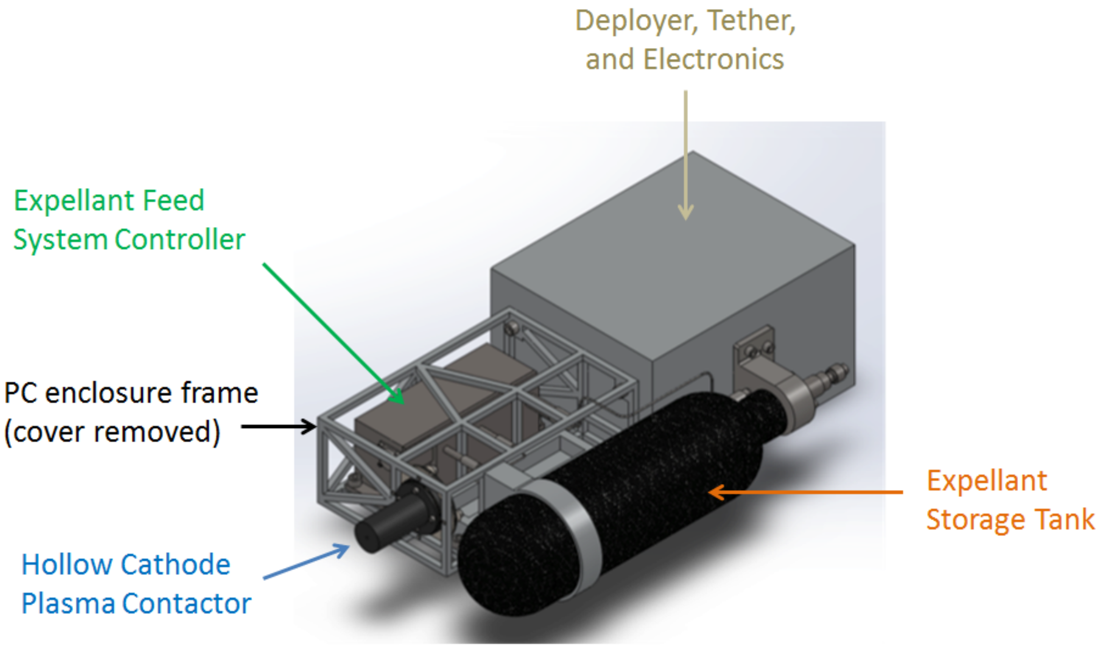

FIGURE 2.17. EDT baseline end mass concept.

2.4.1. TETHER MASS ESTIMATION

To estimate the tether mass, only two pieces of information are needed about each section of tether, the tether section dimensions and the density. The required inputs in SimBETS include the dimensions and density of each section and, therefore, using the rearranged density equation, Equation 10, one can solve for the mass of each section.

$$m = \rho V \tag{10}$$

It should be noted however, the insulated conductive section mass is calculated differently than the other masses. When calculating the conductive or inert section mass, the volume is easily found by multiplying the three dimensions: length, width, and thickness together.

This is not true for the insulated section. The insulated section has a mass per unit length greater than the bare section of tether because it has been coated in a protective insulating layer. Therefore, SimBETS uses the inputs of thickness, length, and density to calculate the additional mass of the layer. The total mass of this result is three masses that when summed together equal the tether total mass, Equation 11.

$$\begin{aligned} m_{tether} &= (\rho l w t)_{inert} + (\rho l w t)_{conductive} + (\rho l)_{insulated}\bigg(\big((w_{conductive} \\ &\quad + 2t_{insulation})(t_{conductive} + 2t_{insulation})t)\big) - (wt)_{conductive}\bigg) \\ &= m_{inert} + m_{conductive} + m_{insulated} \end{aligned} \tag{11}$$

In Equation 11, l is the length of the tether section, w is the width of the tether section, and t is the thickness. On average, a bare tether EDT system would have a mass of $\sim 57\,kg$.

2.4.2. END MASS MASS ESTIMATION

To estimate the mass of the end mass system, SimBETS requires:

- Tether lengths, thicknesses, and densities of bare, insulated, and inert sections.
- Satellite or debris mass to be deorbited along with system dimensions and drag coefficients.
- Plasma contactor characteristics such as expellant flow rates for a given tether current.
- Plasma contactor mass including all components, mounts, fasteners and insulating spacers, and gas flow lines.

- Gas flow subsystem specifics including mass of flow module, electronics, inlet gas flow lines, and flow rate control characteristics
- Initial estimates for gas and tank mass and volume including gas flow line connectors.
- Mass of system integration frame, tank bracket, fasteners, enclosing thermal blankets, and deployer.

Entering these inputs allows SimBETS to calculate the mass of xenon expellant required for a particular mission as well as the gas feed system components. A drawback to the following mass estimation algorithm is that SimBETS must iteratively solve for the correct mass because the estimation requires knowing specifics about the EDT performance. The accuracy of this estimation can be set when the simulation is run or the default accuracy of 10 % can be used.

To determine the input parameters above, a desired system or baseline system must be used. If a desired system is known, these inputs allow for quick entry into SimBETS, however, if a baseline system is used, an estimation scheme must be implemented. This can be challenging because certain components in an EDT system are discrete. For example, Luxfer Gas Cylinders make aerospace composite cylinders that are designed to meet many requirements associated with the aerospace industry. These cylinders however, come in discrete volume sizes. Therefore, the perfect choice for an EDT mission cannot always be chosen and so the next size up is used. This adds mass to the vehicle but is unavoidable for some missions. The components in the system also have certain operating conditions that must be met, for instance, operating temperature limits. These associated system design difficulties result in assumptions that must be made to determine a baseline model. The next section discusses these assumptions and their validity for EDT missions.

2.4.2.1. System Design Assumptions

Multiple assumptions were made to define a baseline plasma contactor system mass. These assumptions are as follows:

- Xenon gas is the most ideal option for an expellant. Xenon is a desirable gas for electrodynamic tethers because of its low ionization energy, high ionization cross sections, relatively large mass, and relative ease in handling and storage.
- A VACCO Xenon Flow Control Module (XFCM) is the best way to control the flow of gas from the xenon gas storage tank to the plasma contactor. VACCO is well known for their flight-ready, highly capable hardware and is therefore a logical option. The VACCO XFCM is extremely light, thoroughly tested, fits a wide variety of configurations when considering an EDT system, is completely self-contained, and has proportional control valves for a wide range of adjustability. A custom system could also be used, however, this would require design work that is not necessary at this time since our current systems model doesn't need this level of fidelity.
- A $0.64\,cm$ hollow cathode with enclosed keeper is the cathodic element of the EDT. A $0.64\,cm$ hollow cathode with enclosed keeper was chosen because of its reliability, sturdy construction, and its heritage on board the International Space Station and other satellites and spacecraft.
- Three Luxfer cylinders are the most viable options to allow for the system to be used in a wide variety of EDT missions. The following tanks are assumed adequate to meet all mission requirements modeled in SimBETS: $0.7\,L\,/\,0.8\,kg$ aluminum cylinder, $2\,L\,/\,1.3\,kg$ composite cylinder, and $3.3\,L\,/\,2.0\,kg$ composite cylinder. Luxfer aluminum cylinders are a valid choice based on the aluminum tank used on the

ProSEDS mission. The main worry is the ability to handle the hoop stress seen when filled with xenon and at high temperatures. The Luxfer aluminum cylinder is small, lightweight, and will suffice for relatively short duration missions. All-aluminum cylinders are manufactured using Luxfer's L6X aluminum alloy, a proprietary formula of 6061 alloy. Luxfer metallurgists have optimized this exclusive alloy to improve its durability, fracture toughness, and resistance to tearing and cracking. Luxfer aluminum cylinders have passed all testing performed by major global gas companies, and Luxfer aluminum cylinders met or exceeded requirements set by every major cylinder regulatory authority in the world. Up to 40% lighter in weight than comparable steel cylinders, aluminum cylinders are also highly corrosion-resistant and well suited for low-temperature applications.

For longer, more challenging missions, Luxfer provides composite cylinders specifically rated and tested for aerospace applications. The composite cylinders are ideal for longer missions because they can handle a greater hoop stress, do not catastrophically fail when punctured, and can withstand higher storage pressures than the aluminum tank.

- $1.6\,mm$ gas feed lines and step-up and step-down adapters can be used to connect the xenon storage tank, XFCM, and plasma contactor. $1.6,mm$ gas flow lines were used to minimize weight, and titanium step-up and step-down adapters were used based on VACCOs choice to use titanium a $0.64\,cm$ outlets tube. The gas flow lines and adapters were assumed to be welded together to prevent leaks and provide sturdy connection that will not fail during launch.

- Tank mounts and connection brackets in combination with the tank represent an adequately strong structural element. The xenon storage tank is itself a stiff component and can therefore be placed outside of the main enclosure. However, attaching the tank to the enclosure can be challenging. The connection brackets need to be stiff enough to handle launch conditions while still not being excessively massive. The tank connection bracket also has to allow for filling and draining of the tank as well as a connection to the XFCM. This requires the connection bracket be thoroughly mounted; most likely welded or bolted if need be, with a completely integrated design to reduce overall mass.
- Surrounding enclosure mass is negligible. The surrounding enclosure was not considered in this design because it was assumed the mass would be negligible. This is because the enclosure would be comprised of extremely light thermal blankets to prevent large temperature variations and maintain a required operating range. The multi-layer blankets will also serve as a Wipple shield to prevent damage due to micro-meteorite impacts.
- The structural frame is a flight quality frame optimized to provide sturdy mounting points and would enclose vital components. The structural frame would be flight quality just strong enough to handle launch conditions, and would act as a mounting point for all the components of the plasma contactor system and associated electronics, excluding the tank connection bracket which would be mounted to the deployer enclosure.

2.4.2.2. Deployer System

The deployer system is one of the most important devices in an EDT system. The deployer is designed specifically to house and unreel the tether to its full length in a controlled manner. Once this objective is complete, the deployer only acts to connect the tether to the plasma contactor and act as a ballast mass to help stabilize the tether.

Currently, the mass of the deployer is an input in SimBETS, however, future work will estimate it from other inputs. The deployer mass is estimated by running a program called BETsMA from Dr. G. Snchez-Arriaga. This estimation is based only on tether dimensions and does not vary with varying orbital parameters.

2.4.2.3. Fasteners and Electronics

The fasteners used in this estimation were assumed to fit into tapped holes present in either a structural or connecting component like the tank clamp bracket. Only stainless steel socket head cap screws were considered and resulted in an additional $\sim 0.02\,kg$ of mass.

The electronics required to power the plasma contactor during start up, when the tether current is below $1\,A$, and to run the VACCO XFCM were not fully analyzed. It was estimated that the componentry necessary for integration of the Electronics subsystem would add an additional $\sim 0.4\,kg$.

2.4.2.4. Hollow Cathode Plasma Contactor

A HCPC has been used on many different satellites in LEO including the International Space Station [72, 73, 74]. This choice is because a HCPC is a robust, charge controlling device with " ...robust construction, long lifetime characteristics, high electron emission current capabilities (in excess of $60A$ [75]), low power requirements, and capacity to produce a cool, neutral plasma" [76]. The downside is that expellant gas is required to use this technology.

The plasma contactor mass is based on four main components: the hollow cathode, the xenon flow control module, the gas feed lines and connections, and the expellant storage tank and associated expellant. The following subsections discusses how each main and associated subcomponent mass was estimated. Figure 2.18 (a), (b), and (c) shows isometric views of three plasma contactor systems in the launch configuration.

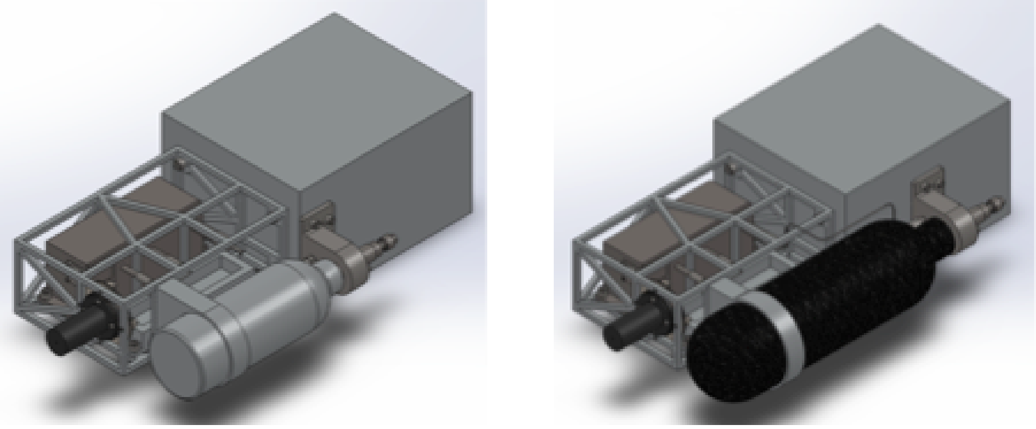

(a) Aluminum tank plasma contactor system.

(b) Small composite tank plasma contactor system.

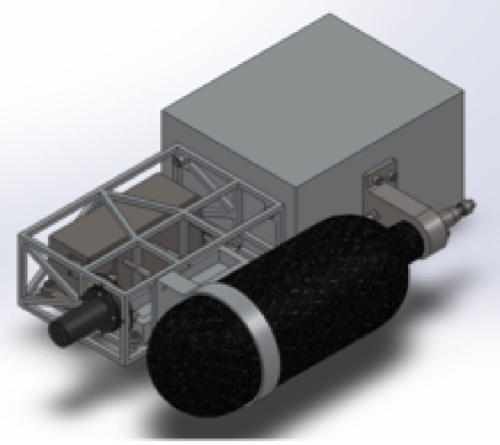

(c) Large composite tank plasma contactor system.

FIGURE 2.18. System configurations due to varying tank size. The large box at the top of each drawing is a rough approximation of the balance of the BETs system, which includes the deployer, tether, and electronics subsystems.

The hollow cathode chosen for this systems analysis was a $0.64\,cm$ diameter tube with an enclosed keeper. The mass used in this systems analysis is an empirical mass that was compared against SolidWorks and its associated material properties database. The hollow cathode assembly is missing some components, however, and so the modeled mass is $0.14\,kg$ lighter than the actual weight of the HCPC of $0.35\,kg$. Figure 2.19 shows the plasma contactor.

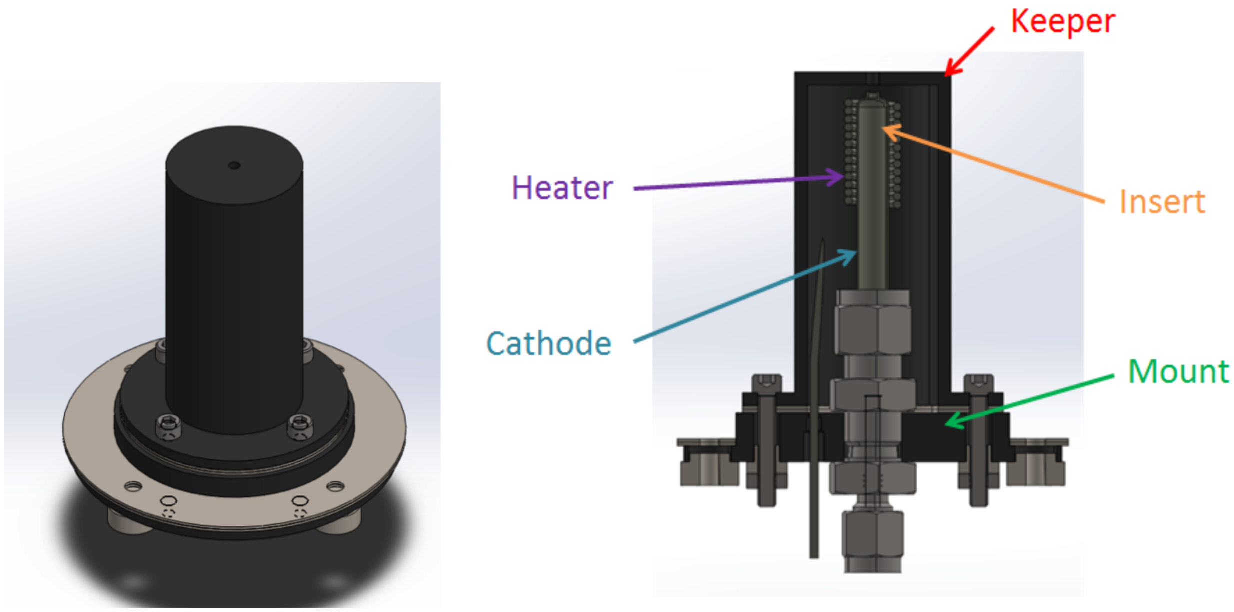

(a) Isometric view

(b) Cut-away view

Figure 2.19. Hollow Cathode Plasma Contactor. Note that the magnet stacks and neutral confinement cylinder are not shown.

2.4.2.5. VACCO Xenon Flow Control Module (XFCM)

VACCO Industries Xenon Flow Control Module is specifically designed for use in space-based applications such as electrodynamic tethers and electric propulsion. The module has multiple redundant latch valves, pressure and temperature sensors, proportional flow control valves, and has ±1% closed loop control flow accuracy. The flow module itself is currently rated at a NASA Technology Readiness Level (TRL) of 5. The XFCM mass is $1.4\,kg$. Figure 2.20 shows the VACCO XFCM configured for two flow channels, however, an EDT plasma contactor would only need one flow channel therefore, further reducing the mass.

FIGURE 2.20. VACCO Xenon Flow Controller Module (XFCM) [77].

2.4.2.6. XENON GAS FLOW LINES

The leads exiting the VACCO XFCM are $0.64\,cm$ titanium tubes. The gas flow lines are assumed to be connected to these tubes by step down adapters that are welded to the outer diameter of the outlet tubes and the outer diameter of the gas feed lines. The stepped down tube diameter is $1.6\,cm$ tube to reduce weight and to prevent any extra ullage waste that could come about from a larger tube diameter. The outlet flow lines exit the outlet tubes and then converge to a single point where the tubes are welded together. The outlet tube of this intersection leads to the inlet of the HCPC and is joined to it via an inlet connection line. It is recommended, however, this be replaced with a welded version to prevent failure during flight.

The inlet tube for the VACCO XFCM is connected via a step-up connector that uses the $1.6\,cm$ line exiting the tank connection bracket. The bracket is connected to this line via a step-down connection adapter. All connections are made by welding the fitting together. Figure 2.21 (a) and (b) show the simple gas line connections between the storage tank, XFCM, and plasma contactor.

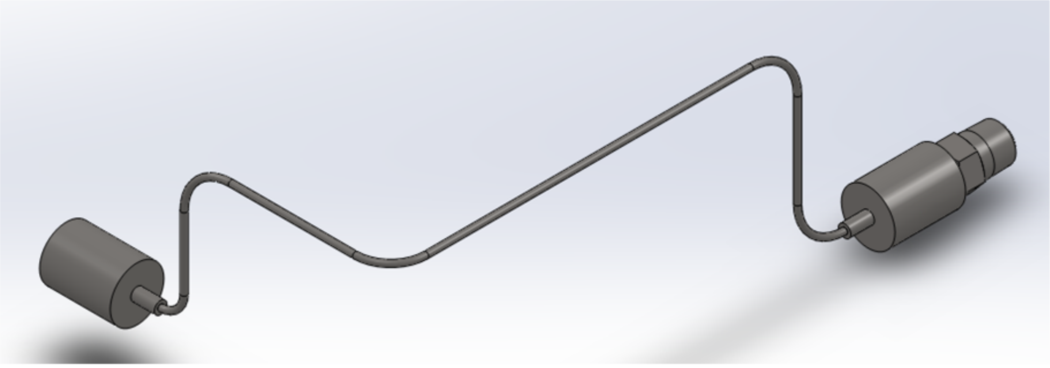

(a) Inlet gas feed line

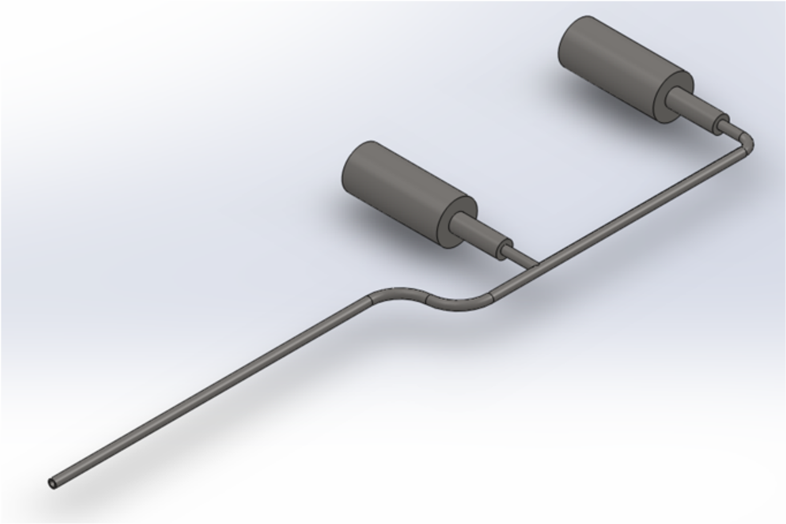

(b) Outlet gas feed line

Figure 2.21. Inlet and outlet gas feed lines.

2.4.2.7. Xenon Storage Tank

The storage tank is chosen based on its volume, mass, and material. Three tanks are available in the SimBETS input file including: a $0.7\,L\,/\,0.8\,kg$ aluminum cylinder, $2\,L\,/\,1.3\,kg$

composite cylinder, and $3.3\,L\,/\,2.0\,kg$ composite cylinder. The actual tank chosen in a given simulation will be based on the mission duration. The algorithm works as follows, the lowest mass cylinder, i.e. the aluminum cylinder, is chosen initially and the simulation is run. If is too small to hold the xenon mass, then next largest tank is chosen. The simulation is then run again until a desired accuracy is reached on the overall system mass.

2.4.2.8. Xenon Mass

The component mass that varies the most in the simulation of the plasma contactor system is the xenon expellant mass. This large variation is due to the orbital environment conditions seen on a particular EDT mission. The main parameters that affect xenon mass are deorbit time, required emission currents, and chosen hardware. To calculate the required xenon gas, the following algorithm was applied.

First, information about a particular deorbit mission was provided to the script. This information is briefly discussed below.

(1) A HCPC requires an expellant, such as xenon, to be flowed past its thermionic emitting insert in order to create a plasma and bridge the HCPC and the ambient environment. This bridge can be highly unstable if proper operating conditions are not met. However, since optimal operating conditions change as the EDT orbits the Earth, the provided flowrate must be a function of emission current. For a less than optimal operating condition, a constant flowrate that is within the stable operating limits of the HCPC in the simulated orbital conditions. SimBETS allows for discrete and continuously varying flowrate versus emission curves. Figure 2.22 (a) shows a continuously varying flow rate as a function of emission current while Figure 2.22 (b) shows a discrete flow rate as a function of current plot.

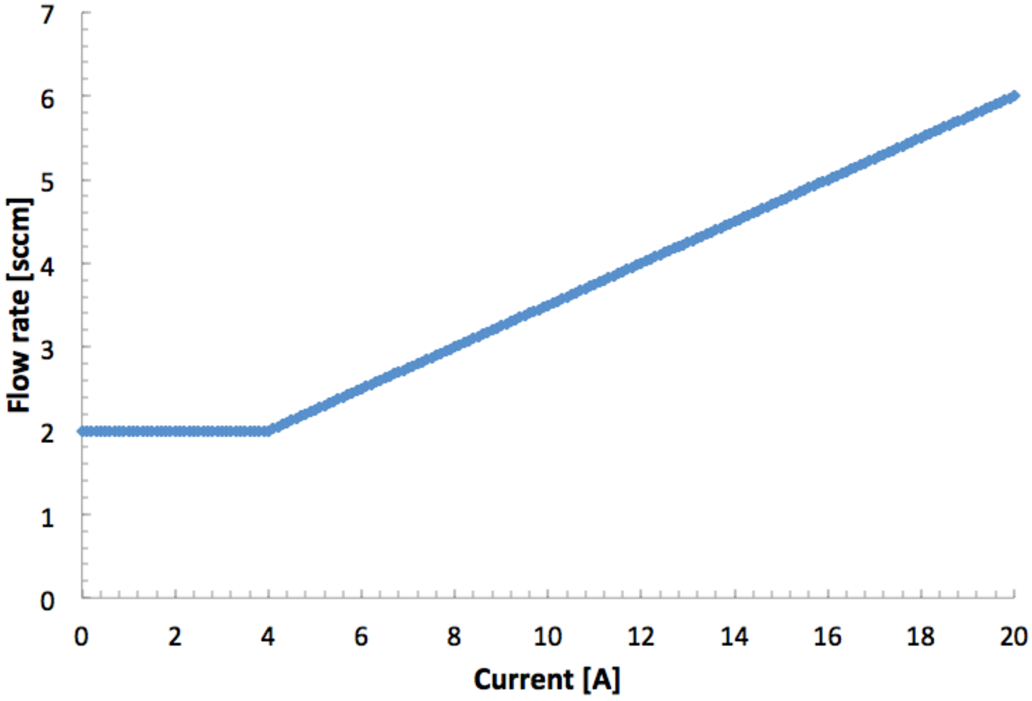

(a) Continuously varying flowrate versus current input.

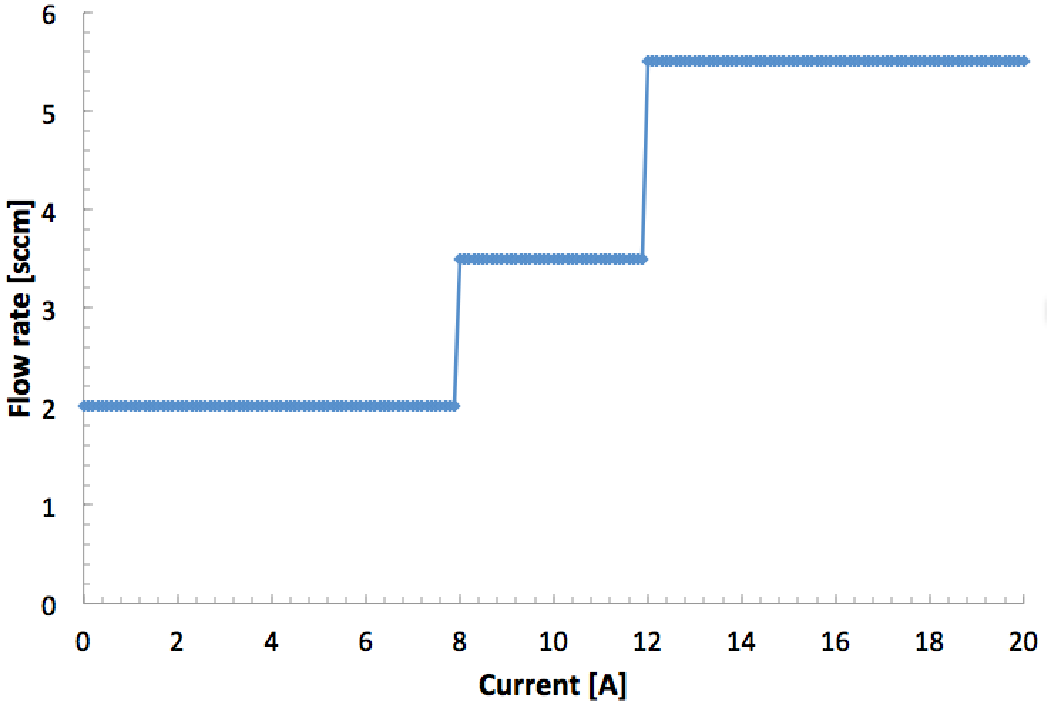

(b) Discretely varying flowrate versus current input.

Figure 2.22. Two types of flowrate versus emission current models that were considered.

(2) The atomic weight of xenon was used.

(3) The VACCO XFCM minimum specifications were provided, specifically inlet minimum and maximum pressures, allowable operating temperature conditions, and the desired safety factor on the inlet pressure and maximum tank pressure.

(4) National Institute of Standards and Technology (NIST) isothermal properties of the expellant being used must be provided. Figure 2.23 shows a plot of the density vs. pressure of xenon gas at an operating temperature of 0^oC and 70^oC.

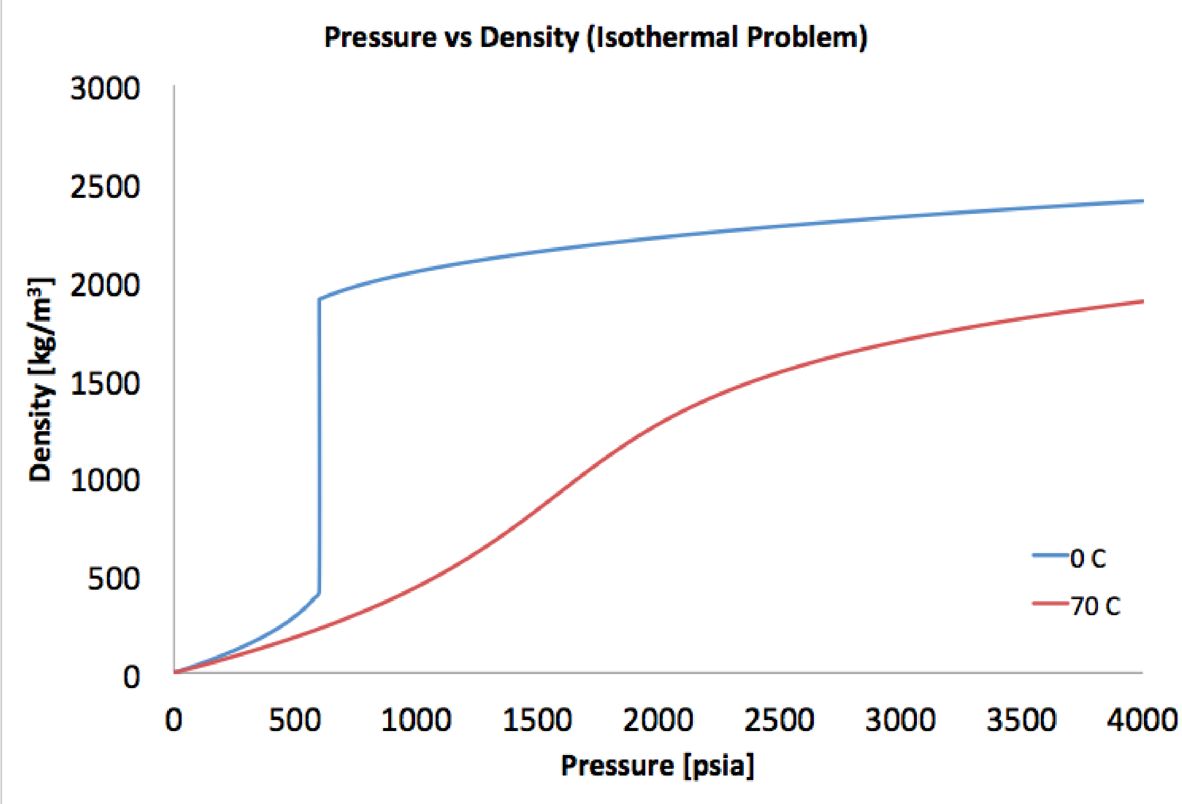

FIGURE 2.23. Isothermal pressure versus density of xenon gas at $T_1 = 0^oC$ and$T_2 = 70^oC$ from reference [78].

(5) The time spent at each flow condition, which corresponds to the time spent between certain current conditions must be provided. Note that the sum of these values should equal the mission time.

Using the volumetric flow rate curves and knowing the time spent at each point, the volume was found using Equation 12.

$$V_{standard} = \int_0^t \dot{q} \mathrm{d}t + u_{waste,standard} \tag{12}$$

In Equation 12, V_{Xe} is the standard volume of the xenon gas, t is the total time of the mission, $\dot{q}$ is the standard volumetric flowrate, and $u_{waste,standard}$ is the standard volume of the left over xenon inside the storage tank due to extremely low pressure and density at the end of lift (EOL). If the emission current versus flowrate curves was discrete, Equation 12 became Equation 13.

$$V_{standard} = \dot{q}_1 \Delta t_1 + \dot{q}_2 \Delta t_2 + \dot{q}_3 \Delta t_3 + \cdots + V_{waste} \tag{13}$$

In Equation 13, $\dot{q}$ is the volumetric flowrate and Δt is the time spent at that flowrate. Knowing the standard volume and standard density ($\rho_{standard}$) of xenon gas expelled allowed for the mass of the xenon gas, excluding ullage waste, to be calculated using Equation 14.

$$m_{Xe} = \rho_{standard} V_{standard} \tag{14}$$

This calculation accounts for $\geq 95\,\%$ of the xenon total volume. The xenon standard density was calculated using the ideal gas law, Equation 14, the total mass can be found.

$$\rho_{standard} = \frac{P_{standard}}{(\frac{R}{\mu_{Xe}} T_{standard})} \tag{15}$$

In Equation 14, R is the universal gas constant, μ_{Xe} is the atomic weight of xenon, $T_{standard}$ is the standard temperature, and $P_{standard}$ the standard pressure.

To determine the ullage waste, a calculation at the EOL of the mission was completed. By using the minimum VACCO XFCM inlet pressure and multiplying it by the user-defined safety factor, a minimum tank pressure was determined. Using the xenon isothermal information provided by NIST [78], the minimum tank density was found at the minimum and maximum operating temperatures. Because the NIST data is discrete, the minimum tank density was found by searching through the NIST data for the two values the minimum tank pressure fell between and then linearly interpolating to find the exact density corresponding to said minimum tank pressure. This also allowed for the state of the gas to be determined. It is important to know the state of the gas because if the gas solidifies, it will increase the ullage waste and result in mission failure.

To determine the ullage mass, the density found at each corresponding temperature and pressure is multiplied by the user-defined tank volume and then averaged, as shown in Equation 16.

$$m_{waste} = \frac{1}{2}(\rho_{NIST,1}(P_{in}, T_1)V_{tank} + \rho_{NIST,2}(P_{in}, T_2)V_{tank}) \tag{16}$$

Besides determining xenon mass, it is important to check and see if the xenon storage tank is suitable for this xenon volume at the minimum and maximum operating temperatures. To determine tank suitability, calculations were done to check the maximum pressure, density, and state seen at the Beginning of Life (BOL).

First, the density of the gas at the BOL wass found using Equation 17.

$$\rho_{BOL} = \frac{m_{standard}}{V_{tank}} \tag{17}$$

Knowing the density at the BOL allowed for the pressure and state of the gas at the corresponding temperature extremes to be found using the user-provided NIST data [78]. The exact value of the pressure was then found using linear interpolation.

Knowing the pressure at the corresponding density allowed for a comparison to be performed between the maximum allowable tank pressure, maximum allowable XFCM pressure, and the pressure of the gas at the BOL. If this gas pressure was greater than the other pressures then a larger tank had to be chosen and the calculations above were repeated. The state was also found to check for solidification of the gas.

2.4.2.9. STRUCTURE

The skeletal structure of the end mass shown Figure 2.24, is depicted as being very sturdy, however, the frame is only meant to provide structural support during launch and a mounting platform for other components. It is believed that the structure can be lightened even further from its listed mass in Section 2.4.3 to a lower mass if a detailed engineering analysis was performed.

Knowing the basic dimensions of the hardware discussed above, the problem of integration can be addressed. Assuming the structural components and mounting brackets will be sturdy yet optimized for weight, a basic assembly can be created. The baseline frame was considered to be made out of $0.64\,cm$ solid aluminum square extrusion at most points and would be welded together for strength and robustness. The mounting points would then be drilled and tapped in these extrusions and the components would be directly bolted on or attached to mounting brackets that would then be bolted to the structural frame. The frame is shown in Figure 2.24.

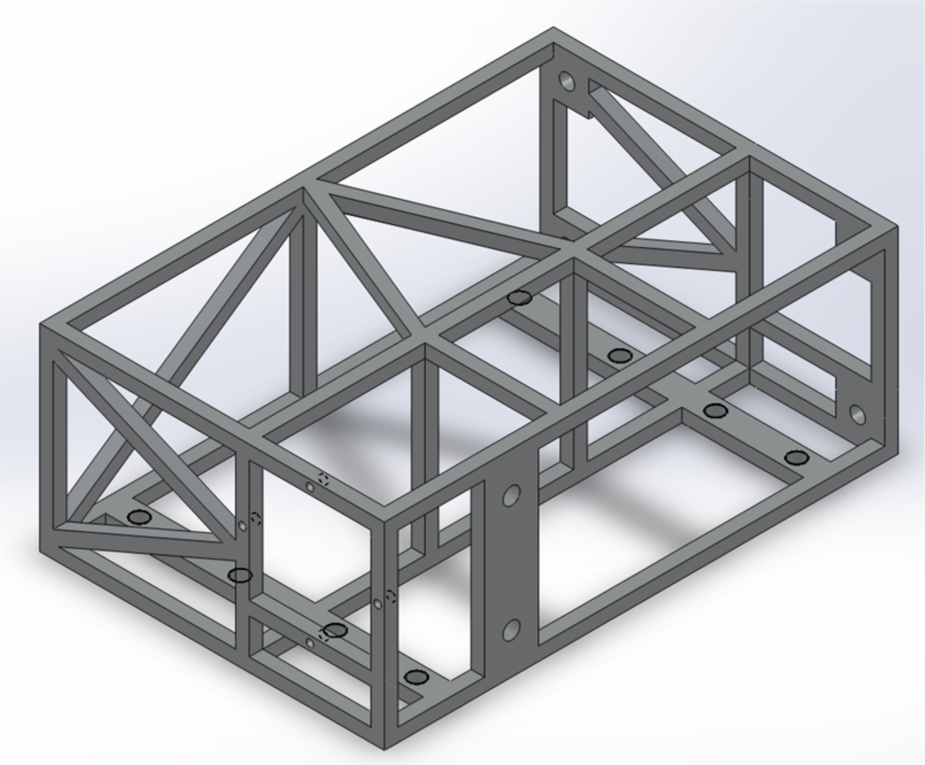

Figure 2.24. EDT end mass structural frame.

The small composite tank mounting brackets, which are very similar to the other tank brackets despite the tank size variation, is shown in Figure 2.25 (a) and (b).

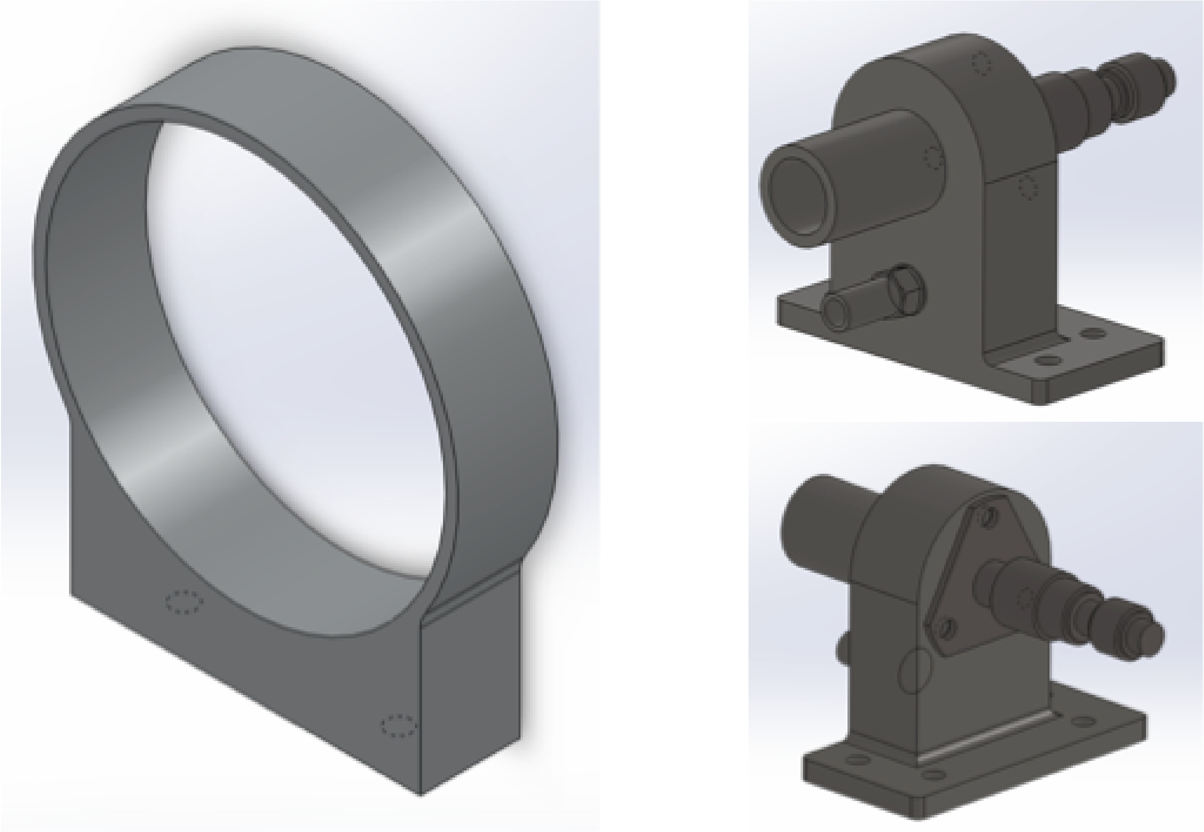

(a) Tank clamp bracket.

(b) Tank connection, fill/drain valve, and throat holding bracket/assembly.

Figure 2.25. Tank connection, fill/drain valve, and throat holding bracket/assembly.

The mass of all other components were assumed to be optimized for weight such that the total baseline mass is less than $\sim 4\,kg$. The structural frame mass came out to be $\sim 0.53\,kg$ and the connecting hardware came out to be $\sim 1.2\,kg$.

For all plasma contactor estimations, it is assumed that the frame and hardware will remain the same except for the tank mounting hardware, which will increase or decrease in size to fit the different tanks.

2.4.2.10. Shielding and Enclosure

Enclosing the end mass system to prevent damage to the inner components is an important consideration. The system, however, does not need to be surrounded in a stiff enclosure. The main reason for an enclosure is temperature control and micro-meteorite defense, therefore, an enclosure consisting mainly of thermal blankets and Whipple Shields (micro-meteorite shielding) will suffice. Because these are sufficiently light, they are not considered in this systems analysis.

2.4.3. System Mass Estimation Summary

The overall plasma contactor mass, excluding xenon gas mass, and the mass of the HCPC components are shown in Table 2.1.

Table 2.1. Plasma contactor mass estimation table.

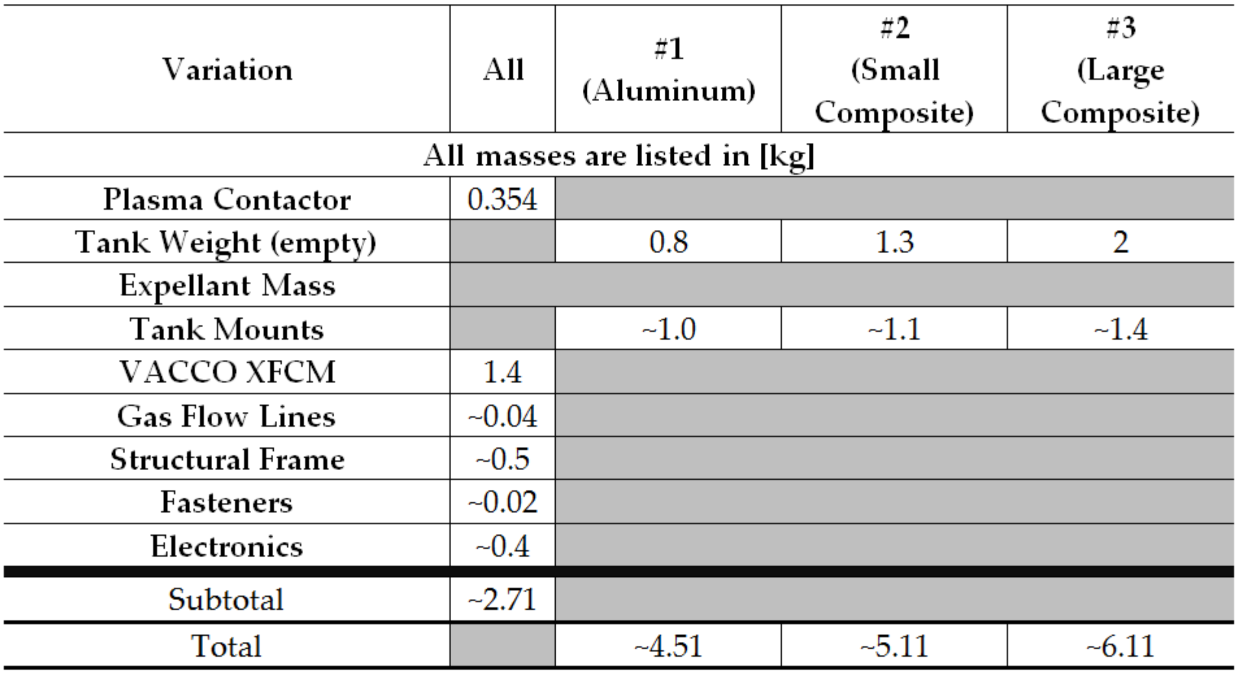

Variation	All	#1 (Aluminum)	#2 (Small Composite)	#3 (Large Composite)
All masses are listed in [kg]				
Plasma Contactor	0.354			
Tank Weight (empty)		0.8	1.3	2
Expellant Mass				
Tank Mounts		~1.0	~1.1	~1.4
VACCO XFCM	1.4			
Gas Flow Lines	~0.04			
Structural Frame	~0.5			
Fasteners	~0.02			
Electronics	~0.4			
Subtotal	~2.71			
Total		~4.51	~5.11	~6.11

An overall system mass can be estimated by calculating a mission deorbit time and using the above table in combination with the xenon mass calculation algorithm. An example of such a procedure would be to assume a mission of ~ 100 days. Knowing this, the tank required for the mission must be the $2\,L$ composite tank. This choice is because the BOL pressure exceeds the maximum allowable pressure for the tank and the XFCM. The resulting plasma contactor system mass excluding expellant mass is $\sim 5.06\,kg$. Applying the expellant mass estimation for xenon gas at a discrete flow rate value of $2\,sccm$ for 90 days, $3.5\,sccm$ for 10 days, and no time spent at $5.5\,sccm$; the resulting xenon mass comes out to $\sim 1.85\,kg$ with a $0.036\,kg$ ullage waste mass. Therefore, the overall plasma contactor system mass including electronics mass, structural mass, and fastener mass comes out to $\sim 6.914\,kg$.

CHAPTER 3

Analysis, Testing, and Results

SimBETS is a compilation of the models and principles discussed in Chapters 1 and 2. The result is a tool that can predict the performance of an electrodynamic tether (EDT) deorbit system. To verify that SimBETS results are correct, data output was compared against other EDT simulations. One other simulation tool, TeMPEST, has been peer-reviewed and compared against flight data such as the TSS-1R and PMG flights. Because a bare EDT system has never flown, however, we have to rely on comparisons between codes to show validity. Presented below are the analyses and results of validations, tolerance requirements, and software-in-the-loop (SIL) and hardware-in-the-loop (HIL) testing.

3.1. Validation and Tolerance Testing

TeMPEST is a tool developed in the late 1990's for analysis of the TSS-1 and TSS-1R experiments. It has been modified since then to account for new types of space tethers like the canceled tether flight ProSEDS. The code is capable of a wide variety of simulations and has been thoroughly validated. This makes it an ideal candidate for comparison and validation of SimBETS. Currently, TeMPEST is outdated in certain areas, specifically the ionospheric and magnetic field models, and because of this issue, comparisons to SimBETS are not going to be exact. The same can be said for SimBETS and the BETsMA code. BETsMA currently has a more up-to-date ionospheric model compared to SimBETS. However, because BETsMA is still in its infancy and is still being developed, much of these comparisons are questionable at the present and will, therefore, not be discussed in this thesis.

Multiple comparisons were completed using TeMPEST. These comparisons include model specific validation such as the orbital propagation model and global comparisons focusing on deorbit time comparisons. It should be noted that TeMPEST was designed to evaluate tether missions where the main mass is the lower mass of the two end masses. This is opposite of SimBETS, but not believed to be a source of error.

3.1.1. TeMPEST Point Comparison

The first validation completed between SimBETS and TeMPEST was a point comparison to check geodetic locations, electromotive forces, anode voltages, current calculations, and drag forces. Due to the variation between the ionospheric models in TeMPEST and SimBETS, the electron density was set to a fixed value typical of LEO and the results were compared. The magnetic field models were also different; however, the variations in these models were small. The results of this point comparison are contained in Tables 3.1 and 3.2.

Table 3.1. TeMPEST/SimBETS location comparison for a 0^o inclination orbit at 0 and $-30\,V$ fixed CBV.

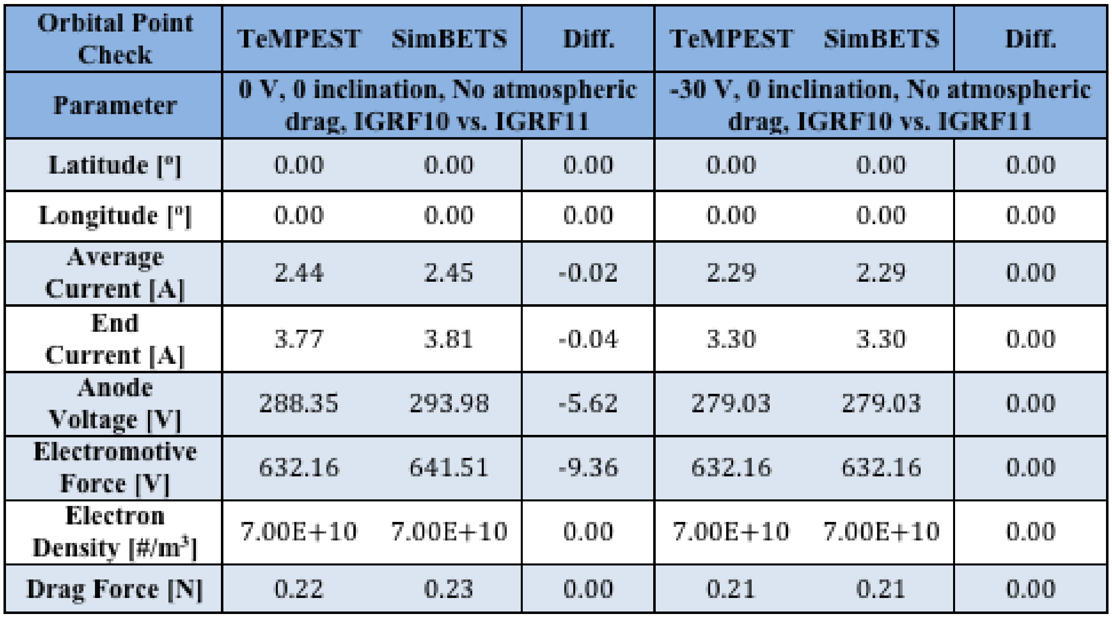

Orbital Point Check	**TeMPEST**	**SimBETS**	**Diff.**	**TeMPEST**	**SimBETS**	**Diff.**
Parameter	**0 V, 0 inclination, No atmospheric drag, IGRF10 vs. IGRF11**			**-30 V, 0 inclination, No atmospheric drag, IGRF10 vs. IGRF11**		
Latitude [°]	0.00	0.00	0.00	0.00	0.00	0.00
Longitude [°]	0.00	0.00	0.00	0.00	0.00	0.00
Average Current [A]	2.44	2.45	-0.02	2.29	2.29	0.00
End Current [A]	3.77	3.81	-0.04	3.30	3.30	0.00
Anode Voltage [V]	288.35	293.98	-5.62	279.03	279.03	0.00
Electromotive Force [V]	632.16	641.51	-9.36	632.16	632.16	0.00
Electron Density [#/m^3]	7.00E+10	7.00E+10	0.00	7.00E+10	7.00E+10	0.00
Drag Force [N]	0.22	0.23	0.00	0.21	0.21	0.00

Table 3.2. TeMPEST/SimBETS location comparison for a 35^o inclination orbit at 0 and $-30\,V$ fixed CBV.

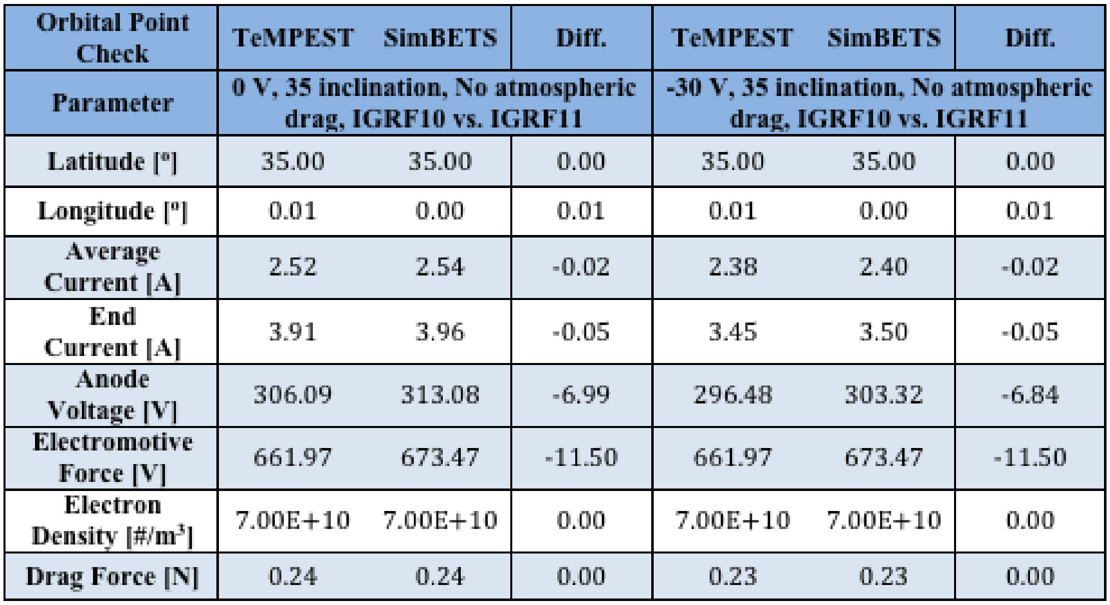

Orbital Point Check	TeMPEST	SimBETS	Diff.	TeMPEST	SimBETS	Diff.
Parameter	0 V, 35 inclination, No atmospheric drag, IGRF10 vs. IGRF11			-30 V, 35 inclination, No atmospheric drag, IGRF10 vs. IGRF11		
Latitude [º]	35.00	35.00	0.00	35.00	35.00	0.00
Longitude [º]	0.01	0.00	0.01	0.01	0.00	0.01
Average Current [A]	2.52	2.54	-0.02	2.38	2.40	-0.02
End Current [A]	3.91	3.96	-0.05	3.45	3.50	-0.05
Anode Voltage [V]	306.09	313.08	-6.99	296.48	303.32	-6.84
Electromotive Force [V]	661.97	673.47	-11.50	661.97	673.47	-11.50
Electron Density [#/m^3]	7.00E+10	7.00E+10	0.00	7.00E+10	7.00E+10	0.00
Drag Force [N]	0.24	0.24	0.00	0.23	0.23	0.00

Each table shows very good agreement in each category. The largest deviation was in the *emf* and amounted to a $11.5\,V$ difference at a 35^o inclinated orbit and $0\,V$ CBV. This variation is likely caused by the use of two different magnetic field models. Since SimBETS uses a more recent edition, it can be assumed that SimBETS produces a more accurate prediction at a single point when compared to TeMPEST.

3.1.2. TeMPEST Orbital Propagation Comparison

Once agreement of TeMPEST and SimBETS at a point was shown, the orbital propagation model in SimBETS was tested. By turning atmospheric and electrodynamic effects, and orbital perturbations “off” and propagating orbits in both TeMPEST and SimBETS, the orbital propagation model of SimBETS could be tested. Tables 3.3 and 3.4 show the results of this comparison.

Table 3.3. TeMPEST/SimBETS orbit propagation comparison for a 0^o inclination orbit.

Orbital Point Check	TeMPEST	SimBETS	% Diff.	TeMPEST	SimBETS	% Diff.	TeMPEST	SimBETS	% Diff.
Time [hr]	0		-	1.52		-	3.02		-
Latitude [º]	0.00	0.00	0.00	0.00	0.00	0.00	0.00	0.00	0.00
Longitude [º]	0.00	0.00	0.00	-60.87	-60.94	0.07	-125.56	-125.67	0.11
Right Ascension of the Ascending Node [º]	-57.30	0.00	-57.30	-57.30	0.00	-57.30	-57.30	0.00	-57.30
Argument of Perigee [º]	-57.30	0.00	-57.30	179.46	0.00	179.46	170.85	0.00	170.85
Eccentricity	0.00	0.00	0.00	0.00	0.00	0.00	0.00	0.00	0.00
Inclination [º]	0.00	0.00	0.00	0.00	0.00	0.00	0.00	0.00	0.00
Semi-Major Axis [km]	7228.14	7228.14	0.00	7228.14	7228.12	0.01	7228.14	7228.11	0.03
True Anomaly [º]	156.45	0.00	156.45	-15.00	-60.94	45.94	-47.44	-125.67	78.22
X-Component [km]	-6625.98	-6625.61	-0.36	-6999.18	-6996.95	-2.23	-3979.77	-3968.41	-11.36
Y-Component [km]	-2888.32	-2889.15	0.83	1804.83	1813.40	-8.57	6033.86	6041.30	-7.45
Z-Component [km]	0.00	0.00	0.00	0.00	0.00	0.00	0.00	0.00	0.00
Radial Distance [km]	7228.14	7228.14	0.00	7228.14	7228.12	0.01	7228.14	7228.11	0.03

Table 3.4. TeMPEST/SimBETS orbit propagation comparison for a 35^o inclination orbit

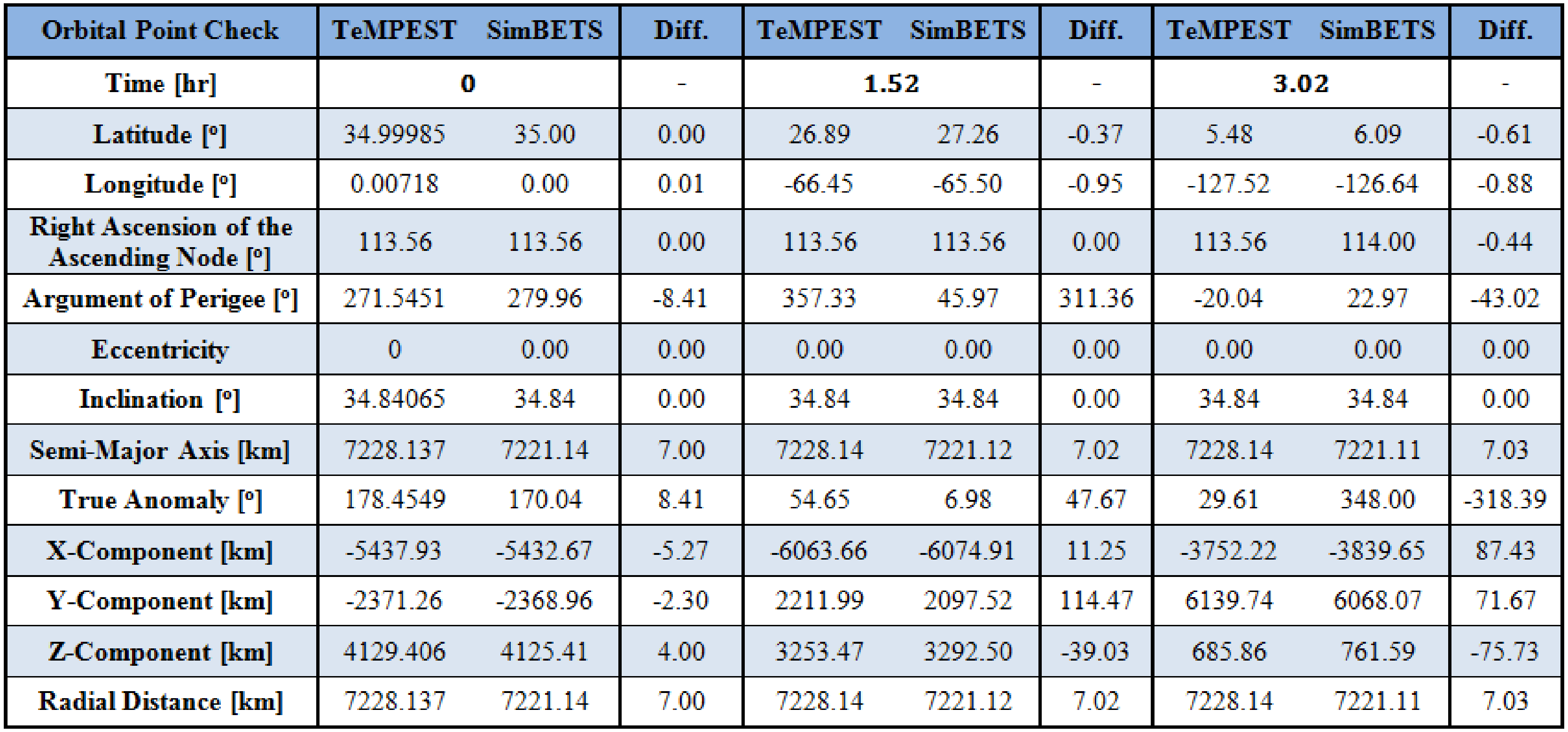

Orbital Point Check	TeMPEST	SimBETS	Diff.	TeMPEST	SimBETS	Diff.	TeMPEST	SimBETS	Diff.
Time [hr]	**0**		-	**1.52**		-	**3.02**		-
Latitude [°]	34.99985	35.00	0.00	26.89	27.26	-0.37	5.48	6.09	-0.61
Longitude [°]	0.00718	0.00	0.01	-66.45	-65.50	-0.95	-127.52	-126.64	-0.88
Right Ascension of the Ascending Node [°]	113.56	113.56	0.00	113.56	113.56	0.00	113.56	114.00	-0.44
Argument of Perigee [°]	271.5451	279.96	-8.41	357.33	45.97	311.36	-20.04	22.97	-43.02
Eccentricity	0	0.00	0.00	0.00	0.00	0.00	0.00	0.00	0.00
Inclination [°]	34.84065	34.84	0.00	34.84	34.84	0.00	34.84	34.84	0.00
Semi-Major Axis [km]	7228.137	7221.14	7.00	7228.14	7221.12	7.02	7228.14	7221.11	7.03
True Anomaly [°]	178.4549	170.04	8.41	54.65	6.98	47.67	29.61	348.00	-318.39
X-Component [km]	-5437.93	-5432.67	-5.27	-6063.66	-6074.91	11.25	-3752.22	-3839.65	87.43
Y-Component [km]	-2371.26	-2368.96	-2.30	2211.99	2097.52	114.47	6139.74	6068.07	71.67
Z-Component [km]	4129.406	4125.41	4.00	3253.47	3292.50	-39.03	685.86	761.59	-75.73
Radial Distance [km]	7228.137	7221.14	7.00	7228.14	7221.12	7.02	7228.14	7221.11	7.03

Noting the values in the difference columns of Tables 3.3, it is evident that some of the COEs are different. This is most likely due to a variation in how the two codes calculate values for circular, non-inclined orbits and the fact that some of the COE's are poorly defined like the RAAN, argument of perigee, and true anomaly. This is shown by comparing the values calculated at 30^o inclination in Table 3.4 with the similar values in Table 3.3. These results allow us to state that both SimBETS and TeMPEST are in agreement in terms of the orbital propagation.

3.1.3. EDT Deorbit Calculation Comparison

SimBETS and TeMPEST EDT deorbit maneuvers were compared for four different sets of orbital input parameters: 0^o inclination, $0\,V$ CBV; 0^o inclination, $-30\,V$ CBV; 35^o inclination, $0\,V$ CBV; and 35^o inclination, $-30\,V$ CBV. These comparisons were done with a fixed ionospheric plasma electron density of $7 \times 10^{-10}\,electrons/m^3$. These validations allowed TeMPEST's magnetic field model and orbital propagation technique to be compared to SimBETS. The orbital perturbations and atmospheric drag effects were turned "off" for both SimBETS and TeMPEST. Due to the variation of the magnetic field models used, it was understood that there would be a small variation between two codes. The main validation desired was the deorbit time. Assuming the deorbit times were similar and the plots overlapped each other, then variations between TeMPEST and SimBETS could be largely attributed to the magnetic field model variations and other small, negligible differences. Figures 3.1, 3.2, 3.3, and 3.4 show the radial distances of the two simulations as a function of time as well as the deorbit time and the difference between the deorbit times. Note all of these comparisons have been performed against radial distance because SimBETS and TeMPEST compare against two different ellipsoids when outputting altitude.

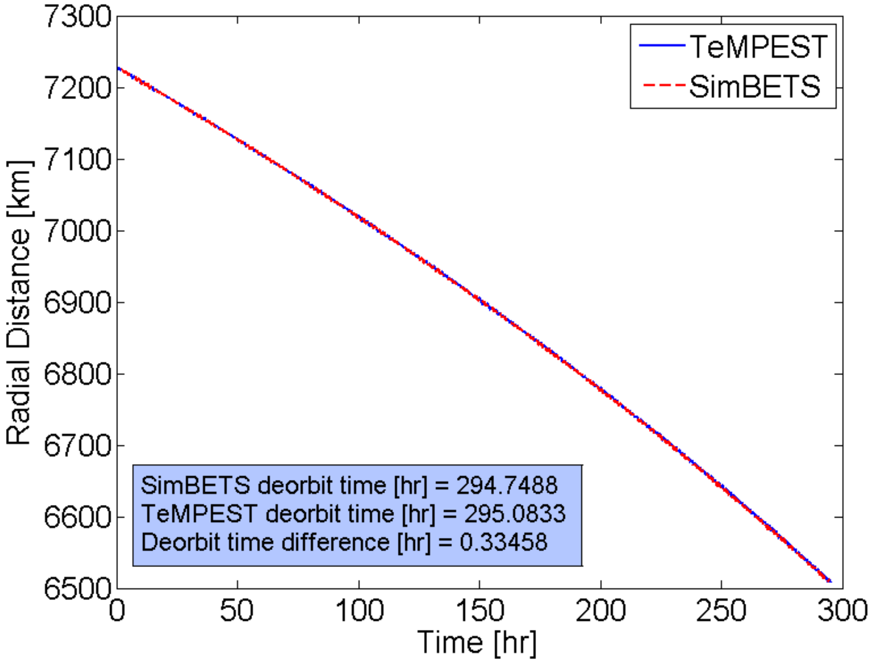

FIGURE 3.1. TeMPEST/SimBETS deorbit comparison for a 0^o inclination orbit and $0\,V$ CBV. Good agreement was observed between the two simulations.

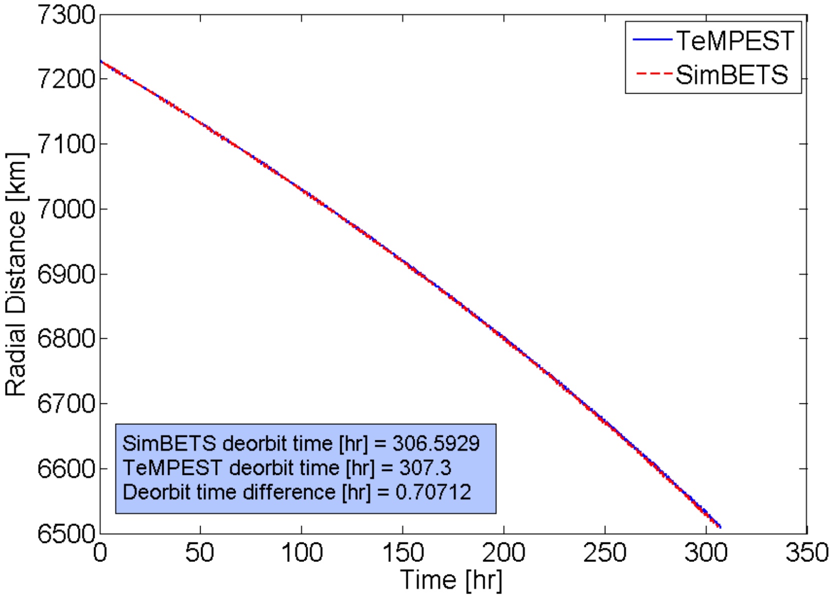

FIGURE 3.2. TeMPEST/SimBETS deorbit comparison for a 0^o inclination orbit and $-30\,V$ CBV. Good agreement was observed between the two simulations.

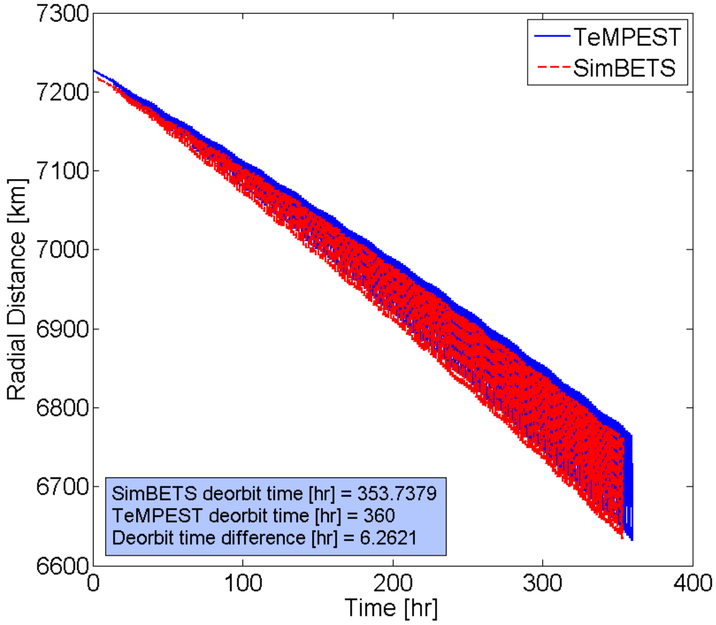

FIGURE 3.3. TeMPEST/SimBETS deorbit comparison for a 35^o inclination orbit and $0\,V$ CBV. Good agreement was observed between the two simulations.

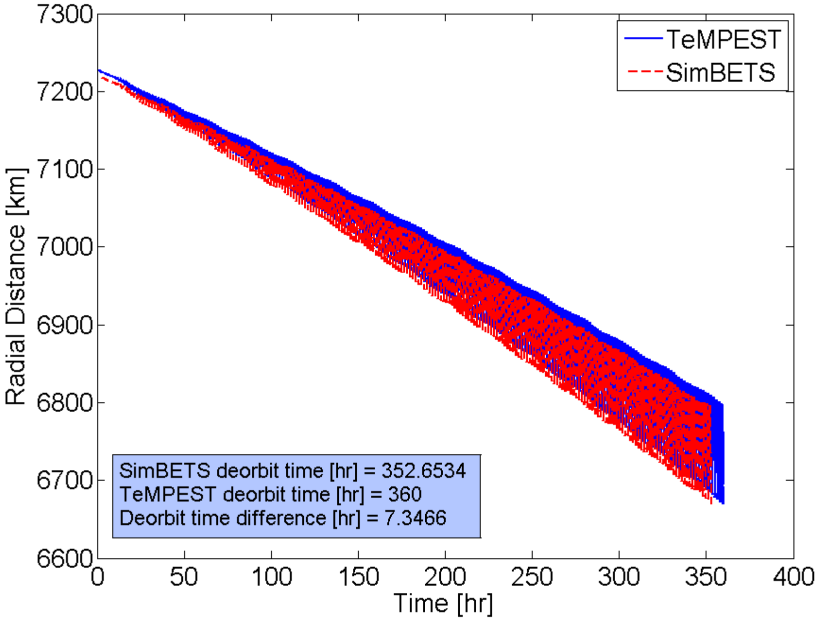

FIGURE 3.4. TeMPEST/SimBETS deorbit comparison for a 35^o inclination orbit and $-30\,V$ CBV. Good agreement was observed between the two simulations.

The deorbit time for each comparison was found to be within $0.5 - 7\,\%$ of the other simulation where $0.5\,\%$ is for 0^o inclined, $0\,V$ CBV and $7\,\%$ for the 35^o inclined, $-30\,V$ CBV. The deviations are believed to be due to the different magnetic field model that were used. It should also be noted that the oscillations present in Figures 3.3 and 3.4 are not present in Figures 3.1 and 3.2. This is because the electron density was fixed and combining this with resonance effects at the equator helped prevent much of the resonant effects seen in the later figures at equatorial orbits.

The final step towards completing the validation process of SimBETS was to show the effect of a varying ionospheric model in comparison to TeMPEST at a fixed electron density. The same deorbit was then also completed for BETsMA, which uses the most accurate electron density model. The result shown in Figure 3.5 indicates that TeMPEST and SimBETS aligning well at high orbital radii, however, below $6,700\,km$, the variations between the simulations become drastic.

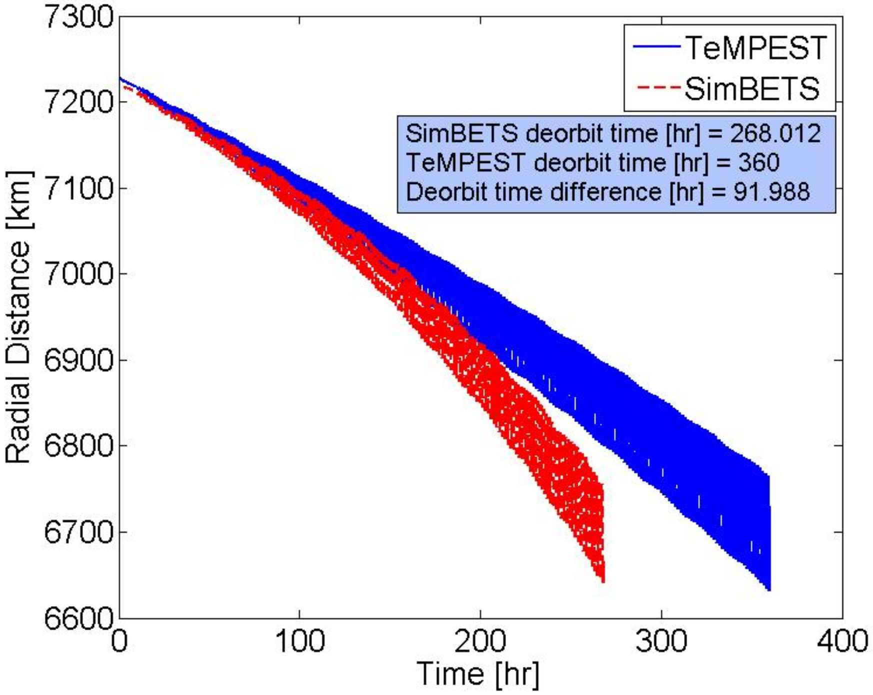

FIGURE 3.5. TeMPEST/SimBETS radial distance versus time comparison for a 0^o inclination orbit at $0\,V$ CBV. Differences between the two simulations are caused by the use of IRI2007 ionospheric model in SimBETS and a constant ionospheric plasma density in TeMPEST as shown in Figure 3.6. TeMPEST has the ability to include an accurate ionospheric model, however, this feature was unavailable to us at the time this validation was completed.

The addition of a varying ionospheric model causes the deorbit time for SimBETS to decrease by nearly $25\,\%$ in comparison to TeMPEST. Most of the difference is due to the change in electron density over time, which, on average, is an exponentially increases down to $\sim 6,700\,km$ as shown in Figure 3.6.

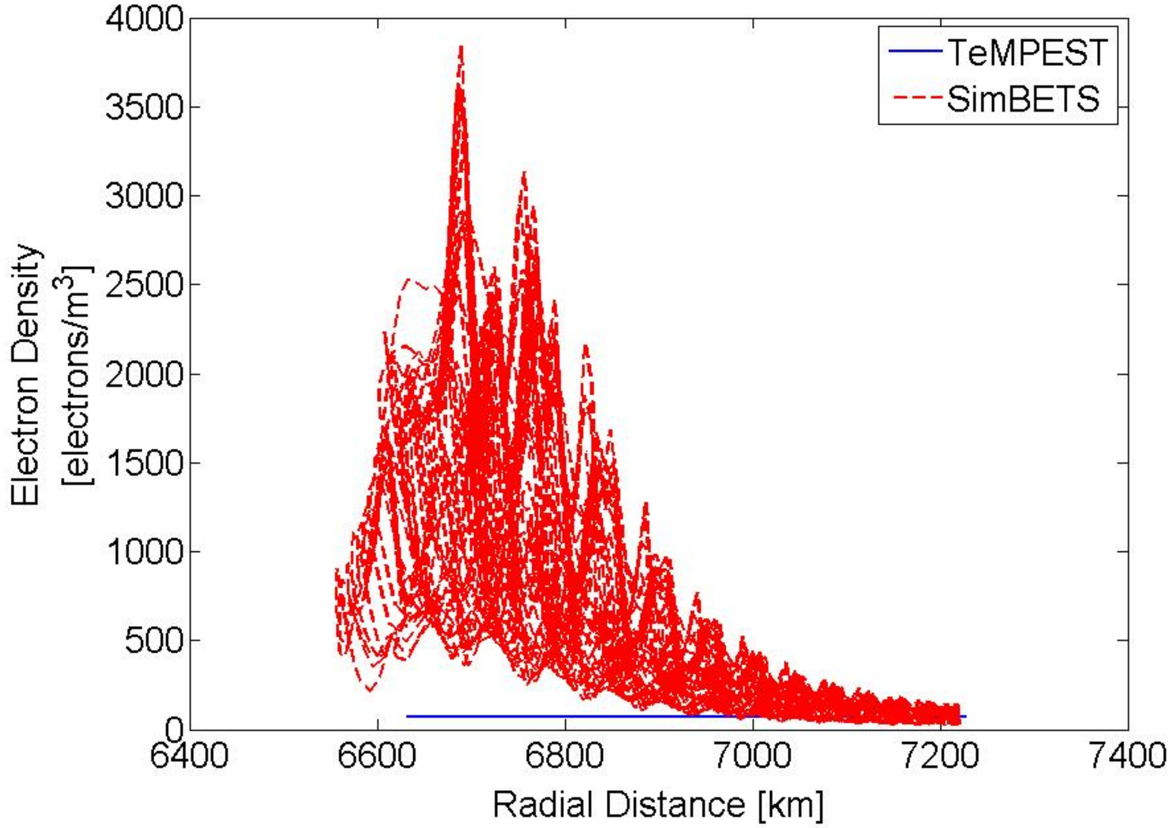

FIGURE 3.6. TeMPEST/SimBETS electron density versus radial distance comparison for the deorbit validation shown in Figure 3.5.

Figure 3.7 compares the SimBETS deorbit time to BETsMA. The two deorbit times are much closer, only differing by $\sim 15\,\%$.

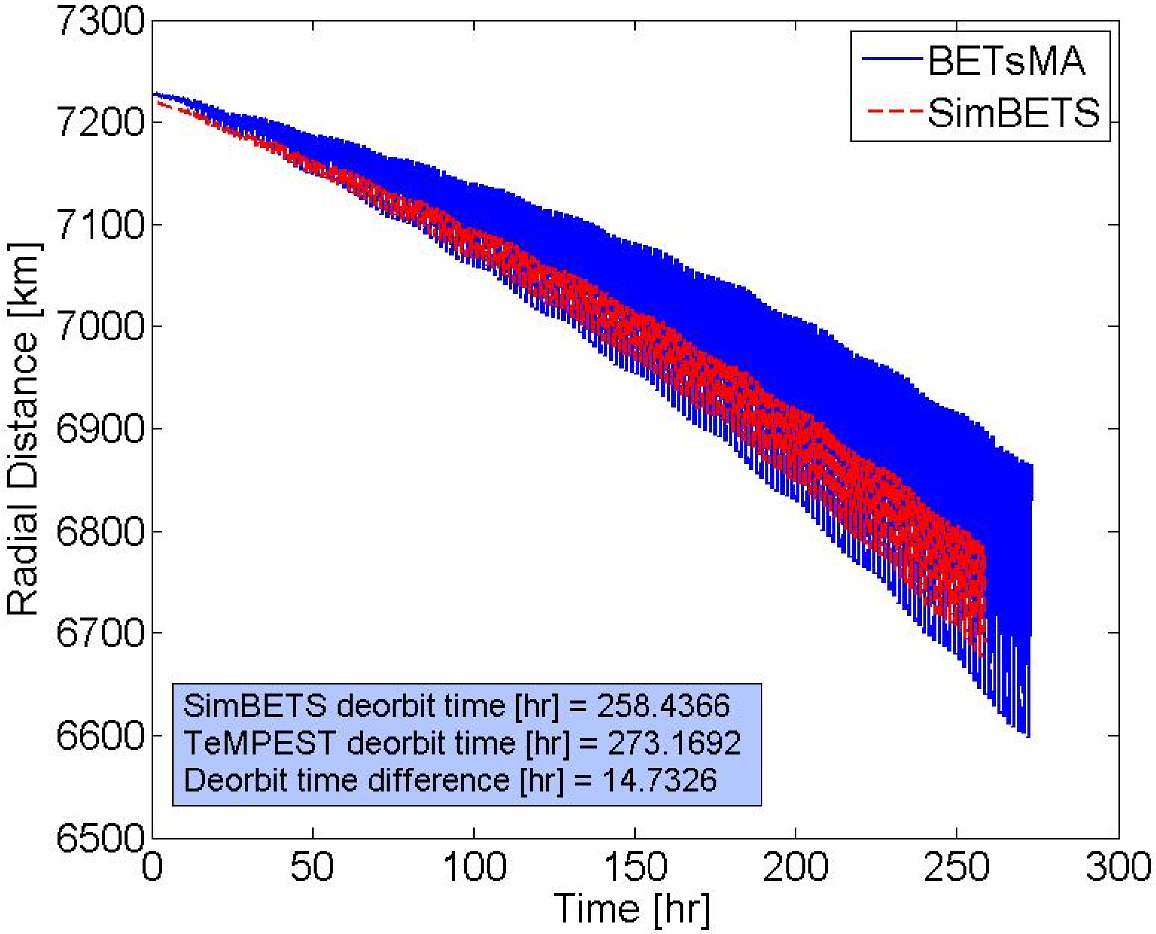

Figure 3.7. BETsMA/SimBETS radial distance versus time comparison for a 0^o inclination orbit at $0\,V$ CBV.

Since BETsMA is still in development, substantial conclusions as to why this variation between the two simulations is present cannot be made, however, it is believed that differences between the two ionospheric models used causes most of the differences observed. Figure 3.8 shows a comparison plot of electron density versus time. Time is chosen as the independent parameter because the variation between the two models is not easily distinguishable with radial distance.

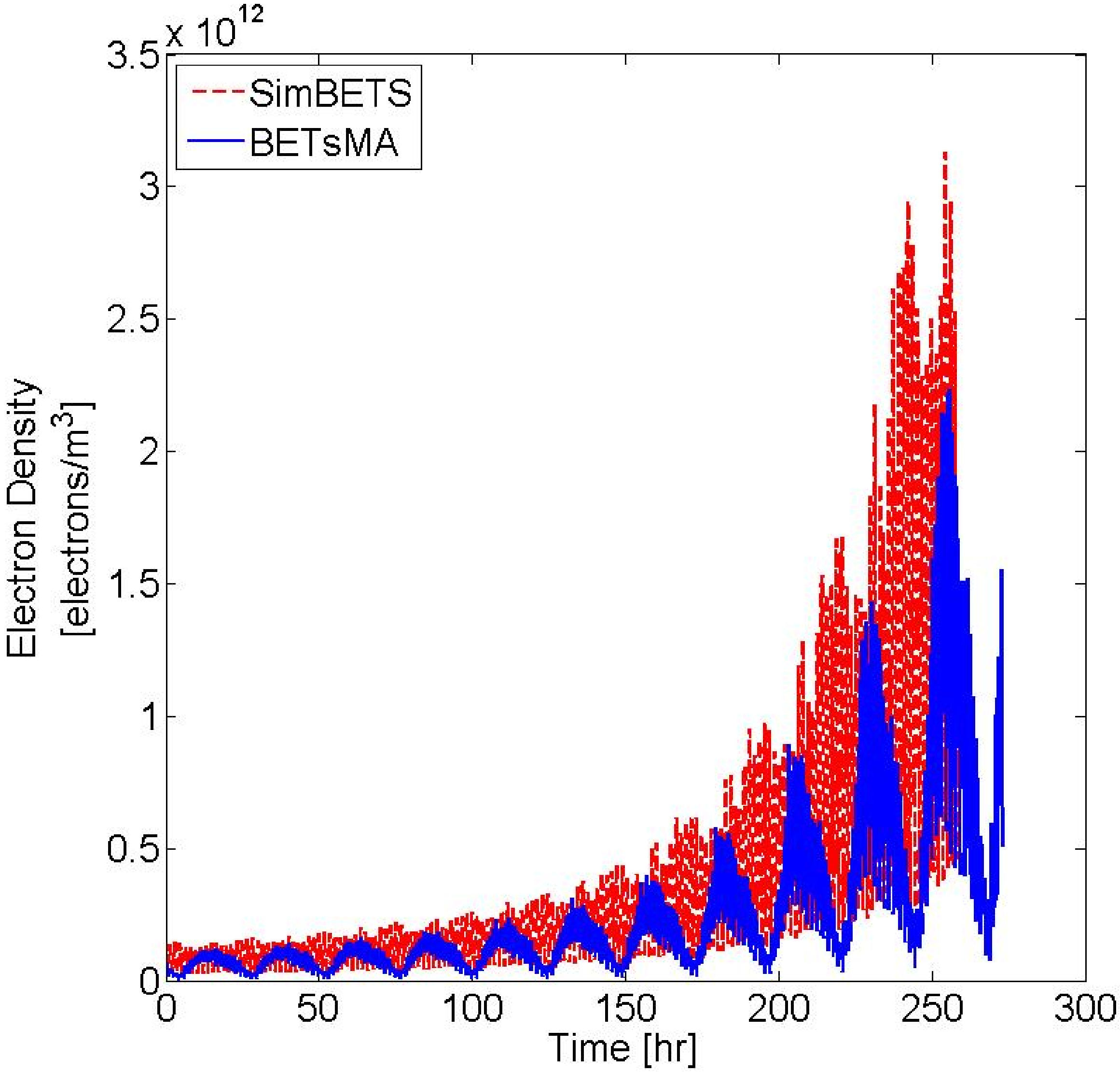

FIGURE 3.8. BETsMA/SimBETS electron density versus time comparison for a 0^o inclination orbit at $0\,V$ CBV.

Note the electron density plots align relatively well, however, the resonances seen in the IRI2012 model used in BETsMA are much lower in frequency and amplitude than the resonances in the IRI2007 model. This result leads us to believe the differences in Figure 3.7 are related to the different IRI models used in the simulations. The IRI2012 model is probably the correct one to use, however, it has not been made available during the time this thesis was written presumably because changes and upgrades are being made to it.

3.1.4. RELATIVE TOLERANCE TESTING

Before any studies could be performed, the relative tolerance of the orbital propagation model had to be determined. By running SimBETS multiple times at different tolerances, information about the performance of SimBETS could be gathered. Of most importance was runtime versus accuracy, which is possible to choose since the Runga-Kutta-Fehlberg implicit, time-dependent solver is used in SimBETS. Tables 3.5 and 3.6 and Figures 3.9 and 3.10 are the results of a tolerance versus runtime test completed for 0^o and 71^o inclined orbits.

TABLE 3.5. Relative tolerance versus simulation runtime/error for a 25 km deorbit at solar median and 0^o inclination of a 2 km, 2 cm, 50 μm tether.

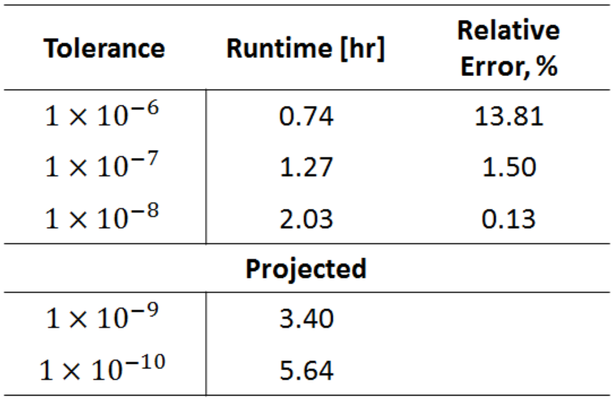

Tolerance	**Runtime [hr]**	**Relative Error, %**
1×10^{-6}	0.74	13.81
1×10^{-7}	1.27	1.50
1×10^{-8}	2.03	0.13
	Projected	
1×10^{-9}	3.40	
1×10^{-10}	5.64	

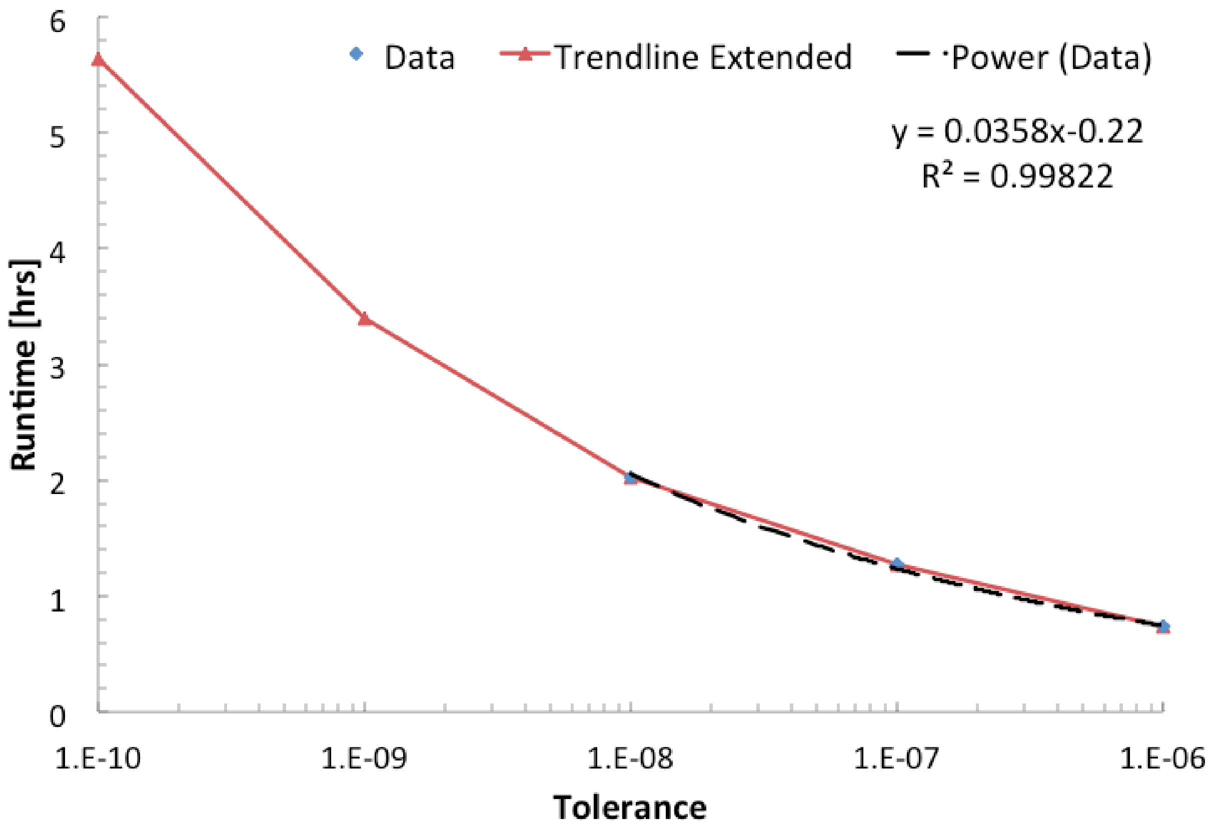

FIGURE 3.9. Relative tolerance versus simulation runtime for a 25 km deorbit at solar median and 0^o inclination of a 2 km, 2 cm, 50 μm tether.

TABLE 3.6. Relative tolerance versus simulation runtime/error for a 25 km deorbit at solar median and 71^o inclination of a 2 km, 2 cm, 50 μm tether.

Tolerance	**Runtime [hr]**	**Relative Error, %**
1×10^{-6}	3.03	61.86
1×10^{-7}	3.03	12.65
1×10^{-8}	10.00	0.088
Projected		
1×10^{-9}	14.88	
1×10^{-10}	27.04	

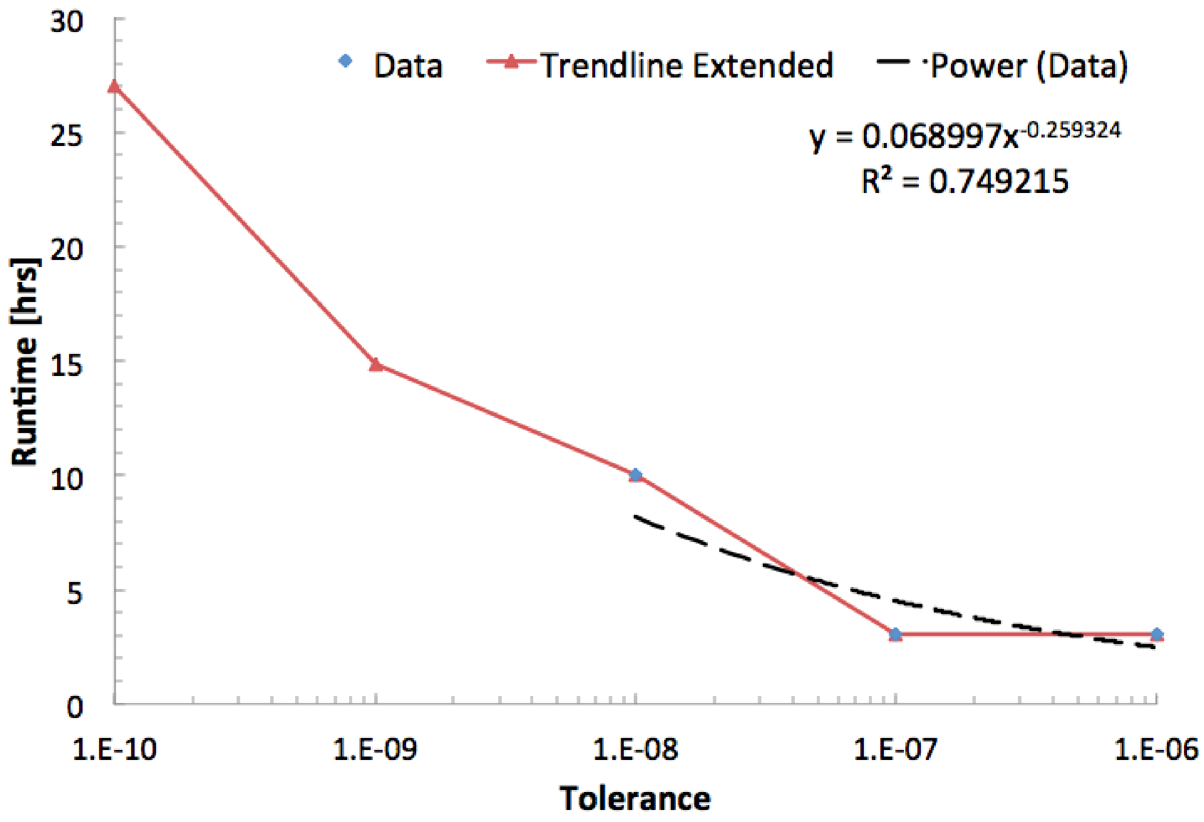

FIGURE 3.10. Relative tolerance versus simulation runtime for a 25 km deorbit at solar median and 71^o inclination of a 2 km, 3 cm, 50 μm tether.

Focusing on Table 3.5, it should be noted that decreasing the tolerance by a factor of 10 from 1×10^{-6} to 1×10^{-7} results in nearly a two-thirds longer runtime, but the error in the solution decreases by up to 1.5 %. The same cannot be said when the tolerance is decreased again by a factor of 10. This next tolerance step decreases the error to below a fifth of a percent; however, the cost is about three-fifths more in runtime.

Turning to Table 3.6, a similar trend can be seen, however, the runtime is the same for the jump from tolerance 1×10^{-6} to 1×10^{-7}. This is most likely because solving the BVP that describes the current and voltage in the tether can be difficult at high inclinations and can lead to multiple iterations failing at a certain time and position. Overall, both tables point to a tolerance of 1×10^{-7} as being suitable for performing comparisons between EDT systems.

3.2. Software In the Loop (SIL) Testing

With the implementation of a realistic hollow cathode plasma contactor (HCPC), multiple studies were completed to study the effects the HCPC model had on each parameter. These studies show key research areas that would advance the EDT field the most. Six different SIL studies were completed and one HIL test to show the effects of an EDT HCPC operated under realistic conditions. Below is a brief discussion of the studies performed, the reasoning behind them, and their results.

3.2.1. SIL Deorbit Testing

The second and third objectives of this thesis focused on the use of SimBETS to highlight operational requirements and shortcomings of the EDT system. These objectives were met by varying five parameter variations that best demonstrate the effects of a non-ideal HCPC on a bare EDT system and its performance. These parameters are: PC model type (constant or varying contactor bias voltage), contactor bias voltage ($0\,V$, $-30\,V$, $-50\,V$ or varying), orbital inclination (0^o, 35^o, and 71^o), satellite mass ($500\,kg$, $1,000\,kg$, and $1,500\,kg$), tether length ($2.5\,km$, $5\,km$, and $7.5\,km$), and tether width ($1\,cm$, $2\,cm$ and $3\,cm$). A single run using the varying PC model and a tether thickness of $100\,\mu m$ was also performed. To relate these to each other and data in the scientific community, a control case was also developed. This case and the other studies are discussed in the following subsections.

3.2.1.1. Control Study

This case consists mainly of an ideal HCPC model; $5\,km$, $2\,cm$, $50\,\mu m$ bare tether with a $5\,km$ inert section and a $300\,m$ insulated section; and a $1,000\,kg$ satellite mass. The date and time were also chosen to be near a solar medium date such that extreme ionospheric conditions were avoided. The EDT end mass system was considered to be the baseline system discussed in Chapter 2.

The results of the control case can be shown in a variety of ways. Of most importance is deorbit time and EDT system outputs such as mass and current. Figure 3.11 is a plot of the altitude above the WGS84 ellipsoid as a function of time. Note the altitude is equal to the radial distance minus the Earth's equatorial radius in this case because the orbit is in the equatorial plane. Also, note the increasing oscillatory effect of Figure 3.11 as time increases. This shows the EDT resonates with the space plasma density and magnetic field naturally wants to induce an eccentricity into the orbit. More detail about this effect is discussed with the eccentricity and inclination plots.

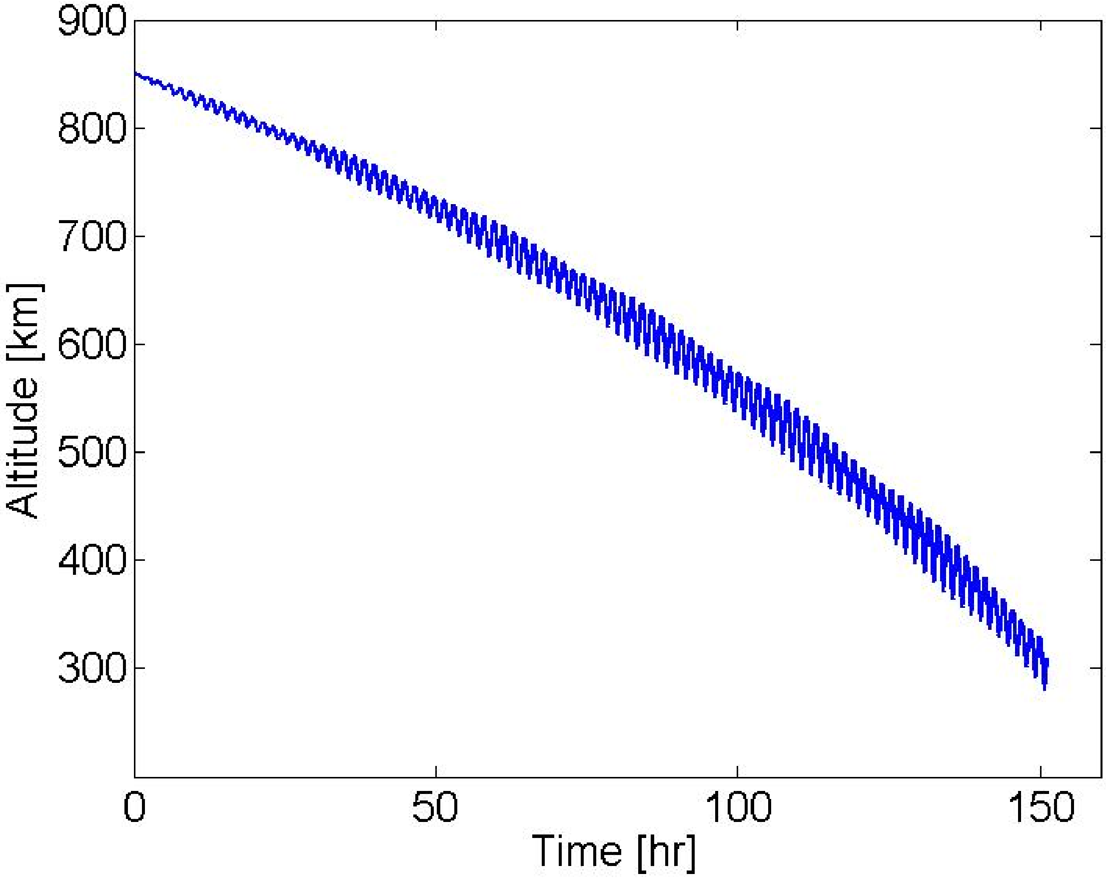

FIGURE 3.11. Altitude above the WGS84 ellipsoid versus time for the simulation of an EDT system with the parameters defined in the control case.

Figure 3.12 shows the semi-major axis of the orbit as a function of time where no oscillations are present. This figure is noteworthy because it shows that the EDT is continually spiraling inward despite the altitude plot suggesting otherwise. The decay of an orbit is not defined by its radial distance or altitude, but rather by its semi-major axis. It is the change in this parameter to a final semi-major axis that is chosen by the SimBETS user that determines the final deorbit altitude.

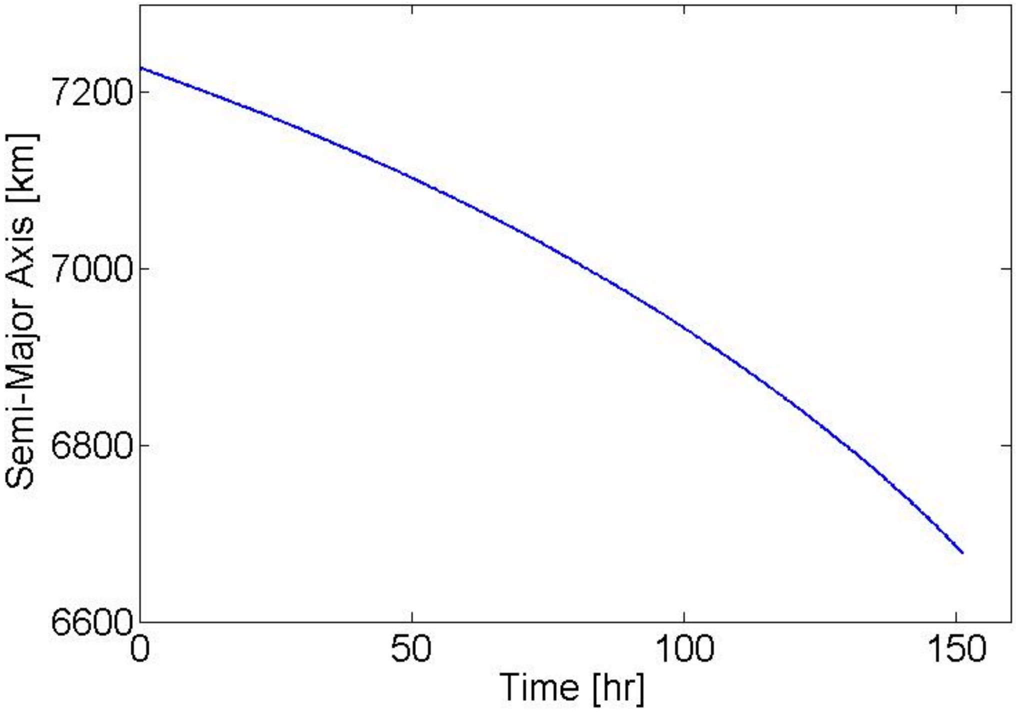

FIGURE 3.12. Semi-major axis versus time.

Once this part of the program has reached an altitude at or below this altitude change, the iterative solver stops and moves to the next line of code. It should be noted that all final deorbit locations are not at the same altitude or time because the final iterative solver step may have passed over the deorbit condition and stopped at a lower semi-major axis value. To account for this, a linear interpolation was completed to determine an accurate deorbit time that could be compared to.

Orbital element related plots are shown in Figures 3.13 through 3.16. Figures 3.13 - 3.16 show how the orbital elements of a deorbiting EDT propagates with time. The most important note is the resonant nature of the eccentricity and inclination. This is important because this result is a product of the relative two body equation used to propagate the orbit and the variations in Earth's magnetic field and ionosphere, not a specific phenomenon hard coded into SimBETS. This mimics what has been predicted by other programs and adds to the validity of SimBETS. The first resonance is caused by variations between the Earth's ionosphere and magnetic field between the night and day side of the Earth. This results in a resonance with a period of one orbit, or $\sim$ 90 minutes. The second resonance is a result of the tilt of the Earth's magnetic field and the rotation of the Earth. As the Earth rotates, the plane created between the magnetic poles and the geographic poles rotates. As this plane rotates, the magnetic field line density and electron density increases and decreases. Combining this behavior with the Earth's magnetic field trying to rotate the EDT's orbit to better align with its equatorial orbit results in the second resonance, which has a period linked to a single rotation of the Earth, $\sim$ 1 day. It should also be noted that the resonant effects increase with decreasing altitude. This relates to the magnetic field line and electron density increasing with decreasing altitude. This has similar affects to other parameters that will be shown later in this section. The odd behavior of the RAAN and argument of perigee is because of the somewhat undefined nature of the COEs in a near circular, non-inclined orbit.

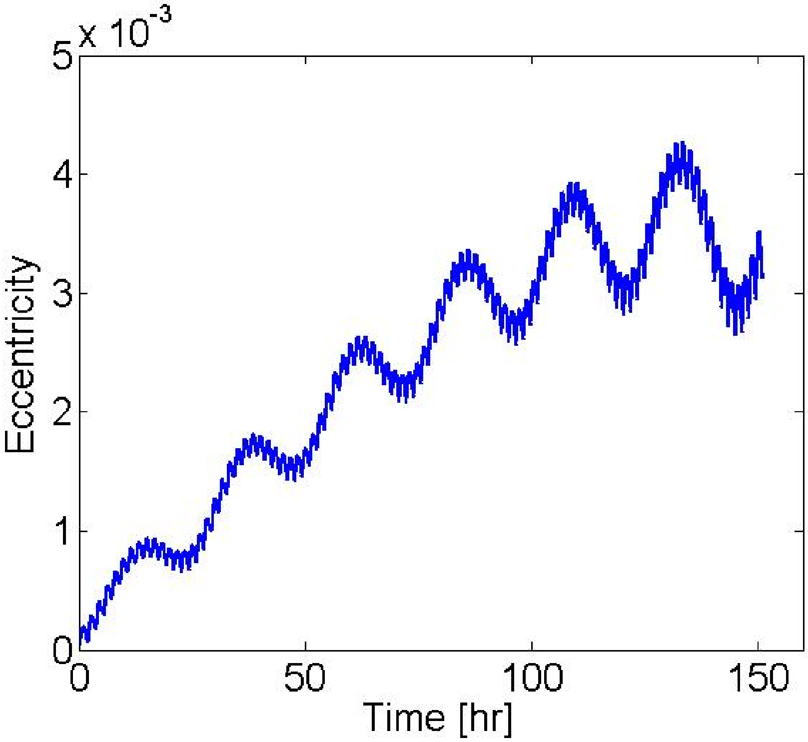

FIGURE 3.13. Eccentricity versus time. Note the very small values of eccentricity, which suggest the orbit remains nearly circular

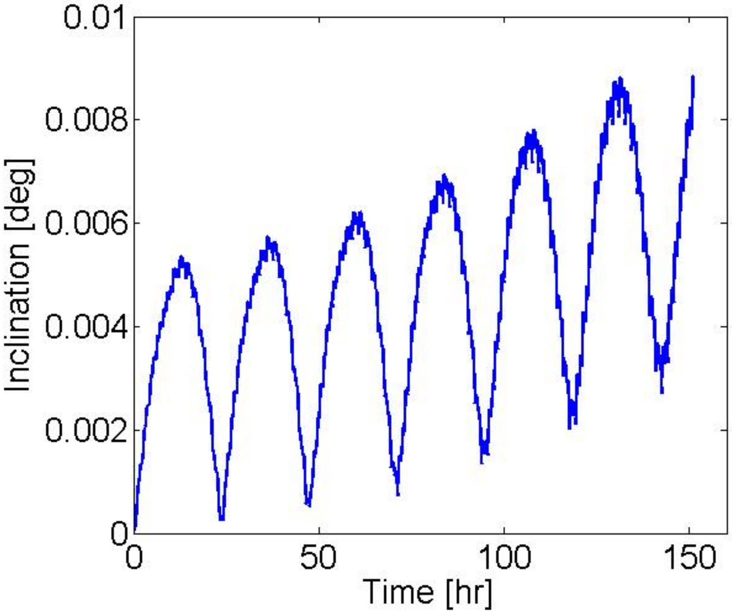

FIGURE 3.14. Inclination versus time. Note the small values of inclination, which suggests the EDT remains in a nearly equatorial orbit.

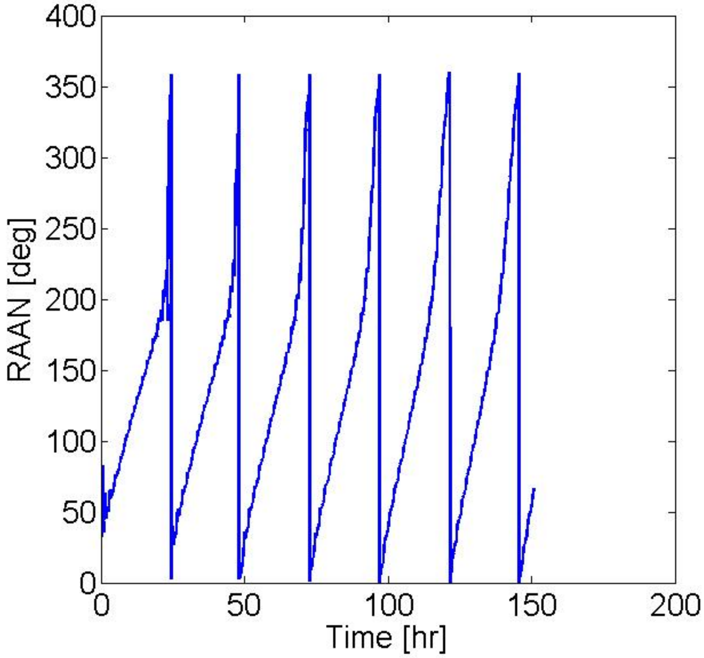

Figure 3.15. Right Ascension of the Ascending Node (RAAN) versus time. Note the relatively quick changes in RAAN. This is expected of an orbit with an inclination near zero that has small forces acting on it due to the slight misalignment of the Earth's magnetic field axis and the Earth's spin axis.

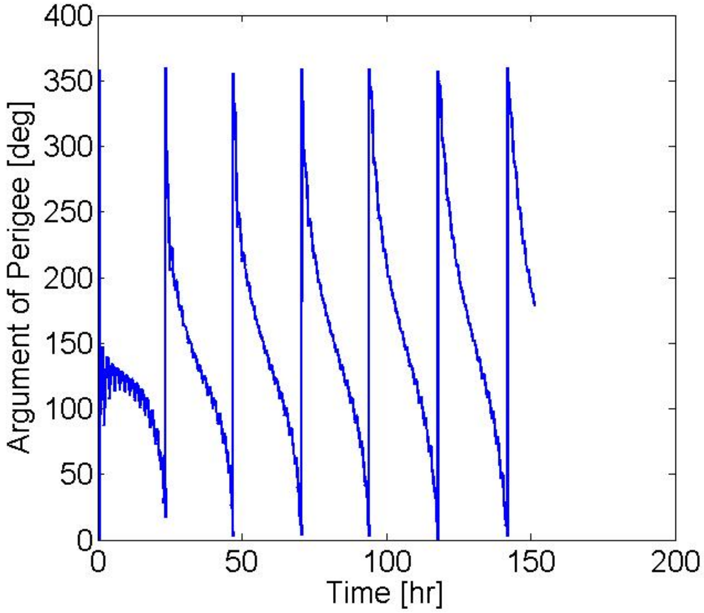

Figure 3.16. Argument of perigee versus time. See Figure 3.15 caption for an explanation of why the argument of perigee varies for an orbit at low inclination that is being perturbed.

Other plots also of interest, include the electromotive force (emf), Figure 3.17; anode voltage (V_A), Figure 3.18; the end current (I_C), Figure 3.19; the magnitude of the total drag force produced, Figure 3.20; and expellant flowrate, Figure 3.21.

The plot of *emf* versus time, Figure 3.17, shows a very steady but increasingly resonant *emf*, moving from an initial trough to peak amplitude to a final trough to peak amplitude of $400\,V$ to $450\,V$, respectively. This steady increase is associated with the change in altitude because with decreasing altitude comes increasing magnetic field strength and relative velocity. A higher *emf* is useful because it allows more current to be gathered and thus more drag force to be produced. This is why at lower altitudes the deorbit rate is much faster compared to higher altitudes. The resonant effect is caused by the second resonances discussed earlier.

The anode voltage plot, Figure 3.18, shows how the tether voltage at point A varies with time. At certain points, the change in voltage is on the order of $500\,V$. As the entire system deorbits, however, these local maximum and minimum points and the average anode voltage decrease to lower voltages. Therefore, it can be said that for equatorial orbits, EDTs see higher anode voltages and larger anode voltage fluctuations the further away they are from the Earth's surface (up to the about $1,500\,km$). This result is due to the smaller currents collected at higher altitudes, which relates to the Earth's magnetic field line and electron density. These currents can be observed in Figure 3.19.

Relating Figure 3.19 to more practical uses, the end current versus time plot is useful because it allows for system engineers to see if the HCPC system will need to use its heater and keeper during operation. For the control case, the current does not drop below $1\,A$ and will, therefore, not require the use of the heater or keeper after start up. The plot also shows that the system must be able to handle up to a maximum of $9\,A$ with a $5\,A$ variation for this particular deorbit mission.

Drag force variations seen in Figure 3.20 range from $100 - 1500\,mN$, a relatively useful amount of thrust when compared to a standard ion or Hall thruster. Another important note about this result is the much larger increase seen in the plot when compared to the current and the *emf* plots. This result is because the drag force is a function of both current and magnetic field strength, which are functions of altitude. Figure 3.19 shows the increase in current with decreasing altitude directly and Figure 3.17 shows a similar increase but indirectly since the *emf* is the cross product of the relative velocity and the magnetic field strength dotted with the length. When these two parameters are crossed, the increase in each parameter affects the drag in the same way but with a multiplying factor. This results in much higher electrodynamic drag forces at lower altitudes.

The current collected by the tether also effects the plasma contactor by varying flowrate based on the flowrate versus emission current curve defined in Chapter 2.2.4. The result of this relation is Figure 3.21. Much like current, the expellant flowrate versus time plot can be used by system engineers to determine the necessary responses an HCPC gas feed system must meet. This control case shows the control scheme must be able to follow a $\sim 1\,sccm$ variation for every orbit completed.

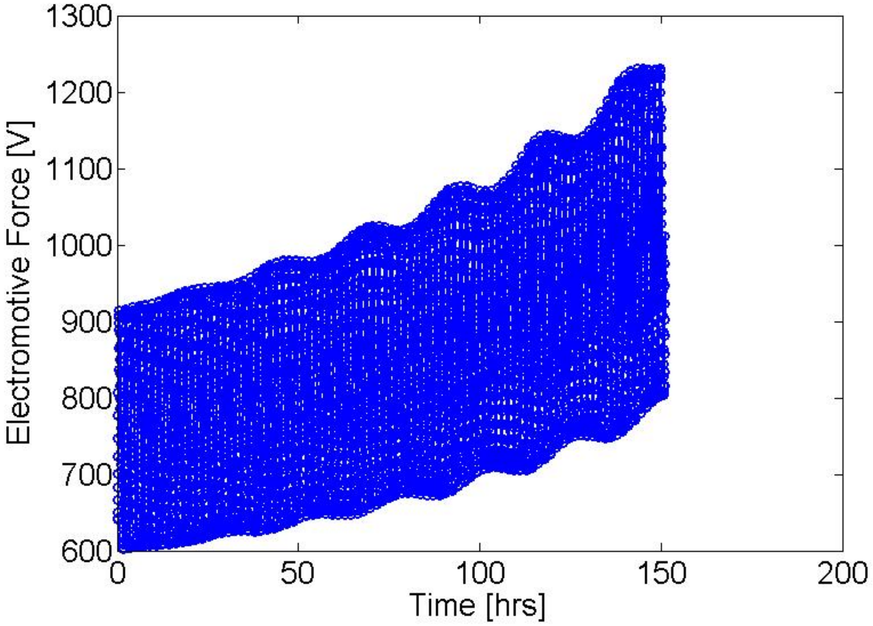

FIGURE 3.17. *Emf* induced in the tether as a function of time. Higher *emf* occurs at lower altitudes because the satellite travels faster here and because the magnetic field is higher closer to the Earth.

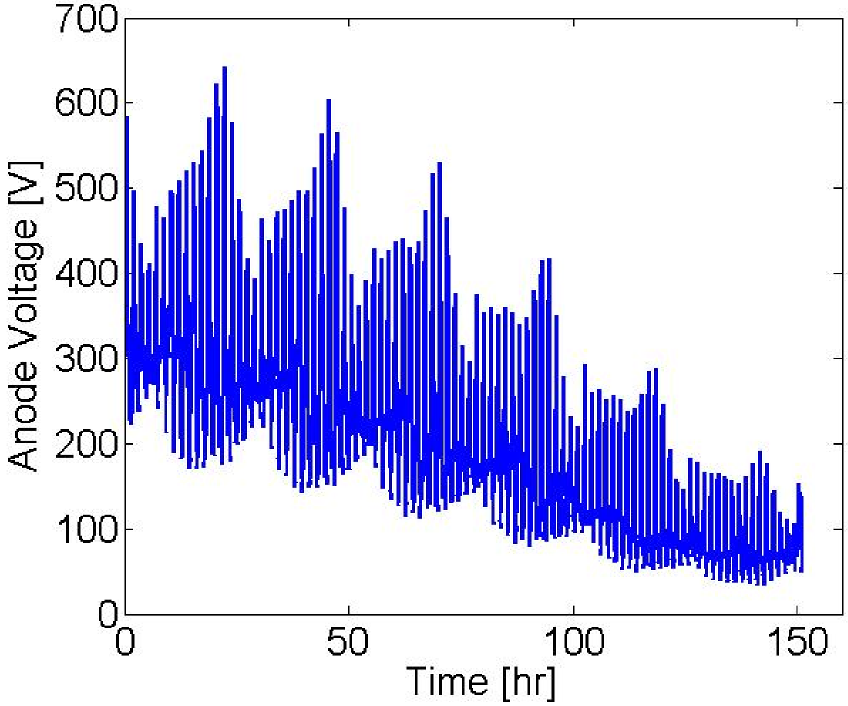

FIGURE 3.18. Anode voltage as a function of time. Although *emf* rises, V_A drops because tether current rises and resistive voltage drops increase as the EDT drops to lower altitudes.

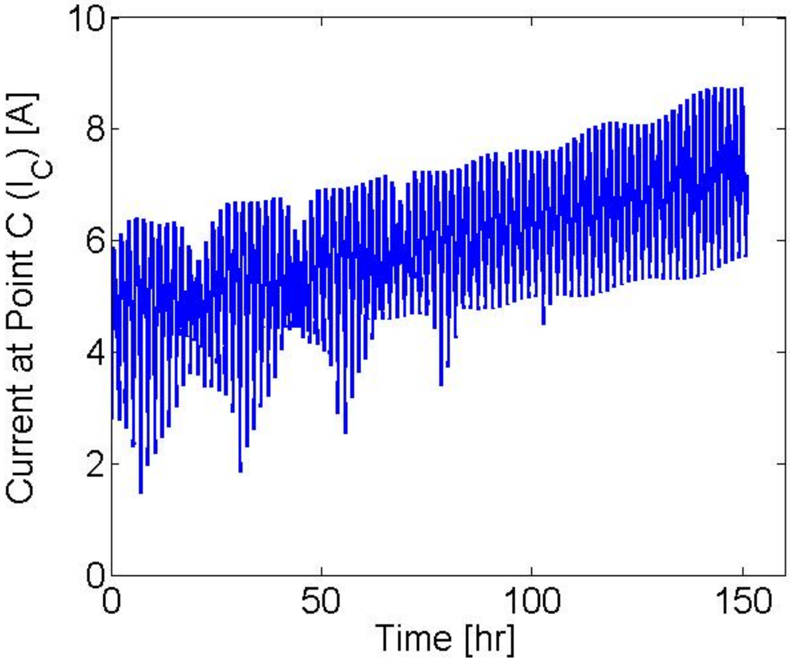

FIGURE 3.19. Current at end of tether as a function of time. This rises because electron density rises as the altitude of the EDT drops.

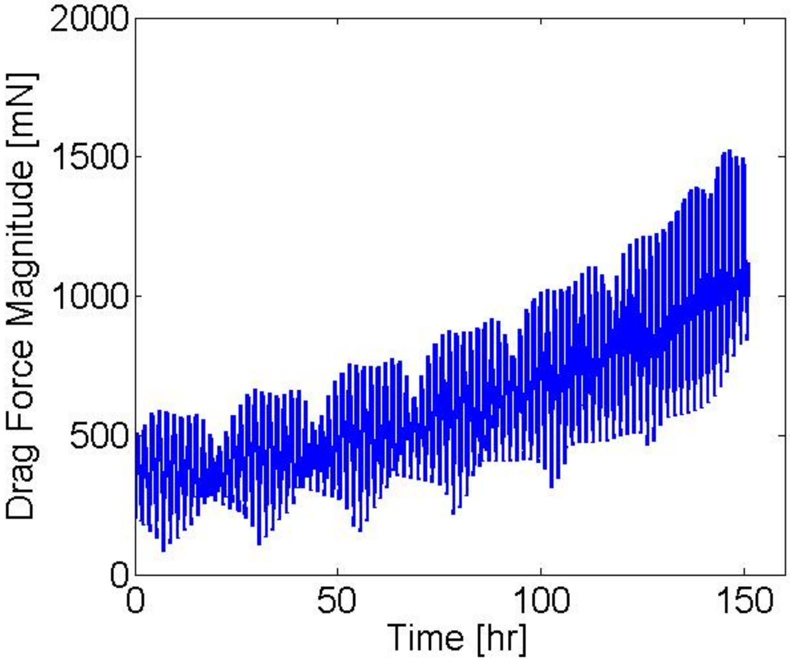

FIGURE 3.20. Magnitude of the total drag force as a function of time. This rises because current and magnetic field magnitudes rise as the altitude of the EDT drops.

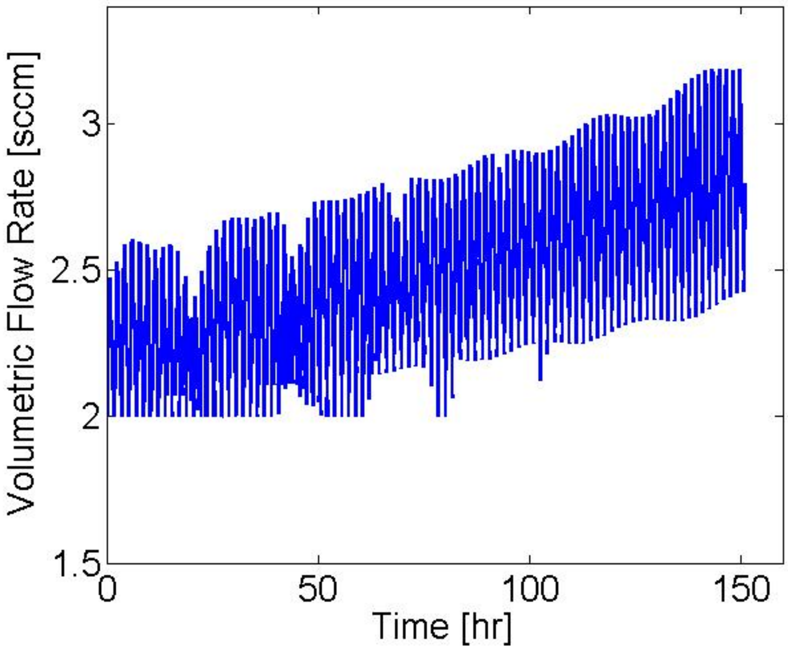

Figure 3.21. Expellant flowrate as a function of time. The flowrate of expellant is directly related to current by the flowrate versus emission current curve presented in Chapter 2.2.4.

Of the outputs provided by SimBETS, the most important is deorbit time. Companies are currently restricted by an imposed regulation of 25 year to deorbit spent satellites, however, it is anticipated that this time will be significantly shortened in the near future to ensure that collisions in LEO do not occur. The control case has a deorbit time of 6.3 days. The deorbit time as well as the variation of the deorbit time due to CBV will be a primary focus in the following studies.

The final SimBETS outputs analyzed were the different component masses. Using the variation in the mass, trends can be determined that can direct optimization. Figure 3.22 shows the mass of the main components.

Figure 3.22 shows the fraction of the EDT system and tether mass with respect to total deorbit mass is less than 6 % of the overall mass, so optimization of the system for cost is a dominant factor. A traditional chemical rocket deorbit from $850\,km$ to $300\,km$ for the same satellite mass of $1,000\,kg$ is expected to have system mass of $\sim 200\,kg$ and use a total of $128.6\,kg$ of propellant, assuming the specific impulse is $\sim 300\,sec$. This results in an additional $271.6\,kg$ of total mass that must be launched into orbit. Comparing costs, the traditional system costs about $\$1.643\,million$ to launch into LEO while the EDT deorbit system would cost around $\$287,000$. This is $\$1.36\,million$ difference. The traditional system has other advantages, however. Specifically, the two main advantages are its much shorter deorbit time and its heritage within the space community. Further highlighting each main component, Figure 3.23 and Figure 3.24 show the masses of each of the sub-components of the tether and EDT system mass.

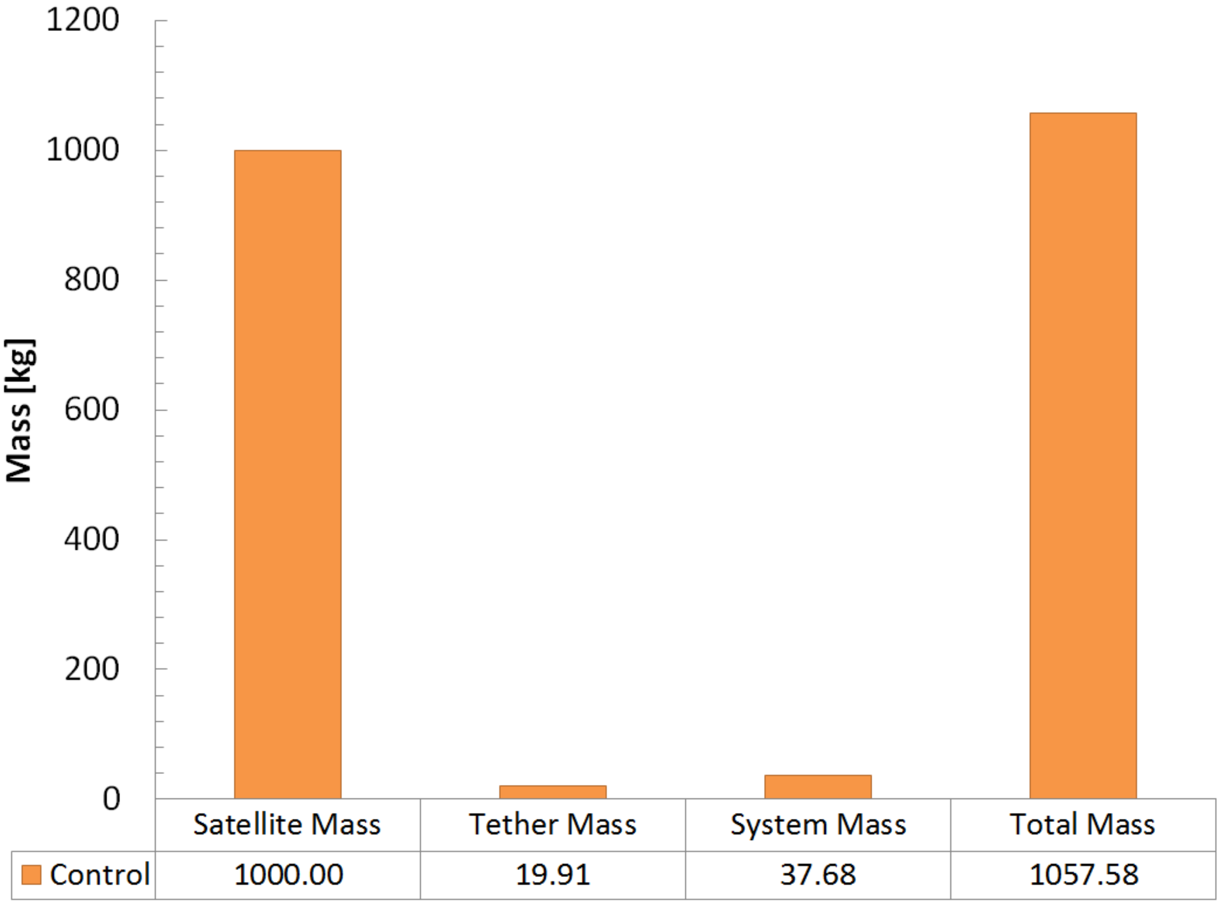

FIGURE 3.22. Main component mass and total mass of EDT system.

Focusing on Figure 3.23, it can be determined that the bare tether mass has the biggest contribution to the overall tether mass. This is mainly due to the material used. Aluminum is currently considered the best option based on its conductivity-to-mass ratio, however, if a shorter or narrower tether was used, say $2\,km$ and $1\,cm$, the mass could be further decreased. In Studies 4 and 5, tether lengths and widths are varied to determine the effects on the overall system.

The most notable component in Figure 3.24 is the deployer, adding nearly twice as much mass as the ten total kilometers making up the tether. Reducing this mass is an obvious conclusion, however, focusing on other components less considered by the scientific community, the flow controller or tank connecting hardware add the next highest amount of mass. An important note to make is the low amount of xenon required for this mission. This amount is nearly trivial compared to the rest of the system showing the cost of launching the HCPC dry mass is about the same as the HCPC mass that includes expellant. Throughout the following studies, the system and more specifically the xenon mass and associated hardware will be analyzed to understand the relationship that different component parameters have with the system.

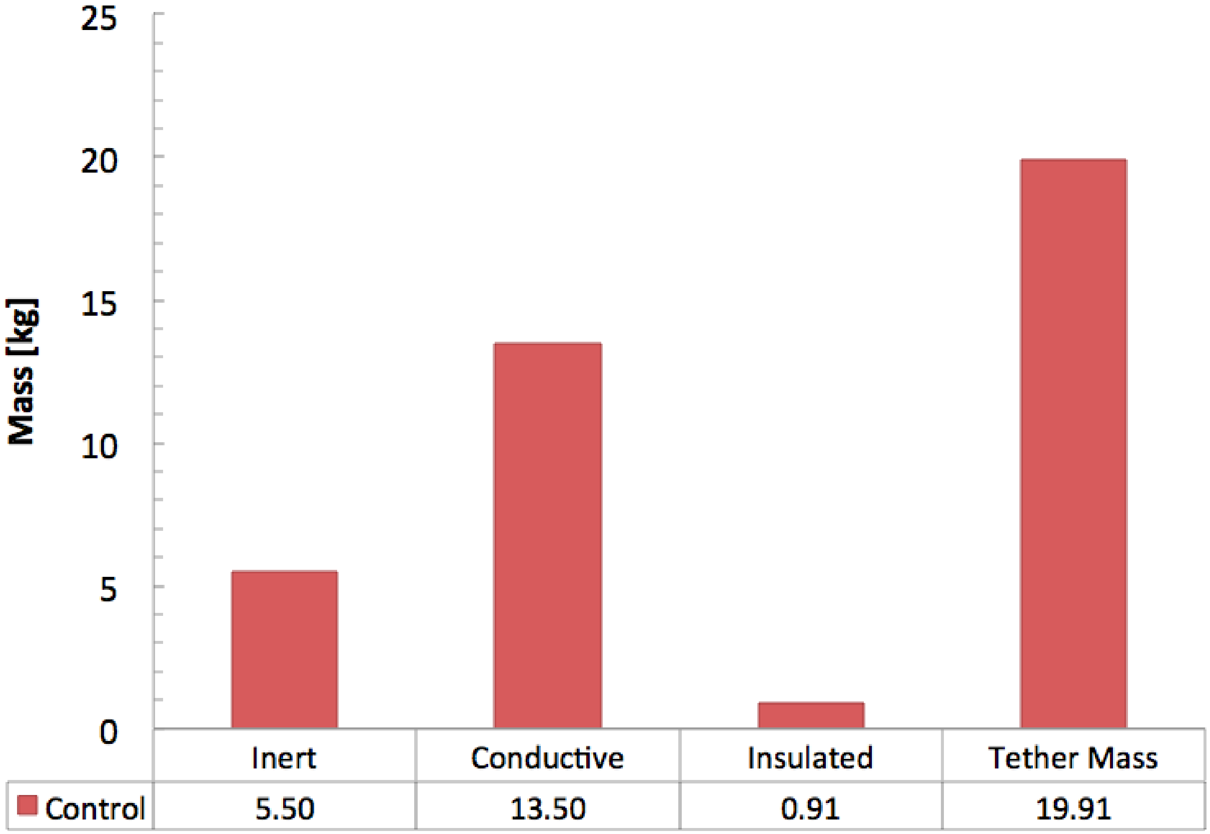

FIGURE 3.23. Tether component mass and total tether mass.

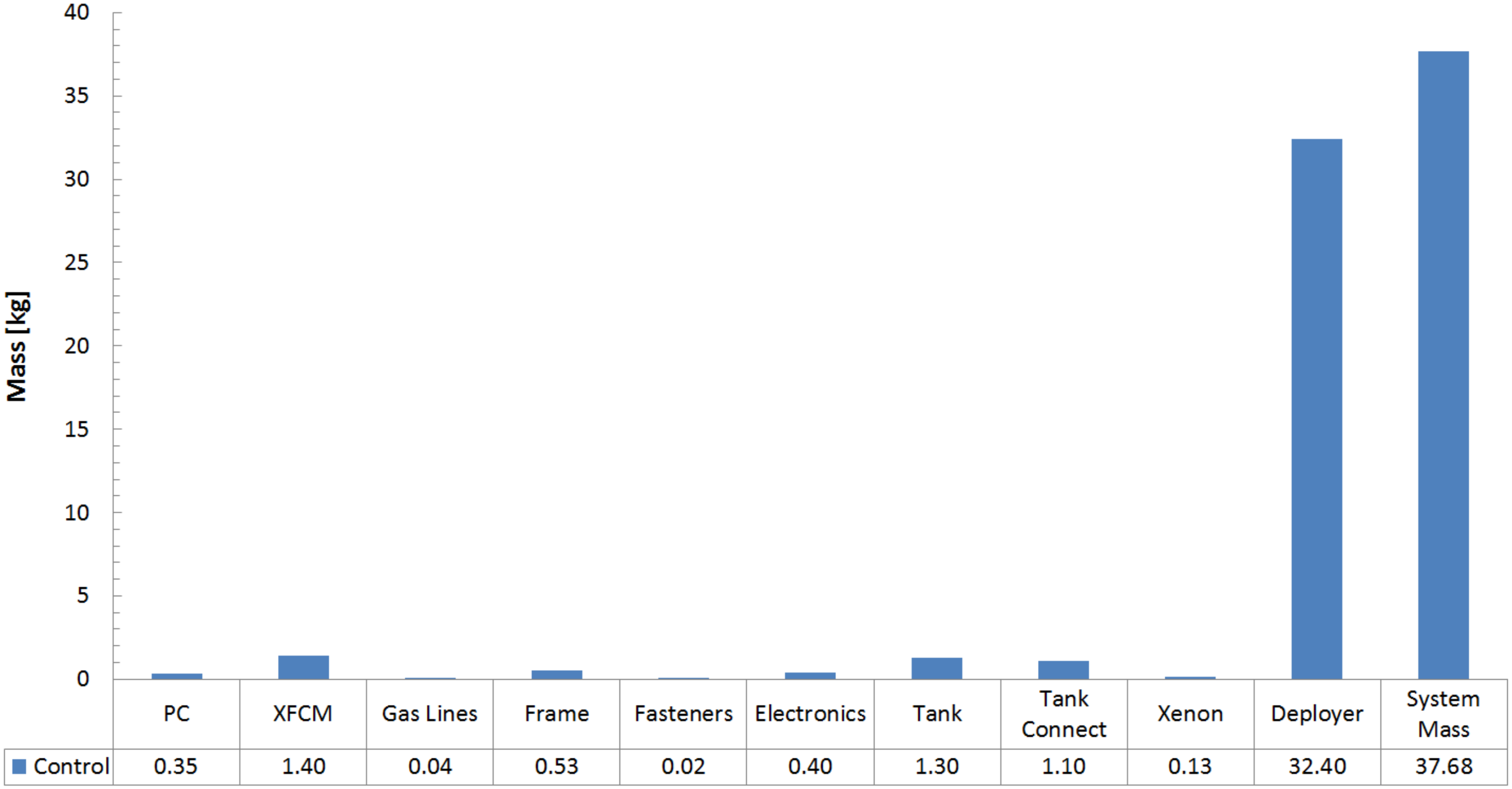

	PC	XFCM	Gas Lines	Frame	Fasteners	Electronics	Tank	Tank Connect	Xenon	Deployer	System Mass
■ Control	0.35	1.40	0.04	0.53	0.02	0.40	1.30	1.10	0.13	32.40	37.68

Figure 3.24. Component masses and total mass of the EDT end mass system.

Each study uses the data provided by this control case to compare to and relate to the scientific community. Due to the large assortment of outputs available for comparison, only notable variations in outputs are shown.

3.2.1.2. STUDY 1: VARIATION DUE TO HOLLOW CATHODE PLASMA CONTACTOR BIAS VOLTAGE

Study 1 focuses on the effects of the HCPC bias voltage. The specific contactor bias voltages (CBV) considered are $0\,V$, $-30\,V$, and $-50\,V$. With increased CBV, it was predicted less current would be produced and, therefore, less drag, which would increase deorbit time. Besides current, drag, and voltage, the CBV can also have an effect on the COEs and EDT system mass. The affects of the CBV for inclined orbits will be discussed in Study 2. Figure 3.25 shows the deorbit time from $850\,km$ to $300\,km$ as a function of CBV. The consideration of CBV for a relatively simple deorbit of $\sim 150\,hrs$ shows up to $\sim 7.2\,\%$ variation in deorbit time can be expected with an increase of $-50\,V$ CBV. For the current configuration, this adds $\sim 11\,hours$, a relatively trivial amount when compared to atmospheric drag related deorbit times. Following this trend, it is expected the deorbit time should increase by another $\sim 4.2\,\%$ with an increase up to a total CBV of $-90\,V$.

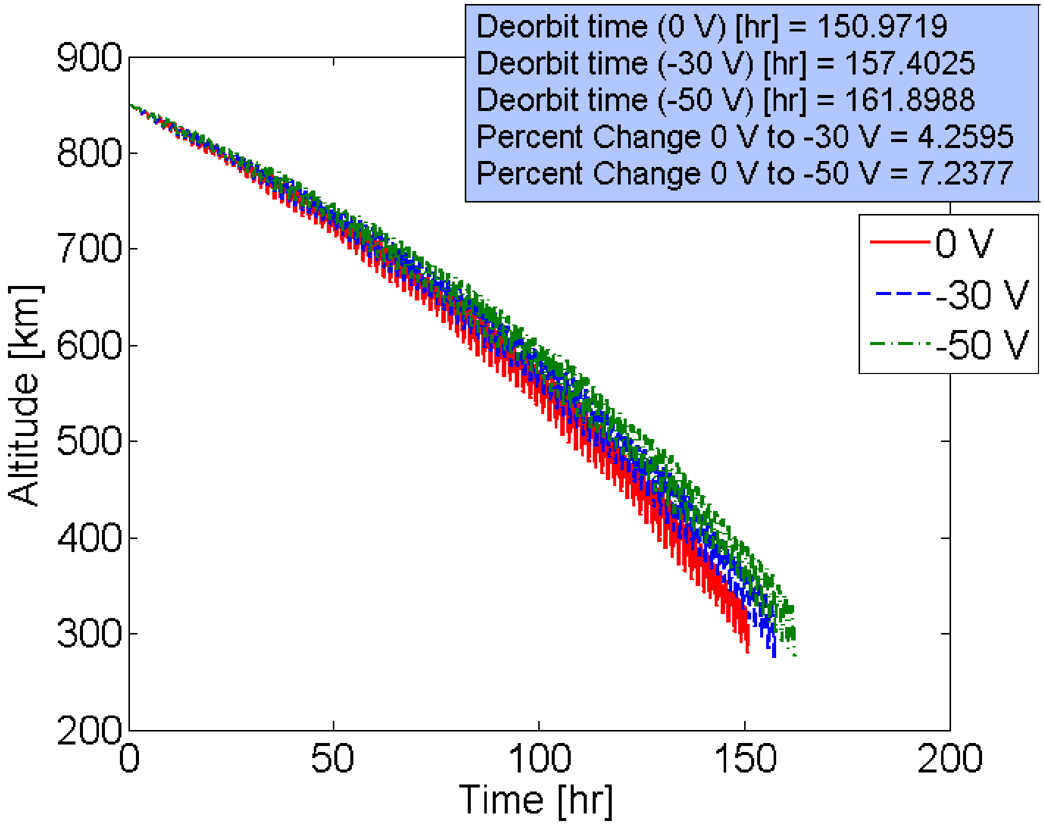

FIGURE 3.25. Comparison of deorbit times for CBV magnitude $0\,V$, $30\,V$, and $50\,V$ using the control case parameters.

Moving to the effect of CBV on the COEs, the CBV is observed to have only small effect on the COEs. The main effect is on inclination. Figure 3.26 shows inclination variation induced by the different CBV. Note the resonant effect is decreased with increasing CBV. This relates to the increased effect the CBV has on the tether's ability to collect current resulting in lower drag forces during more favorable orbital conditions.

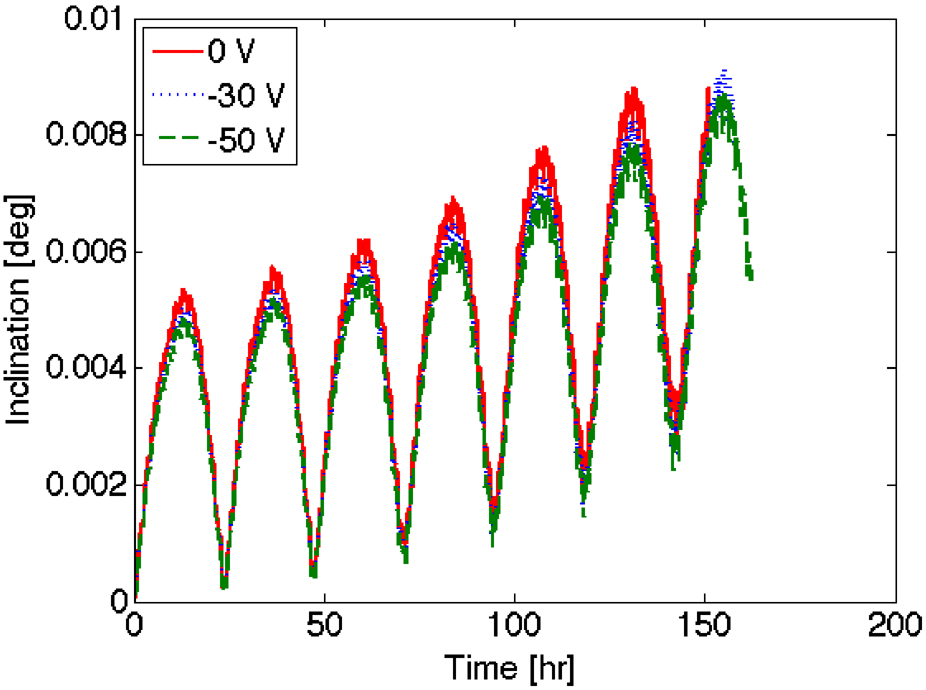

FIGURE 3.26. Variation of the inclination due to CBV.

Moving to a more important parameter, end current, it was observed that the CBV has not affected the shape of the current plot. However, it has decreased the average current by nearly 1 A for the $-50\,V$ case as shown in Figure 3.27. This decrease in current is important because electrodynamic drag force is a function of current and, therefore, reinforces how CBV can affect the deorbit performance.

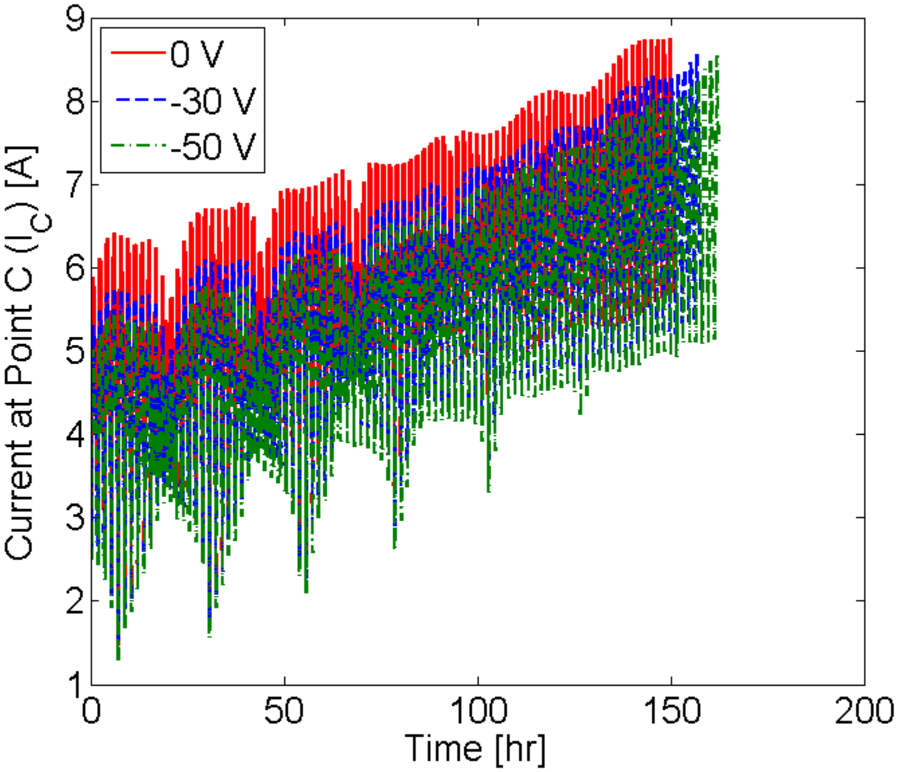

FIGURE 3.27. End current versus time as a function of CBV.

The current profile is also important because it relates to the expellant flowrate. Figure 3.28 shows the expellant flowrate as a function of time and Figure 3.29 shows expellant flowrate as a function of altitude. Much like the current profile, the expellant flowrate profile from Figure 3.21 is unchanged, however, with increasing CBV, more and more of the flowrate profile is pushed down toward the 2 *sccm* minimum. This results in lower fluctuations during the first half of the deorbit mission. This can be deceiving to system engineers if the full mission is not considered. Overall, there is about a tenth of an sccm drop between each CBV profile. Another note is that because flowrate is related to current, it is also related to altitude yielding a lower average flowrate will be required at higher altitudes due to lower currents.

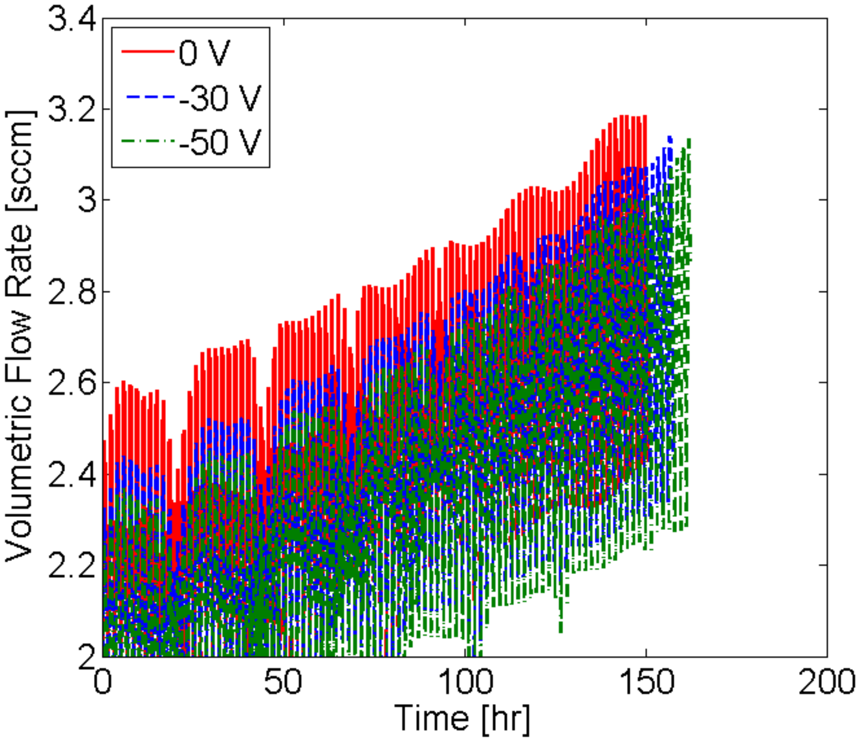

FIGURE 3.28. Expellant flowrate versus time as a function of CBV.

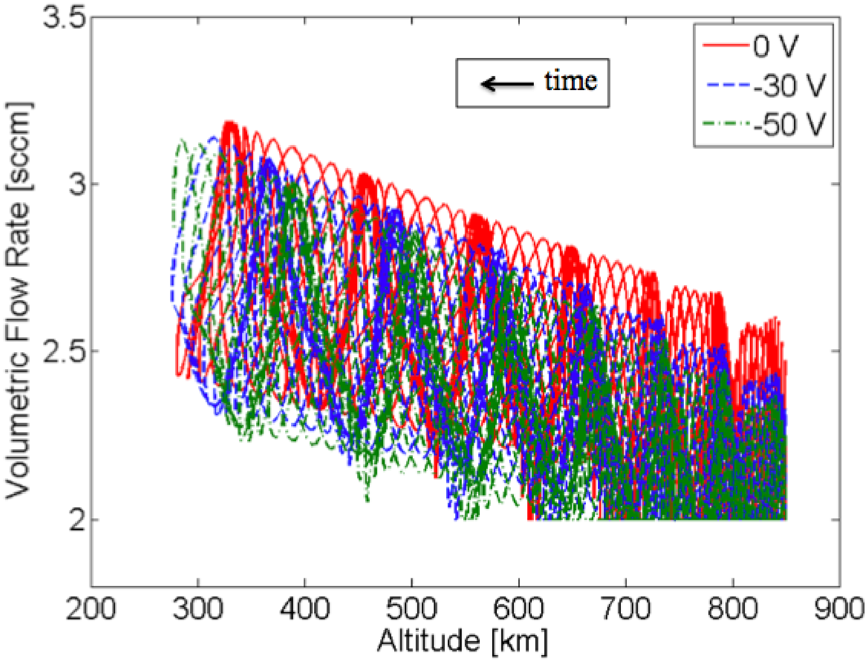

FIGURE 3.29. Expellant flowrate versus altitude as a function of CBV.

Although flowrate does change for each CBV condition, about the same amount of xenon was required to within $0.001\,kg$.

3.2.1.3. Study 2: Variation Due to CBV and Inclination

The next study focuses on the effects of inclination on the deorbit of a bare EDT system. Orbital inclinations of 0^o, 35^o, and 71^o were tested with the same CBV as in Study 1. Because these orbits are no longer in the near ideal location for current and *emf* production it is expected that higher inclination orbits will increase the deorbit time at an increasing rate until a maximum deorbit time is reached near the poles of the Earth. Figure 3.30 shows the altitude of the simulated EDT as a function of time. The deorbit times and percent changes between the different runs are also shown. For the inclinations 0^o and 35^o, the deorbit time is under $\sim 12\,days$, a near doubling when compared to the control case. Considering the deorbit time of the 71^o inclination case, however, it is observed that the deorbit time increases by almost a factor of 10. The last note relating to altitude versus time and CBV is the difference shown in Figure 3.30 between the two 71^o outlying inclined orbital cases, $0\,V$ and $-50\,V$. This difference in deorbit time shows how the CBV becomes increasingly important with longer missions that occur at high inclination. For this particular study, a full 24 % (of a $\sim 75day$ deorbit) change is observed between the $0\,V$ and $-50\,V$ CBV. This is about a $342.2\,hr$ ($\sim 14\,days$) increase in deorbit time.

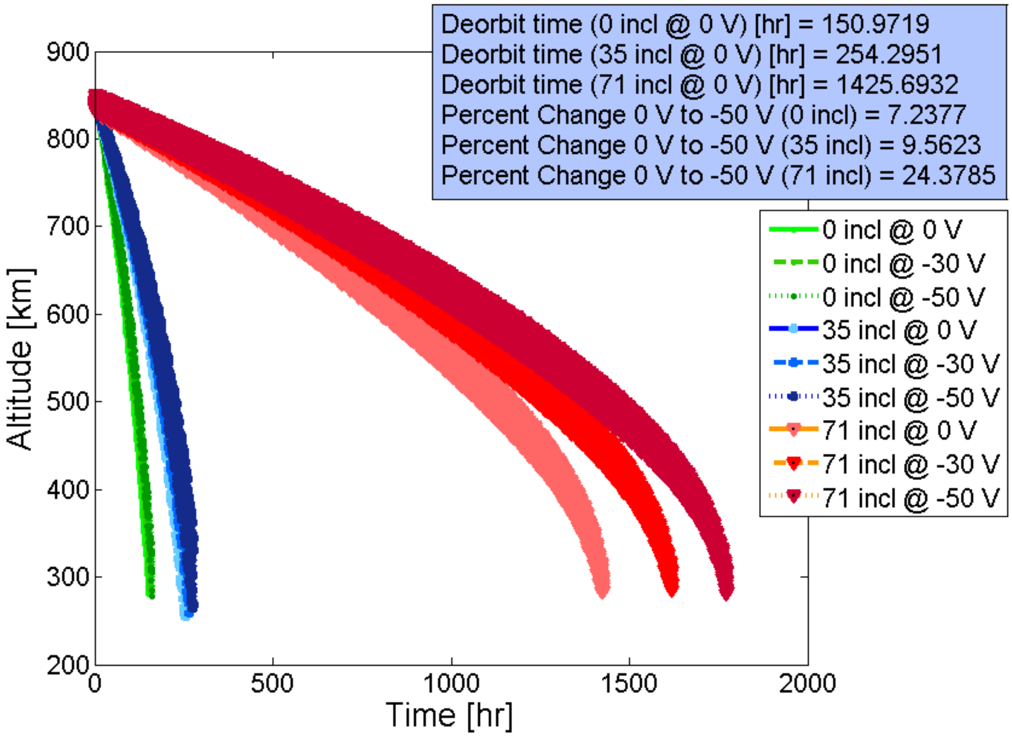

FIGURE 3.30. Altitude versus time of 0^o, 35^o, and 71^o inclined orbits using CBV of $0\,V$, $-30\,V$, and $-50\,V$.

This extreme increase in deorbit time is related to the tether current and *emf* as the object orbits the Earth. Figure 3.31 and 3.32 shows the tether current and anode voltage in the tether for the mission, respectively. The most notable figure, Figure 3.31, shows the extreme difference between the current collected for the $0\,V$ non-inclined orbit and the $-50\,V$, 71^o inclined orbit. This relates to the figures in Chapter 2, Figures 2.9 and 2.10, which shows how the current and voltage profiles are affected by deviating from the ideal orbital environments. Returning to Figure 3.31, the variations observed are caused by the low induced *emf*, shown in Figure 3.32. The low *emf* is caused by the tether crossing the magnetic field lines at acute angles rather than right angles. The solar radiation observed in these high orbits also affects current collection due to the decrease in electron density. These orbits can even cause the current to be zero during certain parts of the orbit when considering the constant CBV model. However, if the tether crosses the magnetic field lines at right angles by deviating from the local vertical, the maximum current for the tether configuration and orbital conditions can be collected. Figure 3.33 shows this occurring for the $-50\,V$, 71^{o} inclined case in an expanded plot at $\sim 27\,days$ into the mission.

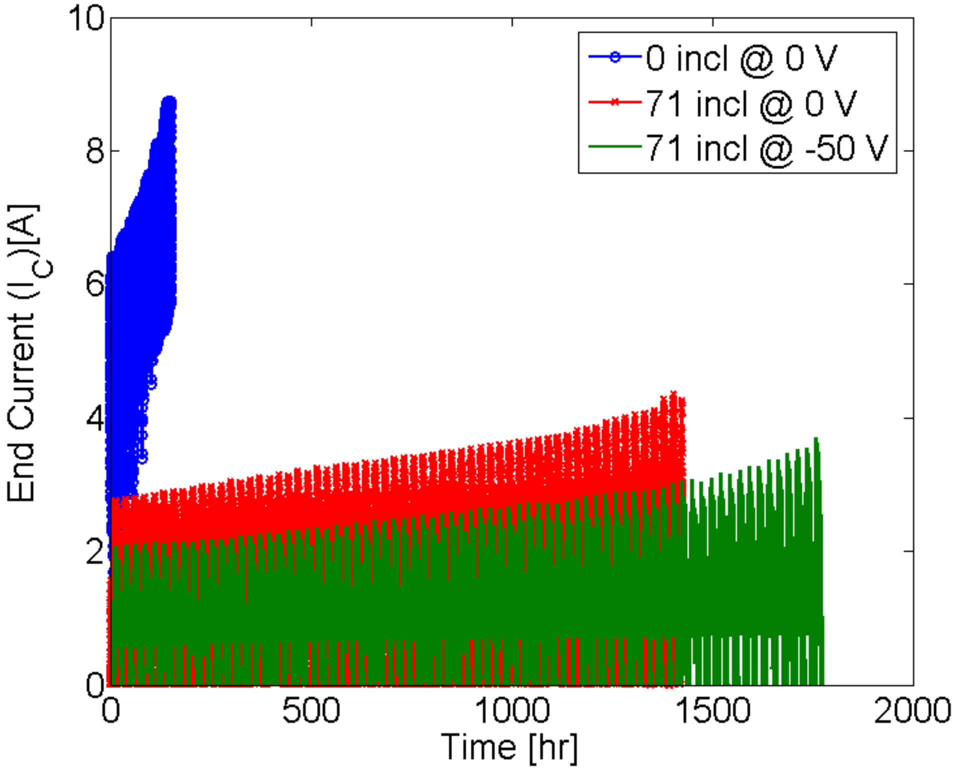

FIGURE 3.31. End current versus time as a function of inclination and CBV.

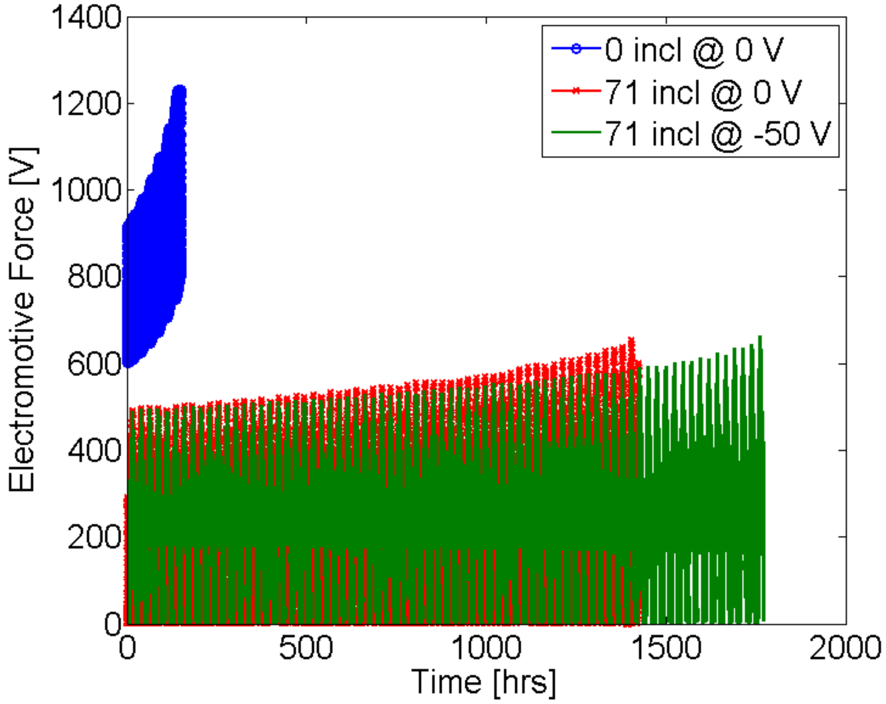

FIGURE 3.32. Emf induced in the tether versus time as a function of inclination and CBV.

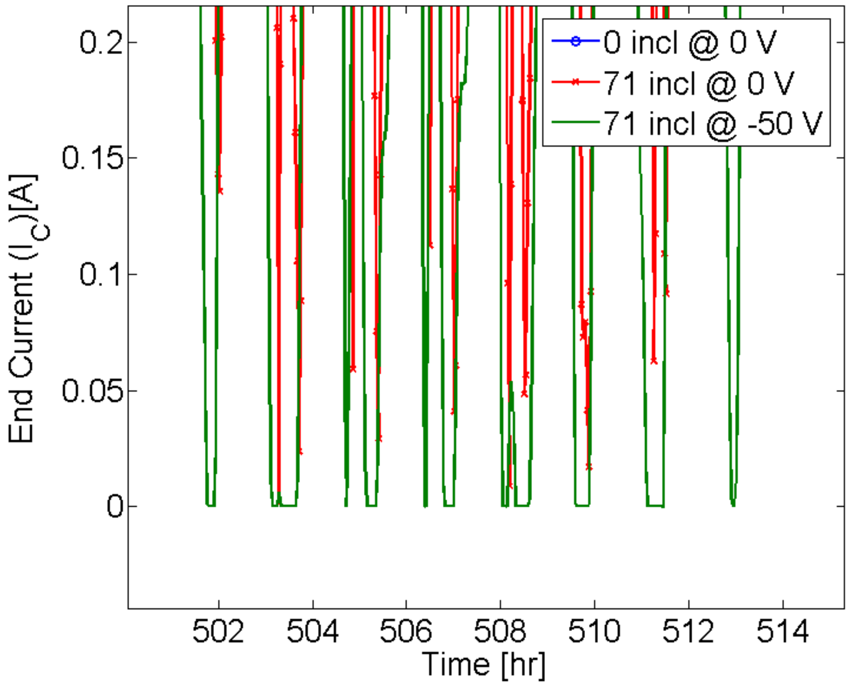

FIGURE 3.33. Location of some points in the deorbit where no current was produced.

These points of zero current are also important because the HCPC is still required to continue to operate. This requirement forces the HCPC to draw more power to operate the keeper and heater as well as having to continue to expel gas. This expelling of this gas is shown in Figure 3.34.

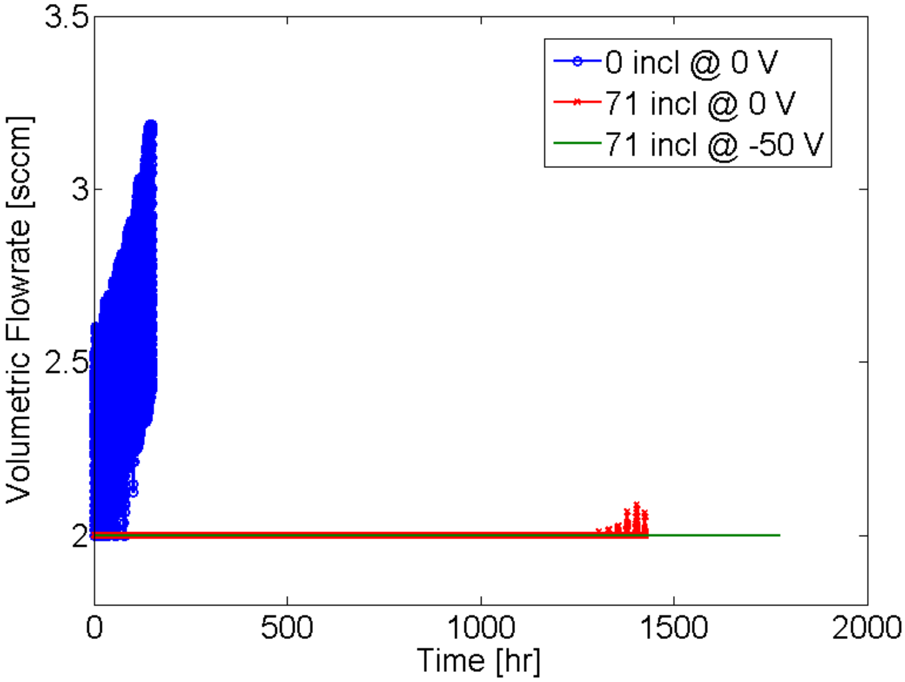

FIGURE 3.34. Expellant flowrate versus time as a function of inclination and CBV. Note how the flowrate never drops below 2 *sccm*. This is because of the continuous flowrate versus emission current scheme shown in Figure 2.15. The positive side of the flowrate plot is that there is almost no control scheme required because the deviations in flowrate are so minimal.

Moving attentions to the COEs, Figure 3.35 shows how the addition of inclination to an orbit has settled the oscillation of the right ascension of the ascending node. As expected, this settling effect is also shown for the argument of perigee. As for the other COEs, a trend of seeing less affects at higher inclinations is seen, however, the effect on increasing inclination is increased.

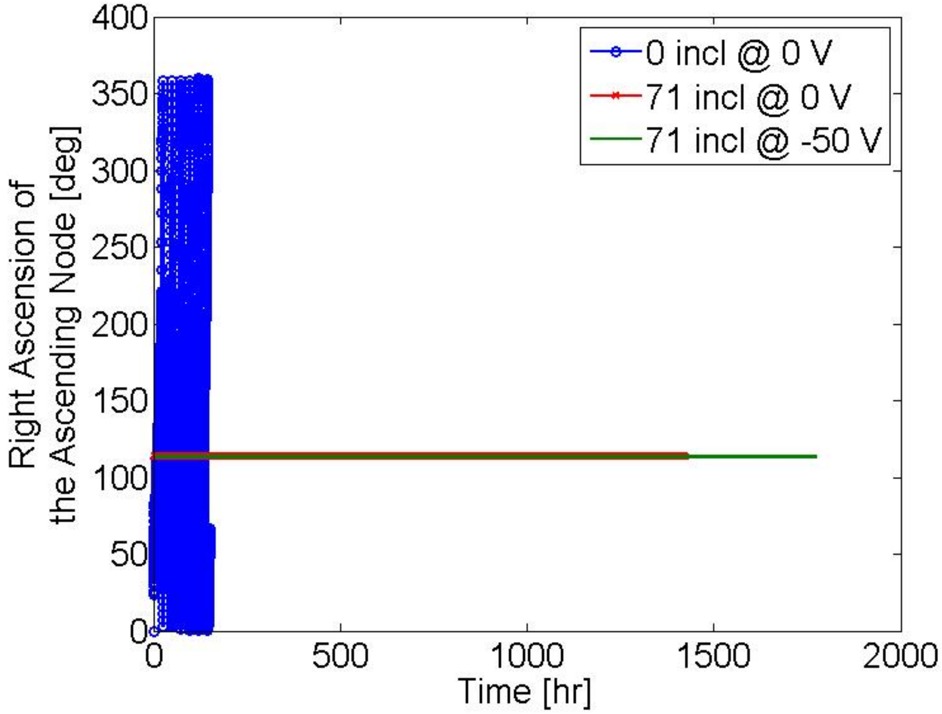

FIGURE 3.35. Right ascension of the ascending node versus time as a function of inclination and CBV. Note how this element settles as inclination is added.

Due to the increase in deorbit time and expellant use, the trends relating to system mass are of some interest. Figure 3.36 shows the masses of the components and how inclination and CBV affects the overall mass.

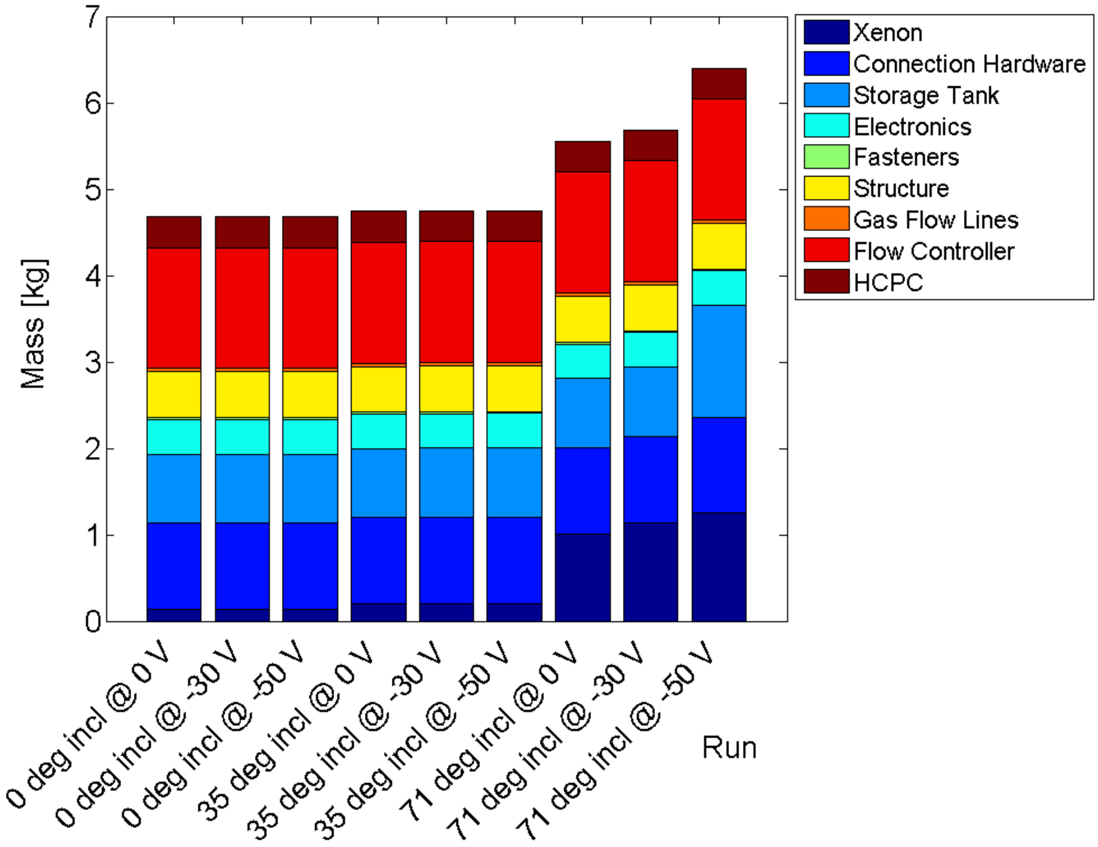

FIGURE 3.36. Masses of different components in the EDT system as a function of CBV and orbital inclination. The deployer mass is 32.4 kg and the tether mass is 19.9 kg.

For most of the cases, the system mass remains unchanged but due to the long deorbit time associated with the high inclinations and high CBV, the xenon mass becomes excessively large forcing the system to use a larger storage tank and mounting hardware. Figure 3.37 shows how the system mass varies with deorbit time for the inclination and constant CBV study.

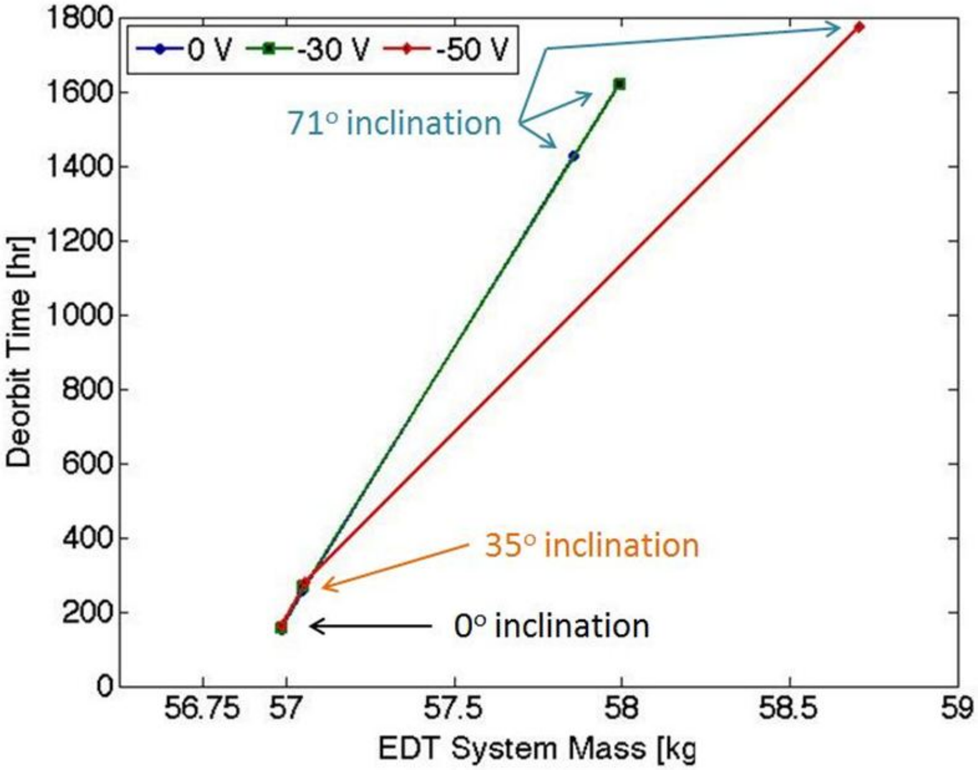

Figure 3.37. Deorbit time as a function of system mass.

Figure 3.37 is useful because it shows that the slope of the system mass plot is dependent upon component make up. If the xenon mass increases or decreases slightly, then the point will appear along this slope, however, if the xenon mass required for the mission exceeds the storage capabilities, a larger storage tank and associated hardware must be selected, and the slope will change. Therefore, the curve created by the deorbit time versus EDT system mass plot extends towards higher EDT system masses with longer deorbit times, only changing slope when components of the system change.

3.2.1.4. Study 3: Variation Due to CBV and Satellite Mass

Study 3 focuses on the effects of CBV and satellite mass on the EDT system and its deorbit performance. By increasing satellite mass, deorbiting becomes more difficult due to its resistance to a change in momentum. Therefore, increased and decreased deorbit times should be seen in relation to the cases examined in Study 1. The satellite masses chosen for this study were $500\,kg$ and $1,500\,kg$ or twice and half the control case satellite mass. Figure 3.38 shows the deorbit of these nine cases and there deorbit performance. Unlike Study 2, the deorbit times are much more evenly spaced, seeing about a $\pm 50\,\%$ change in deorbit time from Study 1. This also applies to the variation in deorbit caused by varying CBV. An increase by $\sim 7\,\%$ is observed for each satellite mass. This observation is different than Study 2 and is an expected result. This was an expected result because the change in satellite mass and CBV affects how much the drag force can affect the satellite's path. With larger satellite masses and CBV magnitudes, the satellite's path is affected much less while the opposite happens with smaller satellite masses and CBV. However, because the system still moves through the same orbital conditions, the affects observed only change by a proportional amount to the change in satellite mass and CBV.

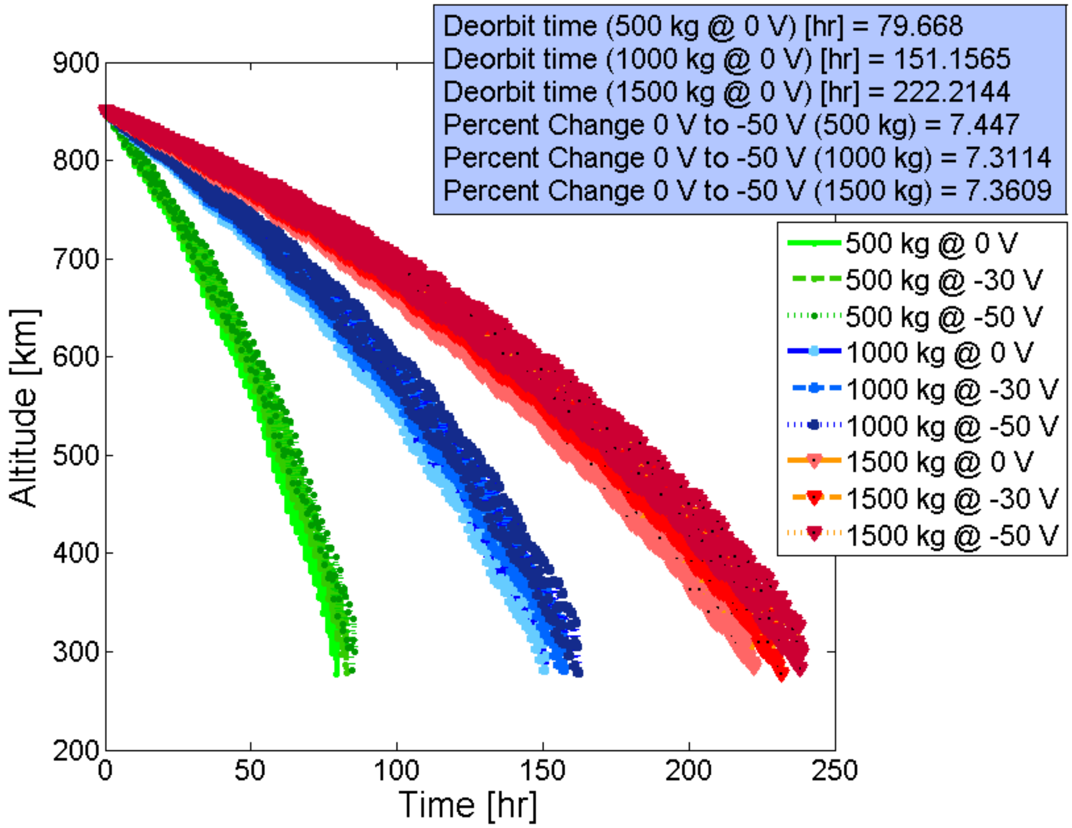

FIGURE 3.38. Altitude versus time of $500\,kg$, $1,000\,kg$, and $1,500\,kg$ satellite masses at CBV of $0\,V$, $-30\,V$, and $-50\,V$.

Considering the orbital elements, the RAAN and argument of perigee, which are not shown, see slight shifts in each of their curves, however, they are almost identical to Figures 3.15 and 3.16. More considerable changes are seen in the eccentricity and inclination elements as shown in Figures 3.39 and 3.40.

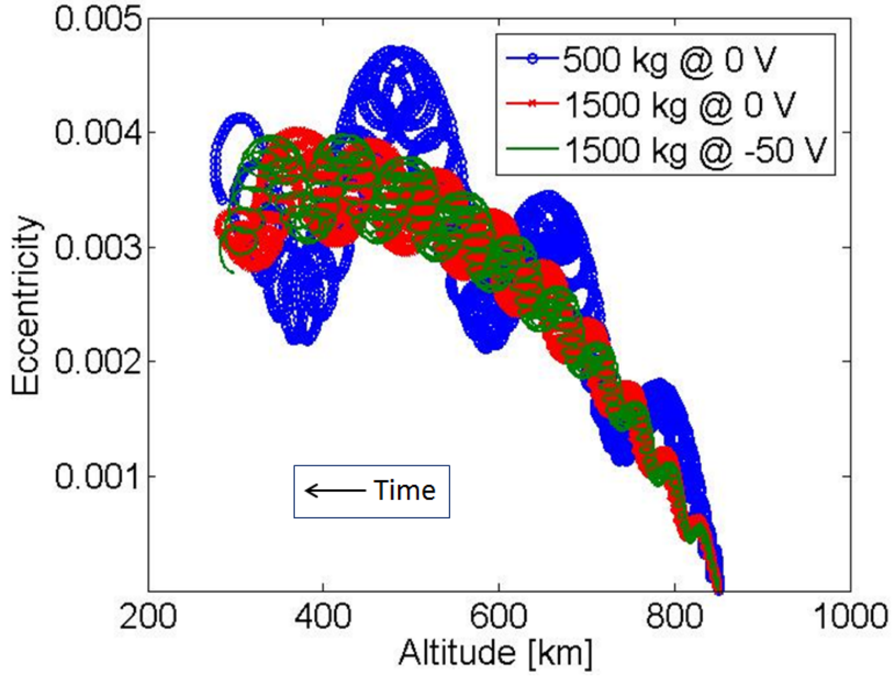

FIGURE 3.39. Eccentricity versus altitude for cases of varying satellite masses of $500\,kg$ at $0\,V$, $1,500\,kg$ at $0\,V$, and $1,500\,kg$ at $-50\,V$.

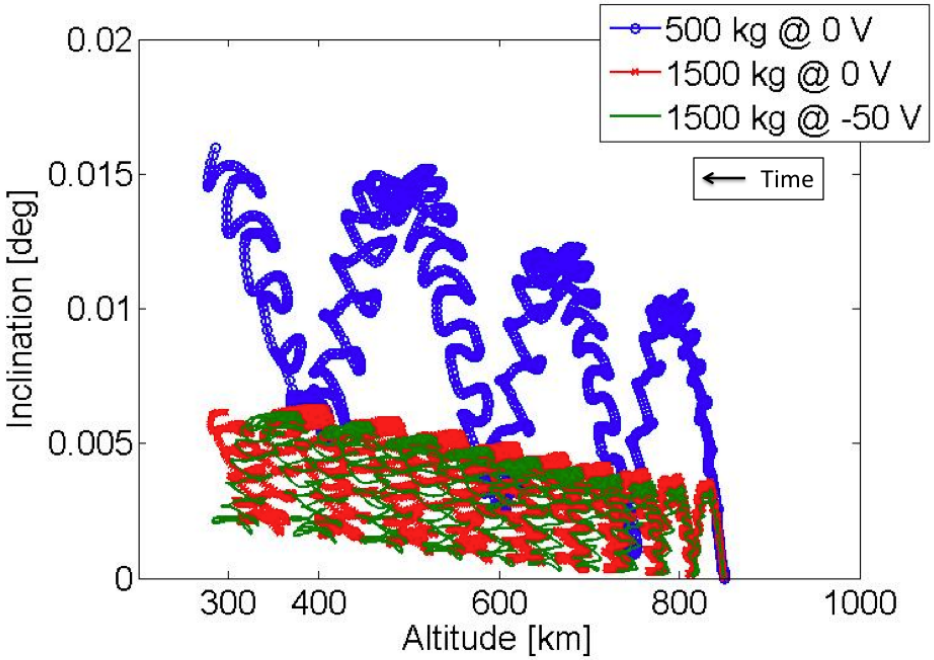

FIGURE 3.40. Inclination as a function of altitude for the varying satellite masses and CBV of $500\,kg$ at $0\,V$, $1,500\,kg$ at $0\,V$, and $1,500\,kg$ at $-50\,V$.

Figure 3.39 shows satellite mass does not prevent or amplify the overall eccentric shape and mean eccentricity. Satellite mass does, however, decrease the excessive inclination amplitudes observed throughout the deorbit. This relates to the drag forces ability to change the momentum of the system's orbital path. Considering CBV, a variation in CBV between $0\,V$ and $-50\,V$ only causes a phase shift in the eccentricity. This is also true for the inclination element, however, not for the mean inclination. Unlike in Figure 3.39, Figure 3.40 shows a change of ~ 0.005. This is because inclination changes are much more difficult to create than eccentricity changes.

Like eccentricity, the satellite mass also has little effect on the current and voltage of the system. Much like Study 1 and Study 2, only CBV affects the current and voltage of the system, and, therefore, the drag force. This is why the orbital elements have not shifted very much from Study 1. The satellite mass also has very little effect on the system mass. This is shown in Figure 3.41.

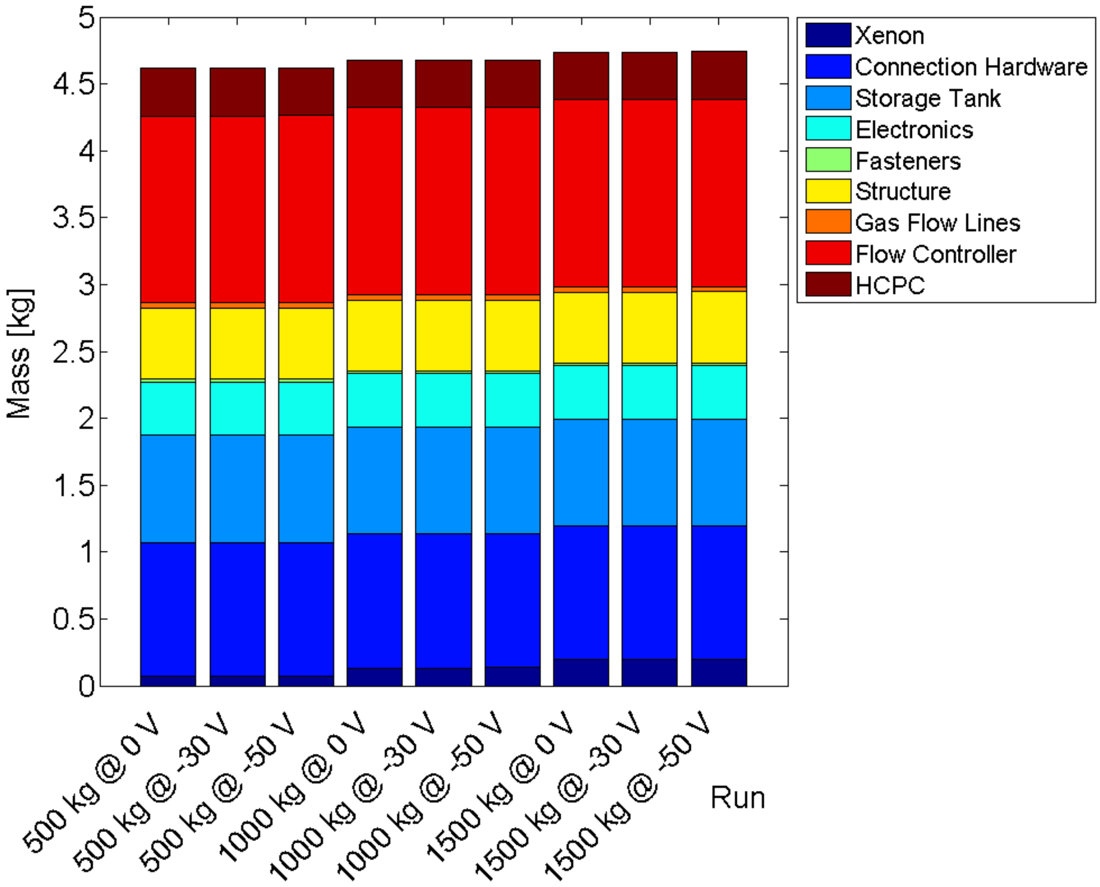

FIGURE 3.41. Masses of the various components in an EDT system as a function of satellite mass and CBV. Note the deployer mass and tether mass, which are not shown, are $32.4\,kg$ and $19.9\,kg$, respectively.

This lack of variation despite increased mission time is because the smallest baseline system can still support all three of these missions, therefore, only slight changes should be expected as verified in Figure 3.42.

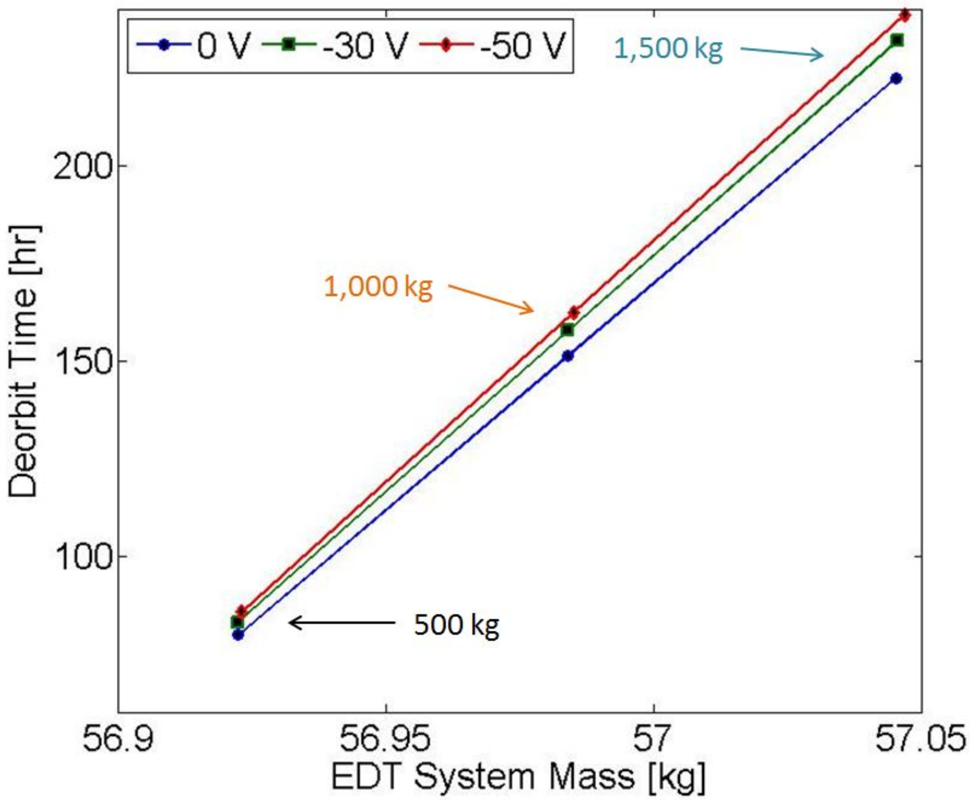

FIGURE 3.42. System mass as a function of deorbit time for CBV of $0\,V$, $-30\,V$, and $-50\,V$. Note how increasing system mass is directly related to increasing satellite mass.

Using this result, it can be said that an EDT deorbit system can be designed to accommodate a large range of systems, removing engineering and modification issues.

3.2.1.5. STUDY 4: VARIATION DUE TO HCPC BIAS AND BARE TETHER LENGTH

The parameter studied next was tether length. The tether lengths chosen were $50\,\%$ greater and $50\,\%$ less than the control case. This equals a conductive tether length of $2.5\,km$ and $7.5\,km$. Accounting for the $1:1$ ratio between the inert and conductive sections considered in this thesis, the total tether lengths became $5\,km$ and $15\,km$. These cases were then compared to Study 1. The tether lengths chosen should increase the deorbit time significantly for the short tether and decrease the deorbit time for the longer tether.

Figure 3.43 shows the deorbit trend of each of the three tether lengths and corresponding CBV as well as some deorbit statistics.

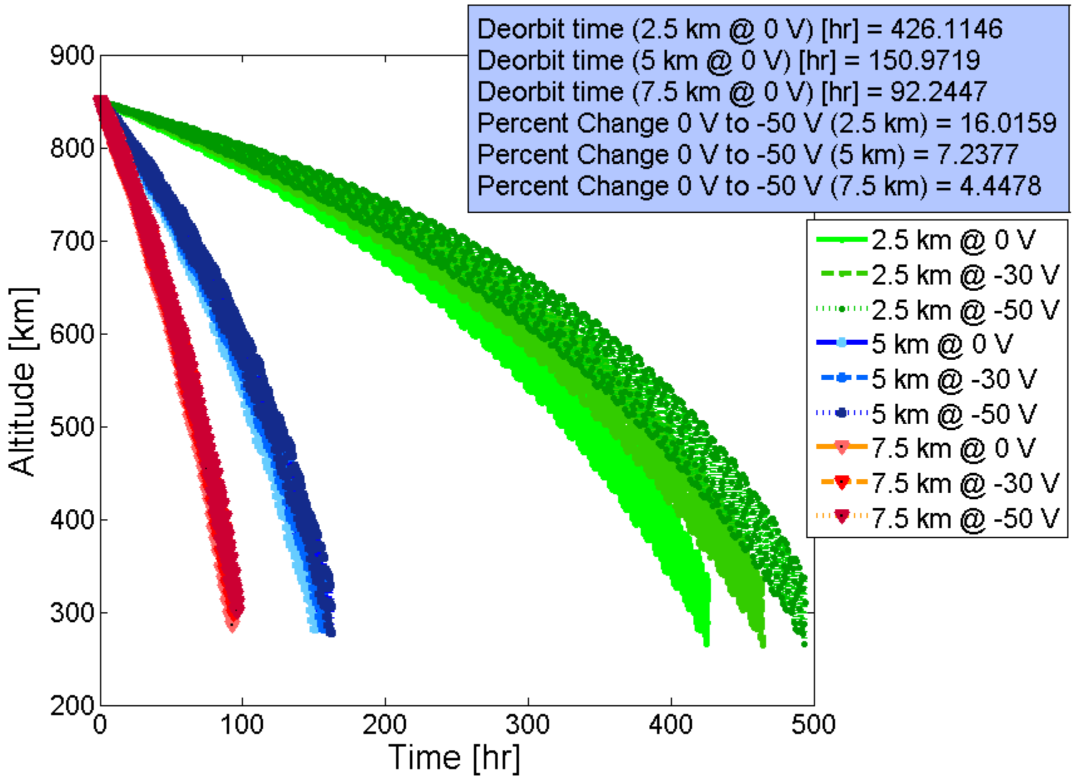

FIGURE 3.43. Altitude as a function of time for $2.5\,km$, $5\,km$, and $7.5\,km$ conductive EDT section lengths using CBV of $0\,V$, $-30\,V$, and $-50\,V$.

Similar to Study 2, the $50\,\%$ decrease in tether length case has lead to a tripling in deorbit time. Between the $7.5\,km$ tether length[1] and the $5\,km$ tether, a $\sim 2\,day$ deorbit time increase is expected, however, the deorbit time increases by a full $10\,days$ when the tether length is shortened by $50\,\%$ to $2.5\,km$. Figure 3.44 shows the deorbit time as a function of tether length. This large change can be attributed to the decreasing available *emf* and current collection area generated in the tether with decreasing tether length. Figures 3.45 and 3.46 show the *emf* and current as a function of time for different tether lengths.

---

[1] To reduce repetition, all tether lengths discussed in this section refer to the conductive tether length.

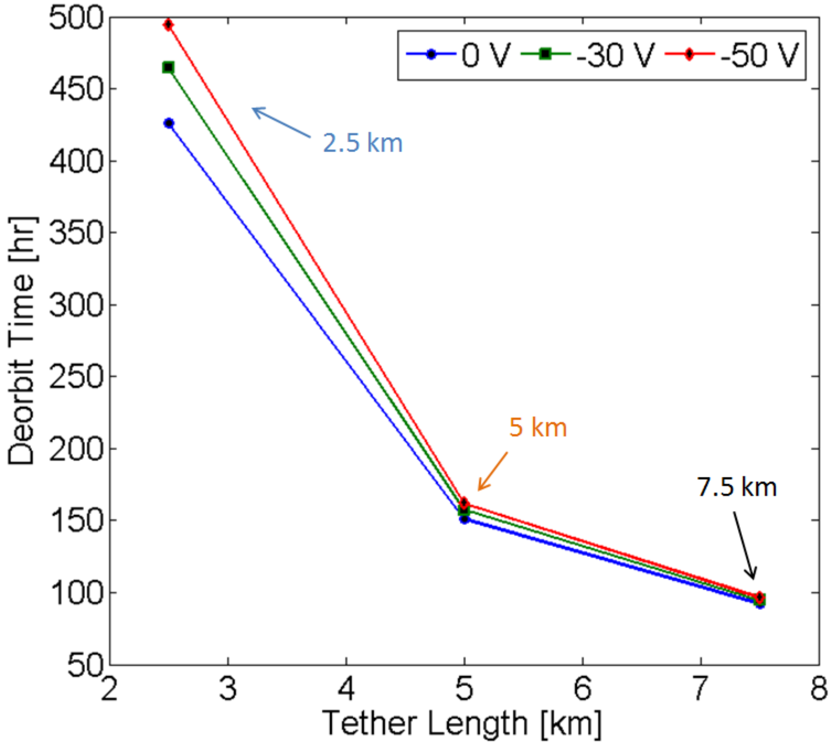

FIGURE 3.44. The variation of deorbit time as a function of tether length.

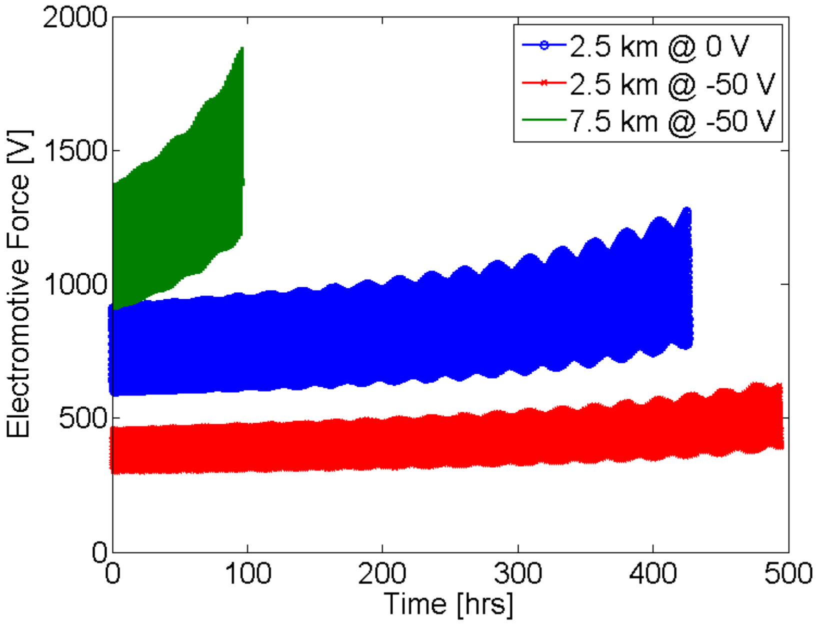

FIGURE 3.45. *Emf* induced in the tether as a function of time for two $2.5\,km$ tethers with a CBV of $0\,V$ and $-50\,V$ and one $7.5\,km$ tether with a CBV of $-50\,V$.

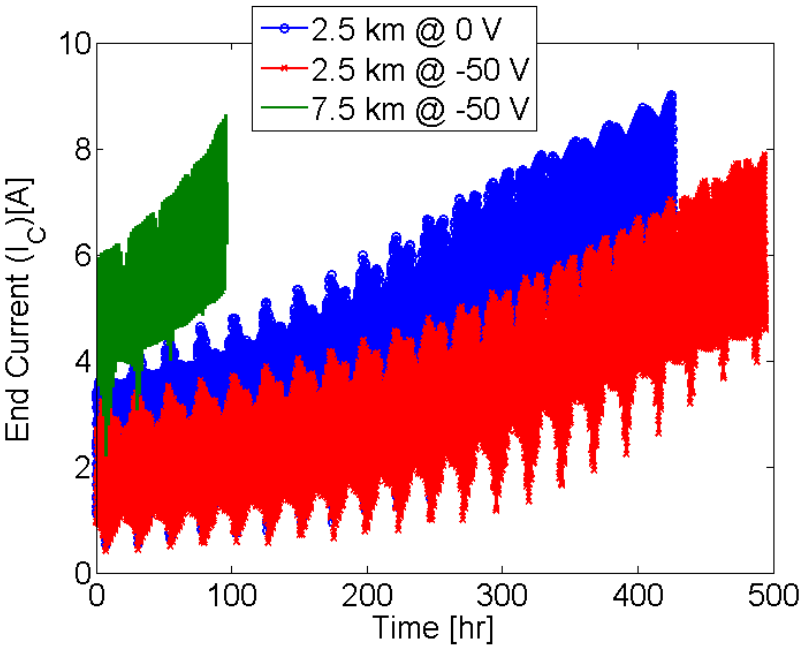

FIGURE 3.46. End current as a function of time for 2.5 km and 7.5 km conductive EDT section lengths using CBV of 0 V and $-50\,V$. Note the longer deorbit time cases are the main focus of this plot.

The increase or decrease in deorbit time can be attributed to the change in *emf* and current collection area. By increasing the tether length, more *emf* can be generated allowing for more electrons to be collected. Increasing the tether length also increases the electron collecting area allowing for the tether to collect more electrons especially at during low electron density conditions. Producing larger currents results in higher drag forces and faster deorbit times. This trend also explains why shortening the tether causes an increase in deorbit time. As more and more of the tether is removed, more and more of a limit is placed on the tethers ability to attract and collect electrons and, therefore, deorbit the system.

Other interesting effects are shown in Figures 3.47 and 3.48. Figure 3.47 shows the anode voltage as a function of time and Figure 3.48 shows the flowrate as a function of time. The anode voltage plot is interesting because it shows the limitation placed on the 2.5 km tether.

This is a direct effect of the smaller available *emf* built up in the tether. Figure 3.48 is interesting because it shows how the current affects the HCPC system when the EDT passes through less than optimal orbital conditions. This effect is not very dramatic but causes the flowrate to vary much more sporadically than in the previous plots. This could affect is noteworthy based on its ability to change the design of the flow control system.

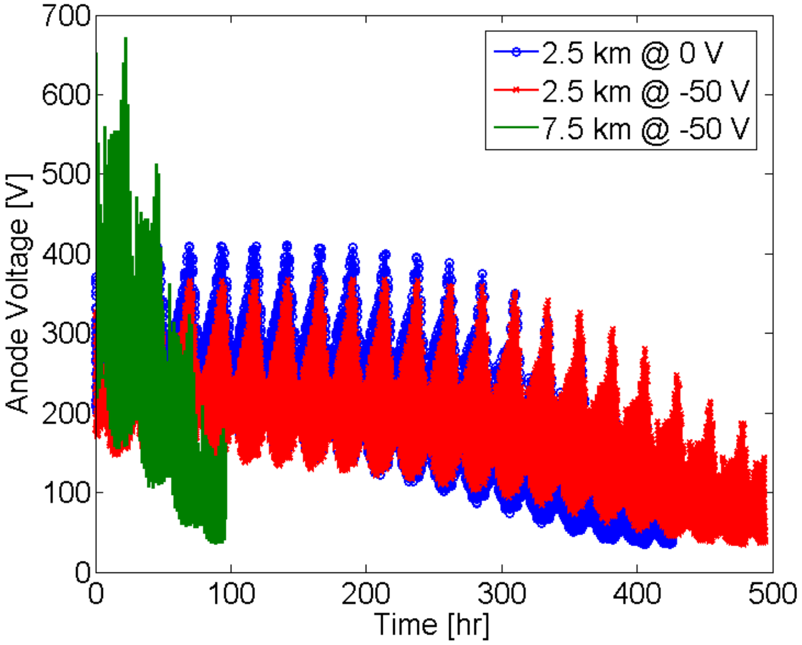

FIGURE 3.47. Anode voltage versus time for two 2.5 km tethers with a CBV of 0 V and $-50\,V$ and one 7.5 km tether with a CBV of $-50\,V$.

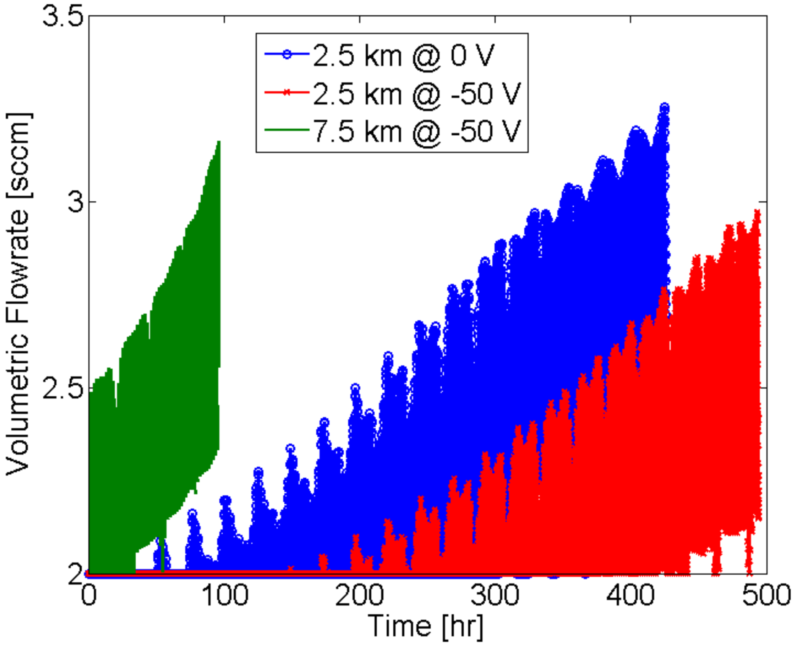

FIGURE 3.48. Flowrate as a function of time for two $2.5\,km$ tethers with a CBV of $0\,V$ and $-50\,V$ and one $7.5\,km$ tether with a CBV of $-50\,V$.

Considering the effect of varying tether length on the COE's, the most interesting effects are shown in the plots of eccentricity, Figure 3.49, and inclination, Figure 3.50, versus time. The eccentricity plot is intriguing because the first and second resonance that is present in the $7.5\,km$ plot is nearly dampened out in the $2.5\,km$ plots with only small secondary resonant effects appearing near the end of the deorbit. However, the maximum eccentricity expected in the $2.5\,km$ cases is nearly twice the maximum of the $7.5\,km$ case. The decrease in resonances is due to the limitation the EDT tether length places on current collection. As such, the variations in collected current are much larger. However, the total eccentricity nearly doubles between the shorter and longer tether lengths. This result is due to the drag force being applied over a smaller section of the orbit. If a force is applied at a about the same point every time a spacecraft orbits the Earth, the eccentricity will increase in a similar way to the $2.5\,km$ cases in Figure 3.49. However, as the EDT decreases in altitude, more favorable orbital environments are reached resulting in larger sections of strong drag force applied each orbit.

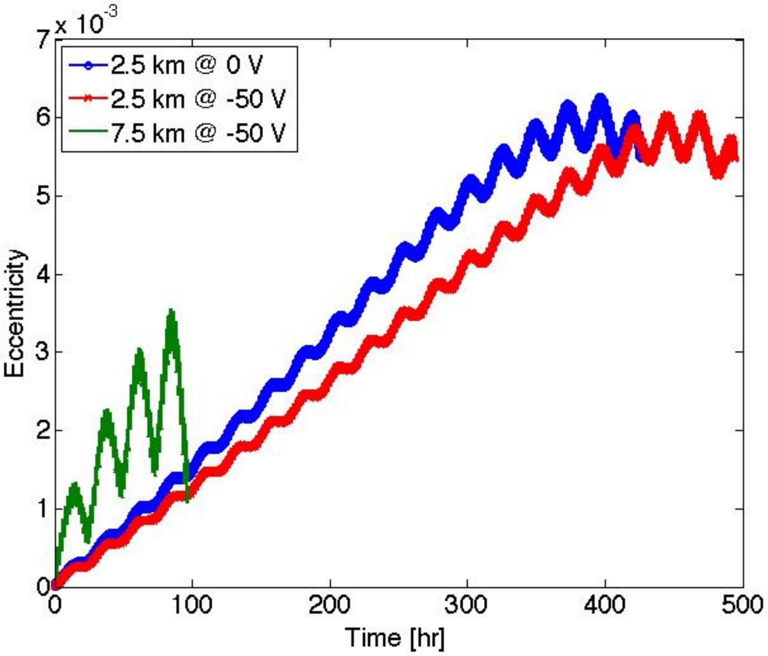

FIGURE 3.49. Eccentricity versus time for two $2.5\,km$ tethers with a CBV of $0\,V$ and $-50\,V$ and one $7.5\,km$ tether with a CBV of $-50\,V$.

The change in inclination due to tether length is opposite of the effects observed in the eccentricity plot. With increasing tether length, the peak inclination increases, but, for shorter tether lengths, more interesting effects are observed. For the $2.5\,km$ cases, the inclination variation starts in a steady resonance, but, at around $120\,hrs$, the amplitude begins to increase towards a maximum of 0.005^o. This is related to the electron density increasing with decreasing altitude. As the electron density increases, the physical limitation placed on the tether due to a smaller electron collection area begins to lift until the limitation is no longer imposed. As the limitation lifts, the EDT's interaction with the magnetic field lines of the Earth increases and the orientation of the Earth's magnetic field increases its effort to try and rotate the EDT's orbital plane.

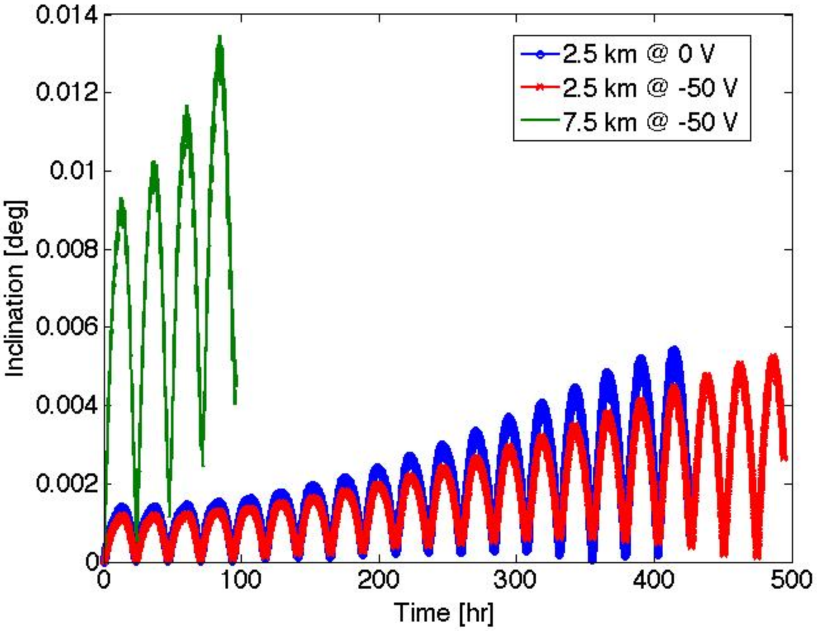

FIGURE 3.50. Inclination as a function of time for two $2.5\,km$ tethers with a CBV of $0\,V$ and $-50\,V$ and one $7.5\,km$ tether with a CBV of $-50\,V$.

The tether length also has an effect on the system mass. Figure 3.51 shows the increase in mass of various components due to increasing tether length. As the tether length increases, the main variation of the EDT system is the tether and deployer mass. This is because as the tether length increases, the deployer mass also increases to account for the extra space required by the tether as well as the increase in mass of the deployment and braking hardware. The opposite is true for decreasing tether length, the deployer and tether mass decrease.

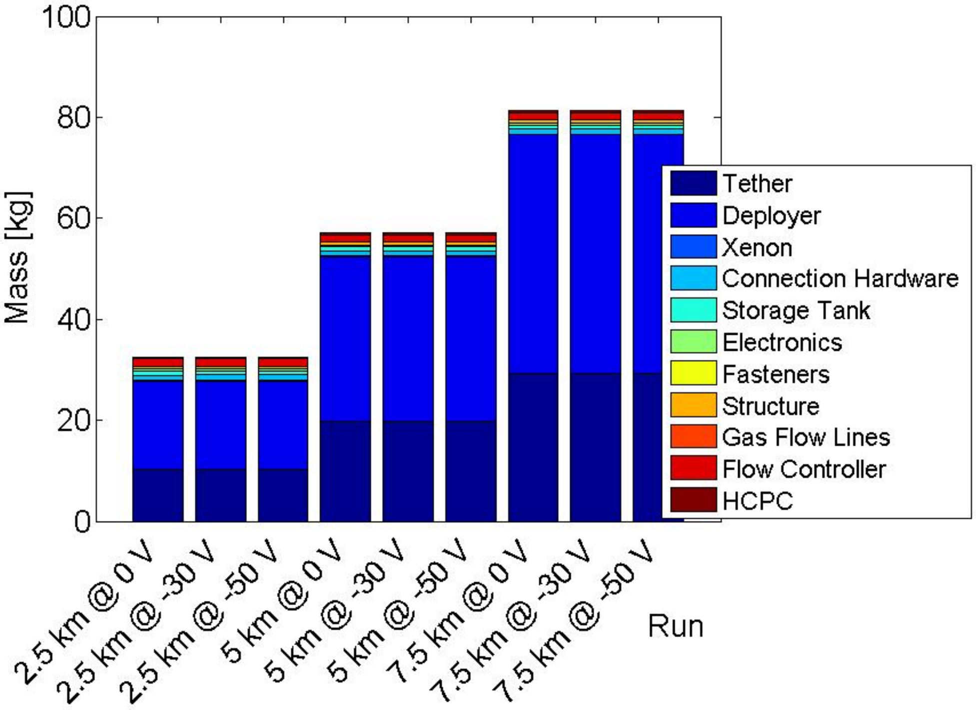

FIGURE 3.51. Masses of components in the EDT system as a function of CBV and tether length. Note the tether and deployer are included in this plot. This inclusion was performed because the tether and the deployer see the largest change with increasing/decreasing tether length.

Figure 3.52 shows how this system varies with deorbit time. Notice how, at smaller tether lengths, the deorbit time is much greater and, therefore, the deviation due to CBV is extreme. However, with longer tethers, this deviation becomes almost negligible. The longer tether is usually not recommended because the extra length adds more mass in both the deployer and the tether. This makes the system much more expensive to launch and more likely to be cut by micro-meteorites. A trade-off comparison can also be observed in the shorter tether cases. As tether length decreases, cut probability decreases, however, deorbit times increase.

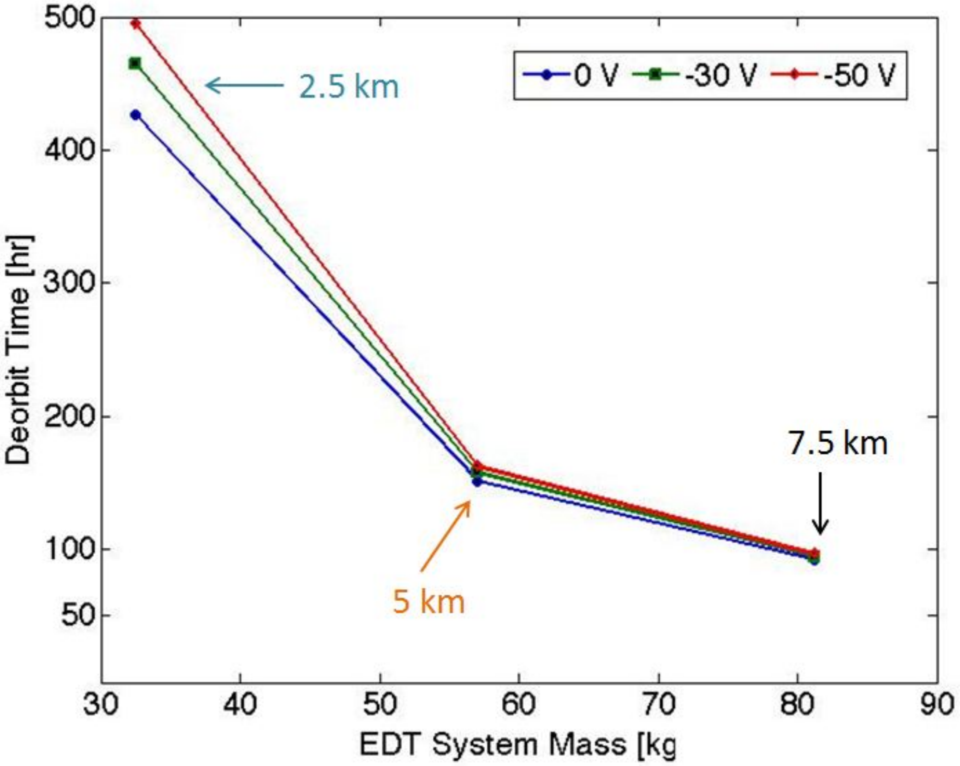

FIGURE 3.52. System mass as a function of deorbit time for CBV of $0\,V$, $-30\,V$, and $-50\,V$. Note increasing system mass is related to increasing tether length.

3.2.1.6. STUDY 5: VARIATION DUE TO HCPC BIAS AND TETHER WIDTH

Another study performed was the effects of tether width on the system and deorbit performance. Much like the previous studies, the tether widths were chosen to be $\pm 50\,\%$ of the $2\,cm$ control case tether width. The study then ran these three different widths at each of the constant CBV considered in Study 1. The effects of changing tether width relates to an increase or decrease in collection area much like the tether length, however, the *emf* does not change with increased collection area. The increase in tether width also decreases tether resistance and causes more current per unit length to be gathered. The overall result is a decrease in the limitation placed on the tether due to the predefined $5\,km$ tether length. Also, the failure probability due to micro-meteorite impacts decreases.

However, as the tether width becomes wider, the electron collection scheme begins to move away from the OML collection discussed in Chapter 2 and the mass of the tether begins to increase. The balancing act created between these different effects can be seen in the following figures. Figure 3.53 shows the altitude of the EDT as a function of time and the final deorbit performance analysis.

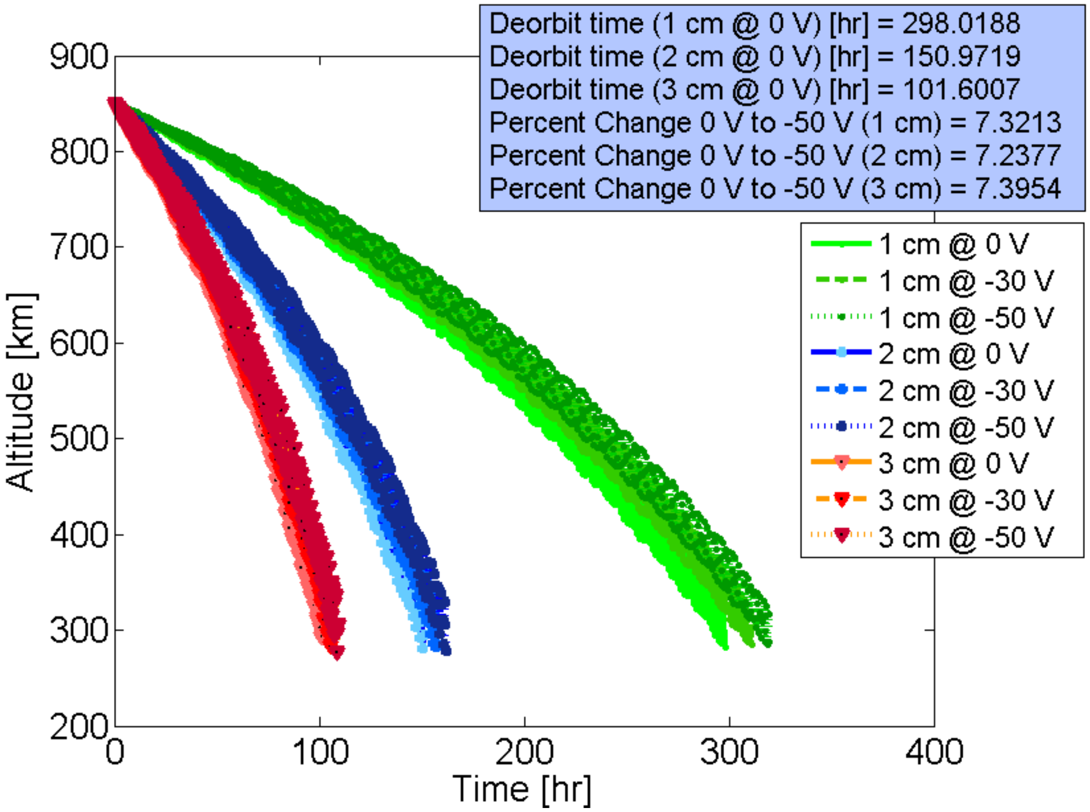

FIGURE 3.53. Altitude as a function of time for $1\,cm$, $2\,cm$, and $3\,cm$ conductive EDT section widths using CBV of $0\,V$, $-30\,V$, and $-50\,V$.

Much like the trend observed in the tether length study, the deorbit time increases by nearly $150\,hrs$ when decreasing the tether width to $1\,cm$. However, a much more subtle decrease of $50\,hrs$ is seen when the tether width is increased from $2\,cm$ to $3\,cm$. This increase is much less drastic than the trends seen in other studies, however, it is a worthwhile consideration when designing an EDT. This consideration is also a more beneficial option then increasing tether length because the increase in tether width does not increase the deployer mass saving around 15 kg of mass when comparing the 3 cm tether to the 7.5 km. Figure 3.54 shows the deorbit time of each tether width and varying fixed CBV.

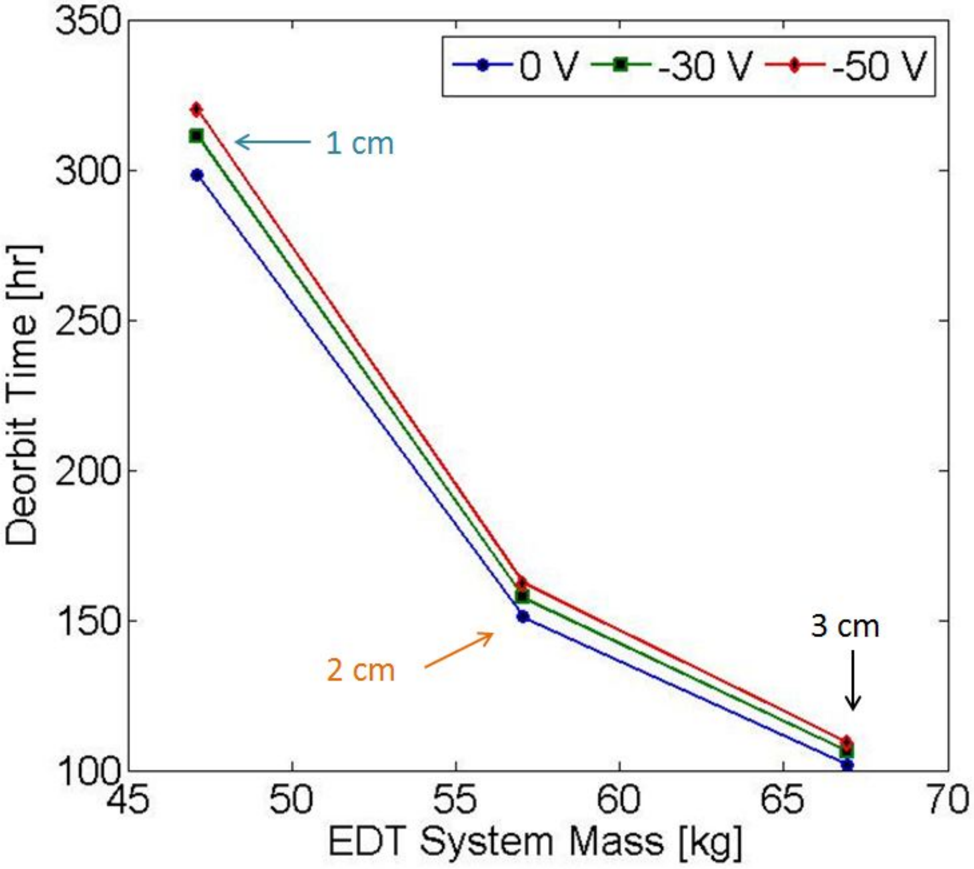

FIGURE 3.54. Deorbit time as a function of EDT system mass where increasing system mass relates to increasing tether width.

Effects on the COEs are much like the effects seen in Study 4, however, the current and flowrates are different. Figures 3.55 and 3.56 are plots of the current and flowrate as a function of time. Figure 3.55 shows the wider tether collects much higher currents, on the order of $6 - 9\,A$ at a CBV of $0\,V$, while the more narrow tether only collects about $2 - 3\,A$ at a CBV of $0\,V$. This increase in current collection is related to the increase in the perimeter and cross-sectional area of the tether. This is important because increasing the tether perimeter increases the available current collection area and increasing the tether's cross-sectional area allows more current to flow in the tether. Conversely, as the tether width decreases, the resistance in the tether becomes more dominant and lowers the available *emf* for current collection. The CBV also plays a large role by decreasing the current by nearly $1\,A$ between the $0\,V$ and $-50\,V$ cases.

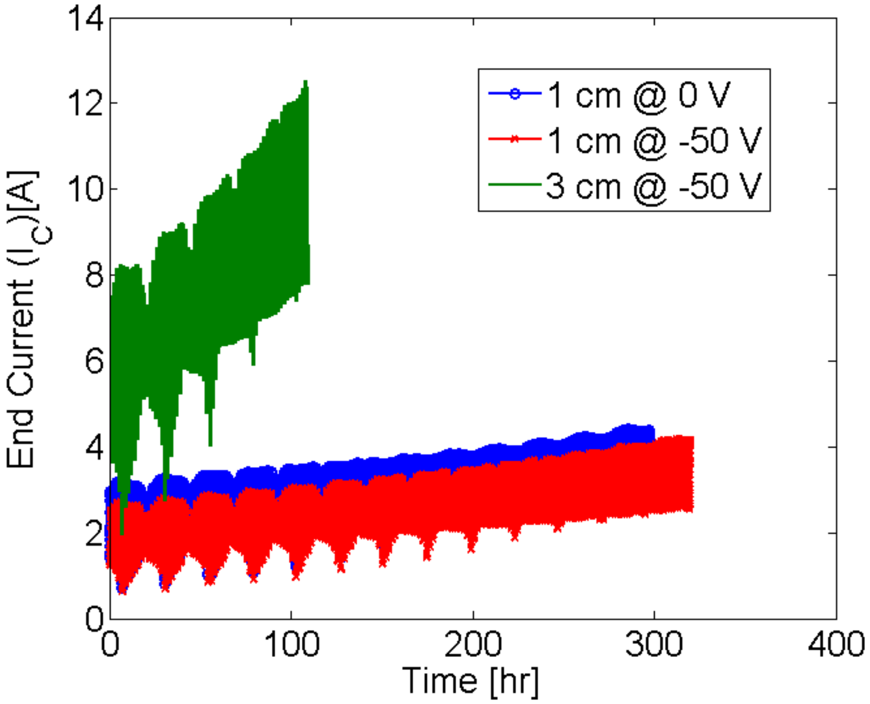

FIGURE 3.55. Current as a function of time for tether widths of $1\,cm$ and $3\,cm$ at $0\,V$ and $50\,V$.

The decrease in current also affects flowrate, shown in Figure 3.56. The flowrate curves are interesting because most of flow is at $2\,sccm$ for the $1\,cm$ case. On the opposite spectrum, the $3\,cm$, $0\,V$ case maintains flowrates between $2.5 - 3.5\,sccm$ with variations of about $1\,sccm$. Such an observation is once again important in defining system requirements.

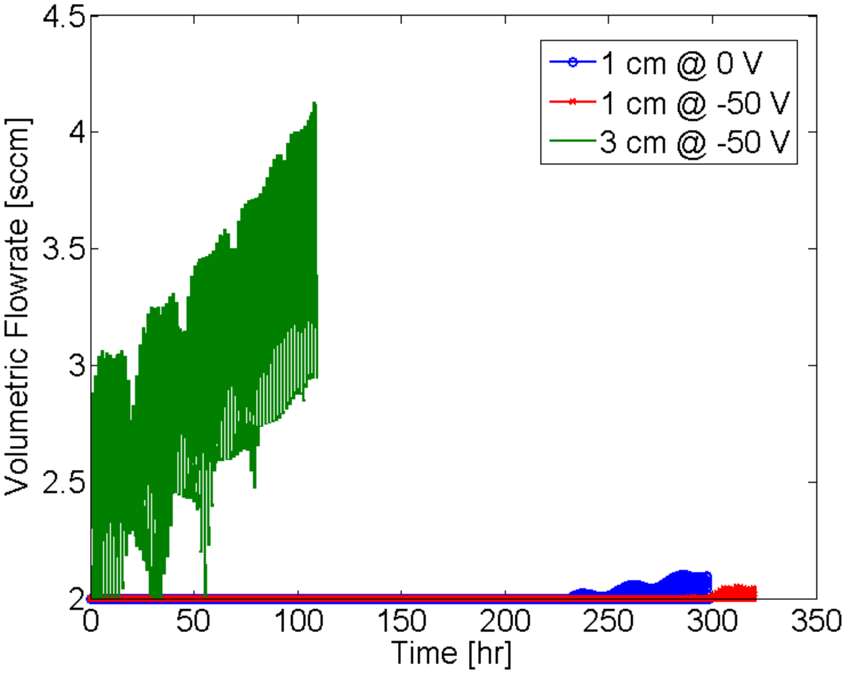

FIGURE 3.56. Flowrate as a function of time for tether widths of $1\,cm$ and $3\,cm$ at $0\,V$ and $50\,V$.

3.2.1.7. STUDY 6: STUDIES 1-5 PERFORMED WITH A VARYING HCPC BIAS

Studies 1 - 5 were completed to understand how CBV affected the performance of different EDT deorbit systems and missions. Study 6 shows how deorbit performance is affected by a varying CBV model, which was discussed in Section 2.2.4. Because the emission voltage versus emission current plot of the varying CBV model has an overall average CBV magnitude of $\sim 35\,V$, the results of the varying CBV model cases were compared against the $-30\,V$ CBV cases of Studies 1-5. Figure 3.57 shows the effect of tether width for an equatorial, circular orbit. There is less than a $0.7\,\%$ percent change between the $-30\,V$ and varying cases. This shows that for relatively fast deorbit times, $\sim 7-10$ days, a varying CBV model is not necessary. Overall, the CBV average for the varying model is around $-35\,V$, which is less than a $20\,\%$ difference from the constant cathode voltage case.

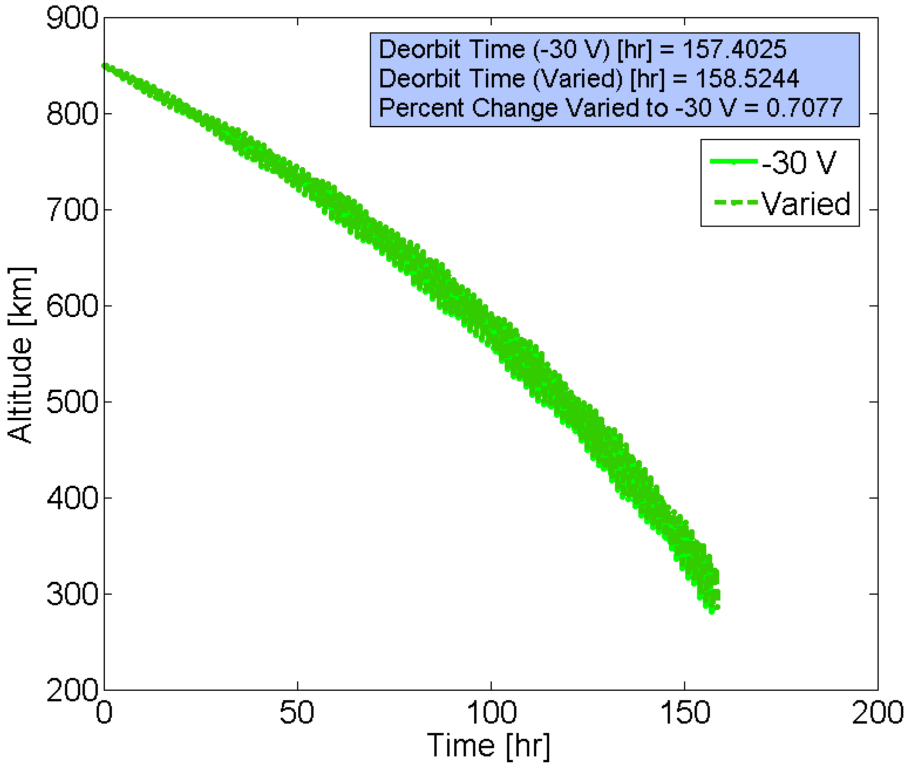

FIGURE 3.57. Altitude as a function of time for a $-30\,V$ CBV control case and the varying CBV model case.

Figure 3.58 shows the CBV as a function of time. Much like the altitude versus time plot, the other parameters output in this particular study change by $\leq 1\,\%$ between the two CBV models.

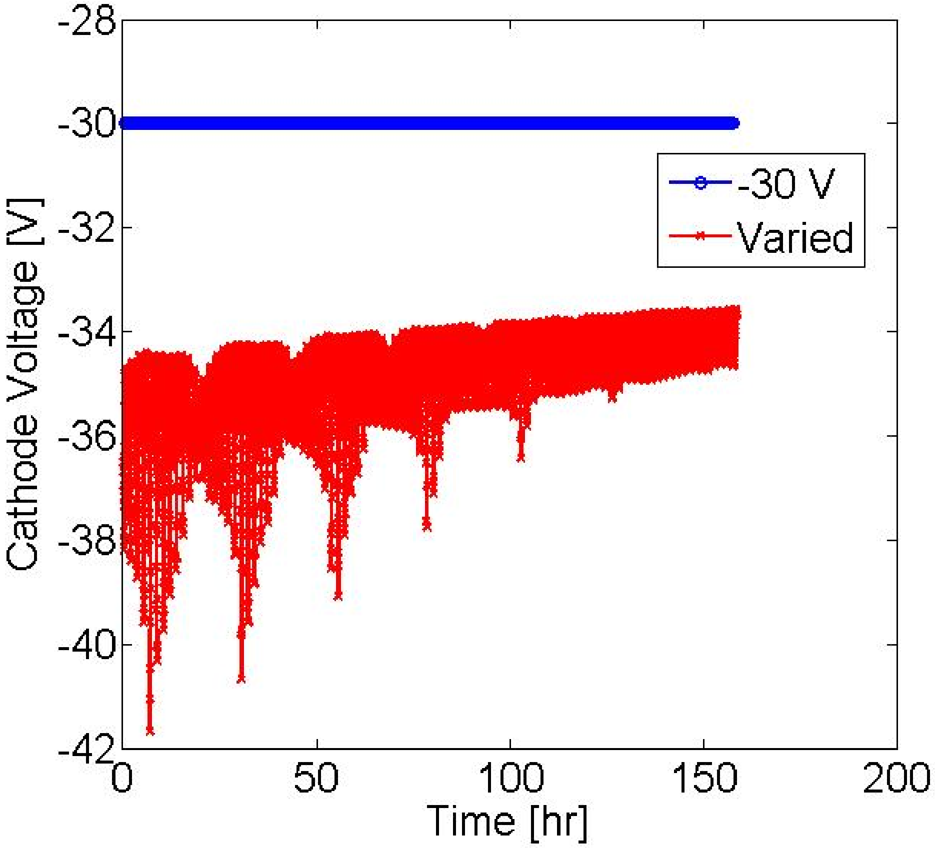

FIGURE 3.58. CBV versus time for set $-30\,V$ CBV and varying CBV models.

Figure 3.59 shows how the system mass varies with CBV. The variation between the two bar graphs is indistinguishable.

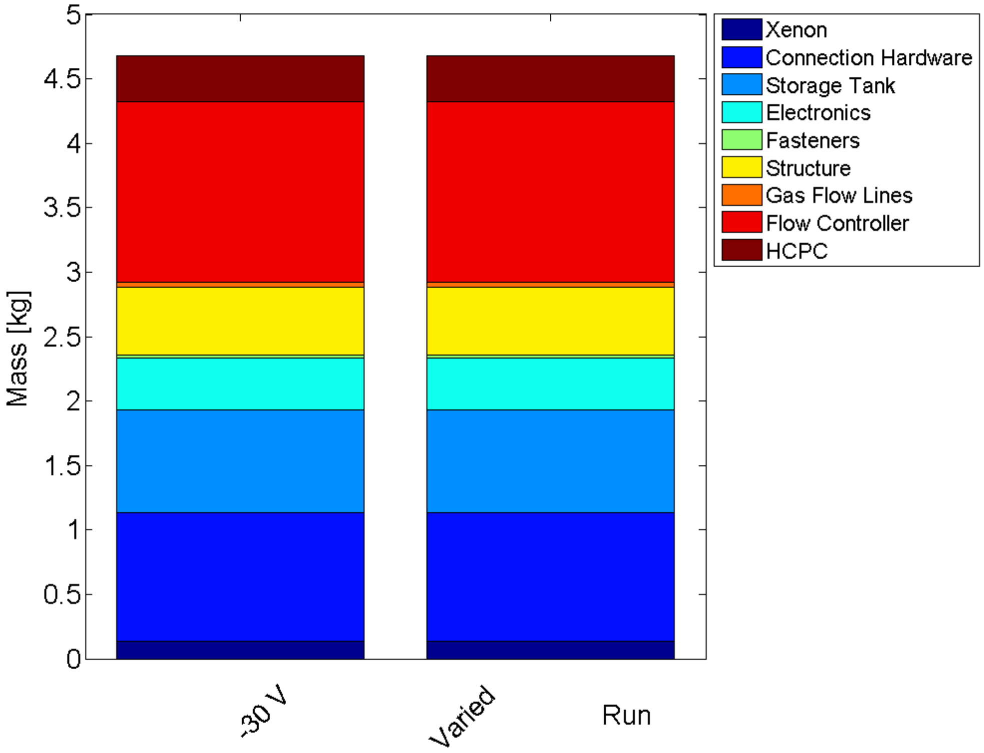

FIGURE 3.59. Balance of plant mass for the $-30\,V$ and varying CBV cases. The deployer is $32.4\,kg$ and the tether is $19.9\,kg$.

Comparing the 0^o and 35^o orbital inclinations, it was observed that a near doubling of the percent change between the $-30\,V$ CBV and varying CBV model is present. This percent change can be seen in Figure 3.60, which is a plot of altitude versus time for this study. However, this increase in percent change is still not high enough for the varying CBV model to be deemed necessary. Note the 71^o inclination study was not completed due to an excessive runtime of 10 to 20 days. As a result, a prediction can be made assuming the same trend in Study 2 is present. Using this trend and applying a similar variation observed in Figure 3.30 and Figure 3.60, it is projected that a large increase in deorbit time due to the varying CBV model will be observed. The resulting varying CBV case will probably vary from the fixed CBV model case by $\sim 5 - 10\%$ change. This result would deem it necessary to include the varying CBV model in simulations of relatively high accuracy.

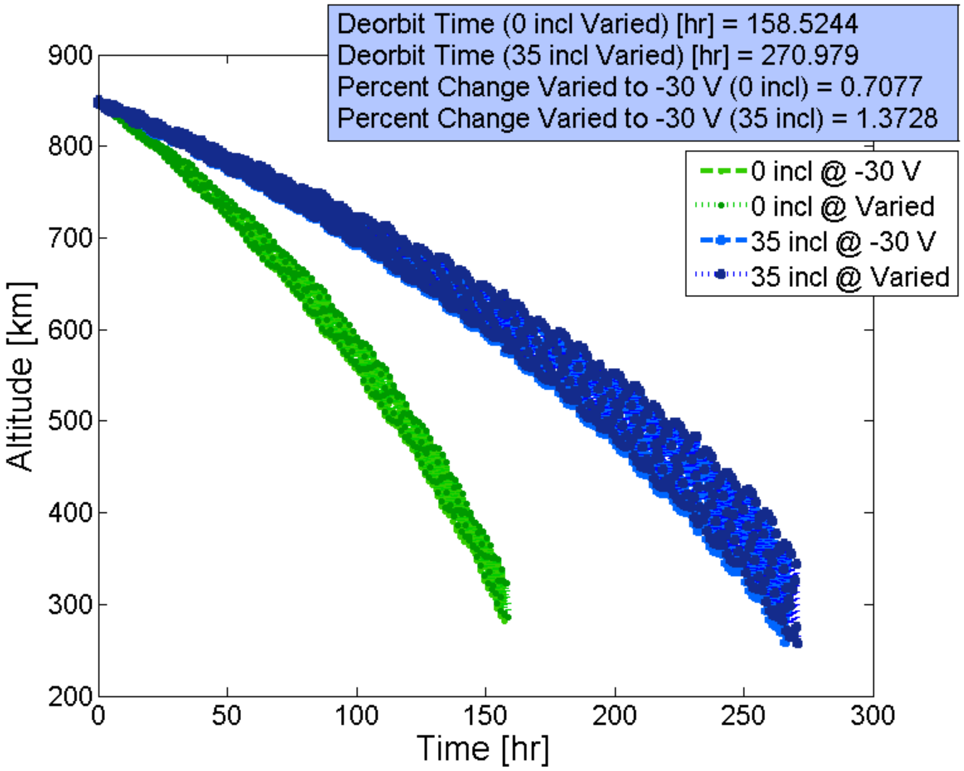

FIGURE 3.60. Altitude as a function of time for the $-30\,V$ and varying CBV model cases at 0^o and 35^o orbital inclinations.

Figure 3.61 shows a plot of CBV versus time, and it is similar to Figure 3.58. The higher inclination orbit resulted in larger oscillations in the CBV. This result is observed with increased inclination because the EDT to experiences larger variations in electron density and current collection. Larger variations in the ionosphere are observed at these higher latitudes because the incoming solar radiation is less. When the solar radiation is lower and this region moves into the dark side of the Earth, the electron density decreases faster leaving less electrons to be collected. The inclined EDT's orbit also does not cross the magnetic field lines at near right angles anymore. This decreases the *emf* produced and, therefore, the available electric potential to draw in electrons.

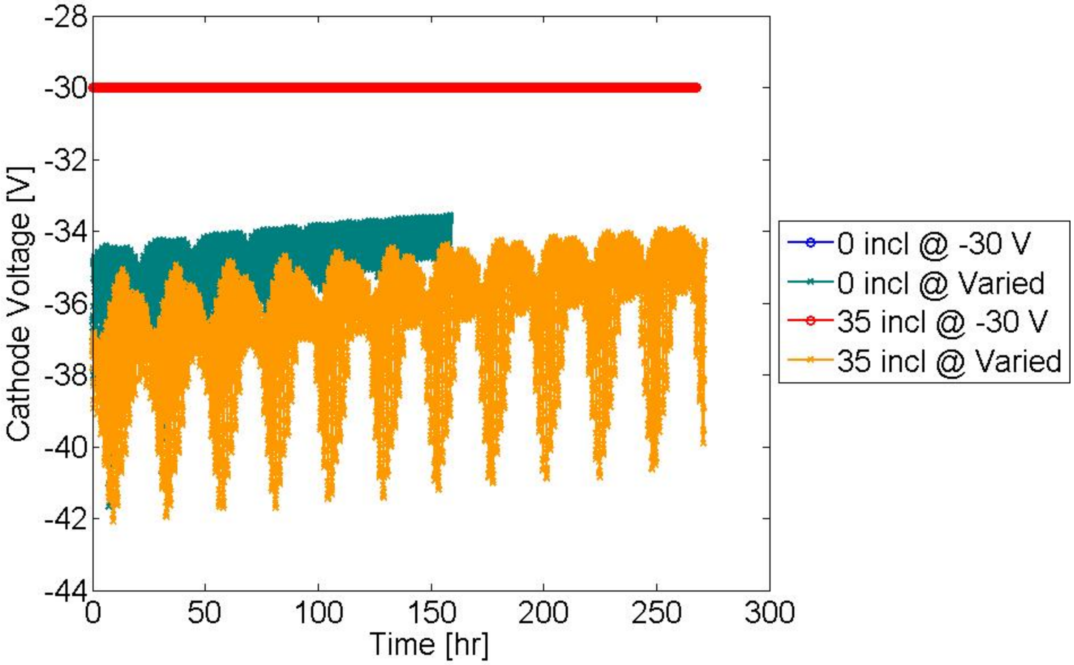

FIGURE 3.61. CBV versus time for fixed and varying CBV models on a 0^o and 35^o inclined orbit.

Similar effects observed in the first study of this section can also be observed for the variation of satellite mass. The cathode voltage for each of the satellite masses have very similar shapes with the only difference being duration of the mission. This result is expected because satellite mass only affects deorbit time. Figure 3.62 shows the cathode voltage variation between the various satellite masses.

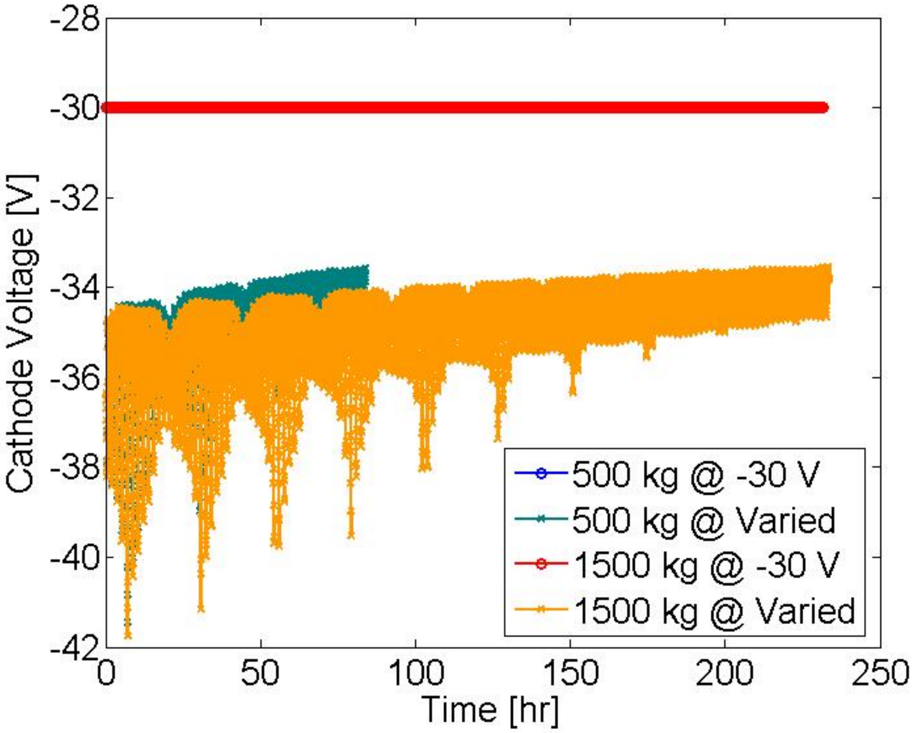

Figure 3.62. CBV versus time for set and varying CBV models for a $500\,kg$ and $1,500\,kg$ satellite.

Another interesting observation is the lack of deviation from the deorbit times due to differing CBV. Figure 3.63 shows the altitude versus time plot of the two different satellite masses. It is important to note that less than a $1\,\%$ variation between the two CBV models is observed.

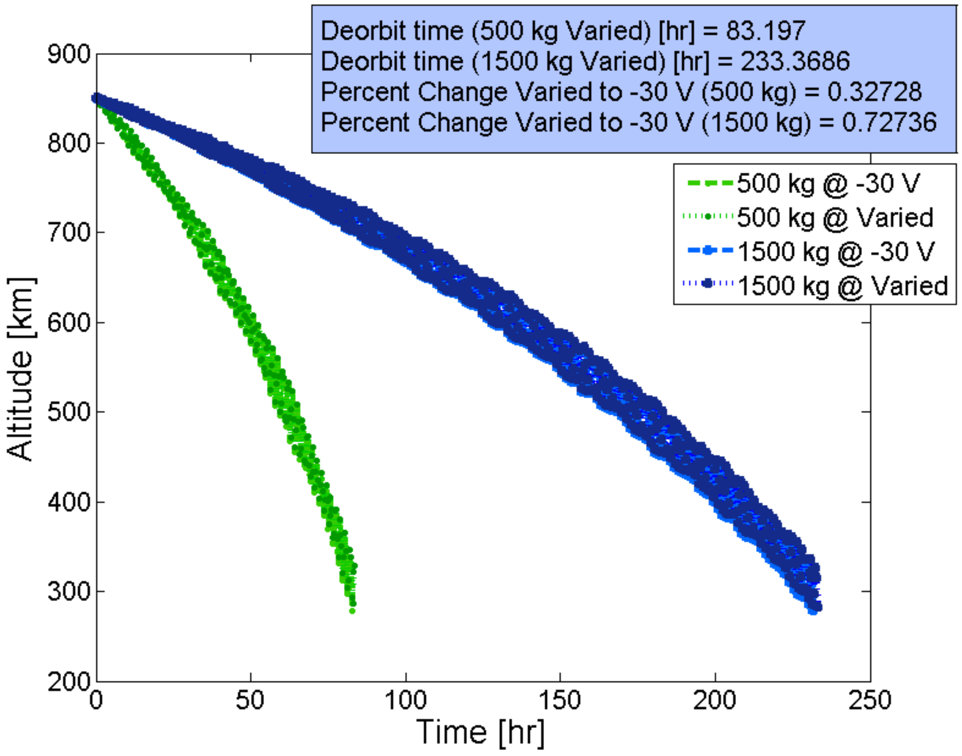

FIGURE 3.63. Altitude as a function of time for a $-30\,V$ and a varying CBV model for satellite masses of $500\,kg$ and $1,500\,kg$.

The effects of the CBV model on tether length cause the percent change to increase by a factor of ~ 4 from $0.56\,\%$ to $2\,\%$. This percent change in deorbit time is inconsequential considering the large deorbit time, about 20 days for the $2.5\,km$ tether. Figure 3.64 shows this result in a plot of altitude versus time for the $2.5\,km$ and $7.5\,km$ tether. This increase in variation is due to the behavior of the voltage as the EDT deorbits. Longer tethers are able to maintain higher current collection rates because the tether length and tether resistance are not limiting the amount of current it can collect.

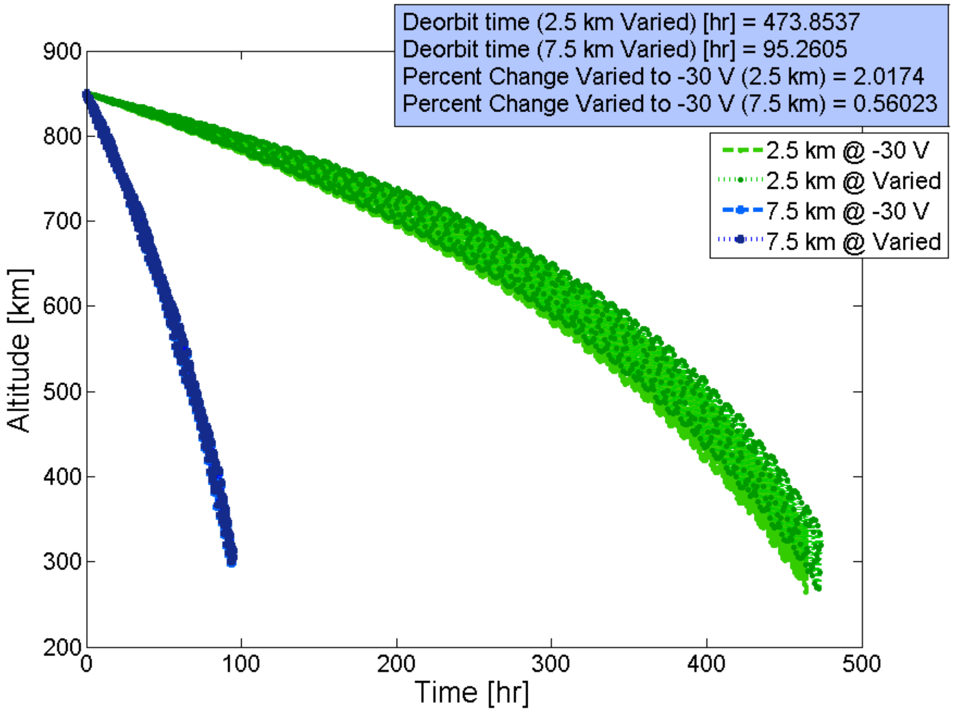

FIGURE 3.64. Altitude as a function of time for fixed $-30\,V$ and varying CBV models and tether lengths of $2.5\,km$ and $7.5\,km$.

Figure 3.65 shows the large variation between the two *emf*s of each case as a function of altitude. Altitude is chosen as the independent variable because *emf* is based on mostly position, not time. The increase in available *emf* causes the current to remain at higher magnitudes for longer and creates more drag force, which deorbits the EDT system faster.

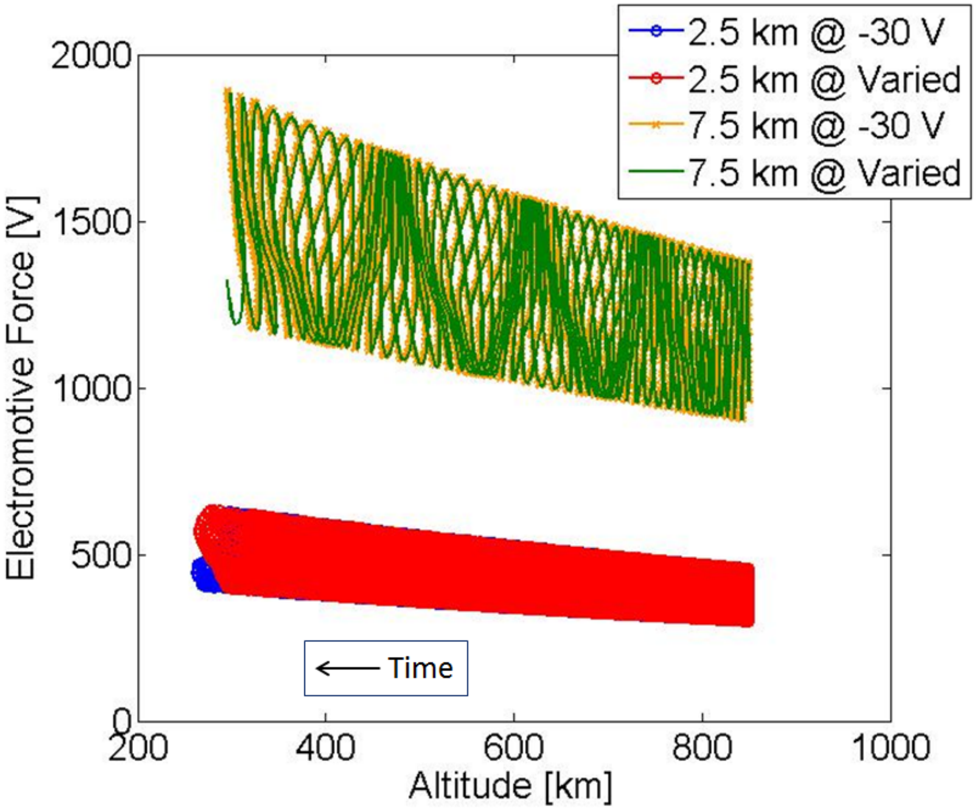

FIGURE 3.65. Electromotive force as a function of altitude for a $-30\,V$ CBV and a varying CBV.

Considering the shorter tether, interesting effects begin to occur due to the much lower currents seen by this tether during the first half of the EDT's mission. The most interesting effect is the CBV magnitude not reaching above $\sim 43\,V$. This maximum is caused by the current remaining in the $0.8 - 1.5\,A$ range, which is associated with the local maximum of the CBV magnitude as shown in Section 2.2.4. The Figure 3.66 shows the CBV as a function of time.

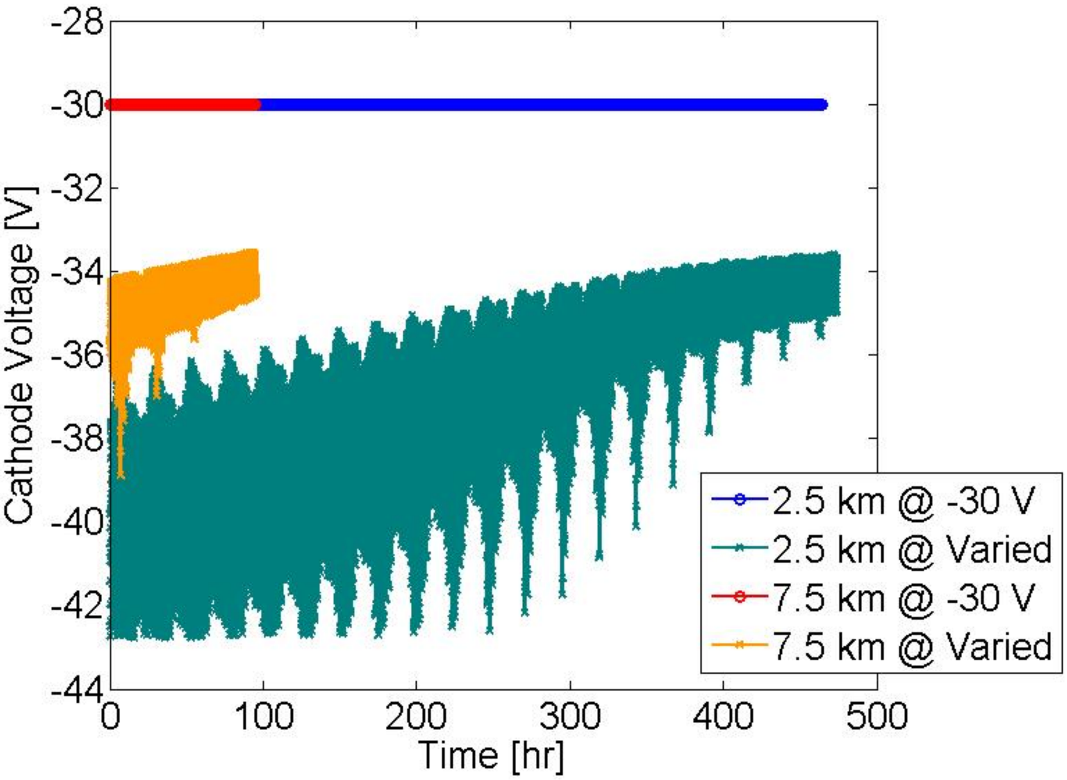

FIGURE 3.66. CBV versus time for constant and varying CBV models for tether lengths of 2.5 km and 7.5 km.

The next study, Study 6.5, relates to Study 5, which focused on the effects of tether width and fixed and varying CBV. Similar circumstances as varying tether length are occurring when tether width is varied. As the tether width increases, the tether collection area increases and resistance decreases, just like in the tether length study. In the tether width study, however, the *emf* remains the same since the tether length remains the same. Figure 3.67 shows the variation in deorbit time between the two CBV models and tether width. Examining the two different CBV models for each of the tether widths, the percent change that results from a decrease in tether width has increased the deorbit time by $\sim 1.2\,\%$. However, only about a $0.5\,\%$ increase in deorbit time for the wider tether is observed.

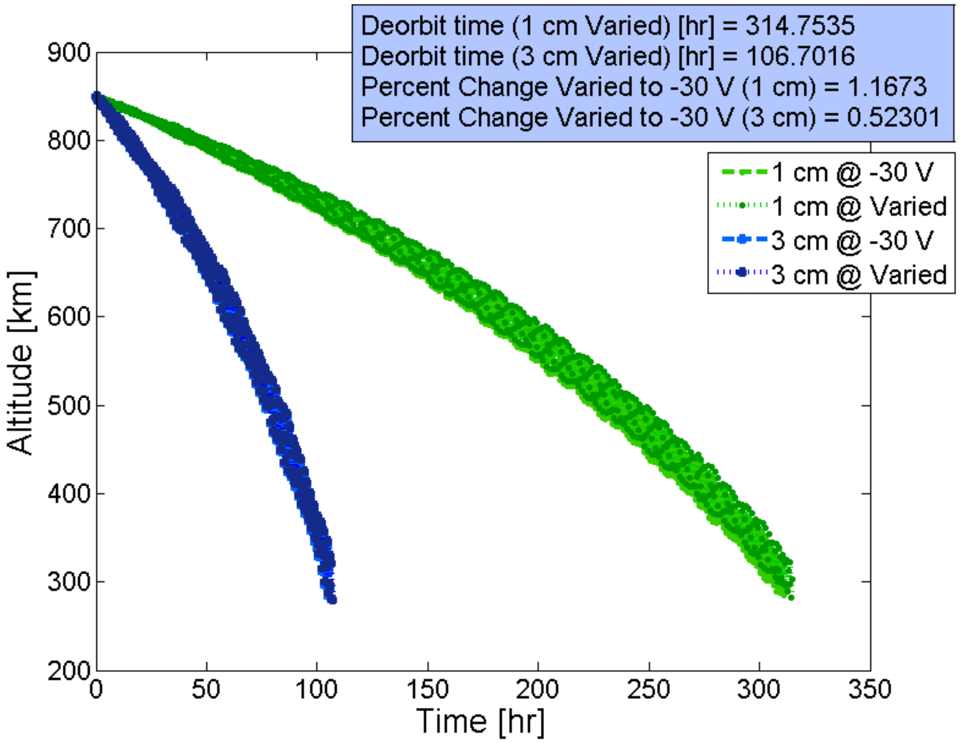

FIGURE 3.67. Altitude as a function of time for fixed $-30\,V$ and varying CBV models and tether widths of $1\,cm$ and $3\,cm$.

Another interesting note is related to the CBV. The voltage oscillation for the more narrow tether experiences CBV peak-to-peak fluctuations on the order of $2\,V$ while the wider tether experiences peak-to-peak amplitudes of less than $1\,V$. This variation is because the change in resistance of the $1\,cm$ prevents more current from flowing through the tether and the $3\,cm$ tether allows more current to flow through the tether. More current in the tether allows for the CBV to move away from the local maximum in the varying model and allow the CBV to vary in a more steady region. This is opposite for the more narrow tether because less current is collected and the tether current oscillates near the lower current local maximum. Figure 3.68 shows the CBV as a function of time.

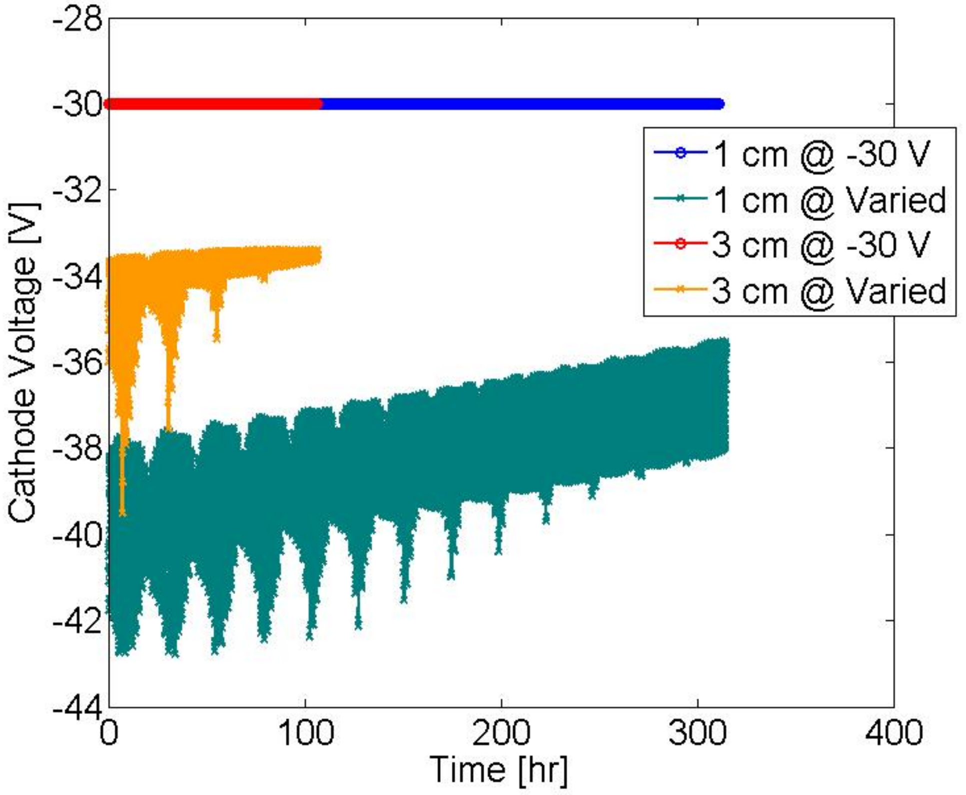

FIGURE 3.68. CBV versus time for constant and varying CBV models for tether widths of 1 *cm* and 3 *cm*.

The last study performed is on the variation of deorbit performance due to tether thickness and the CBV model. Much like varying the tether width, increasing the tether thickness decreases the resistance and increases the collection area of the tether, however, no changes are generated in the *emf*. The case chosen was a tether thickness of 100 μm and it was compared against the varying CBV model control case presented at the beginning of Section 3.2.1.7. Only one case was completed for this study because varying tether thickness is the least effective way of changing deorbit performance.

Figure 3.69 is a plot of altitude versus time for the two cases. The increase in thickness resulted in about a 60 *hr* decrease in deorbit time. This result is comparable to tether width and tether length changes. This is similar due to the 100 % increase in tether thickness, an increase twice as great as the increases in Study 4 and 5.

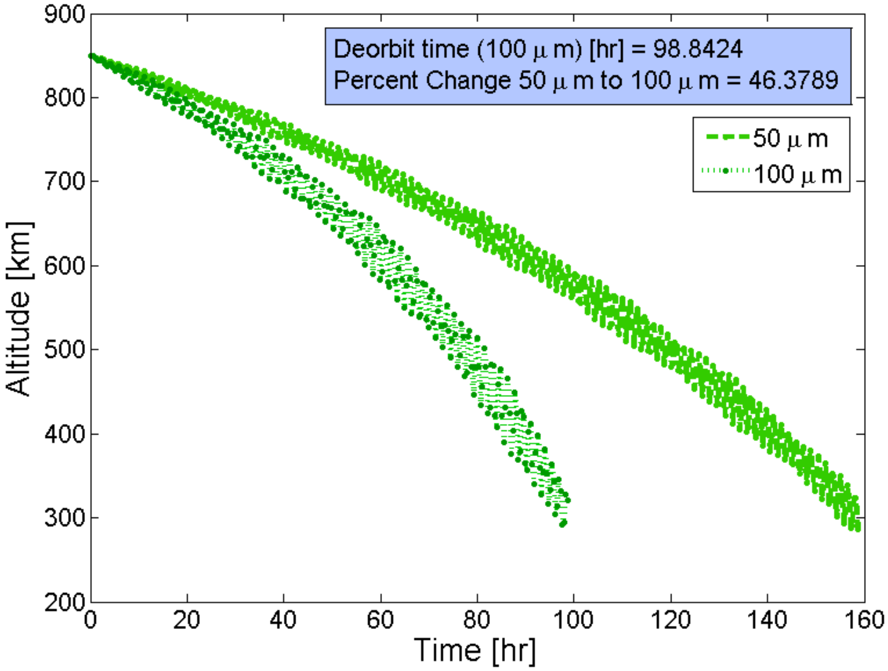

FIGURE 3.69. Altitude as a function of time for 50 μm and 100 μm thick tethers with a varying CBV model.

Discussing the variations relating to the varying CBV model and tether thickness, it can be stated that higher currents are predicted in the thicker tether and results in the CBV sitting in the valley shown between $\sim 5 - 15\,A$ in Figure 2.16. Figure 3.70 and Figure 3.71 show the current and CBV as a function of time.

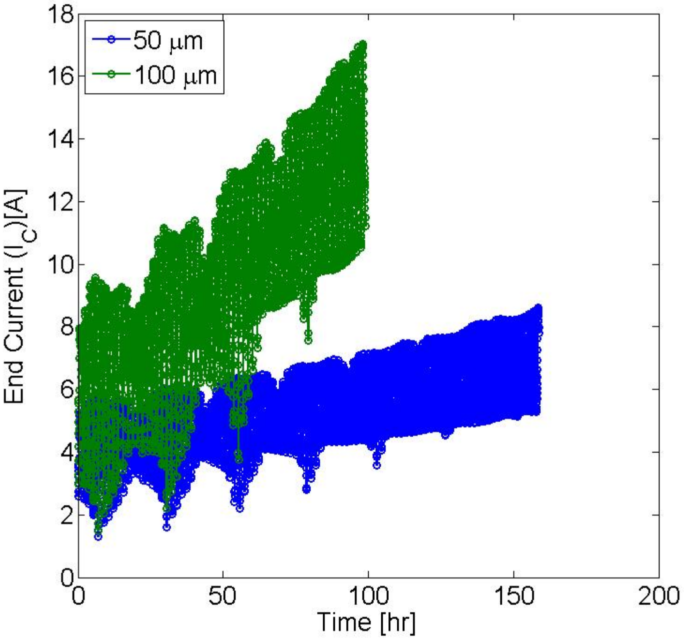

FIGURE 3.70. Current output at point C as a function of time for 50 μm and 100 μm thick tethers with a varying CBV model.

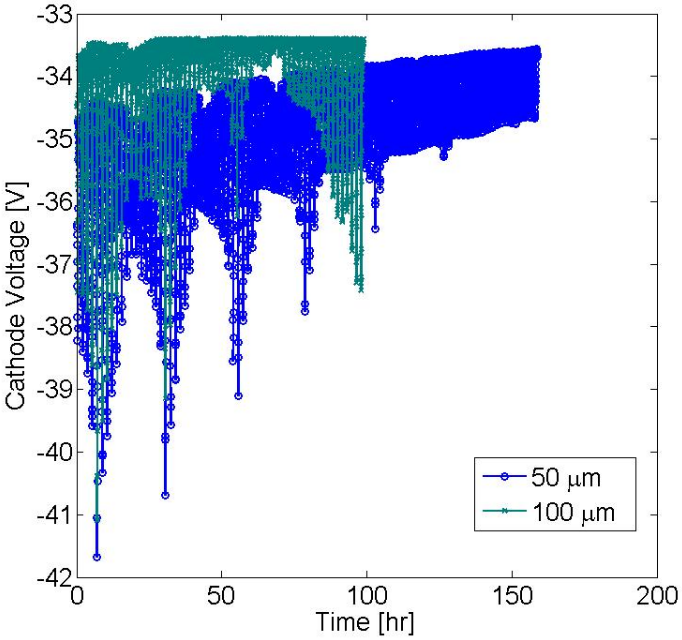

FIGURE 3.71. Cathode voltage as a function of time for 50 μm and 100 μm thick tethers with a varying CBV model.

Note the tether length also causes the HCPC system to expel xenon at a much higher rate. This results in max flowrates of nearly 5.5 $sccm$ and peak-to-peak amplitudes of $\sim 2\,sccm$. Figure 3.72 is a plot of flowrate versus time for the two different tether thicknesses.

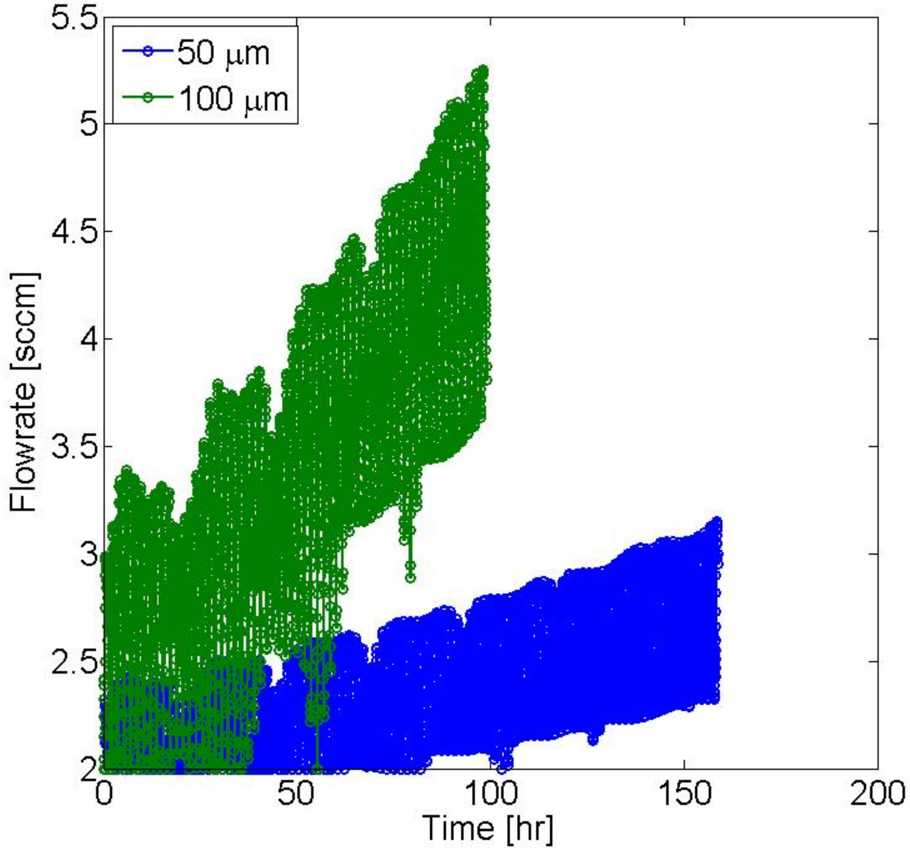

Figure 3.72. Flowrate as a function of time for 50 μm and 100 μm thick tethers with a varying CBV model.

3.2.2. SIL Testing for Gathering Data for HIL Testing

Much like the validation tests completed and compared against TeMPEST in Section 3.1.2, multiple circular, non-deorbiting, ten-orbit SIL simulations were performed. These data were used to perform HIL studies on several HCPCs for bare EDTs. The goal of these simulations was to show the variation in HCPC operations due to realistic EDT supplied current.

The SIL simulations were performed at 300, 450, 600, and 800 km for two different dates, December 14th, 2012 and August 11th, 2012. The starting time was 11:25.03 AM and 7:02.03 AM and the CBV was set to a $-50\,V$. The tether used was a $3\,km$ long, $2\,cm$ wide, and $50\mu m$ thick tether. The resulting outputs are shown in Figures 3.73 and 3.74.

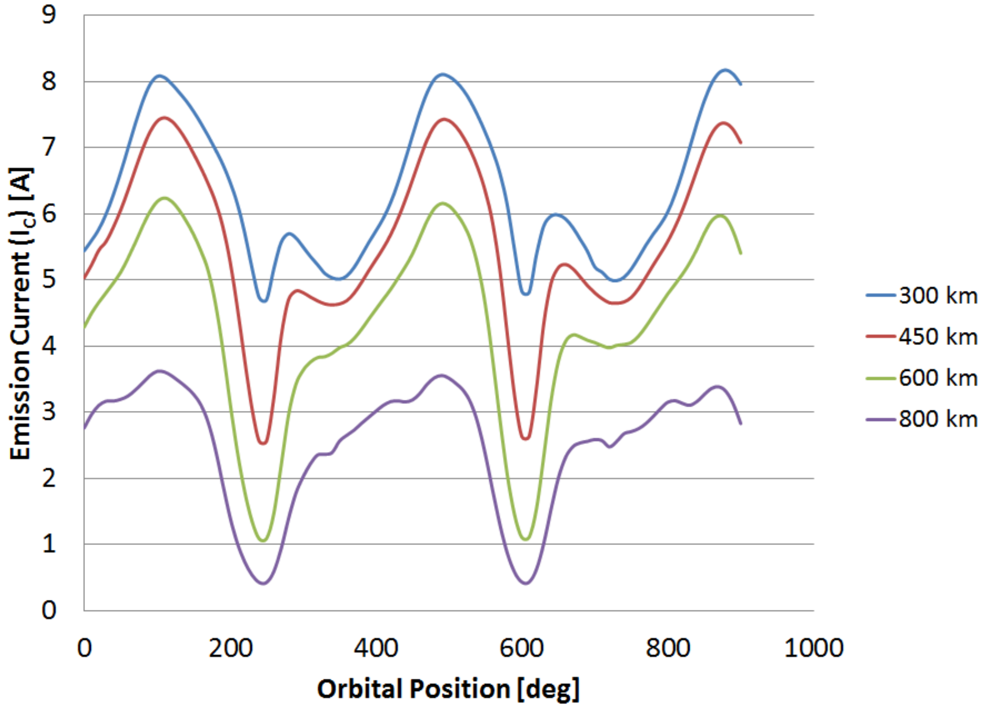

FIGURE 3.73. Tether current output at point B as a function of orbital position. Note that the CBV was assumed to be $-50V$ for these calculations and that no energy was being harvested from the tether system.

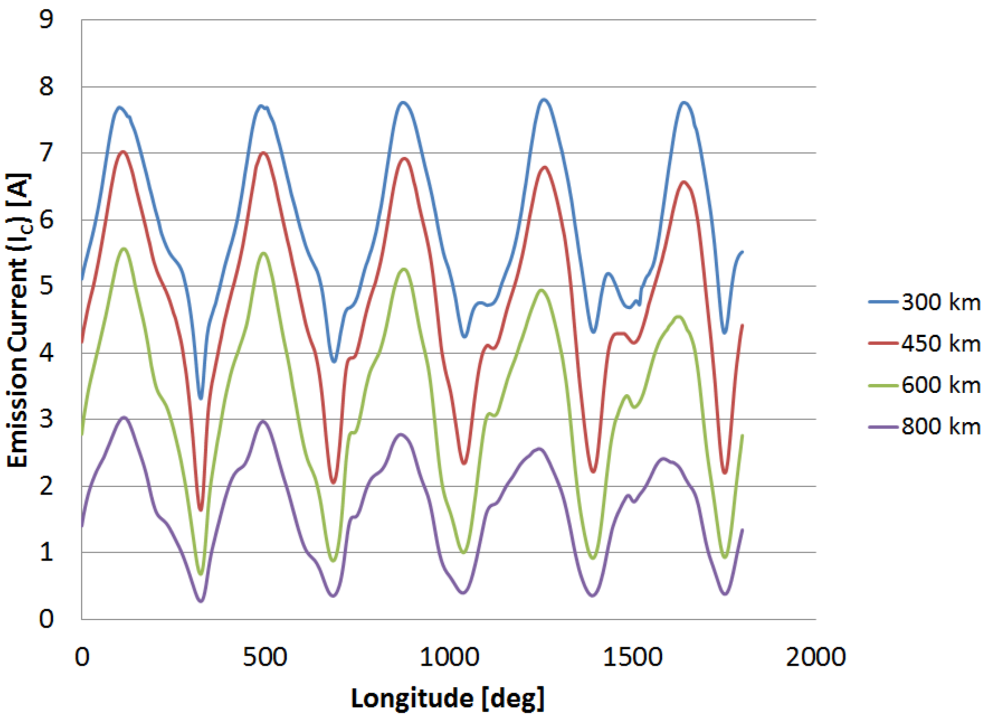

FIGURE 3.74. Tether current at point B as a function of orbital position taken at different time of year. Note that similar to Figure 3 the CBV was assumed to be $-30\,V$ for these calculations and that no energy was being harvested from the tether system.

Note these data were generated with a beta version of SimBETS and was, therefore, not validated.

3.3. HARDWARE IN THE LOOP (HIL) TESTING

A Hardware In-Loop (HIL) simulation setup was used to test several plasma contactors for electrodynamic tether systems in circular, equatorial orbit at altitudes varying from 300 km to 800 km. A systems level schematic of the HIL setup is shown below in Figure 3.75.

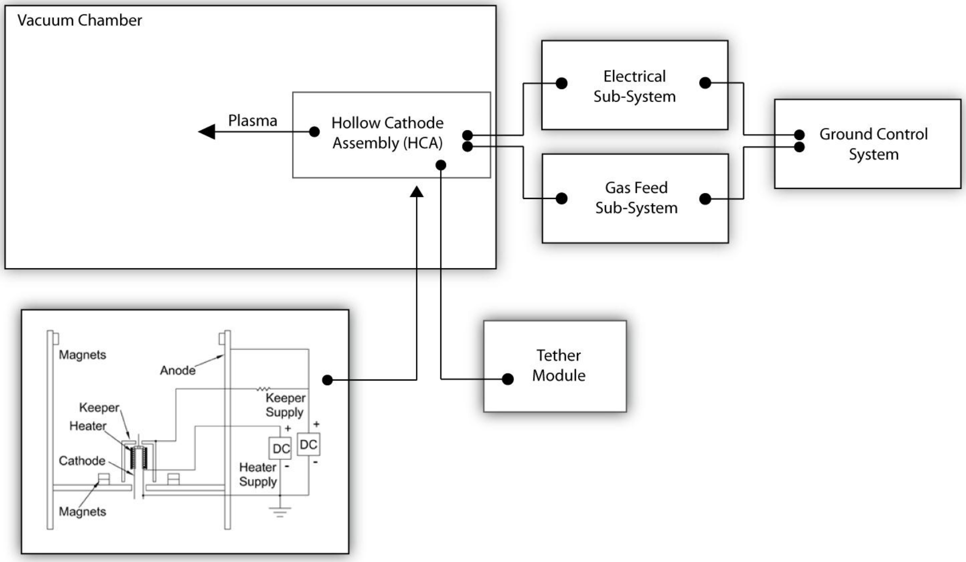

FIGURE 3.75. Hardware in the Loop (HIL) simulation setup to test HCPC systems.

The Hollow Cathode Assembly in Figure 3.75 is the focus of the HIL simulation setup, and it is shown in more detail at the bottom left of Figure 3.75. This configuration consists of a hollow cathode in combination with an ionization stage. Several other plasma contactor configurations were tested including hollow cathodes with open and enclosed keeper electrods, and a configuration where a hollow cathode with an enclosed keeper was combined with a simple, lightweight magnetic circuit.

The Tether Module in Figure 3.75 is the negative output of a power supply, and, in most testing conducted to date, the positive output of this power supply is connected to the vacuum chamber ground. Some HIL testing was also performed with resistors placed in-line with the power supply to simulate the load imposed by a harvesting element. The Electrical Sub-system is used to set the current and voltage of the keeper and heater power supplies that are used to operate the plasma contactor. The keeper and heater supplies are ancillary during a tether mission because, at electron emission currents above $\sim 1 - 2\,A$, they can be shut off. The Gas Feed Sub-system is used to set the flow rate to the plasma contactor. In general, we found that higher gas flow rates are required for the open and enclosed keeper plasma contactor configurations that do not utilize an ionization stage or a lightweight magnetic circuit.

The Ground Control Sub-system shown in Figure 3.75 is also shown in a block diagram in Figure 3.76. This sub-system was used to control Gas Feed and Electrical Sub-systems and to record data. The Ground Control Sub-system consisted of a Labview program and a $National\,Instruments\,6009\,Controller$. Note that an anode dc/dc converter is shown in Figure 3.76, but it was only infrequently used in some tests to power the anode electrode in the plasma contactor configuration that used an ionization stage.

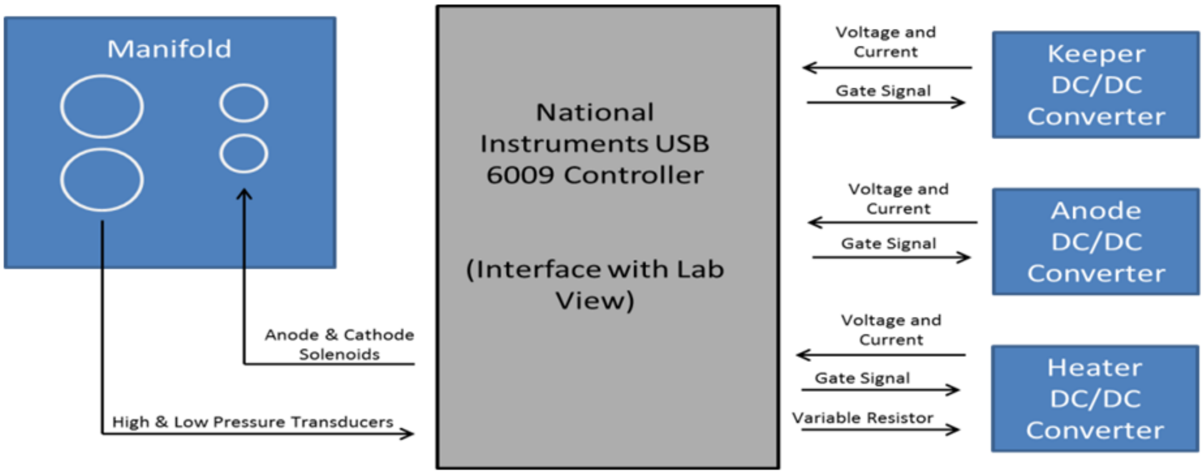

FIGURE 3.76. Ground control sub-system block diagram.

3.3.1. HARDWARE-IN-THE-LOOP SETUP TESTING RESULTS

The following sections present results obtained with the HIL setup in tests of several differently configured plasma contactors.

3.3.1.1. Combined Testing of the Power Control and Gas Delivery System

The power control and gas delivery system were used to operate a $0.64\,cm$ diameter hollow cathode at Colorado State University, which is shown in Figure 3.77. This cathode was configured with a simple ring keeper that was formed from a $1.5\,mm$ diameter tantalum wire. Testing was performed in a $1.2\,m$ diameter by $5\,m$ long stainless steel vacuum chamber that was pumped with a $0.9\,m$ diameter, $20\,kW$ diffusion pump. The base pressure of this facility with no flow was $5 \times 10^{-7}\,torr$ after a 2 hour pump down time. Introducing a xenon flow of $4\,sccm$ to the hollow cathode increased the vacuum pressure to $1 \times 10^{-5}\,torr$.

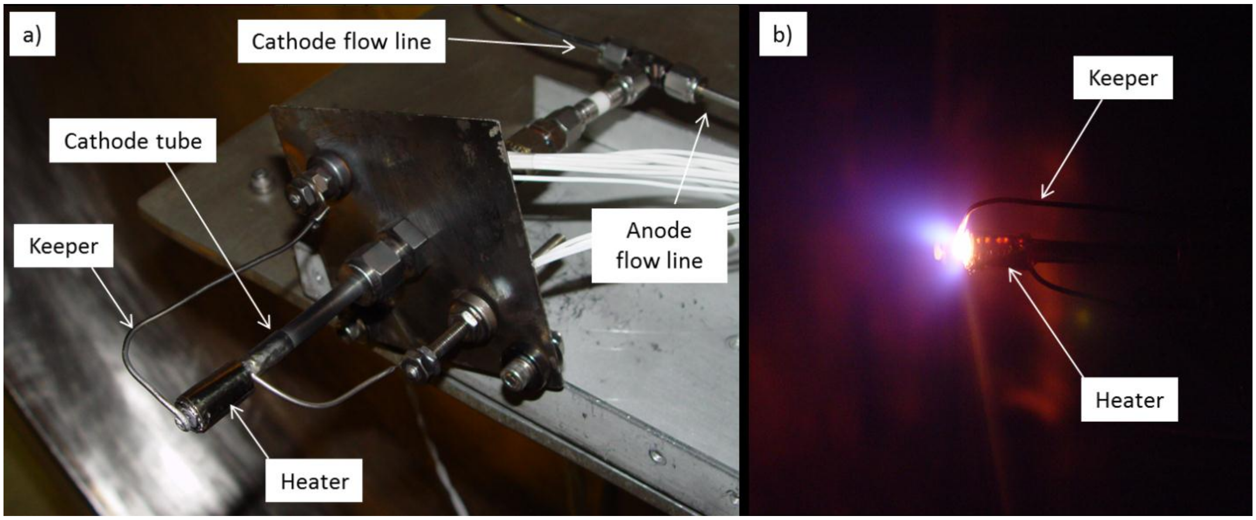

(a) $0.64\,cm$ diameter hollow cathode, heater, and wire keeper. The cathode and anode flow lines were tied together to route both flows through the cathode. The cathode was biased negative of the grounded vacuum chamber to emit electrons to the chamber walls.

(b) Cathode operation at an emission current of $3\,A$.

Figure 3.77. $0.64\,cm$ diameter hollow cathode.

3.3.1.2. Cathode Starting

The hollow cathode was operated on argon and xenon gas at flow rates of 2, 4, and $6\,sccm$. Typically for a hollow cathode, an incremental heating procedure is used to gradually increase the cathode/insert up to the required 1100 ^oC temperature for starting the plasma discharge. In the case of the PCS, the heater voltage is not variable so a variable heating on/off duty cycle was used. The duty cycle percentage was gradually increased from 0 % in 5 % incremental steps, with about 4 minutes at each duty setting. Starting at a heating duty of 35 %, the keeper voltage was applied to attempt to initiate a discharge. Typically, a heating duty cycle of 45 % to 80 % was necessary to reach a high enough temperature for the cathode discharge to start. Once a discharge was initiated, the heater duty was reduced to 20 % to maintain proper cathode temperature, though in most cases the heater could be turned off completely.

3.3.1.3. CBV Voltage versus Emission Current

The cathode could be biased negative of the grounded vacuum chamber to emit electrons to the chamber walls. Figure 3.78 shows a plot of the CBV as a function of the cathode emission current. A resistance of 9.6 and 20.4 Ω was inserted in series with the CBV power supply to simulate the resistance of an energy harvester subsystem. As expected, the CBV increased across the plasma contactor and the energy harvester when the resistance of the harvester was increased. It is noted that the CBV approached 100 V at 3 A of electron emission for the case where a 20.4 Ω resistor was used to simulate the harvester. This would imply that the tether CBV near the satellite relative to the space plasma is nearly $-100\,V$, and care would need to be taken to prevent arcing from the tether. The current to the keeper electrode varied from 2.15 A (at 0 A of electron emission) up to 2.38 A (at 3 A of electron emission) for all three energy harvester resistances. In addition the CBV versus emission current trend was similar for the 2 and 6 *sccm* xenon flows over the electron emission current range from 0 to 3 A. Figure 3.79 shows photographs of the hollow cathode at emission currents of 0, 1, 2, and 3 A at 2 *sccm* xenon flow. It is noted that electron emission currents greater than 3 A could not be achieved with the ring keeper configuration.

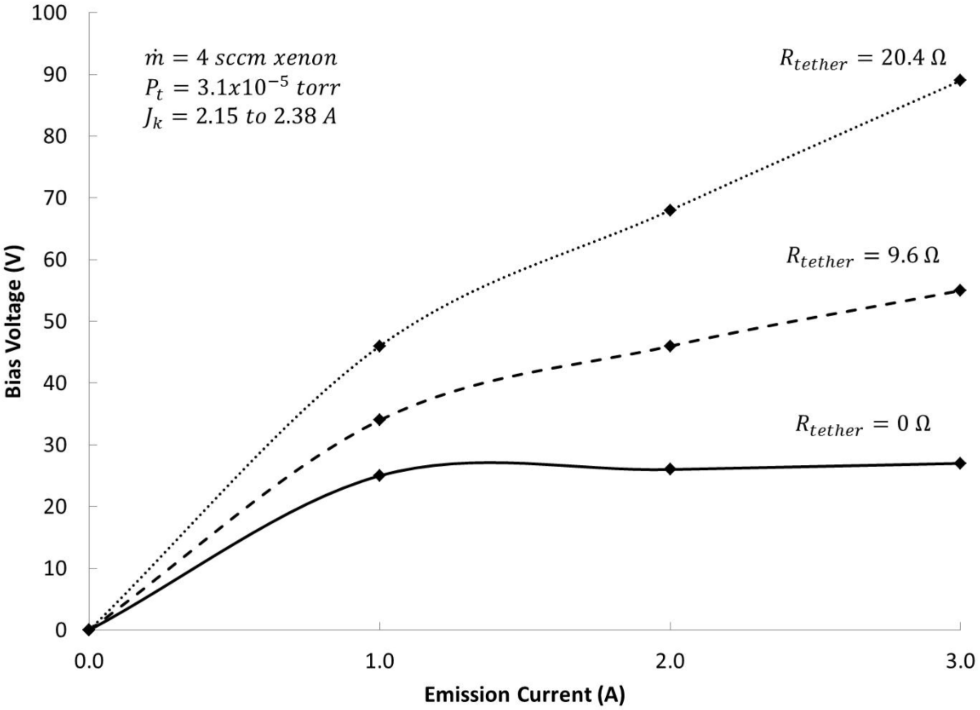

FIGURE 3.78. CBV as a function of emission current from the hollow cathode to the vacuum chamber wall for three simulated energy harvester resistance values.

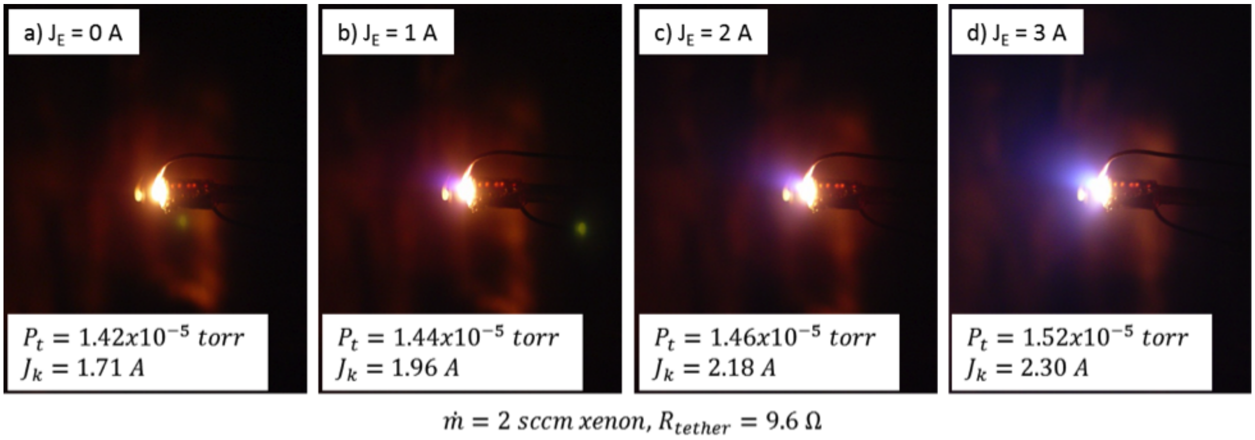

FIGURE 3.79. Photographs of the hollow cathode at emission currents of 0, 1, 2, and 3 A.

A second test was performed to determine the CBV as the emission current profile was varied over a 90-minute period similar to the orbital period in LEO. A sinusoidal emission current profile was arbitrarily chosen for laboratory test purposes having a minimum emission current of 0.3 A and a maximum emission current of 4.0 A. To simulate variations in the collected/emitted current due to the Earths magnetic field, a shorter 5-minute period variation of 15 % of the nominal sine wave amplitude was arbitrarily chosen. The emission current profile is shown in Figure 3.80, and the measured CBV profile is shown in Figure 3.80 for the input emission current profile.

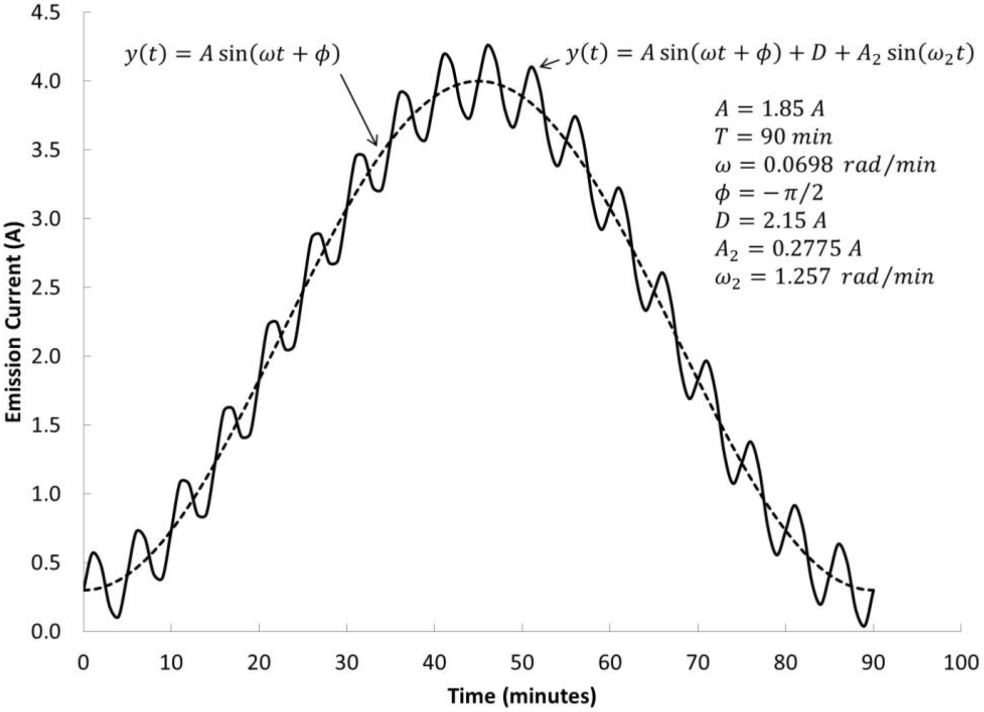

Figure 3.80. Programmed emission current profile over a 90 minute period. The CBV was recorded as a function of the emission current and is plotted in Figure 3.81.

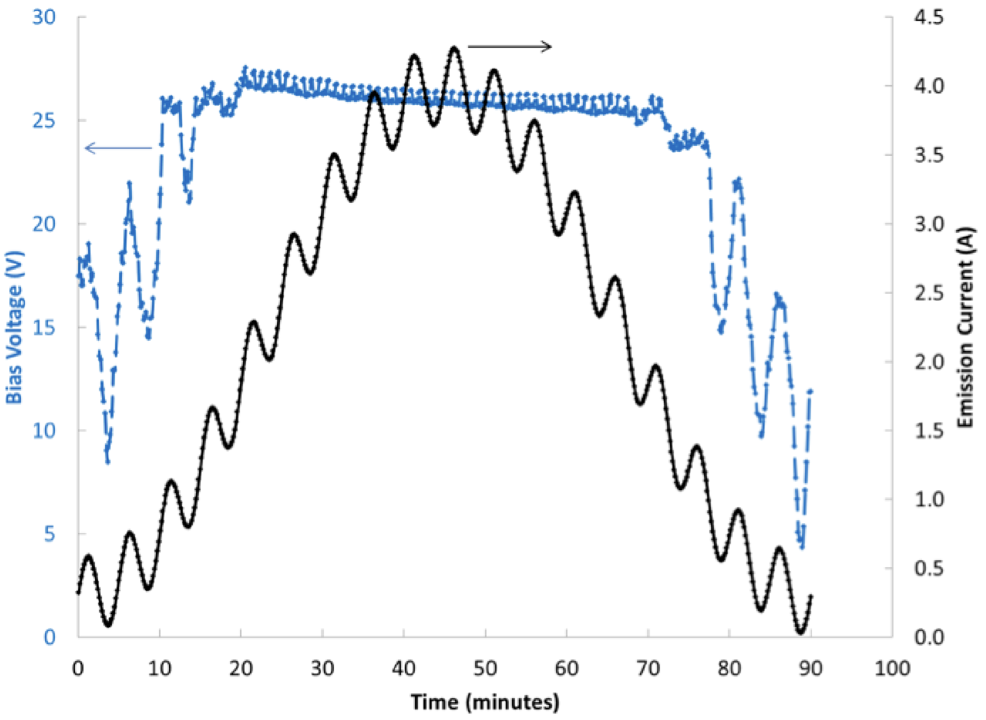

Figure 3.81. Measured CBV and emission current over a 90 minute period.

As described in Section 3.2.2, more realistic tether currents were calculated for several orbits and tests like those described in Figures 3.80 and Figure 3.80 were repeated. Figure 3.82 contains tether current data for circular, equatorial orbits of altitude 300, 450, 600, and 800 km that correspond to a date of Dec. 14, 2012 with an aluminum tether length of 3 km, width of 2 cm, and thickness of 50 μm.

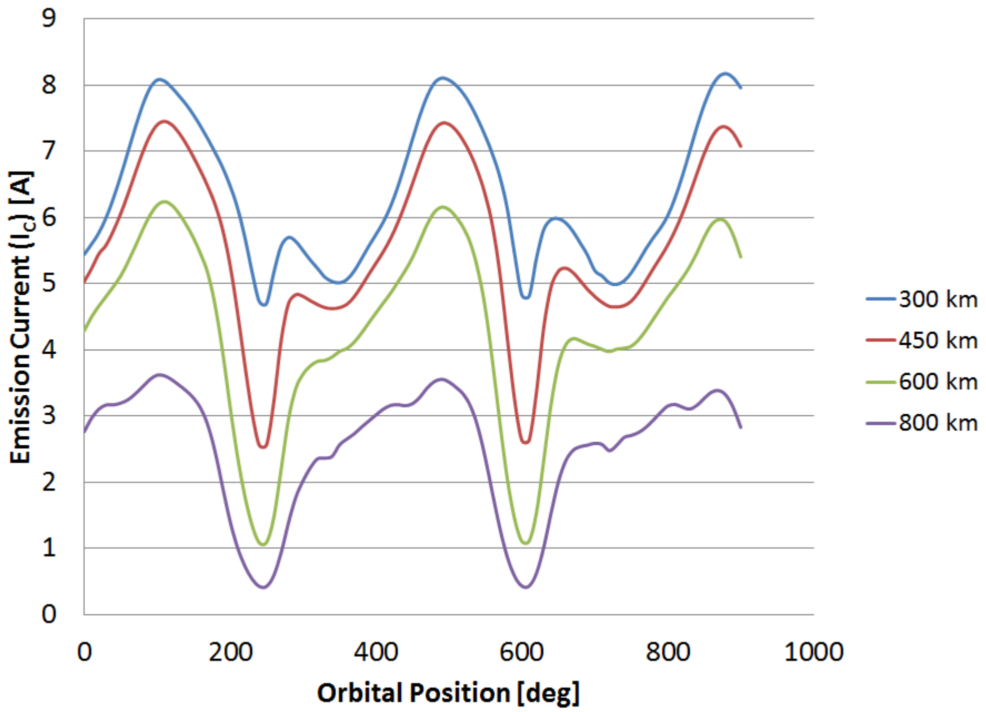

FIGURE 3.82. Tether current variation as a function of orbital angular position. Note that the first 360 degrees of the 600 km orbit were used to perform tests reported in Figures 3.83 - 3.85.

Figure 3.83 contains plots of tether current and plasma CBV measured with the simple ring keeper plasma contactor operated at a flow rate of 6 *sccm* when both the heater and keeper power supplies were shut off and the energy harvester resistor was set to 0 Ω. The plasma CBV is below 30 V for electron emission currents above $\sim 2.5\,A$. At the minimum tether current of 1 A for this test case, the CBV increased to $\sim 40\,V$. Although the CBV is within an acceptable range, the flow rate of 6 *sccm* is considered to be too high for long missions because too much xenon would be required.

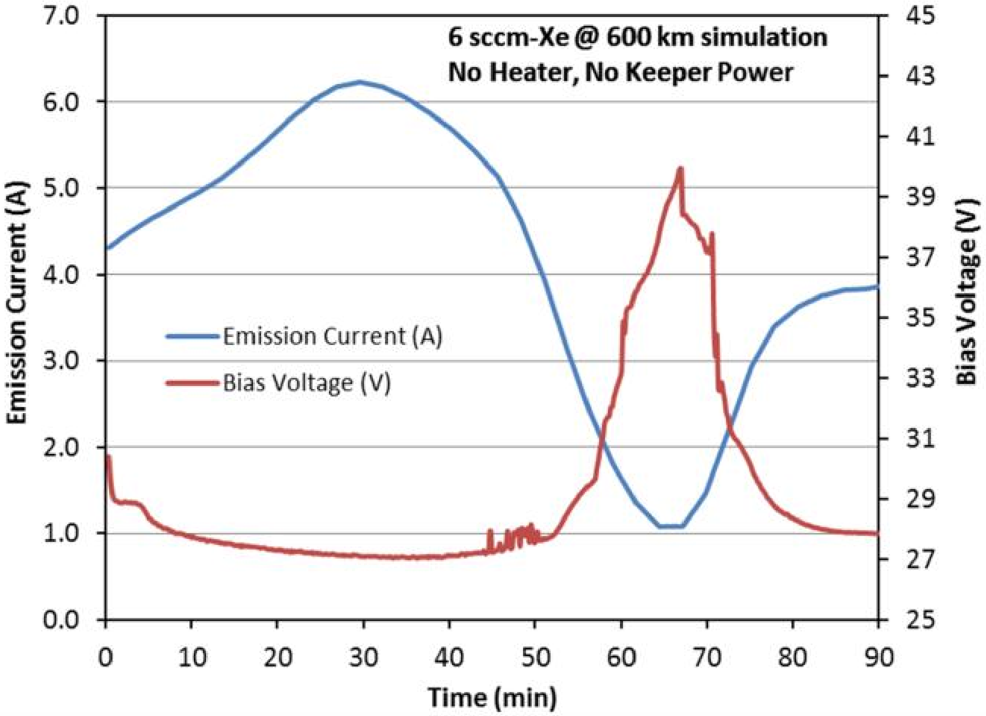

FIGURE 3.83. Measured CBV with varying emission current over a 90 minute period for the simple, ring keeper (open) configuration. Xenon flow rate set to 6 *sccm*.

The data shown in Figure 3.84 is the same as those shown in Figure 3.83 except that we exchanged the simple ring keeper for an enclosed keeper, which was fabricated from lightweight graphite. The enclosed keeper does a better job of forcing all the neutral gas particles flowing from the cathode to flow through the region between the cathode and keeper orifice plates. This enhanced neutral density action allowed the flow to be decreased to 5 *sccm*. Although this is an improvement over the open keeper design, better (lower gas flow) performance is desired.

Finally, the data shown in Figure 3.85 is the same as those shown in Figures 3.83 and 3.84 except that we created a simple magnetic field in the regions downstream of the enclosed keeper. This change allowed us to reduce the flow rate to 3.5 *sccm*. Additional experimentation continued on this lightweight alternative to the heavier ionization stages that has been used in the past. Specifically, we have added an extension to the cylindrical sidewall of the enclosed keeper that is placed downstream of the keeper orifice. This serves to constrain the neutrals released by the cathode to the region where we are drawing the electron emission current through. This improved PC was described earlier in Subsection 2.2.4. HIL simulations were not performed with this configuration.

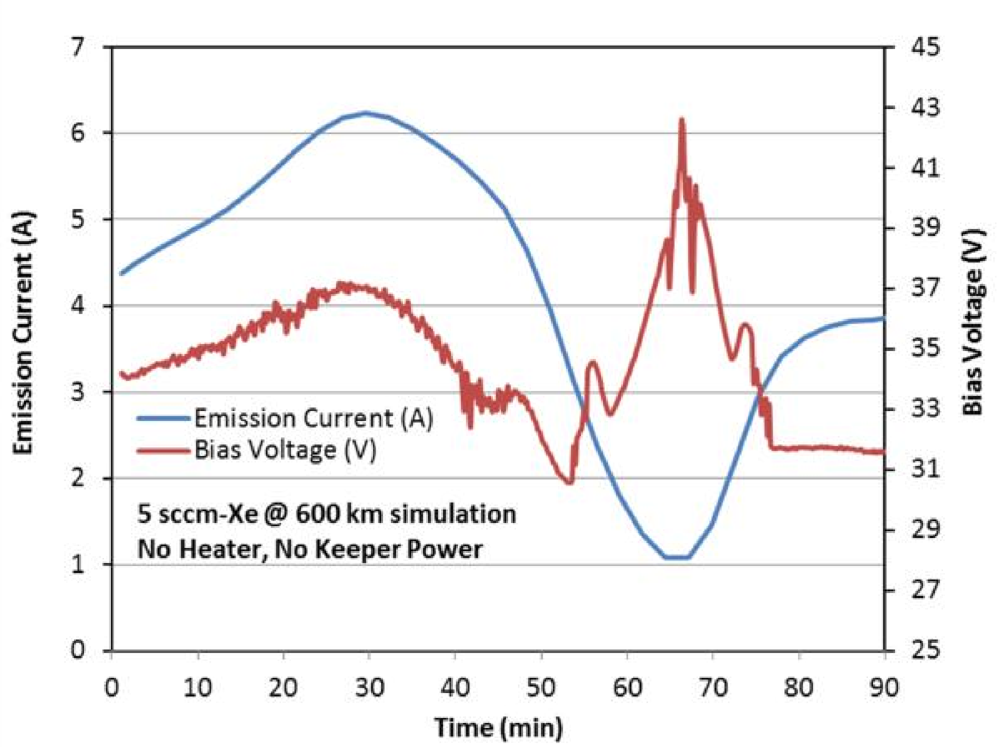

FIGURE 3.84. Measured CBV with varying emission current over a 90 minute period for the enclosed keeper configuration.

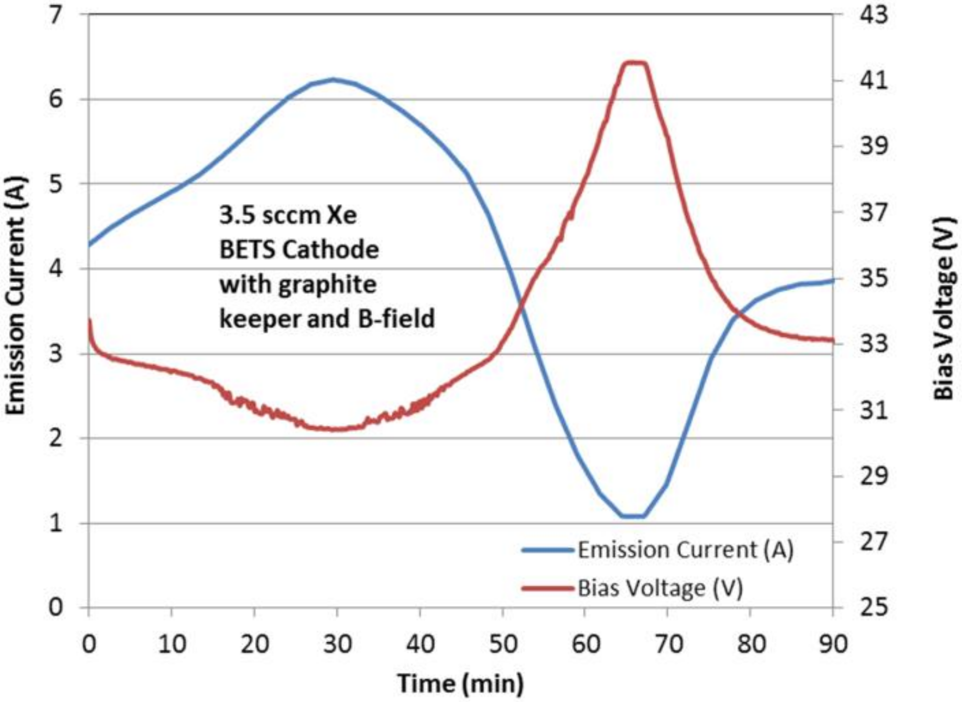

FIGURE 3.85. Measured CBV with varying emission current over a 90 minute period for the enclosed keeper configuration with a lightweight magnetic circuit added to enhance ionization.

CHAPTER 4

Conclusion and Recommendations for Future Work

This thesis involved the creation, validation, and testing of a simulation software tool called SimBETS. The tool was utilized to perform software-in-the-loop and hardware-in-the-loop tests that allowed specifications and requirements for a hollow cathode plasma contactor (HCPC) subsystem to be determined. Specific information and definitions of operating conditions generated with SimBETs included the determination of hollow cathode lifetime, expected maximum and minimum emission currents, detailed temporal behavior of the emission current, expellant mass and storage, and gas flow control. The following paragraphs present findings of this work and recommendations for future work for the electrodynamic tether scientific community in general and SimBETS in particular.

Many observations can be drawn using the SimBETS simulation results presented in Chapter 3. For example, increasing the assumed cathode bias voltage (CBV) produces an increase in deorbit time by $\sim 0.14\,\%\,per\,volt$ at low inclinations. For example, an increase in deorbit time of $7\,\%$ is observed when comparing an ideal $0\,V$ CBV simulation with a worst case $-50\,V$ CBV simulation ($0.14\,\frac{\%}{V} \times 50\,V = 7\,\%$). Although small, this effect can become detrimental with excessively large CBV magnitudes and/or high inclinations. A good HCPC system would minimize CBV magntiude through production of dense plasma in the plasma bridge region using techniques that enhance the neutral density of the expellant gas and contain energetic plasma electrons in this region. Under a given orbital condition, the maximum available CBV magnitude is set by the maximum available emf the EDT system can produce. Consequently, a good HCPC system that operates at low CBV magnitudes would allow more tether current to flow and more drag thrust to be produced in these situations.

Resonance effects that caused orbital parameters to change drastically over the course of a deorbit calculation were detected in nearly all of the simulations performed with SimBETS. This was expected because of variations in plasma density and magnetic field that exist along an orbit. Although resonance effects are interesting to model and observe, they typically will not affect the requirements and specifications of a HCPC system unless the resonances lead to higher inclinations and longer deorbit times. One way to significantly affect the deorbit performance of an EDT would be to reduce the inclination of the orbit as this would increase current collection and result in higher electrodynamic drag. Consequently, an interesting study would be to use resonances created by an EDT to decrease the inclination. For example, variable electrical loads placed within the end mass could be used to modulate the tether current so that inclination is continuously reduced or, at least, not allowed to increase.

SimBETS simulations show that variation in the EDT system parameters such as tether current and anode voltage are smaller at lower altitudes and low inclination because the orbital environments in these regions have less variation between the night and day sides of the Earth. The HCPC system is easier to specify for these orbital regions because the hollow cathode can operate without auxiliary power at tether currents above 1 A, a less extensive end-mass power storage and conditioning system would be needed. However, as the EDT produces more current, larger variations in flowrate are observed, requiring more care be taken in designing the HCPC flow controller.

It was observed that faster deorbit rates are achieved with higher currents. Although not surprising, this suggests that optimization can be performed to achieve a given level of performance. For example, by increasing tether length, width, or thickness; higher tether currents will be generated and faster deorbit rates can be achieved. Although SimBETS can be used for optimization of desired deorbit performance, total system mass, and/or minimization of cut probability; the focus of this thesis was placed on using SimBETS to define the HCPC system and determine the effects of the HCPC on deorbit time and total system mass. It is noted in this regard that other codes, namely BETsMA, are being developed for optimization studies. And it is further noted that good agreement between SimBETS and the EDT system modeling codes TeMPEST and BETsMA was observed in validation efforts, which increased our confidence in the results gathered with SimBETS.

Simulations performed with SimBETS indicate that variations in EDT system mass are only important for simulations of very large deorbit times that occur for highly inclined orbits or short/narrow tethers. This observation results in longer simulation run times. It was found that the simulation run time could be reduced by initially selecting a good rough estimate of the EDT system mass that would not require refinement in subsequent iterative simulations. While iterative simulations were not always performed, the final EDT system mass was always recalculated at the end of a simulation such that a relative tolerance of $10\,\%$ was achieved. Finally, although the EDT system mass wasnt found to strongly affect the deorbit time, SimBETS showed that satellite mass directly affects deorbit time. Specifically, increasing satellite mass by $500\,kg$ increases the deorbit time by a percentage of $75\,\%$, which is similar to the affect CBV has on deorbit time.

With decreasing tether length, tether width, or increasing orbital inclination, deorbit time increases dramatically. It is these types of missions that a varying CBV model is recommended for use because it is more accurate at tether currents below $1\,A$. Before implementation of a varying CBV model is attempted, however, a fixed CBV model using an average CBV similar to the average of the varying CBV model should be used. This will decrease runtime and allow for general results to be acquired quickly. It is suggested that deorbit times $\geq 1,600$ hrs, which is about equal to two months, should use a varying CBV model to ensure that an accurate estimation of deorbit time is obtained.

Overall, many interesting results have been generated by the studies performed using SimBETS. These studies only scratch the surface, however, and further studies using SimBETS and other codes are recommended. This EDT research should focus on uncovering other system-based specifications and requirements related to subsystem components like the deployer and electronics systems. Specification and requirements should also be determined to ensure the survival of the tether from cutting and its dynamic stability during deployment and during the mission. Specific recommendations SimBETS include:

- The code should be rewritten in C++ or Fortran to decrease runtime.
- The boundary value problem solving technique for the tether voltage and current profile should be replaced with the analytical technique developed by Bombardelli et al. [79].
- Further hardware-in-the-loop testing should be conducted using SimBETS and more realistic components such as the BET HCPC and the other components discussed in Chapter 2.

- A statistical micro-meteorite collision model should be included to allow for optimization routines to be implemented.
- Models should be implemented that include power generation and storage so that HCPC power supplies and electronics systems can be operated during low tether current phases of a mission. The HCPC oeration requires no heater and no keeper power above $\sim 1\,A$ of emission. However, operation and less current would require battery power or harvested power to be used to keep the HCPC operating. This is important because harvested power would drop the available emf for drag force generation and increase mission time.
- Studies should be conducted to determine if resonances and load harvesting can be used together to reduce inclination (or prevent it from increasing).

Bibliography

[1] European Space Agency, "About Space Debris,", 2012.

[2] J. R. Quinlan, C. A. Jones, V. Vittaldev, and A. Wilhite, "On the Design of an Active Debris Removal Architecture for Low Earth Orbit Space Debris Remediation," In *AIAA SPACE 2011 Conference & Exposition 27 - 29 September 2011, Long Beach, California AIAA*, pp. 1–15 (2011).

[3] D. J. Kessler and B. G. Cour-palais, "Collision Frequency of Artificial Satellites: The Creation of a Debris Belt," Journal of Geophysical Research **83,** 10 (1978).

[4] European Space Agency, "Hypervelocity impacts and protecting spacecraft,", 2012.

[5] "Falcon 9 Capabilities & Services,", 2013.

[6] F. Sykora, "Guido von Pirquet-Austrian Pioneer of Astronautics," in *History of Rocketry and Astronautics* (1986), p. 151.

[7] J. A. Goff, B. F. Kutter, F. Zegler, D. Bienhoff, F. Chandler, and J. Marchetta, "Realistic Near-Term Propellant Depots: Implementation of a Critical Spacefaring Capability,", 2009.

[8] M. L. Cosmo, E. C. Lorenzini, and Smithsonian Astrophysical Observatory, *Tethers In Space Handbook* (1997), No. December, p. 274.

[9] D. Kushner, "Five Ideas to Fight Space Junk,", 2010.

[10] E. Lorenzini and J. Sanmartín, "Electrodynamic Tethers in Space," Scientific American pp. 50–57 (2004).

[11] L. Johnson and M. Herrmann, "International Space Station Electrodynamic Tether Reboost Study," Technical Report No. July, NASA Marchall Space Flight Center (1998) .

[12] J. A. Carroll, *Guidebook for Analysis of Tether Applications* (1985), p. 47.

[13] D. L. Gallagher, L. Johnson, and J. Moore, “Electrodynamic Tether Propulsion and Power Generation at Jupiter,” Technical Report No. June, NASA Marshall Space Flight Center (1998) .

[14] K. R. P. Fuhrhop, Ph.D. thesis, University of Michigan, Ann Arbor, 2007.

[15] J. K. McTernan, S. G. Bilen, I. C. Bell, B. E. Gilchrist, R. P. Hoyt, N. R. Voronka, A. Arbor, and T. Unlimited, “ENERGY HARVESTING ON SPACECRAFT USING ELECTRODYNAMIC TETHERS,” In *18TH INTERNATIONAL CONFERENCE ON COMPOSITE MATERIALS*,

[16] J. K. McTernan and S. G. Bil, “Development of a Modeling Capability for Energy Harvesting Modules in Electrodynamic Tether Systems,” In *AIAA SPACE 2011 Conference & Exposition 27 - 29 September 2011, Long Beach, California AIAA*, pp. 1–15 (2011).

[17] E. Christiansen, J. Hyde, and R. Bernhard, “Space Shuttle Debris and Meteoroid Impacts,” Advances in Space Research **34,** 1097–1103 (2004).

[18] National Aeronautics and Space Administration, “The Threat of Orbital Debris and Protecting NASA Space Assets from Satellite Collisions,”, 2009.

[19] A. Alpatov, V. Beletsky, V. Dranovskii, V. Khoroshilov, A. Pirozhenko, H. Troger, and A. Zakrzhevskii, *Dynamics of Tethered Space Systems* (2010).

[20] J. R. Sanmartín, M. Martinez-sanchez, and E. Ahedo, “Bare Wire Anodes for Electrodynamic Tethers,” Journal of Propulsion and Power 9 (1993).

[21] J. R. Sanmartin, “A Review of Electrodynamic Tethers for Science Applications,” Plasma Sources Science and Technology **19,** 034022 (2010).

[22] J. R. Sanmartn and R. D. Estes, “The orbital-motion-limited regime of cylindrical Langmuir probes,” Physics of Plasmas **6,** 395 (1999).

[23] G. A. de Wijs, G. Kresse, L. Vocadlo, D. Dobson, D. Alfe, M. J. Gillan, and G. D. Price, “The Viscosity of Liquid Iron at the Physical Conditions of the Earths Core,” Nature **392,** 805–807 (1998).

[24] Wikipedia, “NRLMSISE-00,”, 2013.

[25] Wikipedia, “Atmosphere of Earth,”, 2013.

[26] Wikipedia, “Drag,”, 2012.

[27] C. C. Farnell, Ph.D. thesis, Colorado State University, 2007.

[28] R. Hoyt, R. Forward, G. Heinen, J. Slostad, and B. Minor, “THE RETRIEVE MICROSATELLITE TETHER DEORBIT EXPERIMENT,” Technical report, Tethers Unlimited, Inc. (2002) .

[29] J. A. Carroll and J. C. Oldson, “Tethers for Small Satellite Applications,” In *1995 AIAA/USU Small Satellite Conference in Logan, Utah,* p. 16 (1996).

[30] L. Curtis, J. Vaughn, K. Welzyn, and J. Carroll, “Development of the Flight Tether for ProSEDS,” In *AIP Conference Proceedings*, **608,** 385–392 (Aip, 2002).

[31] S. G. Bilén, J. K. McTernan, B. E. Gilchrist, I. C. Bell, N. R. Voronka, and R. P. Hoyt, “Electrodynamic Tethers for Energy Harvesting and Propulsion on Space Platforms,” In *AIAA SPACE 2010 Conference & Exposition 30 August - 2 September 2010, Anaheim, California AIAA,* pp. 1–11 (2010).

[32] S. D. Kovaleski, M. J. Patterson, and G. C. Soulas, “A Review of Testing of Hollow Cathodes for The International Space Station Plasma Contactor,” In *IEPC-01-276 at the 27th International Electric Propulsion Conference, Pasadena, CA, 15-19 October,*

2001, pp. 15–19 (2001).

[33] D. E. Parks, I. Katz, B. Buchholtz, and P. Wilbur, "Expansion and electron characteristics of a hollow-cathode plasma contactor," Journal of Applied Physics **4,** 9 (1993).

[34] K. R. Fuhrhop, B. E. Gilchrist, S. G. Bilén, and N. R. Voronka, "System Analysis of the Expected Electrodynamic Tether Performance for the ProSEDS Mission," In *39 th AIAA / ASME / SAE / ASEE Joint Propulsion Conference 20 23 July 2003 , Huntsville , AL AIAA 2003 5096*, p. 10 (2003).

[35] Wikipedia, "Space Tether Missions,", 2013.

[36] N. Kawashima, S. Sasaki, K. Hirao, W. J. Raitt, A. B. White, P. R. Williamson, P. Banks, and W. F. Sharpt, "Results from a tethered rocket experiment (charge-2)," Advances in Space Research **8,** 197–201 (1988).

[37] B. Gilchrist, P. Banks, and T. Neubert, "Electron Collection Enhancement Arising from Neutral Gas Jets on a Charged Vehicle in the Ionosphere," Journal of Geophysical Research **95,** 2469–2475 (1995).

[38] S. Williams, B. Gilchrist, and V. Aguero, "TSS-1R Vertical Electric Fields: Long Baseline Measurements using an Electrodynamic Tether as a Double Probe," Geophysical Research Letters **25,** 445–448 (1998).

[39] W. Burke, W. Raitt, and D. Thompson, "Shuttle Charging by Fixed Energy Beam Emissions," Geophysical Research Letters **5,** 725–728 (1998).

[40] V. Aguero, B. Gilchrist, and S. Williams, "Current Collection Model Characterizing Shuttle Charging During the Tethered Satellite System Missions," Journal of Spacecraft and Rockets **37,** 212–217 (2000).

[41] C. Chang, A. Drobot, and K. Papadopoulos, "Current-Voltage Characteristics of the Tethered Satellite System Measurements and Uncertainties Due to Temperature Variations," Geophysical Research Letters **25,** 713–716 (1998).

[42] J. Winningham, N. Stone, and C. Gurgiolo, "Suprathermal electrons observed on the TSS-1R satellite," Geophysical Research Letters **25,** 429–432 (1998).

[43] D. Thompson, C. Bonifazi, and B. Gilchrist, "The current-voltage characteristics of a large probe in low Earth orbit: TSS-1R results," Geophysical Research Letters **25,** 413–416 (1998).

[44] N. Stone, "Electrodynamic characteristics of the Tethered Satellite System during the TSS-1R mission," In *AIAA, Space Programs and Technologies Conference, AIAA*, pp. 1–12 (1996).

[45] H. A. Fujii *et al.*, "Space Demonstration of Bare Electrodynamic Tape-Tether Technology on the Sounding Rocket S520-25," In *AIAA Guidance, Navigation, and Control Conference 08 - 11 August 2011, Portland, Oregon*, pp. 1–12 (2011).

[46] B. Gilchrist, A. Arbor, J. Balance, L. Curtis, L. Johnson, J. Vaughn, and K. Welzyn, "Propulsive Small Expandable Deployer System (ProSEDS): Preparing for Flight," Technical report (2002) .

[47] J. A. Vaughn, L. Curtis, B. E. Gilchrist, A. Arbor, and S. G. Bilén, "REVIEW OF THE PROSEDS ELECTRODYNAMIC TETHER MISSION DEVELOPMENT," In *40th AIAA/ASME/SAE/ASEE Joint Propulsion Conference and Exhibit 11 - 14 July 2004, Fort Lauderdale, Florida*, pp. 1–12 (2004).

[48] L. Curtis and L. Johnson, "Propulsive Small Expendable Deployer System (ProSEDS)," In *AIP Conference Proceedings*, **608,** 261–268 (Aip, 2002).

[49] J. Sanmartín, E. Lorenzini, M. Cosmo, and R. Estes, “ANALYSIS OF PROSEDS BARE-TETHER PERFORMANCE,” Technical report, Universidad Politécnica de Madrid, Spain E.C.Lorenzini) .

[50] E. Ahedo and J. Sanmartin, “Analysis of Bare-Tether Systems for Deorbiting Low-Earth-Orbit Satellites,” Journal of Spacecraft and Rockets **39,** 8 (2002).

[51] K. R. Fuhrhop and B. E. Gilchrist, “Electrodynamic Tether System Analysis Comparing Various Mission Scenarios,” In *41st AIAA/ASME/SAE/ASEE Joint Propulsion Conference & Exhibit 10 - 13 July 2005, Tucson, Arizona*, p. 11 (2005).

[52] R. D. Estes, E. C. Lorenzini, and J. R. Sanmartin, “Short Tethers for Electrodynamic Thrust,” In *AIP Conference Proceedings*, **608,** 548–553 (Aip, 2002).

[53] K. Fuhrhop, B. West, and E. Choiniere, “Current Collection to Electrodynamic-Tether Systems in Space,” In *2nd International Energy Conversion Engineering Conference (IECEC), AIAA*, pp. 1–9 (2004).

[54] M. Leamy, A. Noor, and T. Wasfy, “Dynamic Simulation of a Tethered Satellite System using Finite Elements and Fuzzy Sets,” Computer Methods in Applied Mechanics and Engineering **190,** 4847–4870 (2001).

[55] R. Hoyt, J. Slostad, and R. Twiggs, “The Multi-Application Survivable Tether MAST Experiment,” In *39th AIAA/ASME/SAE/ASEE Joint Propulsion Conference and Exhibit, AIAA*, pp. 1–7 (2003).

[56] T. Kelso, “Orbital Coordinate Systems, Part III,”.

[57] National Geospatial Intelligence Agency, “World Geodetic System 1984,”, 2013.

[58] W. Fraczek, “Mean Sea Level, GPS, and the Geoid,”, 2003.

[59] Wikipedia, “Geodetic Datum,”, 2013.

[60] H. Curtis, *Orbital Mechanics for Engineering Students* (Elsevier Ltd., Florida, 2010), p. 740.

[61] T. Kelso, "Orbital Coordinate Systems, Part I,".

[62] Wikipedia, "Earth-Centered Inertial,", 2013.

[63] Wikipedia, "Earth-Centered, Earth-Fixed,", 2013.

[64] J. Sanz-Subirana, J. Juan Zornoza, M. Hernandez-Pajares, and S. Technical University of Catalina, "Transformations between ECEF and ENU,", 2011.

[65] Wikipedia, "RungeKutta methods,", 2013.

[66] N. H. Stone and C. Bonifazi, "The TSS-1R Mission: Overview and scientific context," Geophysical Research Letters **25,** 409–412 (1998).

[67] "bvp5c,".

[68] R. Samanta Roy, D. Hastings, and E. Ahedo, "Systems Analysis of Electrodynamic Tethers," Journal of Spacecraft and Rockets **29,** 1–10 (1992).

[69] I. Katz, J. R. Anderson, J. E. Polk, and J. R. Brophy, "A Model of Hollow Cathode Plasma Chemistry," In *38th AIAA/ASME/SAE/ASEE Joint Propulsion Conference and Exhibit 8-1 0 July 2002 Indianapolis, Indiana*, pp. 1–14 (2002).

[70] D. Bilitza, "International Reference Ionosphere,", 2013.

[71] I. A. of Geomagnetism *et al.*, "International Geomagnetic Reference Field: the eleventh generation," Geophysical Journal International **183,** 1216–1230 (2010).

[72] M. D. Rayman, P. Varghese, D. H. Lehman, L. L. Livesay, Jet Propulsion Laboratory, and California Institute of Technology, "RESULTS FROM THE DEEP SPACE 1

TECHNOLOGY VALIDATION MISSION," In *50th International Astronautical Congress, Amsterdam, The Netherlands, 4-8 October, 1999, IAA-99-IAA.11.2.01 Acta Astronautica 47, p. 475 (2000).*, **475,** 4–8 (2000).

[73] C. Carpenter, "Comparison of On-Orbit and Ground Based Hollow Cathode Operation," In *39th AIAA/ASME/SAE/ASEE Joint Propulsion Conference and Exhibit Joint Propulsion Conferences*, p. 7 (2003).

[74] "CEPPE Lab: A Little History,".

[75] V. Friedly and P. Wilbur, "High Current Hollow Cathode Phenomena," Journal of Propulsion and Power **8,** 635–643 (1992).

[76] J. D. Williams, Ph.D. thesis, Colorado State University, 1991.

[77] VACCO Industries, "VACCO Space Products: Xenon Flow Control Module,", 2011.

[78] National Institute of Standards and Technology, "Thermophysical Properties of Fluid Systems,", 2013.

[79] C. Bombardelli, J. Pelaez, M. Sanjurjo, and Technical University of Madrid (unpublished).